A FORCE BALANCE SYSTEM FOR THE
MEASUREMENT OF SKIN FRICTION DRAG FORCE

Quarterly Progress Report
for the period 9-15-69 to 12-15-69

NASA Grant No. NGL 47-005-026

Submitted by:

E. S. McVey and J. W. Moore

with

H. M. Sabella and D. A. Kettler

Research Laboratories for the Engineering Sciences

University of Virginia

Charlottesville

Report No. EME-4029-110-70U

January 1970

A FORCE BALANCE SYSTEM FOR THE
MEASUREMENT OF SKIŃ FRICTION DRAG FORCE

Quarterly Progress Report
for the period 9-15-69 to 12-15-69

NASA Grant No. NGL 47-005-026

Submitted by:

E. S. McVey and J. W. Moore

with

H. M. Sabella and D. A. Kettler

Divisions of Electrical and Mechanical Engineering
RESEARCH LABORATORIES FOR THE ENGINEERING SCIENCES
SCHOOL OF ENGINEERING AND APPLIED SCIENCE
UNIVERSITY OF VIRGINIA
CHARLOTTESVILLE, VIRGINIA

ELEVATED TEMPERATURE EFFECTS ON A

PROPORTIONAL FLUIDIC AMPLIFIER

A Thesis

Presented to

the Faculty of the School of Engineering and Applied Science
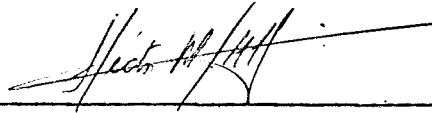
University of Virginia

In Partial Fulfillment

of the Requirements for the Degree

Master of Mechanical Engineering

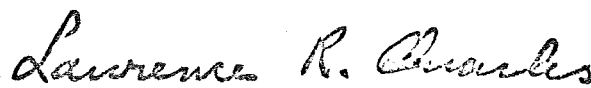
by

Héctor Mario Sabella

June 1970

APPROVAL SHEET

This thesis is submitted in partial fulfillment of

the requirements for the degree of

Master of Mechanical Engineering

_____
Author

Approved:

_____
Faculty Adviser

_____
Dean, School of Engineering and
Applied Science

June 1970

ii

TO MY PARENTS

ABSTRACT

This thesis is a study of the effects of elevated temperatures on the performance of a vented jet proportional fluidic amplifier. A model was built according to the design principles found in the literature. Tests were conducted to obtain the static and dynamic response for several different temperatures from 70 to 2000°F.

Test results obtained from the static response of the amplifier are presented in several charts. Most of these results were used to evaluate the theoretical dynamic response of the amplifier. Finally these values are compared with the experimental values obtained from the dynamic response tests.

To obtain the dynamic response it was necessary to design a pneumatic sinusoidal signal generator which could be located inside the test oven and be able to cover a wide range of frequencies.

Good correlation, particularly at room temperature, was found between the theoretical and experimental dynamic response. Differences were mostly due to transmission line effects which were only approximated in this study.

ACKNOWLEDGMENTS

TABLE OF CONTENTS

TABLE OF CONTENTS (continued)

LIST OF TABLES

LIST OF FIGURES

LIST OF FIGURES (continued)

LIST OF SYMBOLS

A   area, in^2

a   effective channel width, inches

C   fluid capacitance, in^5/lb

d_1 diameter nozzle signal generator, inches

d_2 diameter chamber nozzle signal generator, inches

E   distance from the cross point of the power and control jets, to the output ports, inches

F   force, pound

f   frequency, cps

G   amplifier pressure gain, dimensionless

g_c = $32.2 \dfrac{lb_m \ ft}{lb_f \ sec^2}$

h   grooves depth, inches

j   imaginary factor, $\sqrt{-1}$

K_p amplifier pressure amplification factor, dimensionless

L   fluid inductance, $lb \ sec^2/in^5$

l   length, inches

l_1 constant width output ports section, inches

l_2 variable width output ports section, inches

$\dot{m}$ mass flow rate, lb_m/sec

P   static pressure, psig

Q   volumetric flow, ACFM

R   fluid resistance, $lb \ sec/in^5$

S   distance from the center line of the power jet to control ports, inches

s   Laplace operator, 1/sec

T   temperature, °F

T_1 lower temperature, °F

T_2 higher temperature, °F

t   time, seconds

U   volume, in^3

V   velocity, in/sec

$\bar{V}$ average velocity, in/sec

W   channels width, inches

ΔP_C = $P_{CL} - P_{CR}$, psig

α   phase angle due to pure time delay, degrees

β   power jet deflection angle, degrees

φ   total phase angle, degrees

θ   angle between power nozzle center line and output ports, degrees

ρ   mass density, slugs/in^3

ω   angular velocity, rad/sec

Σ   summation

Subscripts

a   interaction region

ab   absolute

C   control port

CD   control differential

d	delay
eff	effective
in	input
L	left
ℓ	load
0	output port
OD	output differential
out	output
R	right
S	supply
T	total
x	coordinate axis
y	coordinate axis

CHAPTER I

INTRODUCTION

The increasing number of applications of fluidic systems in automatic control areas have brought up the necessity of studying and developing these systems considering environmental effects. Research work dealing with a pneumatic skin friction sensor for a ramjet is presently being considered in the Department of Mechanical Engineering at this University [1]. This research, which has been sponsored by the Force Measurement Group of NASA at Langley Field, Virginia, has shown that a pneumatic proportional fluidic amplifier could be used in two ways:

1) Included in the closed loop system as a pure gain amplifier or as an element of a pneumatic compensating network for the stability of the whole system.

2) To amplify the flapper valve readout signals.

Because the whole system is supposed to be located in an area of the airplane where temperatures can be as high as 2000°F, the performance of the amplifier will be studied at different temperatures ranging from room temperature, 70°F, up to 2000°F.

Background

In 1962 the Diamond Ordnance Fuze Laboratories (now Harry Diamond Laboratories) presented a fluidic amplifier with no moving parts, giving a new advance in the field of control and fluidic logic [2]. Many

I

researchers have been subsequently dealing with this new idea in control engineering. References [3],[4],[5],[6],[7] give a very good background on this new subject. Most of these investigations were performed using etched glass models.

In 1968, at the Laboratories of McDonnell-Douglas Astronautics Co., temperature effects on several pure fluidic amplifiers at temperatures up to 1500°F were analyzed. Acoustic, vibration and shock effects were studied as well [8].

Figure 1 shows a plan view of the top and bottom plate of the test amplifier. Its main dimensions are given in Figure 2. High energy fluid is supplied through the power nozzle, becoming a power jet when it reaches the interaction region. Two control or low energy jets, set normal to the power jet are also directed to that region. In operation a small deviation from the balanced condition in the pressure of one of the control jets deflects the power stream and causes one output to collect more fluid than the other. In other words, if a differential control pressure exists, a differential output pressure will be obtained. If both control pressures are equal no deflection is supposed to happen in the power jet, and the differential output pressure will be nil. In this way the amplifier is capable of providing a large differential output signal that is proportional to a small differential input signal.

The imbalance between control pressures which produces a deflection on the power jet was studied by Moynihan and Reilly [9] and is also analyzed in the report presented by Chui and Man [10]. These authors used for the analysis the control volume presented in Figure 3. The boundaries of this control volume in the control and power nozzles were
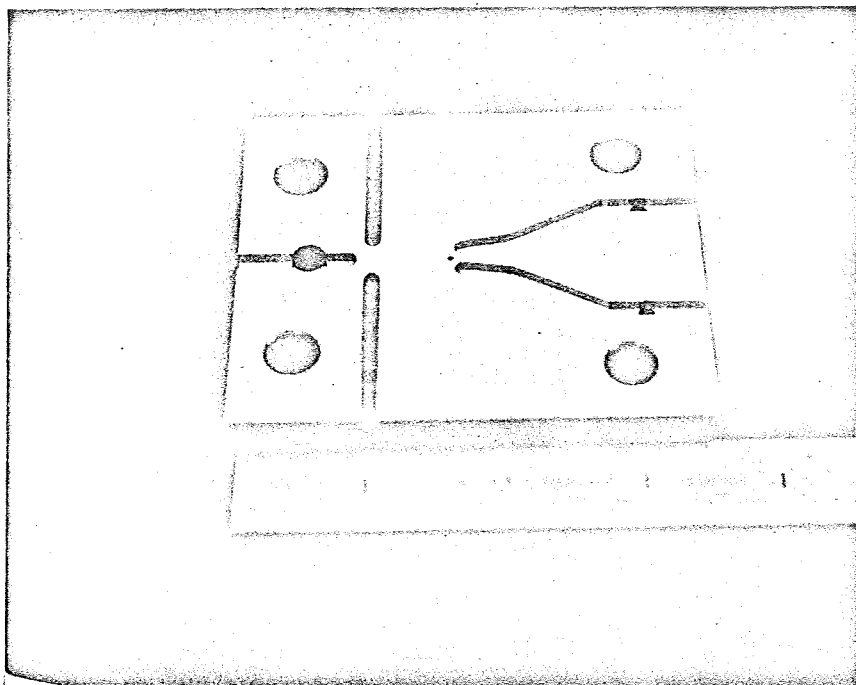
Top Plate
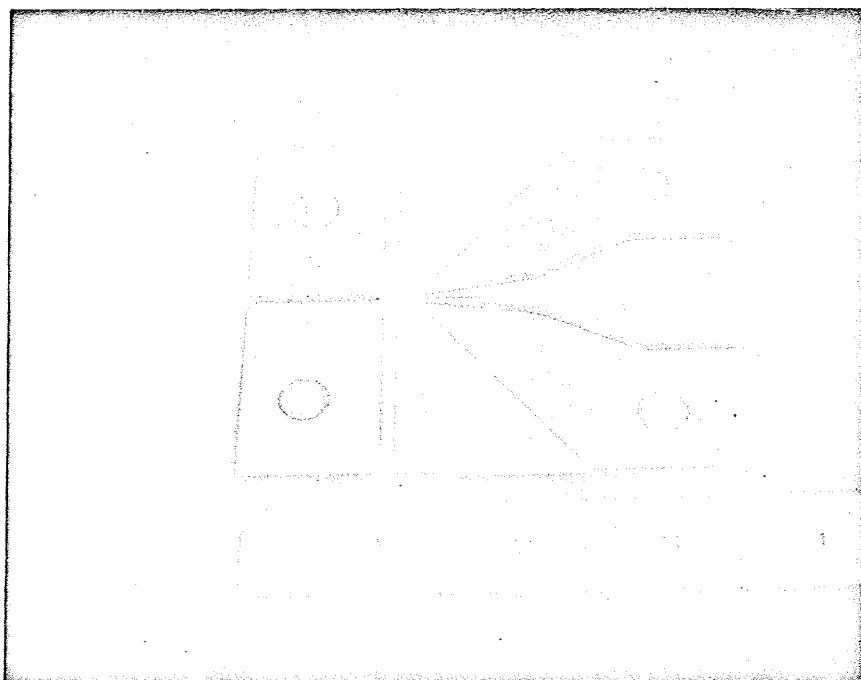
Bottom Plate

Figure I. Amplifier Top and Bottom Plates

Left output port ———

Right output port ———

Vent ———

Interaction region

Left control port

Right control port

Supply port ———

$E = 0.240$
$W_S = 0.021$
$W_C = 0.032$
$W_O = 0.032$
$S = 0.037$
$l_1 = 0.250$
$l_2 = 0.180$
$h = 0.046 \text{ (depth)}$
$\text{aspect ratio} = \dfrac{h}{W_S} = 2.19$
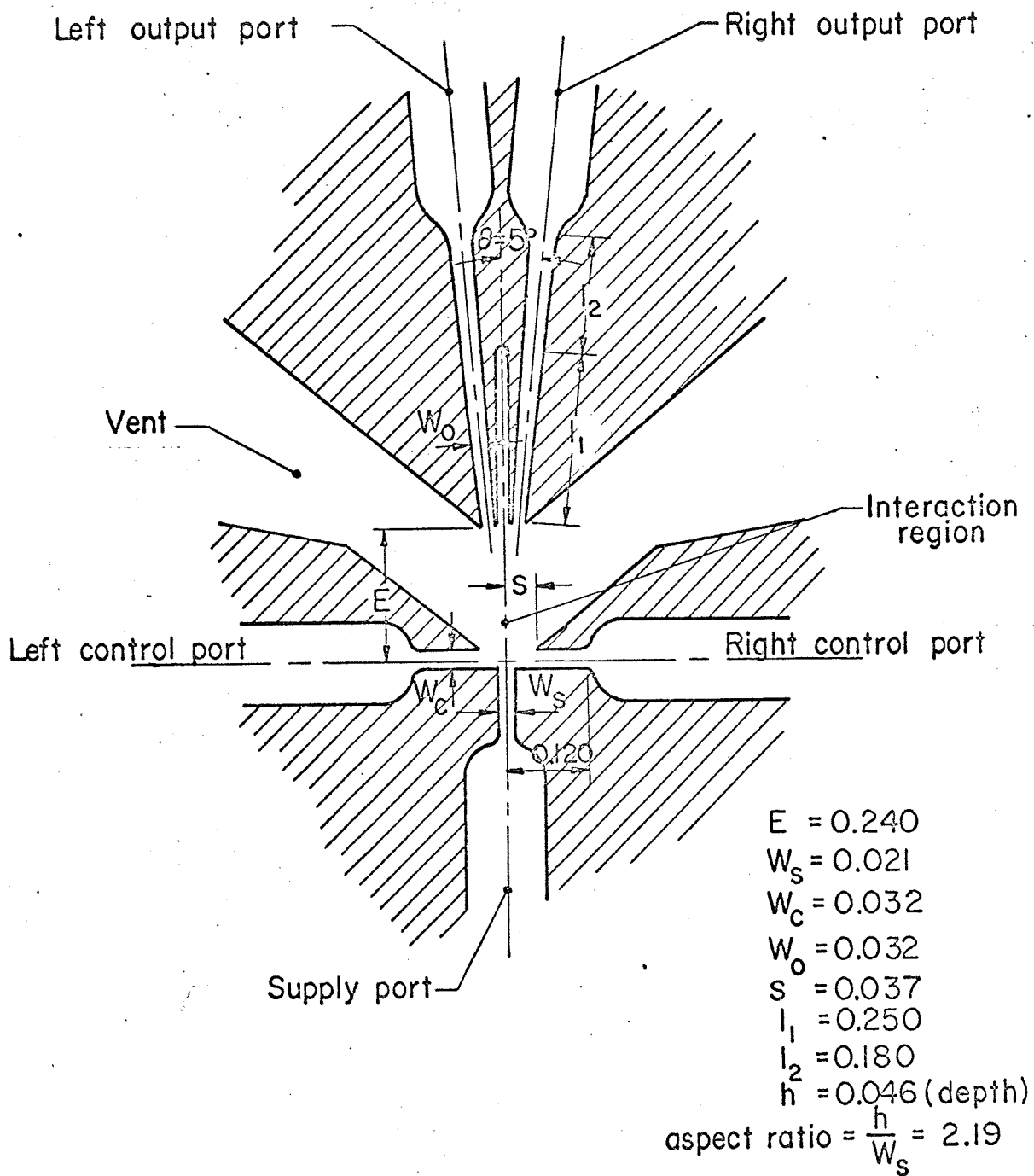
Figure 2.   Amplifier Main Dimensions

determined by Moynihan and Reilly experimentally through measurement of the static pressure distributions. It was found that approximately one channel width upstream from the exit of the control and supply ports the flows were uniform because the static pressure distributions were also uniform. Also the internal centrifugal forces of the deflected power jet originated transverse pressure gradients.

The downstream limit of the control volume was drawn so all of the exit flow was through the face B-C. The analysis was based on the following assumptions:

1) The flow direction through B-C is uniform.

2) The static pressure outside the control volume is uniform and equal to the ambient pressure. This is correct if B-C is sufficiently far downstream.

3) The flows through A-B and D-C (entrained flow) are equal in magnitude but opposite in direction.

4) The static pressure distributions along A-B and D-C are equal.

Considering these assumptions and using the momentum equations for the control volume we can write:

In the X direction,

$$\dot{m}_a \bar{V}_a \sin\beta - \dot{m}_{CL} V_{CL} + \dot{m}_{CR} V_{CR} = W_C P_{CL} - W_C P_{CR} + \Sigma F_x \qquad (1.1)$$

In the Y direction,

$$\dot{m}_a \bar{V}_a \cos\beta - \dot{m}_S V_S = W_S P_S - a P_a + \Sigma F_y \qquad (1.2)$$
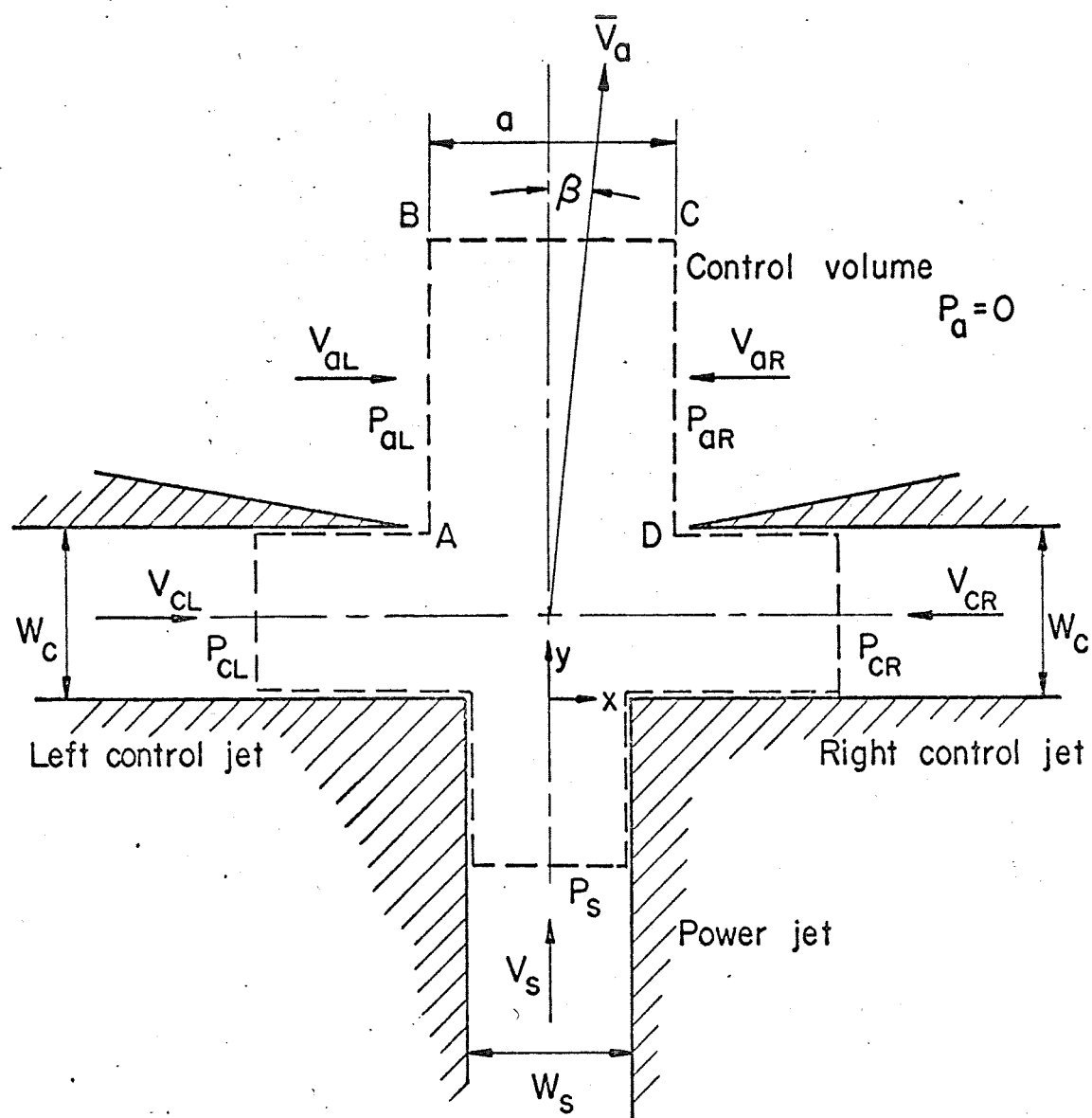
Figure 3   Control Volume for Analysis of
Power Jet Deflection

where F is the pressure forces of the walls on the fluid in the respective directions. Taking P_a (reference or ambient pressure) equal to zero, and combining (1.1) and (1.2) we get,

$$\tan\beta = \frac{\dot{m}_{CL}V_{CL} - \dot{m}_{CR}V_{CR} + W_C(P_{CL} - P_{CR}) + \Sigma F_x}{\dot{m}_S V_S + W_S P_S + \Sigma F_y} \quad . \tag{1.3}$$

If only momentum forces are considered in the analysis, the equation for the deflection angle can be reduced with sufficient accuracy to this simple form,

$$\tan\beta = \frac{W_C}{W_S} \frac{P_{CL} - P_{CR}}{P_S} \tag{1.4}$$

This formula is also given in a paper by Dexter [3].

Scope

This thesis covers the development and testing of a vented jet proportional fluidic amplifier in its static and dynamic response for six discrete temperatures going from 70 to 2000°F.

Input, output and transfer characteristics, which are defined in Chapter IV, were plotted for each one of the temperatures aforementioned. From the input and output characteristics the values of the fluid resistances, capacitances, inductances, pressure amplification factor and time delays were obtained. The transfer characteristics gave us the variation of the amplifier gain, null shift and linear range as function of temperature, and for some particular values of temperature, as a function of the supply pressure as well.

These parameters enabled us to draw the theoretical Bode plots and to see how the values experimentally obtained in the dynamic response of the amplifier matched with those predicted by theory.

The design and construction of a sinusoidal signal generator was required as part of the dynamic analysis of the amplifier. The generator had to be used under the same environmental conditions as the test amplifier.

CHAPTER II

DESIGN PARAMETERS OF THE AMPLIFIER

The design of a fluidic amplifier can be considered a trial and error problem. Even though a good idea can be obtained from different reports presented by researchers [4],[5],[7] who have tested several devices at room temperature conditions, there is not too much information about the effects of temperature on the amplifier parameters. The study concerned with high temperature effects on proportional amplifiers done by Madonna, Anderson and Harris [8] can be considered useful but not general because only six amplifiers were tested and temperatures reached 1500°F. For this reason designs of room temperature models already tested were taken as a baseline extracting from these researches all possible values.

Based on the characteristics of commercial amplifiers known to date, a pressure gain between 5 and 5.5 at room temperature, was expected to be obtained. The supply nozzle of these commercial amplifiers is around 0.020 inches wide. This dimension was adopted for the design of the test amplifier (i.e., W_S = 0.020 in). Figure 2 shows dimensions and nomenclature used throughout this chapter.

Peperone, et al. [11] show that the pressure gain is relatively sensitive to the load acting on the output ports; the shape of the pressure profile at the entrance of the output apertures $P = P(\beta_0)$; the distance E from the supply nozzle to the receivers; the stream deflection β and width W_0 of the output ports.

Let us define what is meant by a load acting on the amplifier. The load is in direct relationship with the flow demanded from the amplifier in the circuit. For example, an amplifier is unloaded when an infinite impedance is connected to the amplifier output receivers. By impedance is meant a passive fluidic element which requires a pressure drop to establish a flow through it. Therefore, a complete similitude with an electric circuit can be defined. To achieve the correlation, voltage has to be substituted for air pressure and current intensity for air flow.

The slope of the pressure profile, shown in Figure 4, is affected by
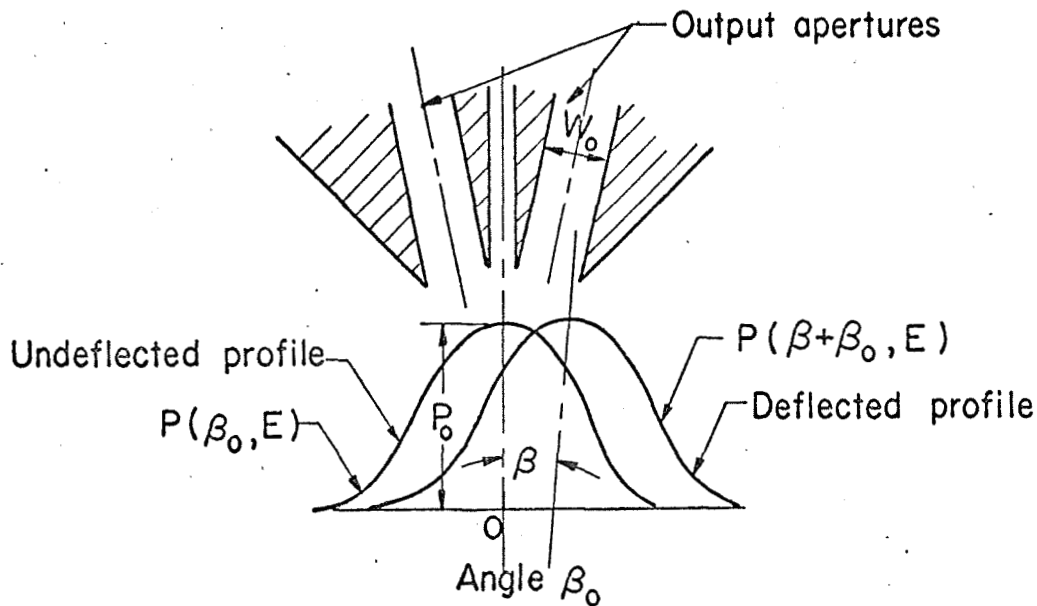
Figure 4. Typical Pressure Profile at the Output Receivers

the width of the control nozzles and their distance from the power nozzle, in such a way that increasing these dimensions, increases the amount of control flow. This fact does not change the downstream center

line value of the pressure profile but lowers the slope of the profile
and consequently less pressure gain is obtained. This pressure gain
loss is found when the control flow is higher than 30 per cent of the
supply jet flow. If the control flow is kept less than this percentage
stipulated before, the pressure profile is not appreciably affected and
it is even possible to obtain a pressure gain increment by increasing
the control nozzle width but keeping the control flow within the
limitations mentioned before [6].

Experiments developed by Van Tilburg and Cochran [5] also pertained
to the influence of the distance S from the power nozzle to the control
nozzles upon the amplifier pressure gain. They say that S has little
in effect on the amplifier gain for small percentages of the control
flow with respect to supply flow. Taking values from this last research
work the control edge width was chosen equal to 3.7 W_S and the control
nozzle width 1.55 W_S.

After considering the report presented by Dexter [3] the output
port width, W_0, was taken equal to the control nozzle width W_C (i.e.,
W_0 = 1.55 W_S).

The aspect ratio defined as the ratio of the depth of the supply
nozzle to its width, was chosen equal to 2.3. In this way the depth
of all grooves was h = 0.046 in.

As mentioned before, the distance E from the power supply nozzle
to the output ports or receivers is important. Increasing the value
of E produces a center line degradation in the pressure profile and
in consequence a lower pressure gain. But also, the increment of E

gives a higher pressure gain because the pressure profile displacement is increased. For the zero deflection of the power jet, a maximum pressure gain of 11.1 was obtained for $E = 13.5 \, W_S$ [6]. Dexter [3] also found that for zero deflection of the power jet, the maximum momentum gain of 13.4 occurs at about $E = 9 \, W_S$. To be within the values maximum pressure and momentum gain, E was taken equal to $11 \, W_S$.

The length of the output ports was divided into two sections and their values chosen according to Reid [12]. The first section, with a constant width equal to $1.55 \, W_S$, was 0.250 in long and the second one, which behaved as a diffuser, had an ending width equal to 0.046 in and a total length of 0.180 in.

The output nozzles were designed with an angle of $\theta = 4°$ between their center line and the power jet center line. For higher values of this deflection angle the amplifier becomes nonlinear and gain is considerably reduced [6].

Finally vents were designed such that they provided an area or angle between their walls large enough to avoid any wall attachment (Coanda effect) in the interaction region.

In summary, the proposed main dimensions of the amplifier can be detailed as follows:

W_S = 0.020 in

W_C = 0.030 in

W_0 = 0.030 in   S = 0.037 in

E = 0.220 in   h = 0.046 in

l_1 = 0.250 in θ = 4°

l_2 = 0.180 in   Aspect ratio = 2.3

CHAPTER III

AMPLIFIER DEVELOPMENT

The model investigated was constructed using two plates 3.50 in long, 3.00 in wide and 0.75 in thick. In order to get minimum amplifier dimensional changes and avoid all possible corrosion, both effects being produced by high temperatures, stainless steel RA 330 (AMS 5592). was selected as the proper material. The same is produced by Rolley Alloy Inc.

The dimensions of the plates were chosen so that there would be room on the top plate to locate the taps to measure the supply, control and output pressures. The amplifier itself had the following dimensions: 1.125 x 0.750 x 0.750 in.

As explained below a much better result in the construction of the amplifier profile could have been obtained by etching it on the plates. Because this process was not available at this University, the grooves were made using a milling machine. This limited the design of the amplifier and therefore it was not possible to get the dimensions stipulated at the end of Chapter II.

Downstream distance of the input ports and their angle with respect to the supply nozzle were particularly affected. It was necessary to build a dump at the center as shown in Figure 2 and the angle of the receivers was enlarged. Its minimum possible value was .5°. To get sharp edges at the receivers entrance, the distance E was increased up to 0.240 in.

After machining, the final dimensions of the amplifier were:

W_S = 0.021 in

W_C = 0.032 in

W_O = 0.032 in S = 0.037 in

E = 0.240 in h = 0.046 in

l_1 = 0.250 in θ = 5°

l_2 = 0.180 in   Aspect ratio = 2.19

Upstream in the power and control nozzles and downstream in the outputs, the grooves were made 0.125 in wide and 0.090 in high in each plate. This was done to obtain symmetry of flow in each nozzle. As they were built, the amplifier ports were at the center of the larger grooves. Also, on these larger grooves and on the top plate only, five holes were drilled to set the taps to measure pressures. These orifices can be seen on the top plate shown in Figure 1.

All channels were polished by the author as best as possible. Also the contact surfaces were polished and lapped, afterwards, obtaining a perfect contact between them. Finally both plates were brazed together. A vacuum oven at NASA Langley Field was used for this purpose. Nicrobraz 30, produced by Wall Colmonoy Corporation, was used as filler metal. Besides having excellent strength properties and oxidation resistance, it has low diffusion at the brazing temperature of 2175°F [13]. This prevented the grooves getting clogged during the brazing process.

The brazing compound was put along the edges of the contact surfaces and also in four small cavities at the central part of the amplifier.

Internal or external leakages due to any possible gap between surfaces were avoided in that way.

Temperatures of the supply, control and output flows were measured with chromel-alumel exposed junction thermocouples. In these thermocouples the sheath insulation is sealed at the point of entry to prevent penetration of air. The thermocouples were manufactured by Omega Engineering Inc. Their model is CAIN-316E-12.

The supply flow was preheated before going into the amplifier to obtain flow temperatures close to oven temperatures. A 3 ft long coil located inside the oven was satisfactory to get the temperatures required.

For air flow and pressure measurements, 316 stainless steel tubes, 0.250 in O.D. and "Swagelok" fittings of the same material, were used in the project. High temperature lubricant, "Silver Goop" was applied to all fittings. This allowed some of them to be taken apart after the static test was performed and rectify the setup for the dynamic test. Both lubricant and fittings are produced by Crawford Fitting Company.

CHAPTER IV

EXPERIMENTAL DETERMINATION OF THE AMPLIFIER STATIC RESPONSE

The next step in this research was to obtain the static response
of the amplifier. This enabled us to obtain the input, output and
transfer characteristics. From them it was possible to compute the
parameters already mentioned in the scope of this thesis. Some of
these parameters were required later in determination of the theoretical
dynamic response.

During some trials at room temperature it was observed that a high
frequency noise was produced at the interaction region. This problem
was eliminated with two side walls on the vents. Several dimensions
of these walls were tested until the most adequate one was obtained.
Finally the aperture of the vents on the side of the plates was
approximately 0.300 in. It was also found that by using these walls
the pressure gain increased a little. This solution and result of
the problem were also treated by E. M. Dexter [3].

Temperatures at 70, 500, 1000, 1500, 1800 and 2000°F were selected
for the experiment. The respective values of pressures and flows were
taken at each temperature in order to plot the amplifier characteristics
curves previously mentioned. After the temperature had reached 2000°F,
some of the values obtained in the preceding steps were verified as the
temperature went down. Readings did not show appreciable differences
with those taken when temperature was increasing. When temperature
became normal again (70°F), it was necessary to clean up tubes and
grooves with high pressure air. It was possible to observe from the

16

external aspect of the elements that corrosion affected mainly fittings and tubes, while the amplifier was fairly clean.   After the amplifier was cleaned, room temperature data were taken again and values coincided with those taken at the beginning of the experiment.

Approximately two hours were required to take the data at each temperature. This includes the time required for the oven to reach the equilibrium temperature at each value selected for the experiment (15 minutes approximately).

The speed of the supply flow inside the tube where the thermocouple was located varied approximately between 28 ft/sec at room temperature, and 75 ft/sec at 2000°F. This says that temperature errors due to fluid velocity could be neglected.   In the control and output lines the speed was lesser, and therefore errors were also neglected. Because the tube wall temperatures were not measured it was not possible to compute the radiation error in the flow temperature measurements.

Experimental Setup

A schematic diagram of the experimental setup is shown in Figure 5, and a general view of Figure 6. All tests were performed in an electric oven (11 x 11 x 11 in). Figure 7 shows the amplifier located in the test position.

Besides the element tested, the experimental setup consisted of a manifold, flowmeters, pressure gages, water or mercury manometers and potentiometers.

The instruments were placed far enough from the oven to avoid any temperature effect upon the readings. To be certain that air leaving
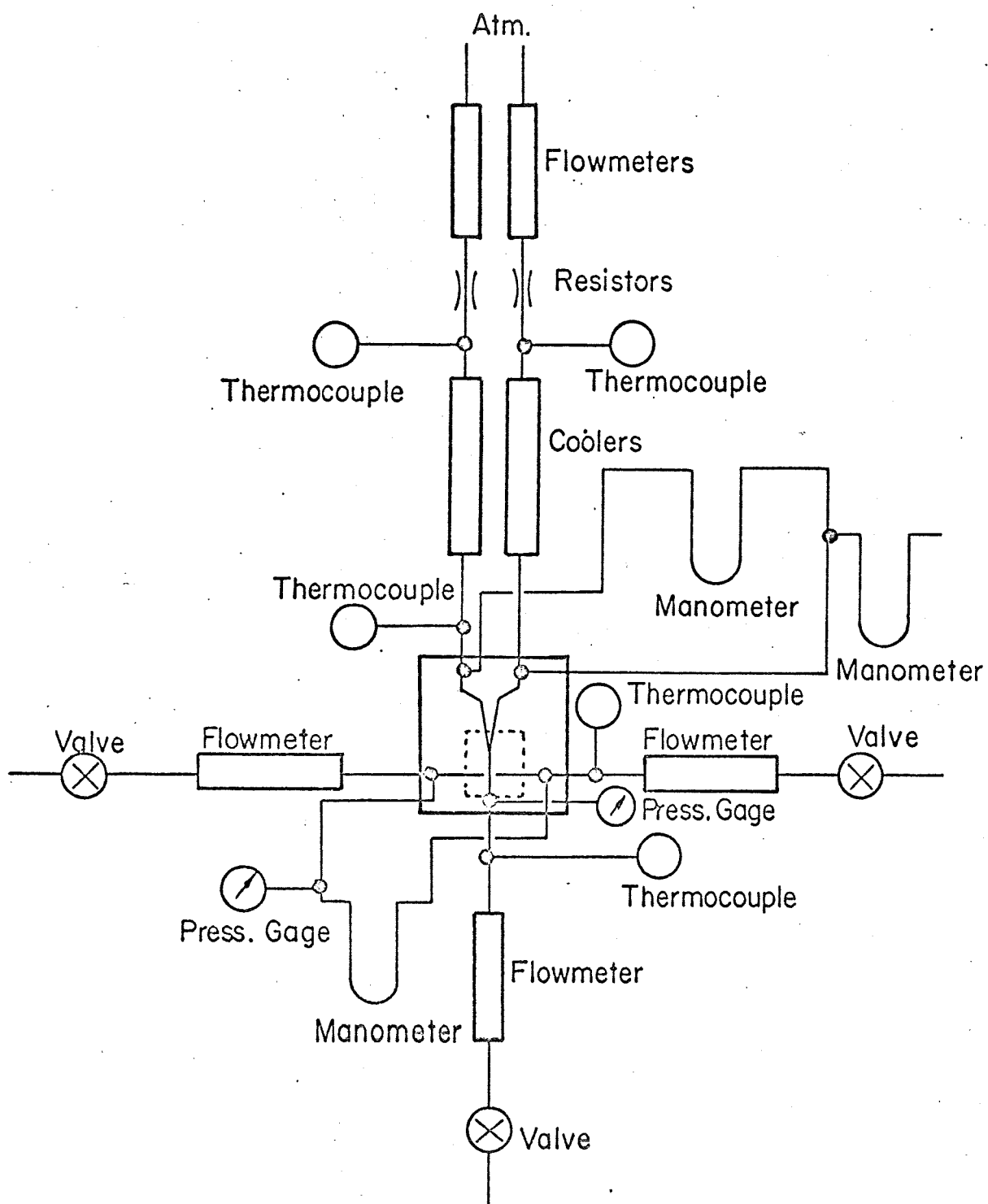
Figure 5   Schematic Diagram of the Static Test Circuit
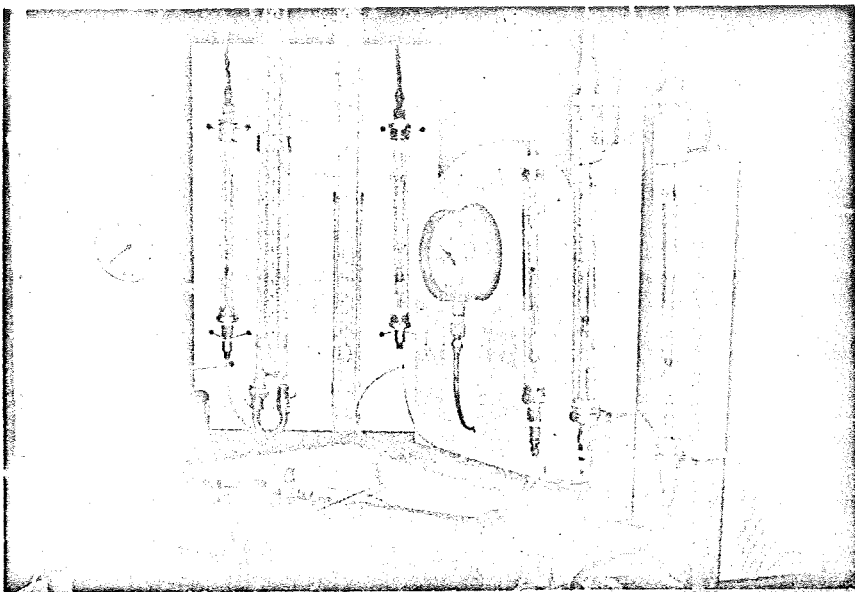
Figure 6. Experimental Setup - Static Response Test
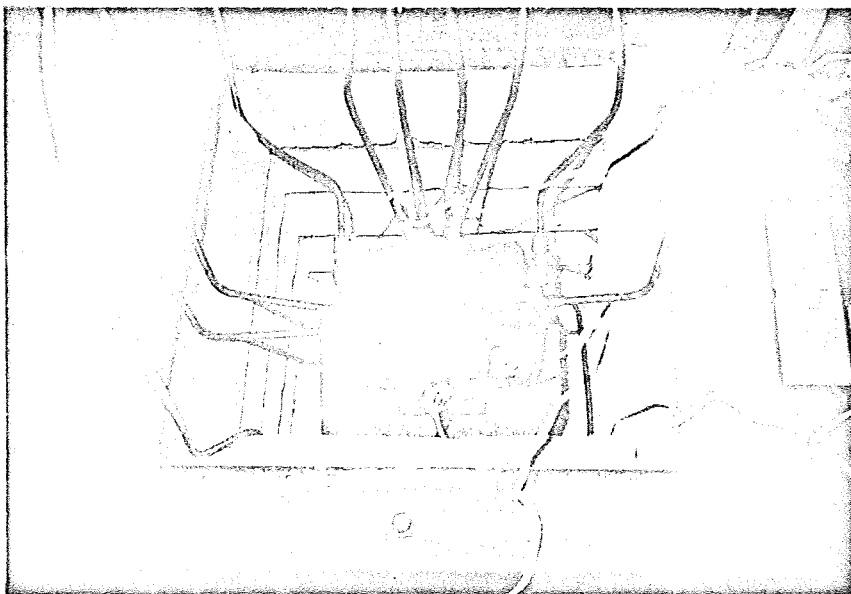
Figure 7. Amplifier in Oven (Top Removed) - Static Response Test

the output ports kept a constant temperature (about 70°F) when passing through the flowmeters, two water coolers were located between the amplifier and flowmeters. This was done to reduce the output air temperature to standard temperature (70°F) and prevent any damage to the instruments.

Temperatures were measured at the supply, control and output ports inside the oven. A second reading of the output flow temperatures was obtained before passing through the flowmeters. The thermocouples were monitored by double range potentiometer indicators. Reference junctions were at 70°F.

As explained in the preceding chapter, pressures were measured through taps located on the amplifier top plate. This means that measurements showed undisturbed or static pressures, rather than stagnation pressures. This was done to simplify the setup inside the oven where there was not room enough to locate tanks and make possible the stagnation pressure measurement.

Experimental Results

At the temperature steps previously mentioned data were taken in order to plot the power jet, input, output and transfer characteristics. Their descriptions are explained below.

Power jet characteristics. With a constant 5 psig supply pressure and no loads on the outputs, the supply pressure was measured for each oven temperature. As predicted, the volumetric flow increased as temperature increased. This variation presented in Figure 8 followed approximately the relation $\sqrt{T_2/T_1}$.
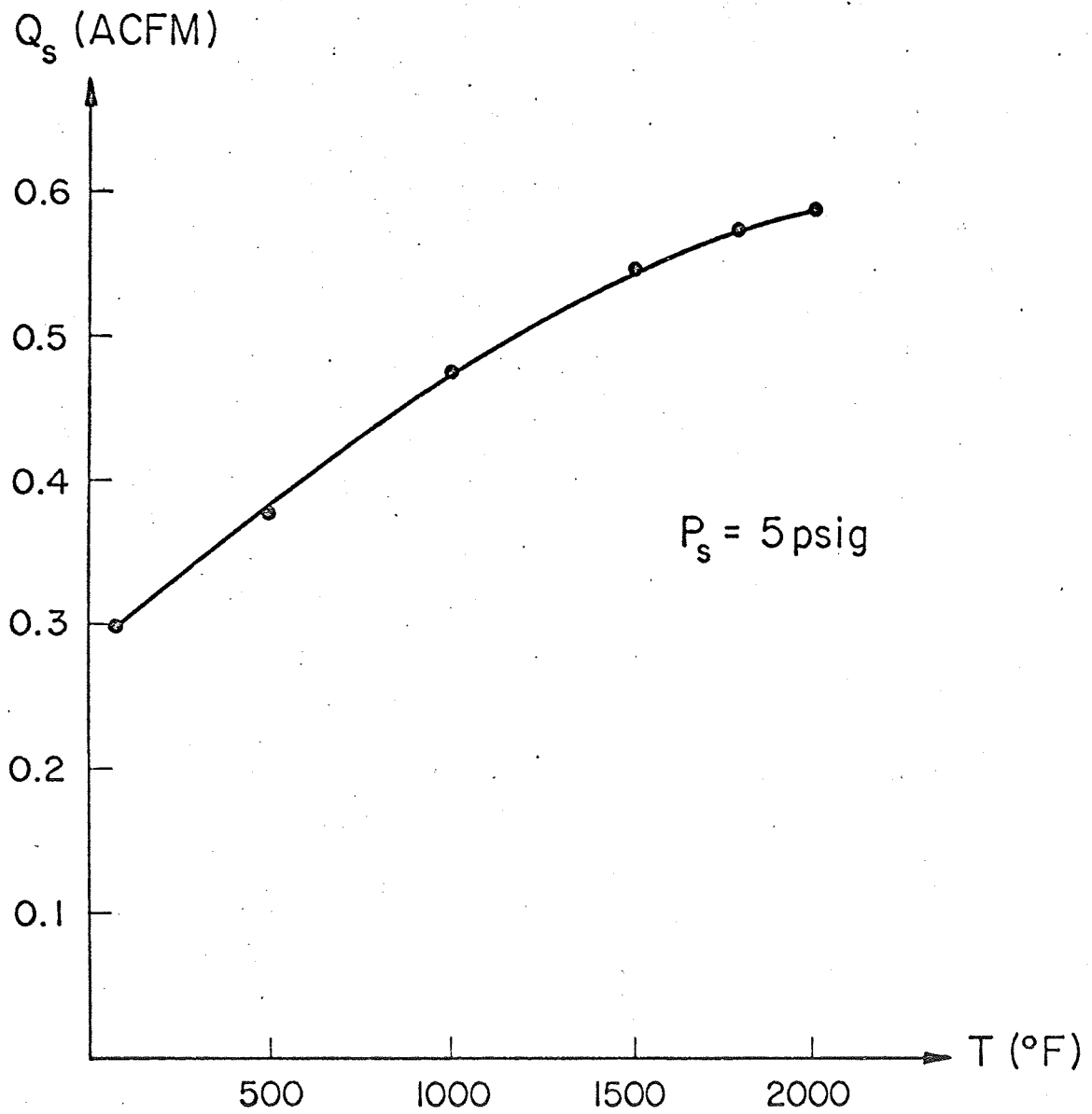
Figure 8   Power Nozzle Supply Flow versus Temperature

Input characteristics. The load that an input signal "sees" when it is applied to the control port can be derived from the input characteristics. These relate the control flow with the pressure applied on the same port.

Even though it is not a strict rule in amplifier design, the control bias pressure is generally taken as 10 per cent of the supply pressure. Adopting this convention, control pressures were taken equal to 0.5 psig.

Varying the control pressure from 0 to 1.2 psig and with no load on the outputs, the control flow versus control pressure, for one control port, was recorded. The values of bias points in Figures 9 to 14 represent the values where the left control pressure P_{CL}, was equal to the right control pressure P_{CR} (i.e., $P_{CL} = P_{CR}$).

To obtain the values of control resistances, both control pressures were set at the point where $P_{CR} = P_{CL} = 0.5$ psig. Then one of the pressures was varied from 0.7 to 0.30 psig. The other control pressure was set at such a value to keep the relation $P_{CL} + P_{CR} = 0.5$ psig constant. In that way the respective values of control flow for different pressures were obtained. From these curves it was possible to find the control port resistances.

Values of control pressures and flows were normalized with respect to supply pressure and flow as can be seen in the figures previously mentioned. This was done in order to compare the normalized data for each value of the temperature taken in consideration. These normalized data show that rather similar values were obtained for the temperature range considered. Thereby it is possible to say that input characteristics can be predicted for other temperatures besides those tested.
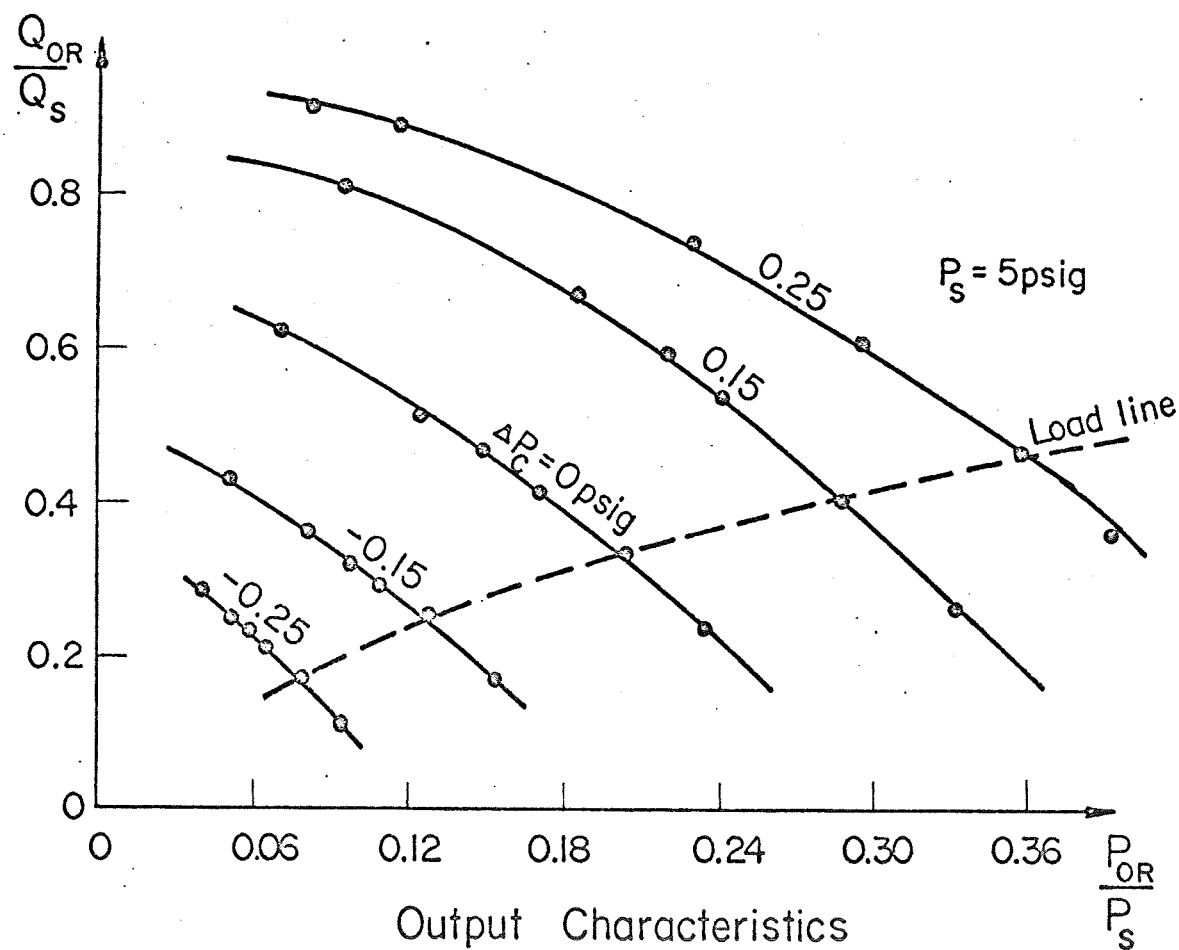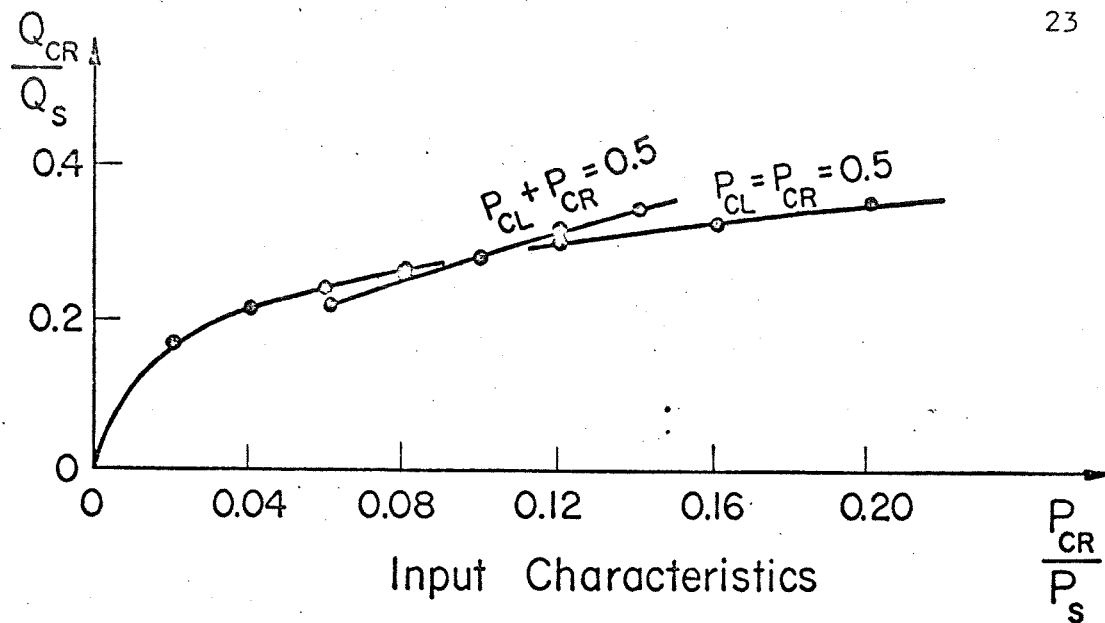
Figure 9   Normalized Input and Output Characteristics (70°F)
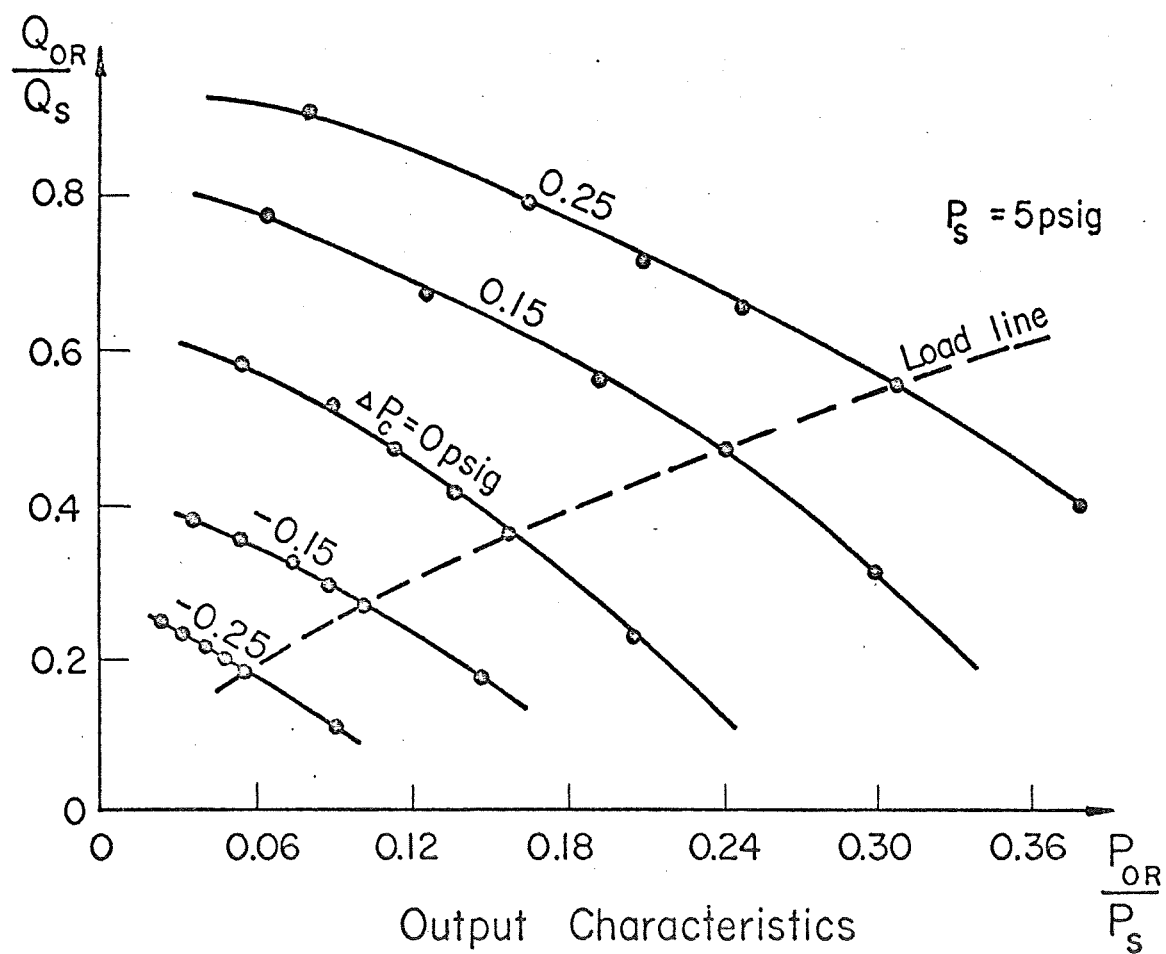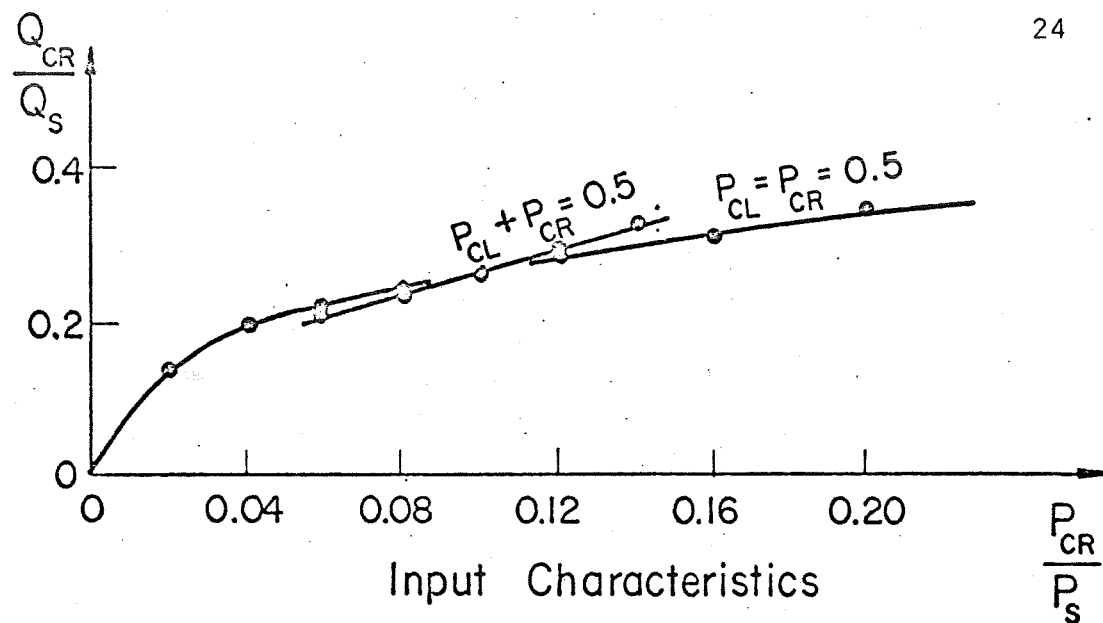
Figure 10   Normalized Input and Output Characteristics (500°F)
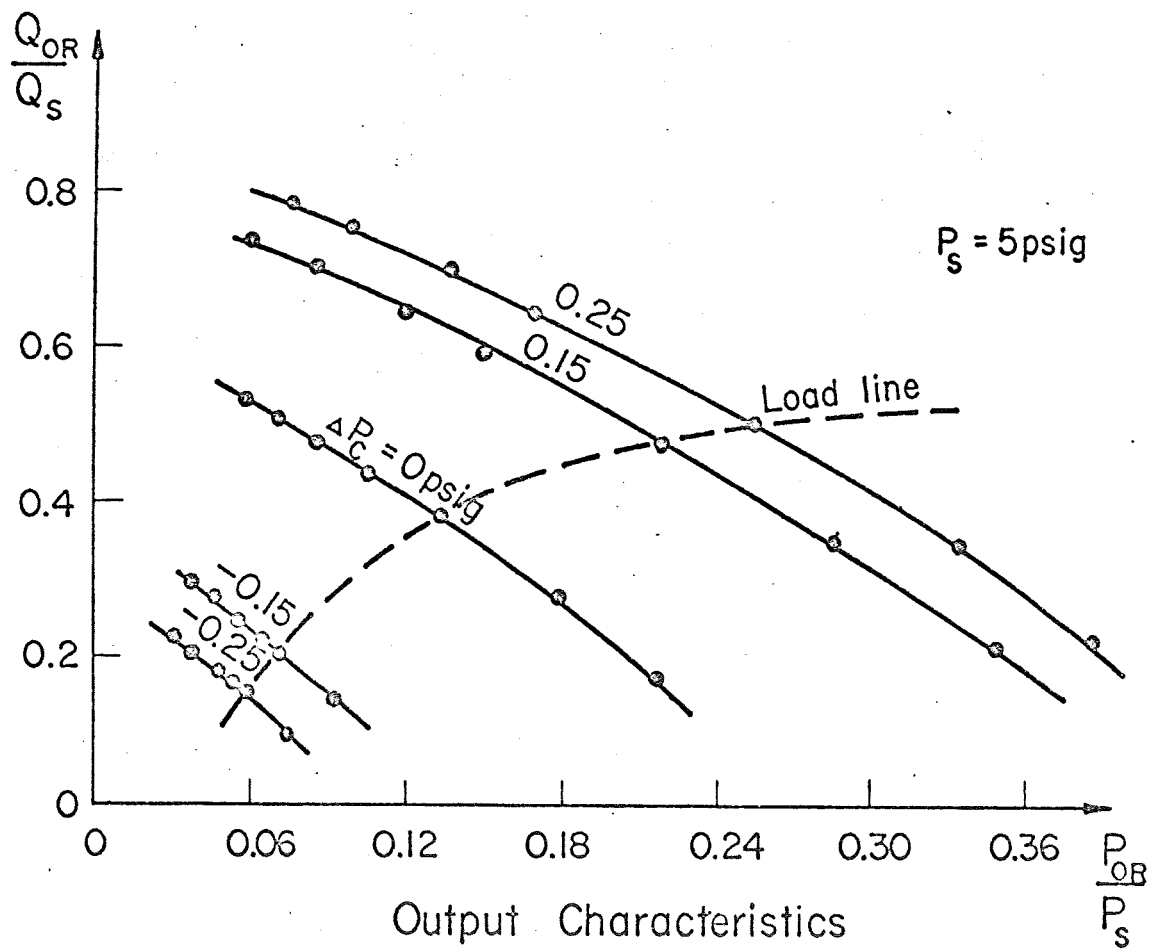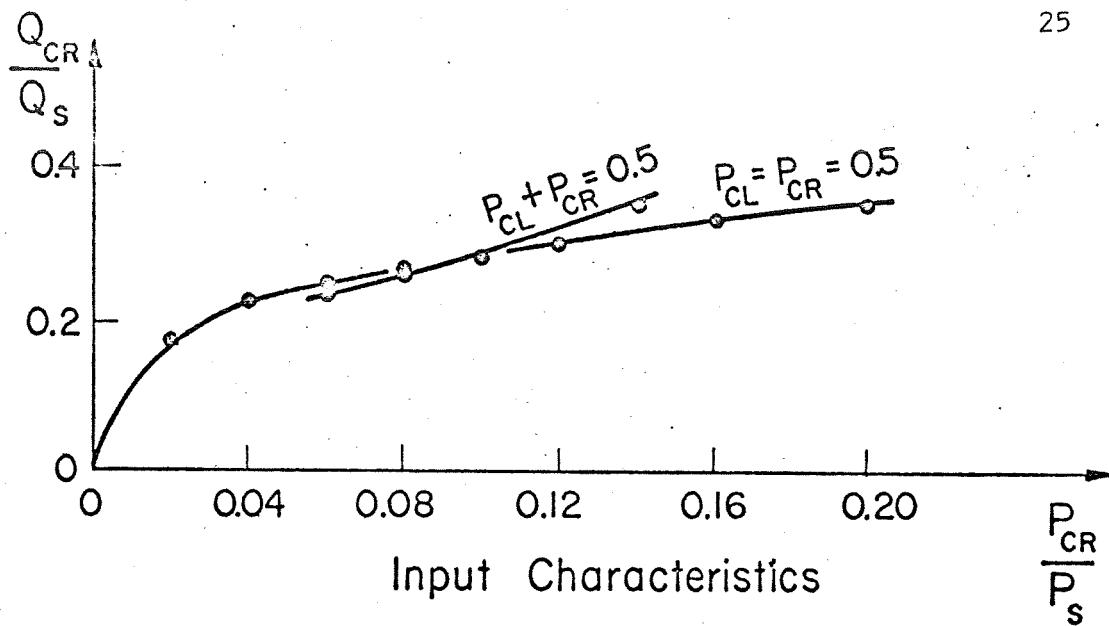
Figure II   Normalized Input and Output Characteristics (1000°F)

Figure 12   Normalized Input and Output Characteristics (1500°F)
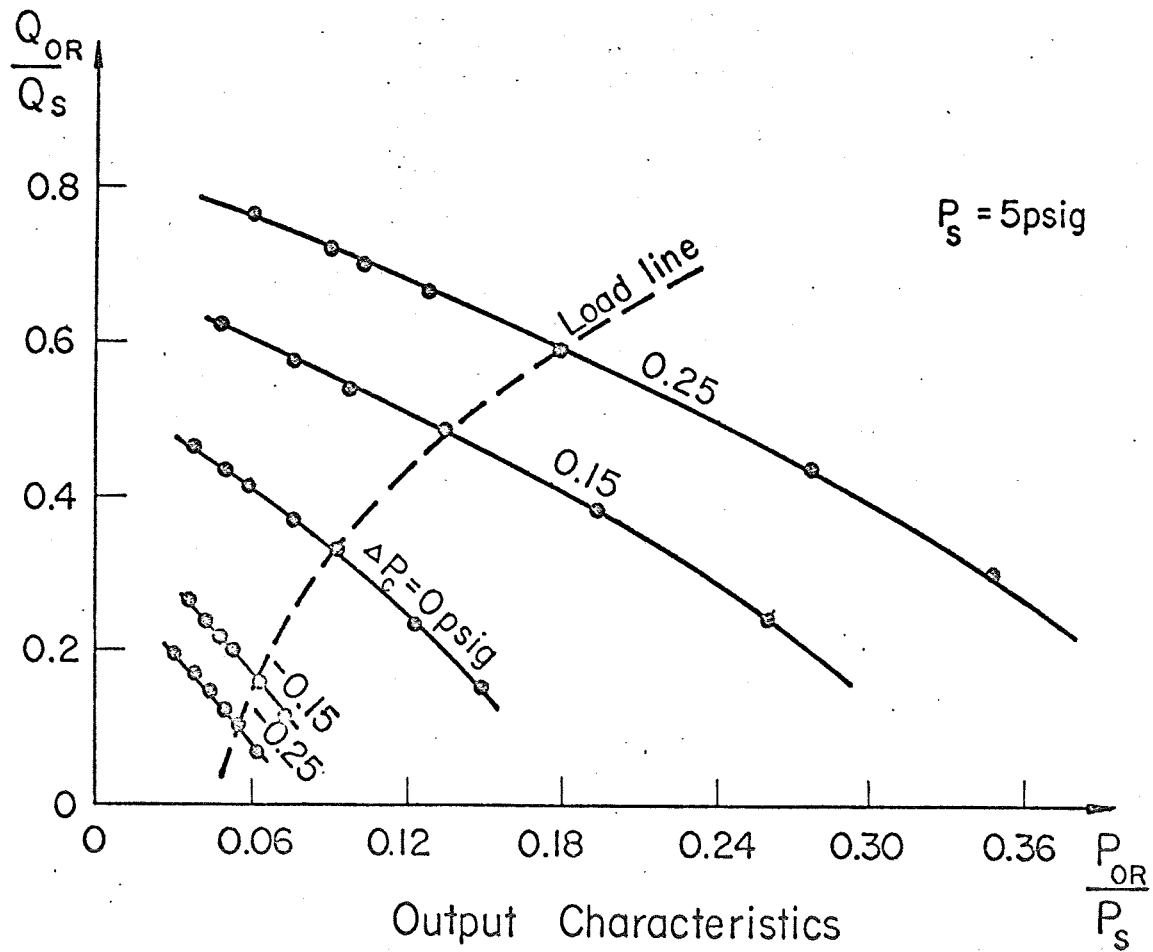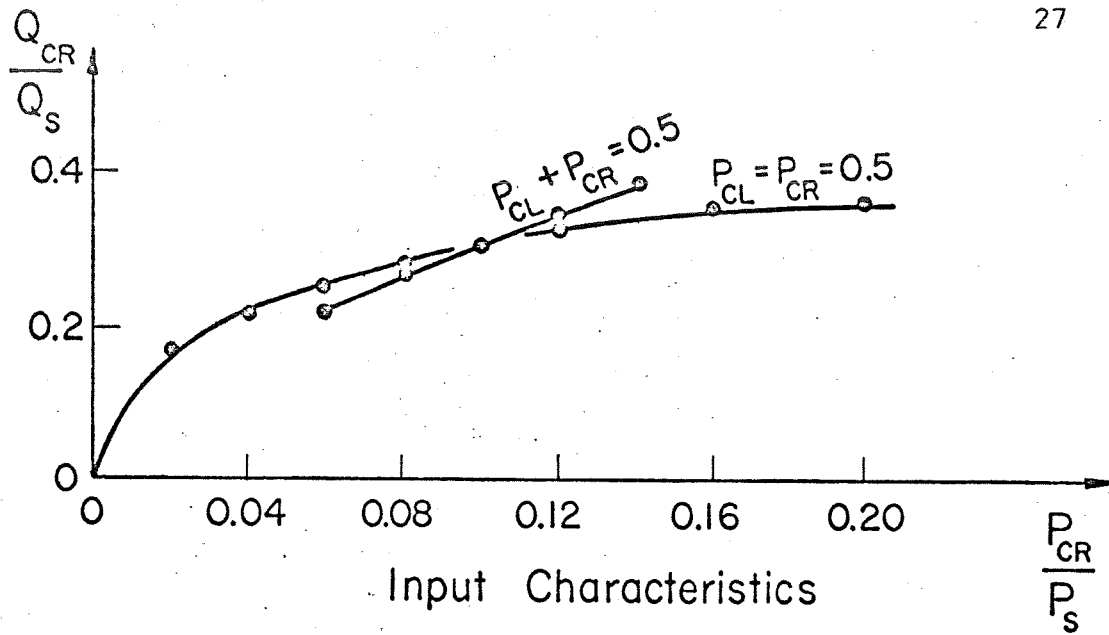
Figure 13   Normalized Input and Output Characteristics (1800°F)
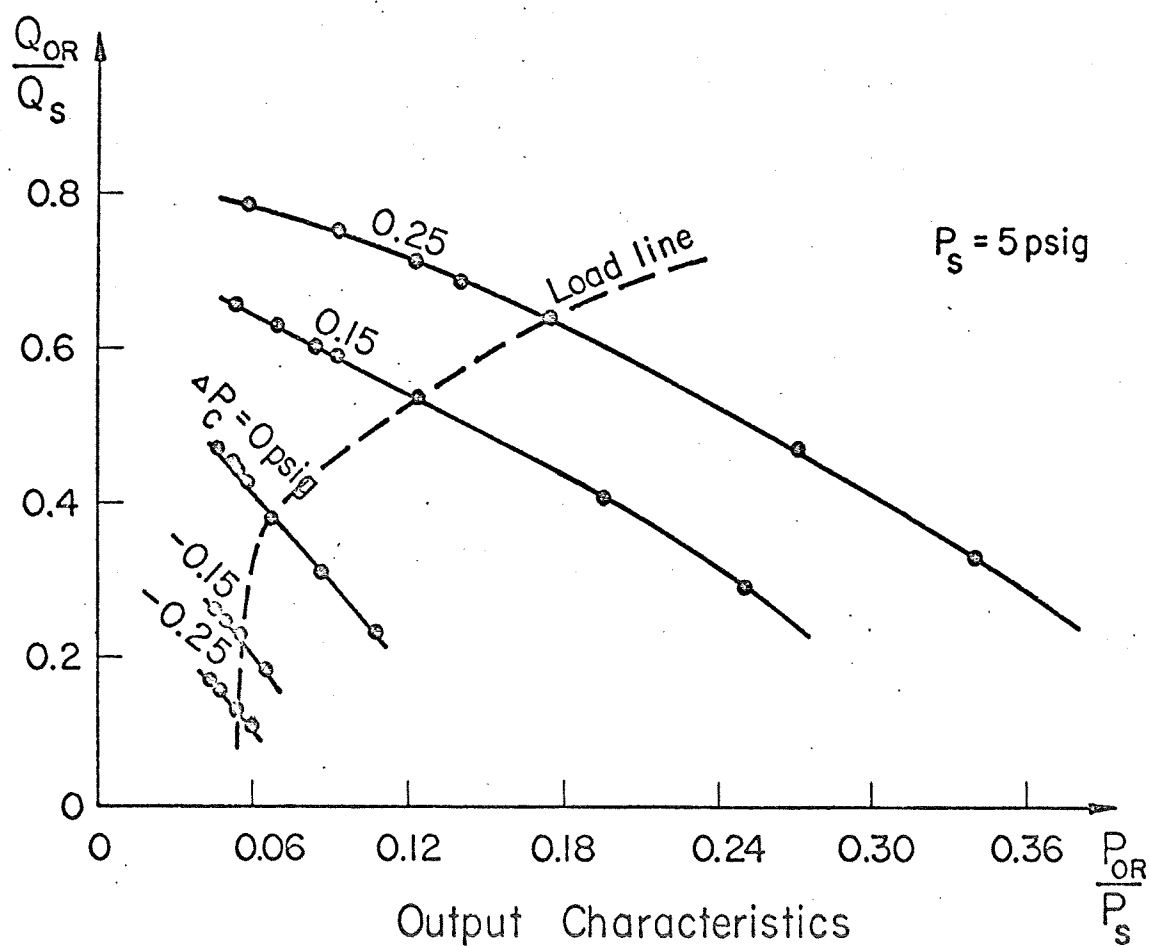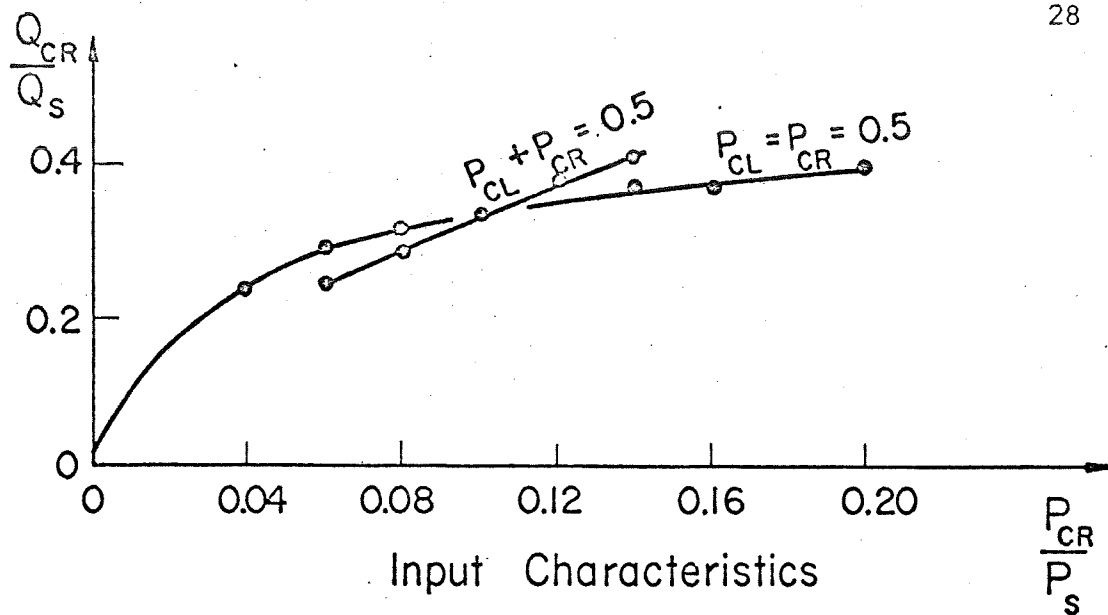
Figure 14   Normalized Input and Output Characteristics (2000°F)

Transfer characteristics. These amplifier characteristics define
the relation between input and output. Three important parameters were
obtained from these plots: the amplifier gain, linear range and null
shift.

Because amplifier gain is considerably affected by output loads,
it is necessary to define under what load the amplifier transfer
characteristics were obtained. The load used in this research to
obtain these curves, gave 1.0 psig pressure recovery for zero differen-
tial control pressure. Figure 15 shows the transfer characteristics for
the temperature range studied.

Variation of the supply pressure for room temperature, 1000 and
2000°F were also investigated. For these cases the control pressures
were also kept equal to 10 per cent of the supply pressure. From
Figures 16 to 18 it is apparent that all parameters considered for
these amplifier characteristics varied for different supply pressures.

Output characteristics. Output characteristics show how the
output signal is affected by loads located on the output ports.
Graphically, the output characteristics of a single output port is the
plot of output flow versus output pressure for different loads varied
from almost zero to almost infinite impedance values. These character-
istics are also a function of the differential control signal, giving
in that way a family of curves with the differential control pressure
as a parameter.

Several pairs of resistors were made to be located in the output
ports to get in that way the same variable load in each output. One
of these loads was the one already described in the transfer character-
istics. The load line is the locus obtained with this particular load.
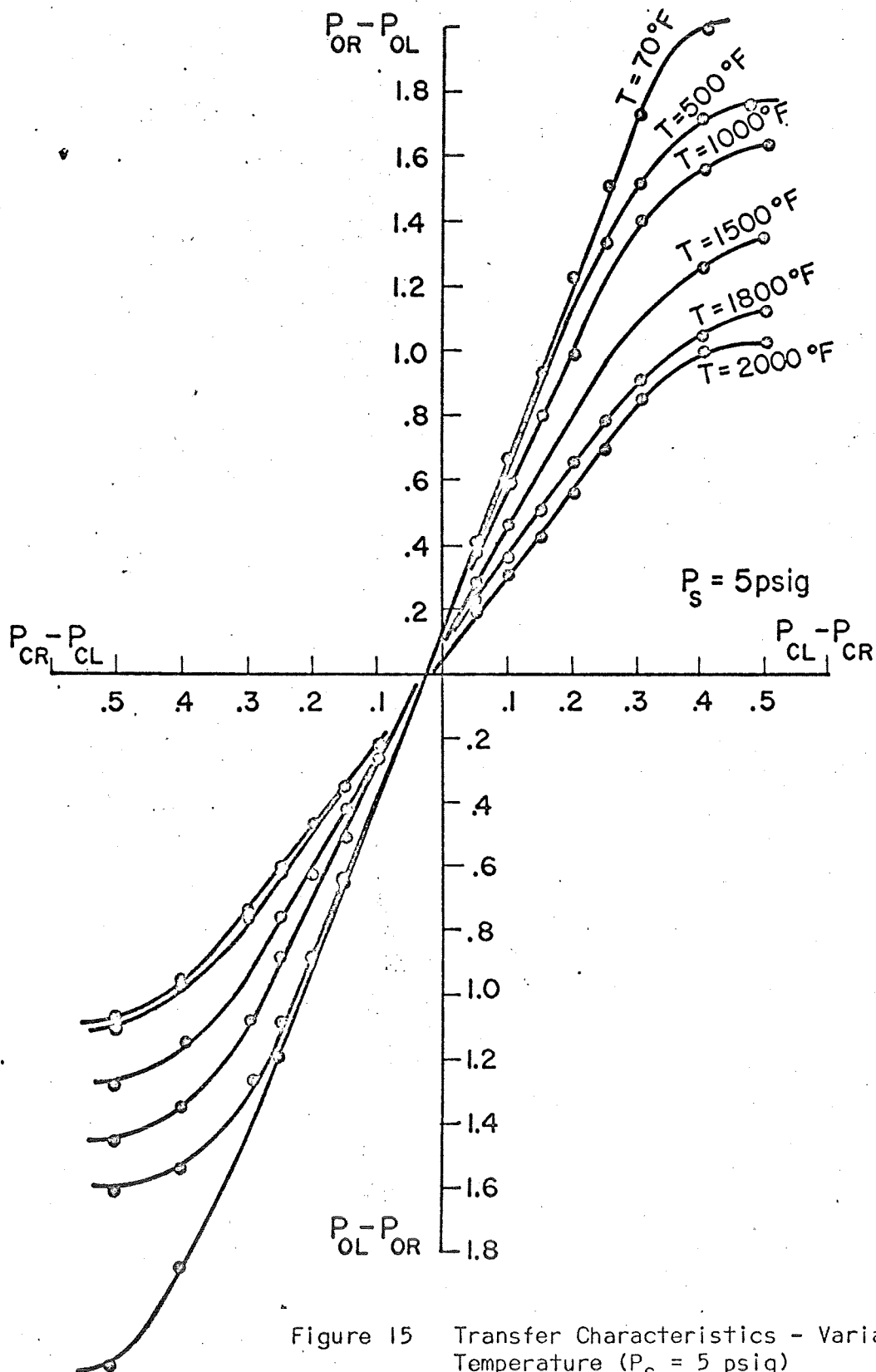
Figure 15   Transfer Characteristics – Variable
Temperature (P_S = 5 psig)
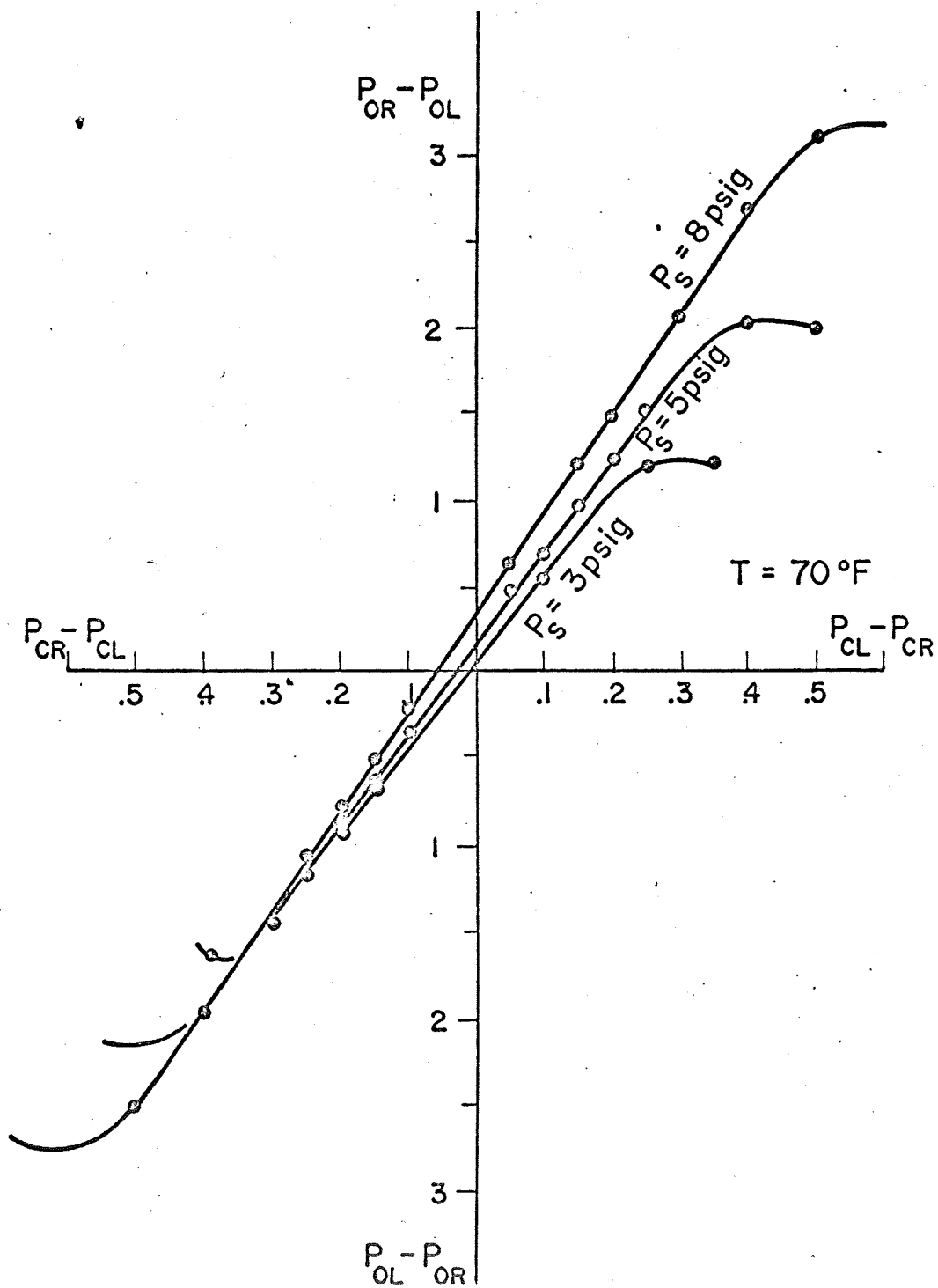
Figure 16   Transfer Characteristics – Variable Supply Pressure
             (70°F)
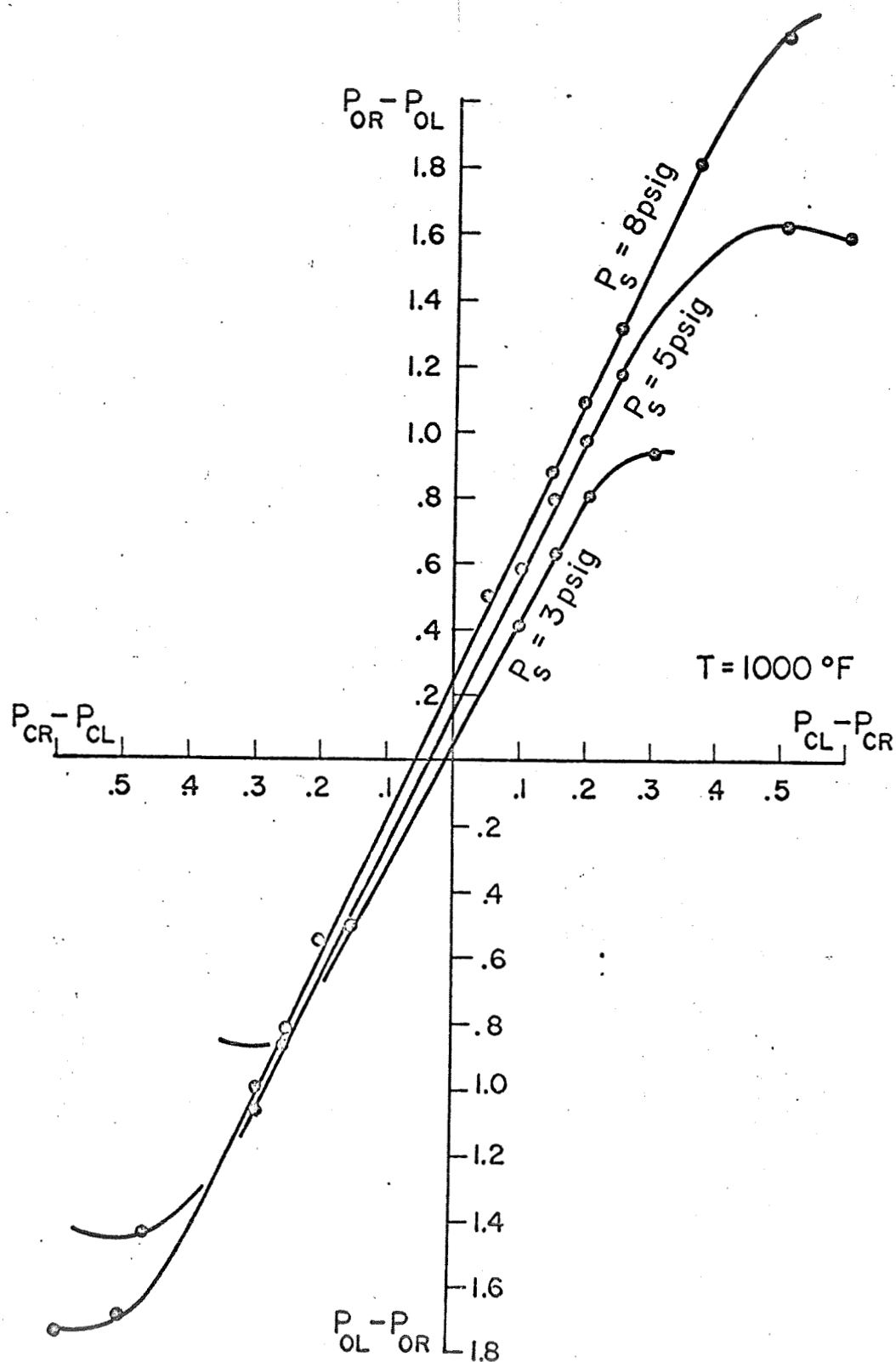
Figure 17   Transfer Characteristics – Variable Supply Pressure
        (1000°F)
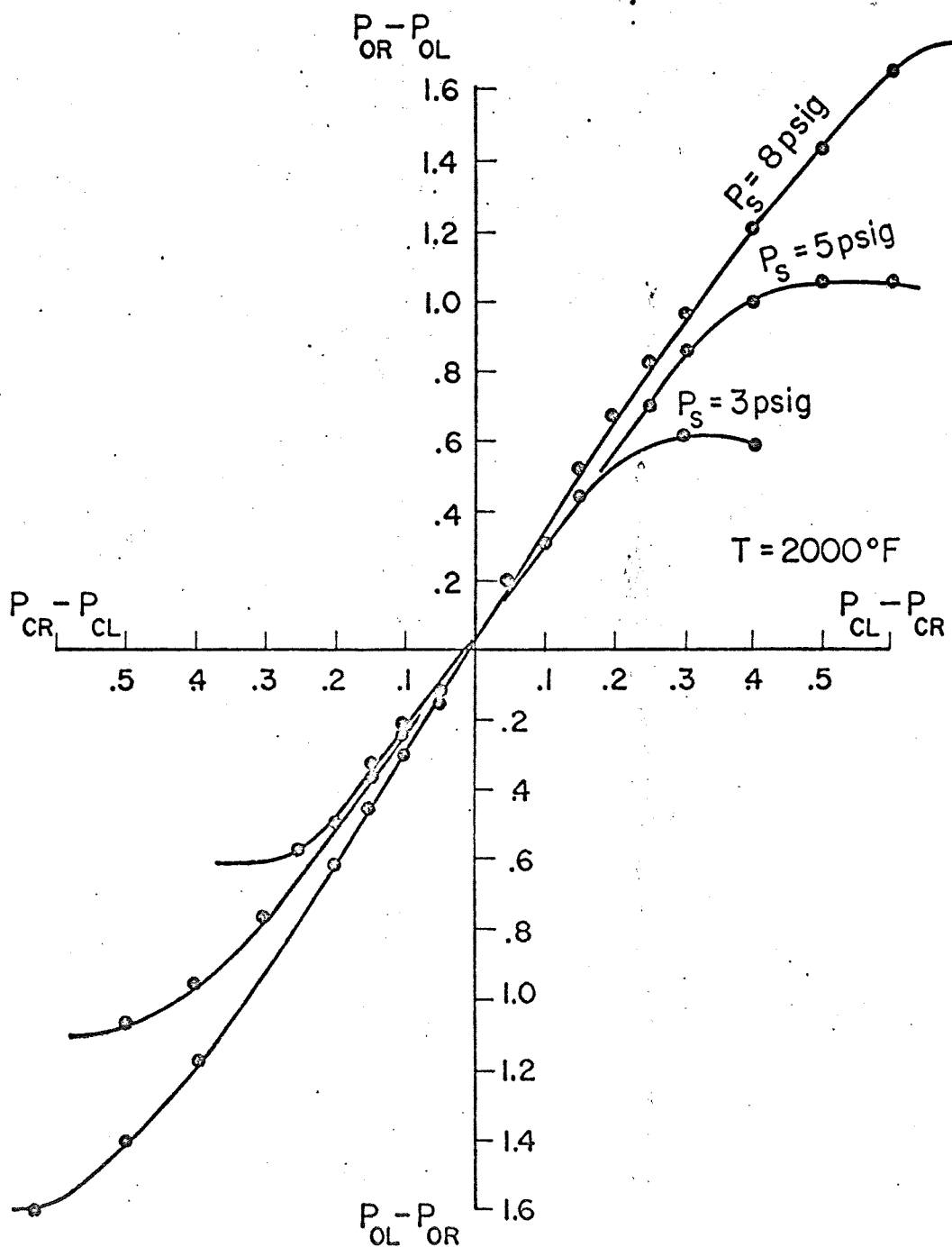
Figure 18   Transfer Characteristics – Variable Supply Pressure
             (2000°F)

Figures 9 to 14 show the output characteristics for different temperatures. Five values of differential control pressures were taken to obtain the data: $\Delta P_C = P_{CL} - P_{CR} = 0; \pm 0.15; \pm 0.20$ psig. These differential values were obtained as follows. For example, for $\Delta P_C = -0.15$ psig, P_{CR} was taken equal to 0.575 psig and $P_{CL} = 0.425$ psig. For $\Delta P_C = -0.25$ psig, P_{CR} was 0.625 psig and P_{CL} equal to 0.375 psig. In both cases the average of the control pressures was always equal to 0.50 psig.

The plot of the output characteristics for room temperature showed that the load line was very close to the unstable region. The amplifier became unstable for high values of the impedance located in the outputs. Even though pressure and flow readings on the load line were not affected by the oscillations produced because the amplifier was operating close to the unstable region, they were expected to affect the dynamic response. As temperature went up the load line moved away from the unstable region, and oscillations were considerably reduced.

For higher temperatures and negative values of ΔP_C, the variation of the output flow with output pressure for different loads was rather small, giving a very short line on the plots.

Output characteristics were also normalized with respect to supply pressure and flow. Figures 9 to 14 show that there were differences with temperature in the normalized values obtained for each ΔP_C considered. This says that it is not possible to predict accurately the output characteristics for any other temperature except those tested.

CHAPTER V

PERFORMANCE PARAMETERS

In order to describe or calculate the behavior of the amplifier, it was necessary to determine first the values of its parameters. These parameters, described particularly in reference [7], are analyzed in the following paragraphs.

Input Resistance

Input resistances were obtained from the input characteristics. They are defined as the ratio of the change in control pressure to the change in control flow when bias pressure is held constant. That is,

$$R_C = \left. \frac{\Delta P_C}{\Delta Q_C} \right|_{P_{CL} + P_{CR} = constant} \tag{5.1}$$

Because the slope of the curve for $P_{CL} + P_{CR}$ = constant changes at each point, the values of the input resistances were taken at the bias point (i.e., $P_{CL} = P_{CR}$ = 0.5 psig). Figure 19 shows the control resistance decreased as temperature increased, except between 1800 and 2000°F where a very small increment in the value of the resistance was observed.

Output Resistance

The output resistance is defined as the ratio of change in output pressure to the change in output flow when control pressure is fixed at
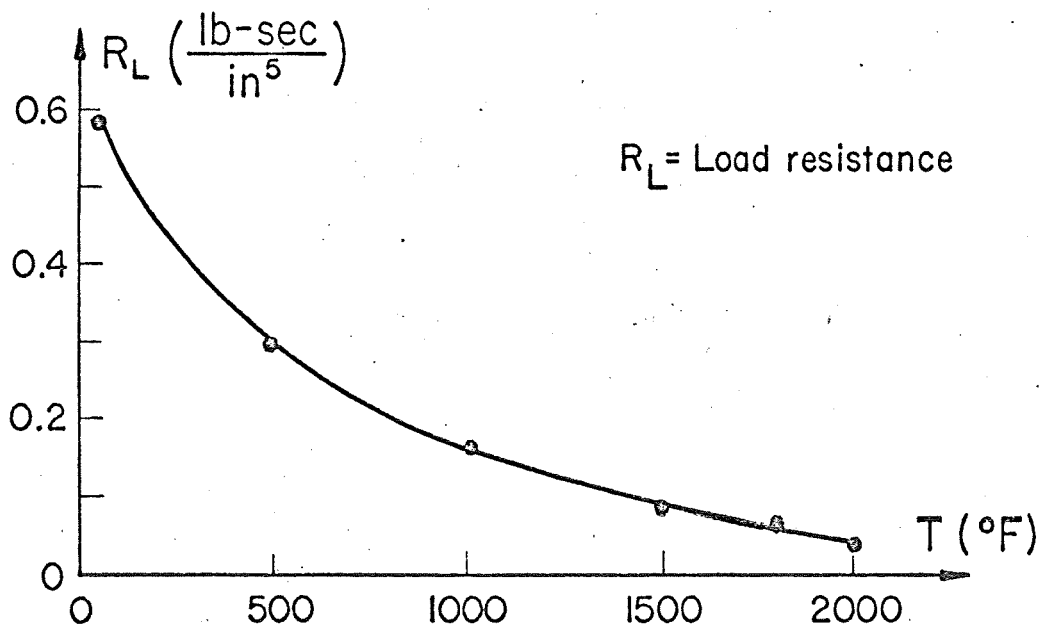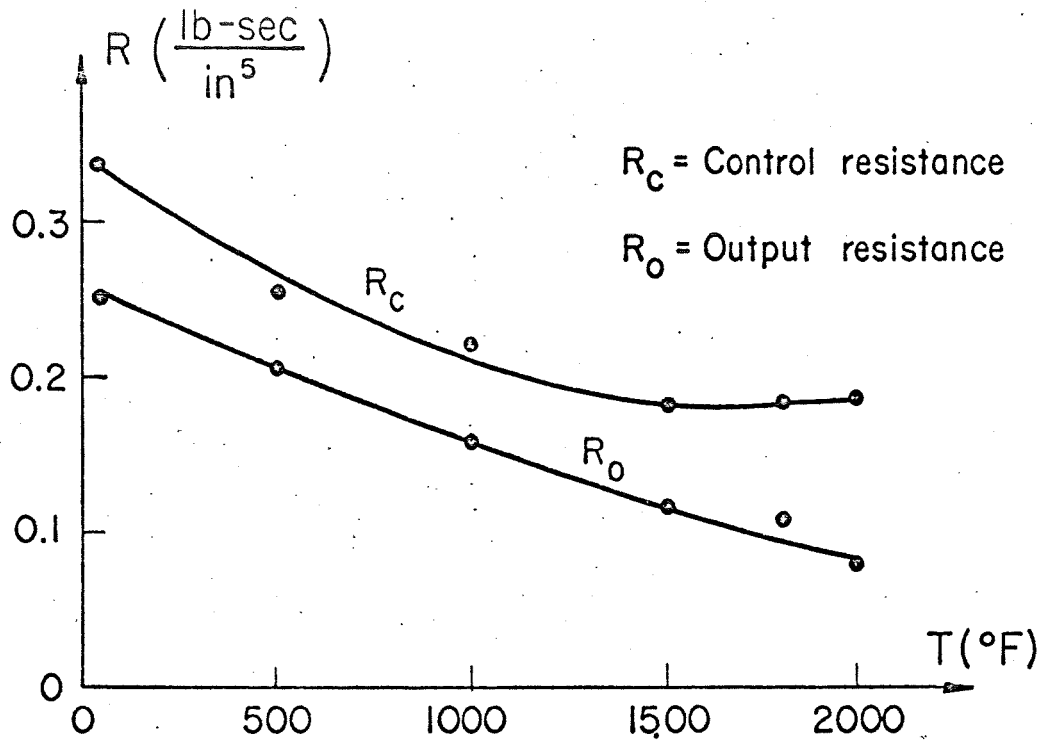
Figure 19   Control, Output and Load Resistance

a constant value. Then,

$$R_0 = \frac{\Delta P_0}{\Delta Q_0} \Bigg|_{\Delta P_C = constant} \tag{5.2}$$

Graphically it is the slope of one of the family of curves of the output characteristics obtained for different values of ΔP_C. Because the slope was continuously changing, the resistances were calculated at the point of interaction of the curve $\Delta P_C = 0$ with the load line, that is the operating point or the point at which the amplifier was operated when connected to the circuit.

Values of the output resistances are shown in Figure 19. It is apparent that the output resistance continuously decreased for increasing temperatures.

Load Resistance

Load resistances were obtained by inspection of the output characteristics. Measuring the slope of the load line at the interception point with the line $\Delta P_C = 0$, it was possible to compute the values of the load resistances for different temperatures. The equation used was

$$R_\ell = \frac{\Delta P_0}{\Delta Q_0} \Bigg|_{Load = constant} \tag{5.3}$$

Values plotted in Figure 19 show that the load resistance was highly decreased for increasing values of temperature.

Capacitance

The equivalent capacitance is defined as the ratio of the trapped volume to the absolute static pressure. That is,

$$C = \frac{U}{P_{ab}} \quad \text{(for isothermal flow)} \quad (5.4)$$

Because the values of pressure depended on the operating point, this point had to be known to find the values of the capacitances. From the input characteristics, was obtained the operating point for the control nozzles, and from the output characteristics the corresponding operating point for the output ports and loads. This permitted the evaluation of the control, output and load capacitances. Finally the values of the total capacitance C_T was obtained. Total capacitance is defined by the relation:

$$C_T = \frac{C_0 + C_\ell}{2} \quad (5.5)$$

where C_0 is the output capacitance and C_ℓ the load capacitance. At the end of this chapter are detailed the values of the amplifier and load capacitances for different temperatures.

Inductance

The quotient between the product of mass density and length to the effective cross sectional area, is defined as the inductance of a fluidic device. Hence,

$$L = \frac{\rho \cdot l}{A_{eff}} \quad (5.6)$$

Temperature and pressure at the operating point, obtained as
explained in the preceding section, defined the corresponding values
of mass density. On the other hand, the effective cross sectional area
was obtained by the relation:

$$A_{eff} = \frac{A_{in} - A_{out}}{\ln \frac{A_{in}}{A_{out}}}$$
(5.7)

The constant area section of the control ports was equal to
$0.032 \times 0.046 = 1.472 \times 10^{-3}$ in^2. For the output ports, which had a
variable area, it was required to use the formula of the effective area.
The value obtained was $A_{eff} = 1.770 \times 10^{-3}$ in^2.

Both control and output inductances showed decreasing values as the
temperature increased. The values are shown at the end of this chapter.

Amplifier Pressure Gain G

The ratio of the change in amplifier output differential pressure
to the input differential pressure is defined as the pressure gain.
From the transfer characteristics defined in the preceding chapter, it
was possible to obtain the pressure gain.

It can be concluded that the slopes of the curves were not constant,
and therefore the gain was not constant either. For this reason gain
was taken at the interception of the axis $(P_{CL} - P_{CR})$ and $(P_{OR} - P_{OL})$.
Figure 20 shows that pressure gain decreased from 5.17 at room tem-
perature down to 2.9 at 2000°F. Supply pressure was equal to 5 psig.
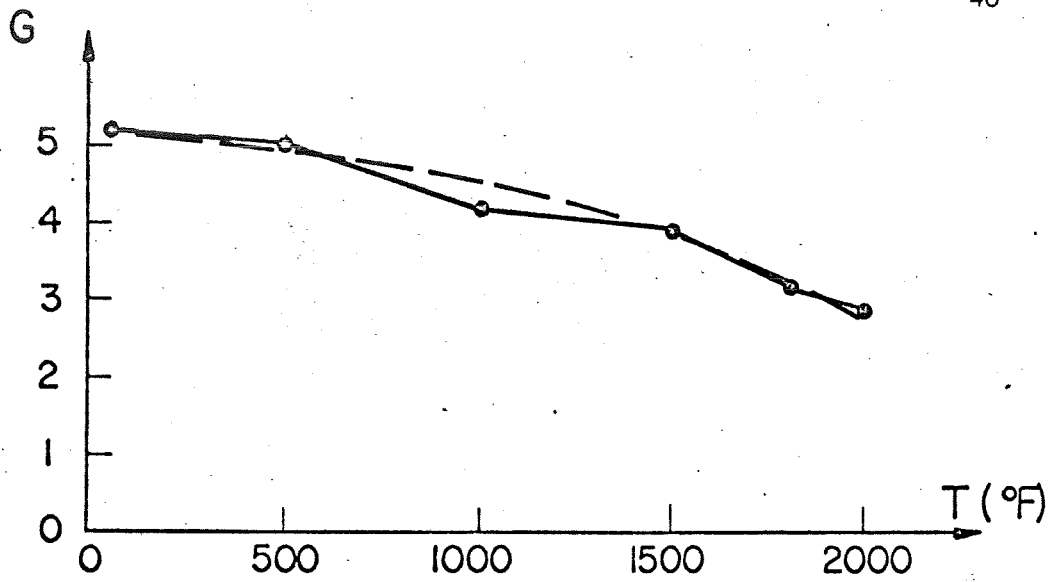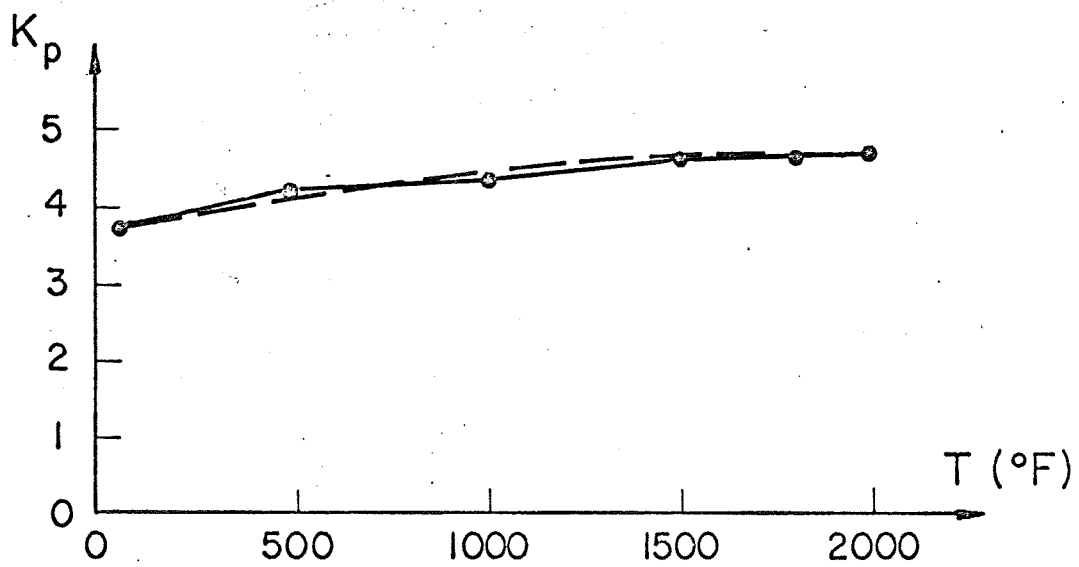
Figure 20   Amplifier Pressure Gain and Pressure Amplification Factor

From Figures 16 to 18 it is apparent that increasing and decreasing the supply pressure, for the same value of temperature, the pressure gain increased and decreased respectively.

Amplifier Pressure Amplification Factor K_p

The ratio of the change in amplifier output pressure to a change in control differential pressure at a constant flow, is defined as the pressure amplification factor.

$$K_p = \frac{\Delta P_0}{\Delta Q_0} \bigg|_{Q_0 = \text{constant}} \qquad (5.8)$$

Through the output characteristics it was possible to find the values of this parameter and these values were plotted in Figure 20, which shows how K_p increased with increasing temperature.

Because the distance between constant ΔP_C curves in the output characteristics was not constant, the values of K_p were taken at the interception point of the load line with the curve defined by $\Delta P_C = 0$ psig.

Time Delay

According to Belsterling and Tsui [16] four separate areas must be considered to calculate the time delay produced in the transmission of the dynamic signal.

A) Due to the pressure wave propagation through the fluid, there was a delay in the control passages given by,

$$t_1 = \frac{\text{length of control nozzle}}{\text{velocity of sound} + \text{velocity of flow}} \qquad (5.9)$$

B) In the interaction region fluid velocity was fast and pressures were negligible. Therefore only the transit time required from the fluid in the power stream to go from the power nozzle just to the receivers, was considered. Hence,

$$t_2 = \frac{\text{length of interaction chamber}}{\text{velocity of fluid flow}} \qquad (5.10)$$

The velocity of the fluid flow in the interaction chamber was found by taking the average between the power jet exit velocity and the receiver impact velocity.

The first one is,

$$V_s = \frac{Q_s}{A_s} \qquad (5.11)$$

and at the receivers (considering the pressure at the operating point in psig):

$$V_0 = \sqrt{\frac{2P}{\rho} \, g_c} \qquad (5.12)$$

Finally the average velocity was taken as

$$\bar{V} = \frac{V_s + V_0}{2} \qquad (5.13)$$

C) In the output ports the same analysis done in the control nozzles was considered. Therefore there was a wave propagation in the moving medium, or

$$t_3 = \frac{\text{length of output apertures}}{\text{velocity of sound} + \text{velocity of fluid flow}} \qquad (5.14)$$

D) In the external circuit, because the area was considerably larger than the output apertures, the fluid velocity was very low. The transmission was primarily by wave propagation. Then,

$$t_4 = \frac{\text{length of output circuit}}{\text{velocity of sound}} \qquad (5.15)$$

In this formula the length of the output circuit was taken equal to the distance from the external end of the output receivers up to the taps for measuring the output pressure. This distance was equal to 1.45 in. No time delay was considered due to the tubes for measuring the input and output pressure. Because both tubes had the same length the delay was the same on both lines.

The sum of the four times delays previously considered gave the total time delay t_d. At the end of this chapter, the total time delays are specified. These values showed decreasing values for increasing temperatures. Small increment of the time delay was found from 1500°F up.
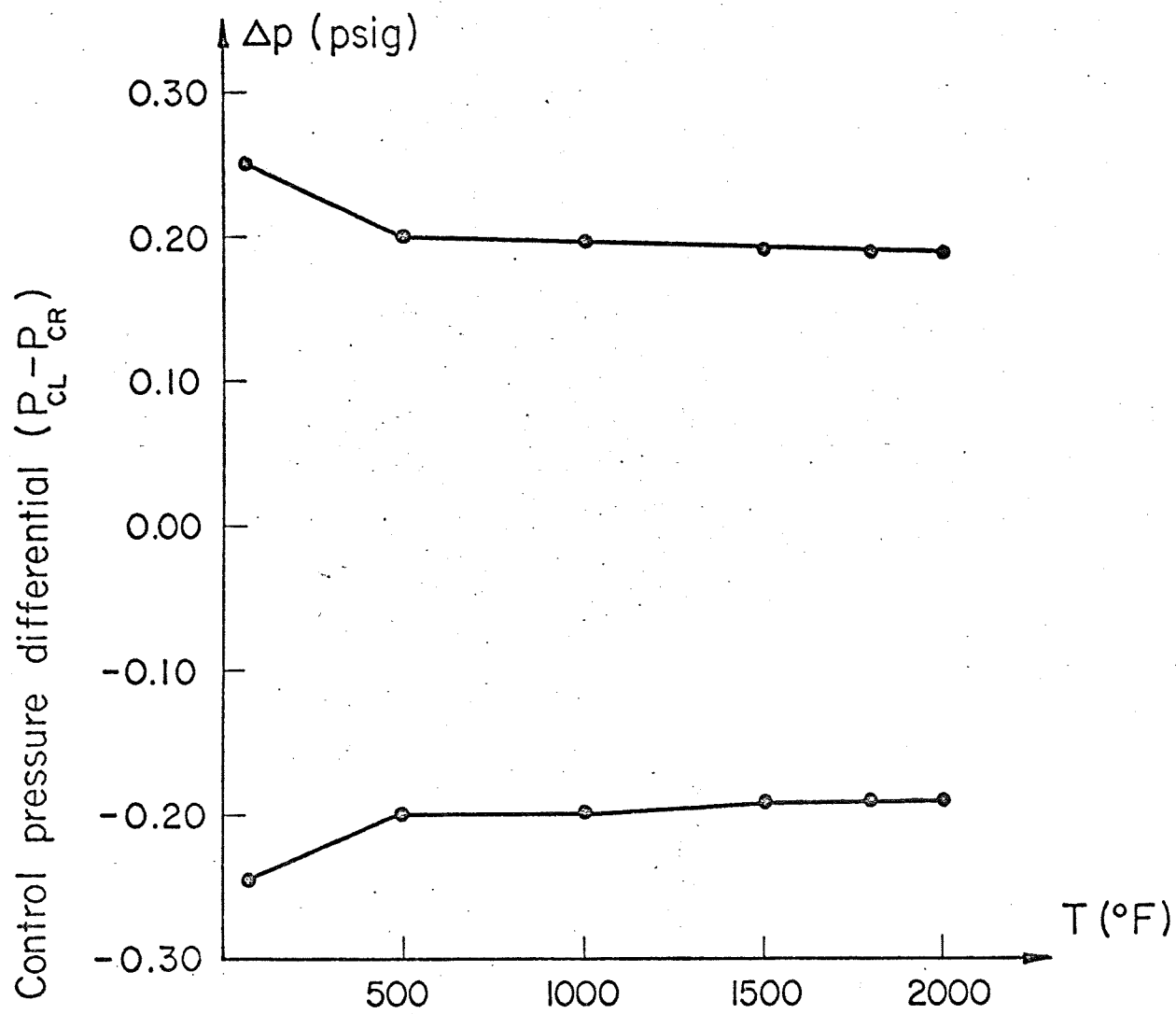
Figure 21   Linear Range Variation with Temperature
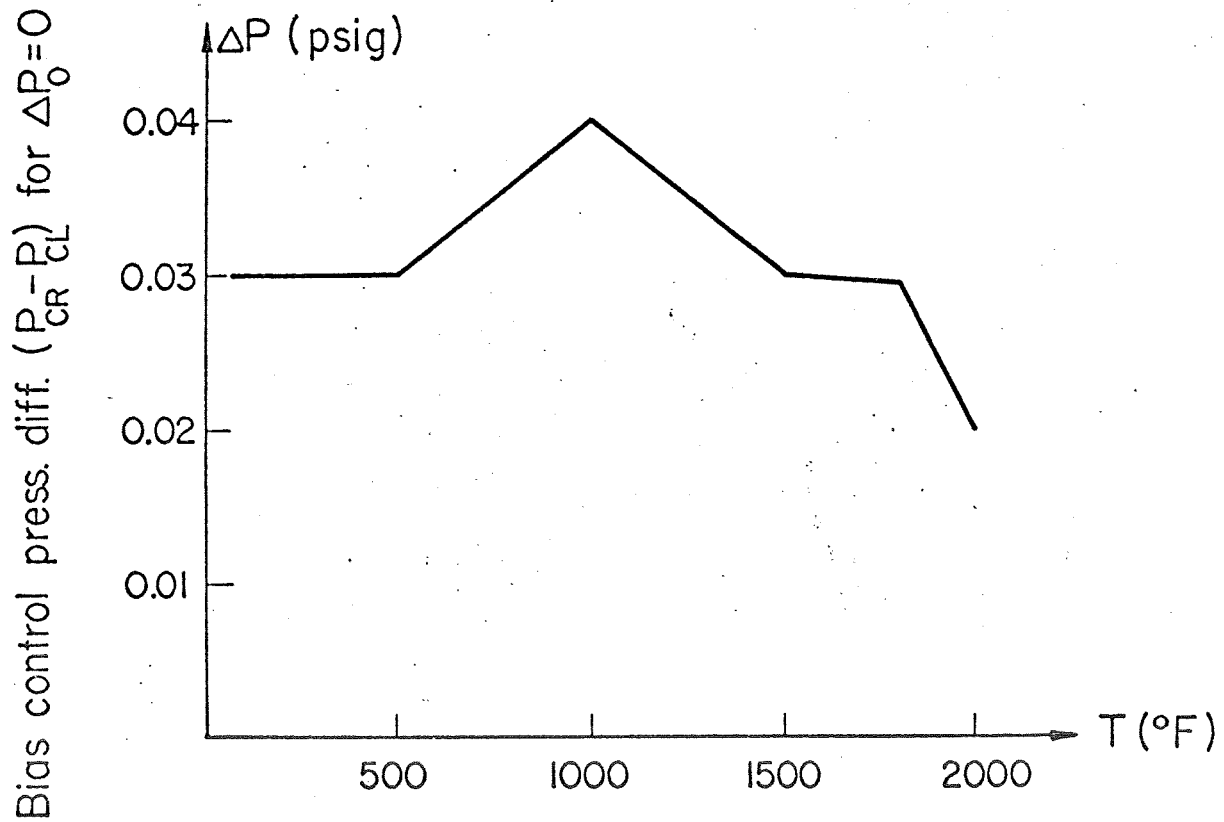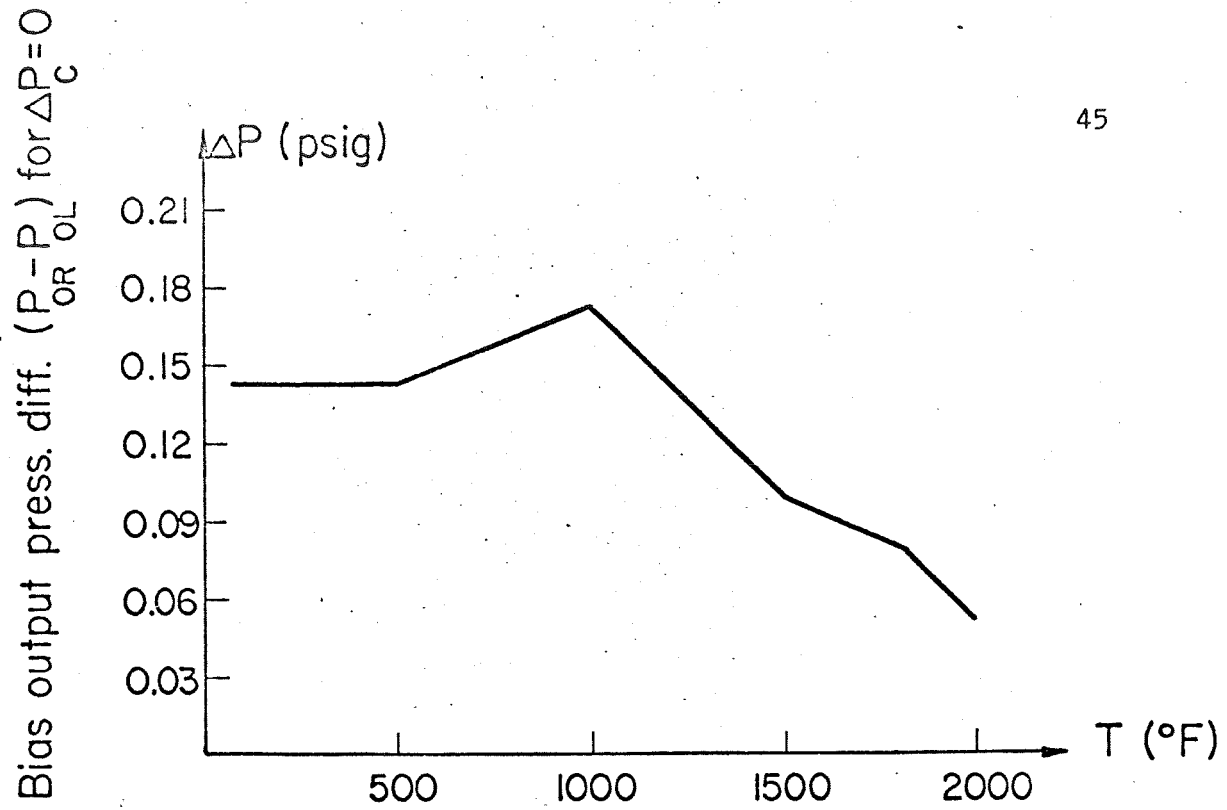
Figure 22   Null Shift versus Temperature

Linear Range

It is important to mention that the linear range of the amplifier indicated in Figure 21 was almost constant, particularly from 500 to 2000°F. Also from Figures 16 to 18 it can be deduced that the linear range was enlarged for higher supply pressures and lowered for the opposite.

Null Shift

Null shift is defined as the differential output pressure required for zero control differential pressure or as the differential control pressure for zero differential output pressure. This amplifier parameter was affected by the variation of the temperature. Values of the null shift are shown in Figure 22 which indicates a random distribution as function of the temperature.

Parameters Values

The next table is a summary of the values obtained through the static test of the amplifier. Values not explained in this chapter will be considered in the following one.

Table I

Amplifier Parameters Values

Temperature °F Parameter	70	500	1000	1500	1800	2000
Input resist. $R_C \left[\dfrac{lb\ sec}{in^5}\right]$	0.332	0.256	0.219	0.181	0.181	0.187
Output resist. $R_0 \left[\dfrac{lb\ sec}{in^5}\right]$	0.249	0.205	0.159	0.107	0.109	0.075
Load resist. $R_\ell \left[\dfrac{lb\ sec}{in^5}\right]$	0.580	0.298	0.163	0.086	0.066	0.034
Input capac. $C_C \left[\dfrac{in}{lb}\right] \times 10^5$	0.803	0.803	0.803	0.803	0.804	0.804
Output capac. $C_0 \left[\dfrac{in^5}{lb}\right] \times 10^5$	4.68	4.75	4.79	4.86	4.89	4.89
Load capac. $C_\ell \left[\dfrac{in^5}{lb}\right] \times 10^5$	2650	2693	2718	2756	2775	2774
Total capac. $C_T \left[\dfrac{in^5}{lb}\right] \times 10^5$	1327	1349	1361	1381	1390	1389
Tube capac. for output press. measurement $C' \left[\dfrac{in^5}{lb}\right] \times 10^5$	3409	3454	3484	3534	3559	3558

Temperature °F

Parameter	70	500	1000	1500	1800	2000
Complete capac. $C_T^t \left[\frac{in^5}{lb}\right] \times 10^5$	3032	3076	3103	3147	3169	3169
Input induct. $L_C \left[\frac{lb\ sec^2}{in^5}\right] \times 10^5$	0.67	0.39	0.24	0.18	0.15	0.14
Output induct. $L_0 \left[\frac{lb\ sec^2}{in^5}\right] \times 10^5$	2.88	1.71	1.00	0.74	0.64	0.57
Pressure gain G	5.18	4.98	4.20	3.90	3.20	2.90
Pressure amplification factor K_p	3.70	4.21	4.30	4.60	4.62	4.70
Total time delay t_d [sec] $\times 10^3$	0.170	0.142	0.137	0.065	0.066	0.066

Table I (continuation)

Amplifier Parameters Values

CHAPTER VI

EXPERIMENTAL DETERMINATION OF THE AMPLIFIER DYNAMIC RESPONSE

The experimental frequency response of the amplifier was conducted

for the same temperatures as the static response was previously considered.

A theoretical dynamic response was computed based on the parameters

obtained through the experimental static response. This allowed plotting

of the theoretical Bode plots for the system, and permitted the theoretical

values to be compared with those obtained by experimentation.

To perform the dynamic response it was necessary to design a

sinusoidal signal generator. A schematic representation of the dynamic

test circuit is shown in Figure 23.

Design of the Sinusoidal Signal Generator

The signal generator consisted mainly of two nozzles and a rotating

plate. It was mounted on top of the amplifier as shown in Figures 24

and 25. In Figure 25 the main dimensions of the generator are presented.

Two important specifications were required in the design of the generator:

A) It had to be located inside the oven. Short tubes from the

generator nozzles to the control ports were obtained in that way. Total

tube length was equal to 9 in.

B) The generator had to have a large range of frequencies available.

Because it was not possible to support the shaft with a bearing inside

the oven, the speed of the motor used to rotate the disc to produce the

variable pressure was limited. Therefore a wobble plate was used to
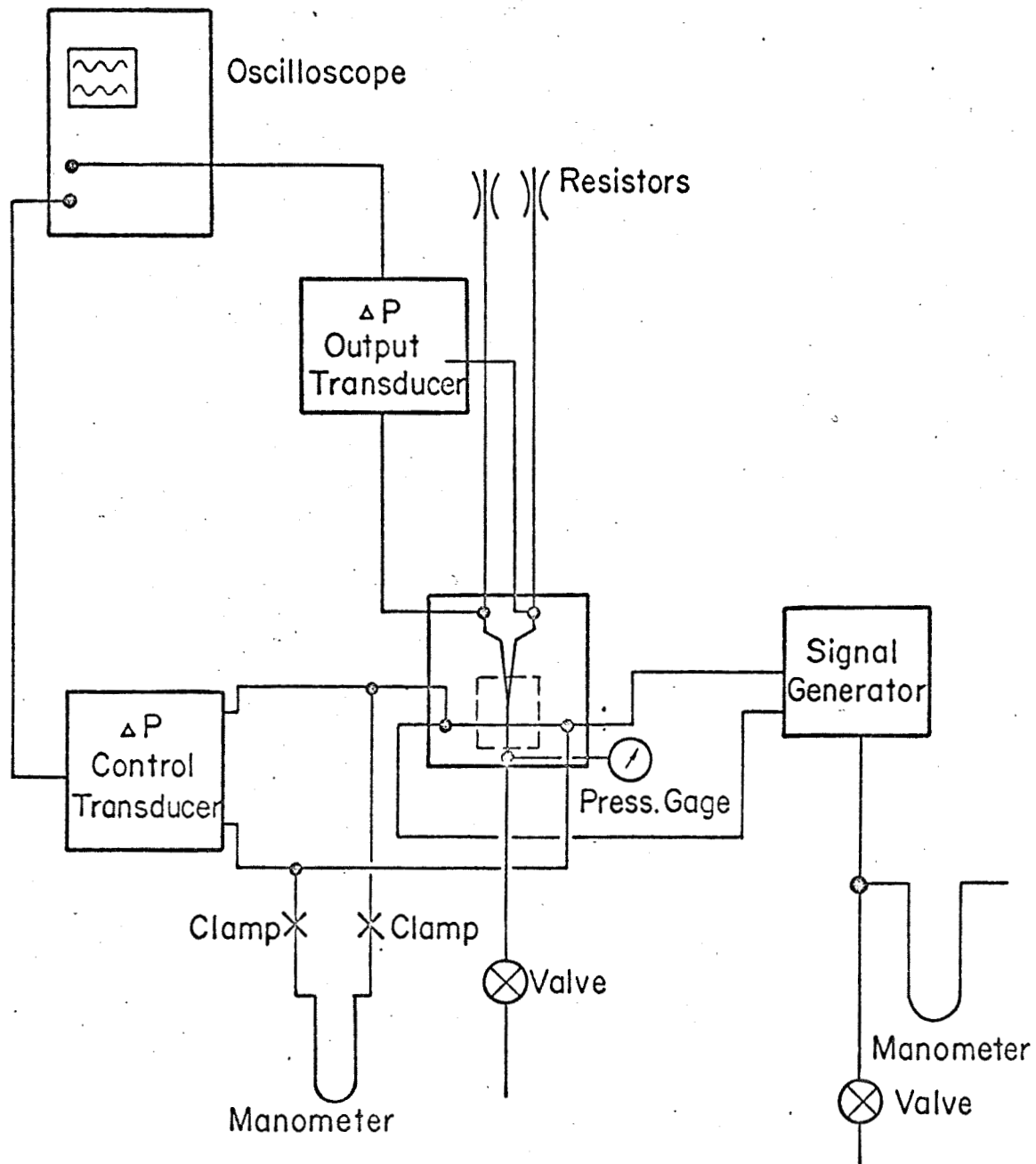
Figure 23   Schematic Diagram of the Dynamic Test Circuit
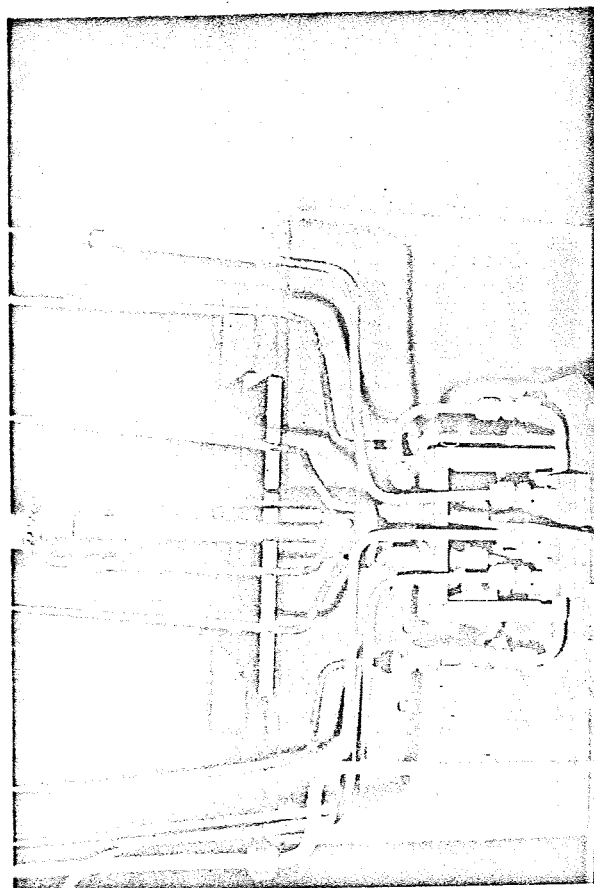
Figure 24.   Experimental Setup – Dynamic Response Test

Nozzle chamber

$d_1 = 0.125''$

$d_2 = 0.250''$

OVEN

Rotating plate

Nozzle

1.194

Resistor

Input signal

Signal generator supply press.

Fluidic amplifier
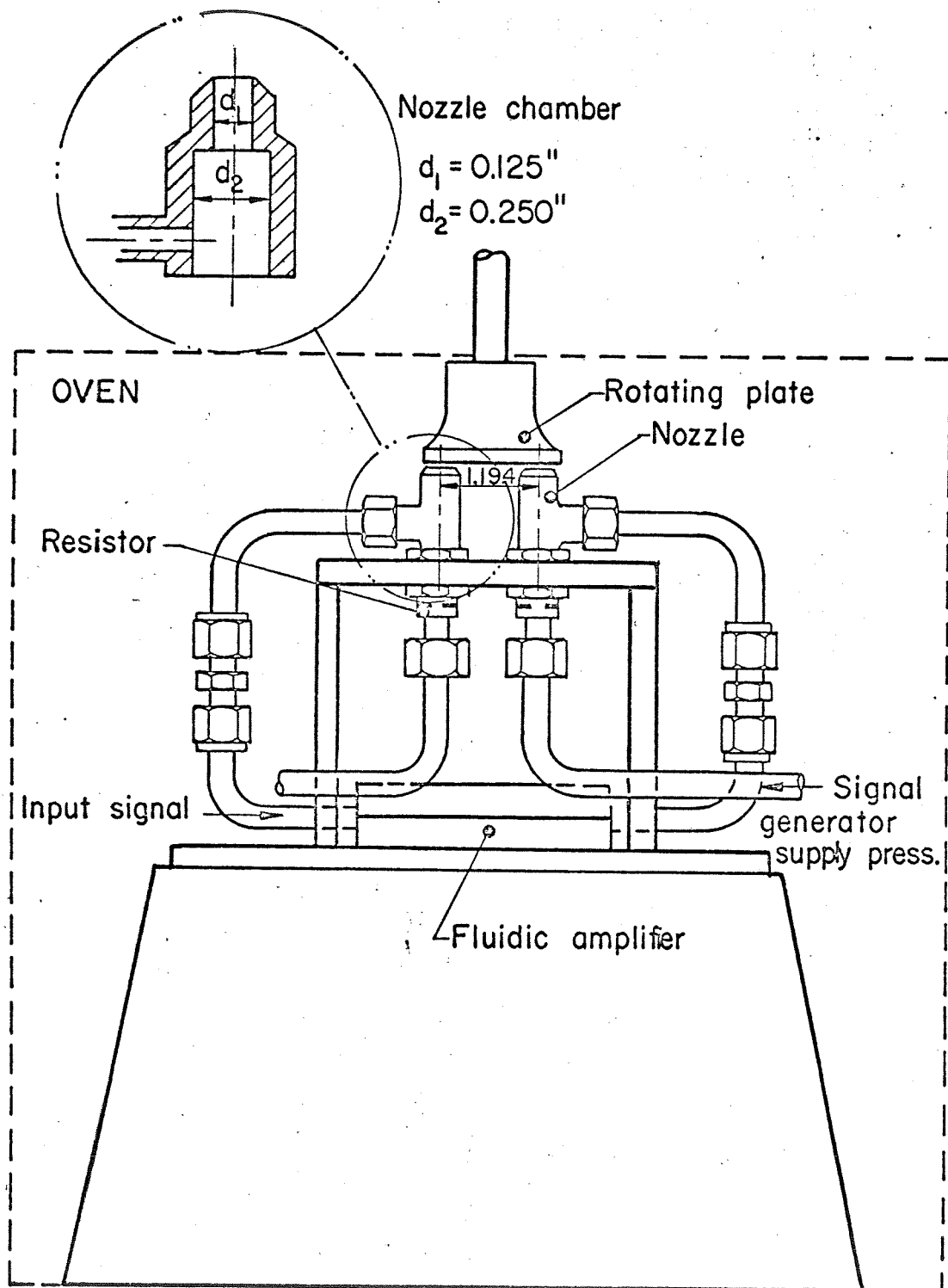
Figure 25.   Schematic Diagram of the Signal Generator

generate low frequency signals and a notched plate for high frequencies. Figure 26 shows both plates. Reference [14] was useful in designing the nozzles and the plates.

The two nozzles had a diameter d_1 equal to 0.125 in. The diameter d_2 of the nozzle chamber was equal to 0.125 in. A resistor located at the bottom of the chamber was designed with a diameter equal to 0.0937 in. The diameter of the nozzles was taken equal to 0.125 in because this was also the width of the notches on the circumference described by the nozzles when the plates rotated on top of them.

Because the plates were to be interchangeable, the number of notches was taken equal to fifteen. In that way, the nozzles being 180° from each other, when the highest pressure was at one of the nozzles, the lowest was at the other, using either the notched or the wobble plate.

The other possible value for the number of notches was forty-five. This value was rejected because the diameter of the plate would have been too large.

The distance between the nozzles and the plates was set with a micrometer located on the top end of the plate shaft. This adjustment permitted setting of the amplitude of the input signal and permitted readjustment to compensate for changes due to temperature and frequency.

The signal generator was built of stainless steel RA 330.

Frequency Response

Based on the lumped parameter technique developed by Boothe [15], Belsterling and Tsui [16] worked out an analogy between a differential electronic amplifier and the beam deflection amplifier. As a final result the circuit shown in Figure 27 was presented.
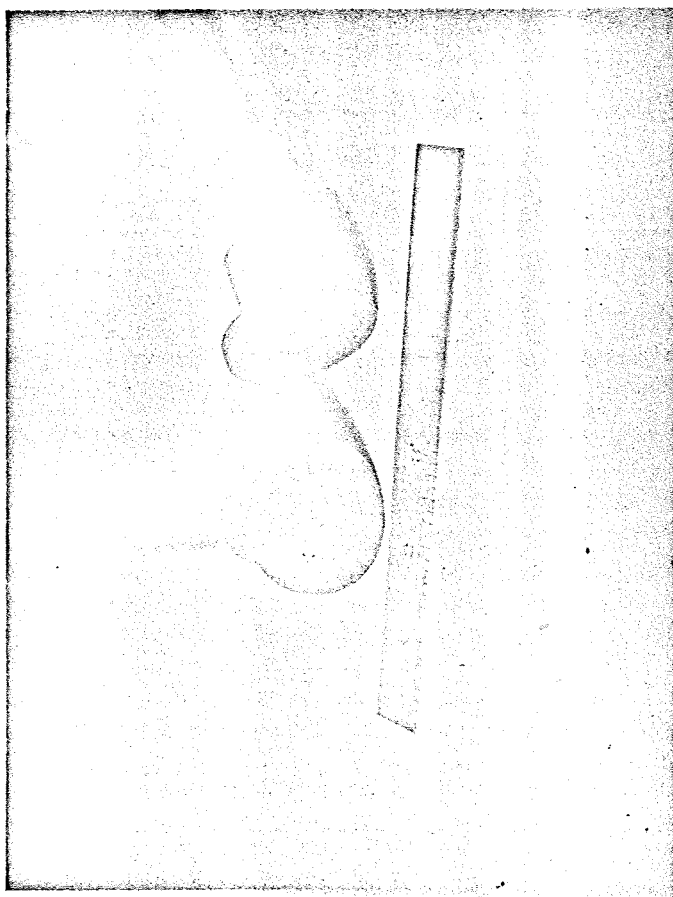
Figure 26. Wobble and Notched Plates
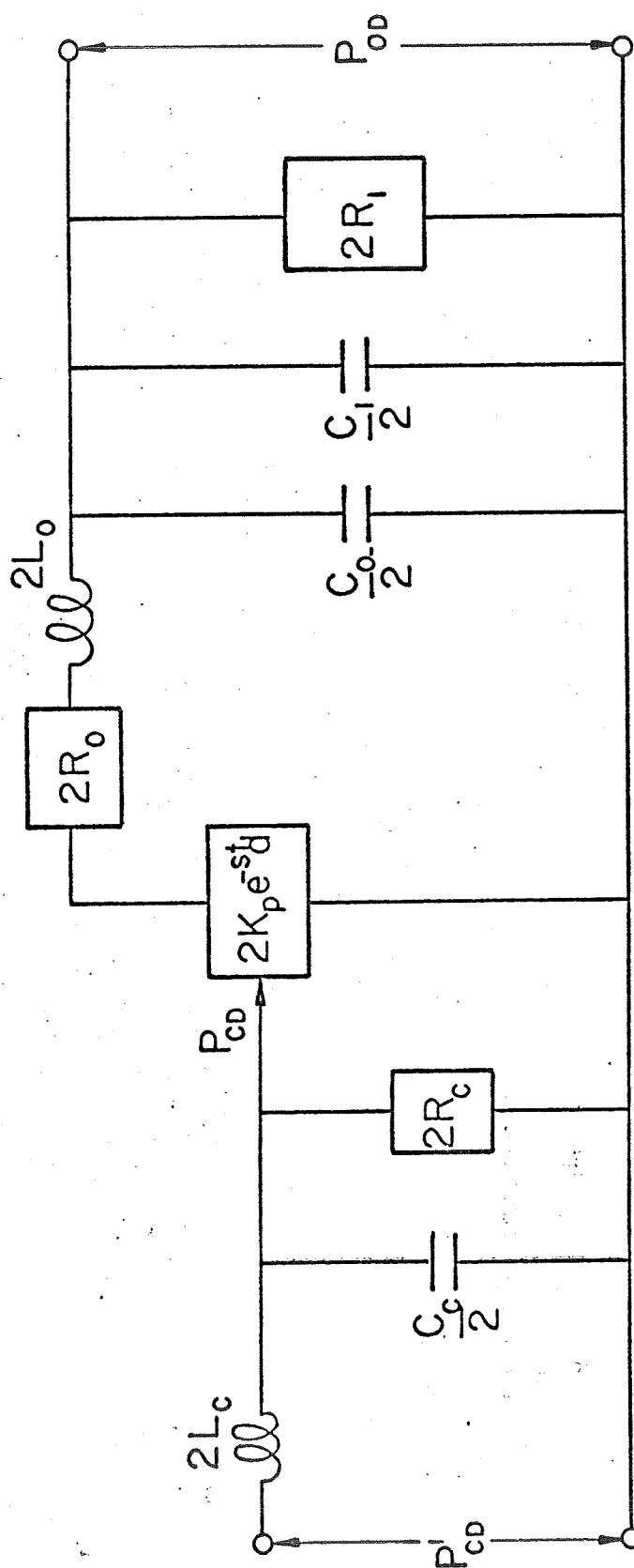
Figure 27   High Frequencies Equivalent Circuit

The transfer function of the amplifier is:

$$\frac{P_{OD}}{P'_{CD}} = \frac{2K_P R_\ell \; e^{-s t_d}}{R_0 + R_\ell (1 + s \frac{L_C}{R_C} + s^2 L_C C_C)[1 + s(C_T \frac{2R_0 R_\ell}{R_0+R_\ell} + \frac{L_0}{R_0+R_\ell}) + s^2 \frac{2C_T L_0 R_\ell}{R_0+R_\ell}]}$$

$$(6.1)$$

Values at the end of Chapter V were used in this equation with the correction mentioned below. In this formula with the exception of the term $e^{-s t_d}$, the other part is the minimum phase transfer function of the system. Therefore substituting $s = j\omega = 2j\pi f$ it was possible to plot the theoretical frequency response.

Even though the length of all the tubes was reduced as much as possible, it was necessary to run them a certain distance to avoid temperature effects, particularly upon the pressure transducers. This produced a considerable effect on the amplifier gain and phase angle.

Therefore in the theoretical analysis of the frequency response it was necessary to include the capacitance of the output pressure measurement lines. A better correlation between theoretical and experimental values of frequency response, was obtained with this correlation. This means that the circuit of Figure 27 was modified in the following way:
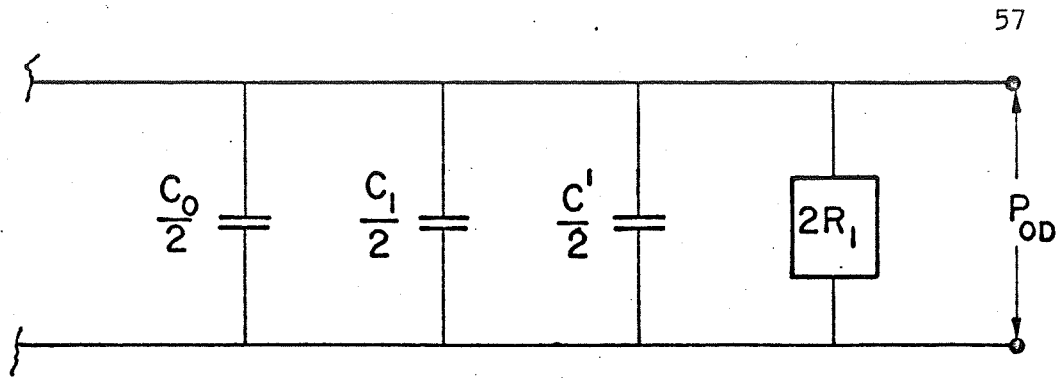
Figure 28.   Modification on High Frequencies
Equivalent Circuit

With this new configuration of the circuit the new total capacitance,

defined as the complete capacitance C_T' was used in formula (6.1) instead

of C_T. The value of C_T' was equal to:

$$C_T' = \frac{C_0 + C_\ell + C'}{2} \tag{6.2}$$

where C' is the capacitance of the output pressure measurement lines,

obtained according to formula (5.15). Values of C' and C_T' are given at

the end of Chapter V.

The effect of the dead time was to delay the output wave a fixed

time without affecting the amplitude. Thereby there was a phase shift

depending on the frequency of the sine wave. In fact, the phase shift

was a linear function, given by

$$\alpha = 360 \times f \times t_d \quad \text{(degrees)} \tag{6.3}$$

which is logical because if the frequency was 1 cps and the total time

delay 1 sec the wave was shifted by 360°. In the preceding chapter the

analysis of the different time delays was performed.

During the dynamic response test the supply pressure was held equal to 5 psig. The supply pressure for the signal generator was kept at a value close to the amplifier supply pressure. Finally the distance from the generator nozzles to the rotating plates was adjusted in order to obtain a differential control pressure that always varied between -0.15 and +0.15 psig, keeping also a bias pressure equal to 0.5 psig.

The dynamic test circuit also included two pressure transducers. Calibration charts for both of them are given in Appendix A. A pressure transducer, Statham TM 131, was used for input signal and a Consolidate Electrodynamics Corp. (CEC) 4-312-0002 for the output signals.

Data were recorded with a type 502 A dual beam oscilloscope and a C-12 camera, both manufactured by Textronix Inc. It is important to note that the upper beam (output signal) always showed a 0.3 cm delay on the screen. Therefore all values of output signals were advanced by this difference to obtain the right measurements. Before taking any data both oscilloscope beams were carefully calibrated.

With the aid of the camera several pictures of input and output signals were taken. Some of them are presented in Figures 29 to 31. Also from these pictures the experimental values of the frequency response were obtained and finally plotted in Figures 32 to 37. These plots, where the theoretical dynamic response was also drawn in, show the good correlation obtained between experimental and theoretical values. Most differences are due probably to the influence of the different tube lines. Another source of error could be that there was not consideration of the effects of the vents in the transfer function.

TOP: Output

Sweep: 50 m sec/cm

Amplitude: 0.5 m V/cm

BOTTOM: Input

Sweep: 50 m sec/cm
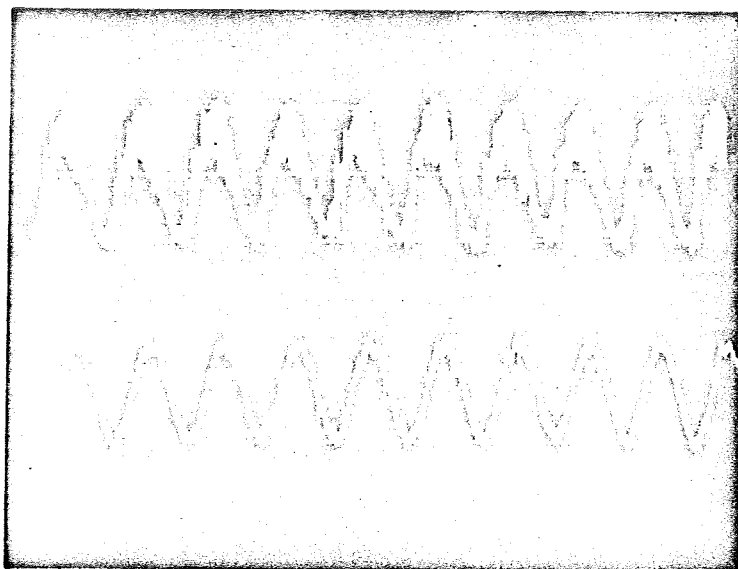
Amplitude: 0.2 m V/cm

70°F - 18 cps - wobble plate

TOP: Output

Sweep: 20 m sec/cm

Amplitude: 0.5 m V/cm

BOTTOM: Input

Sweep: 20 m sec/cm
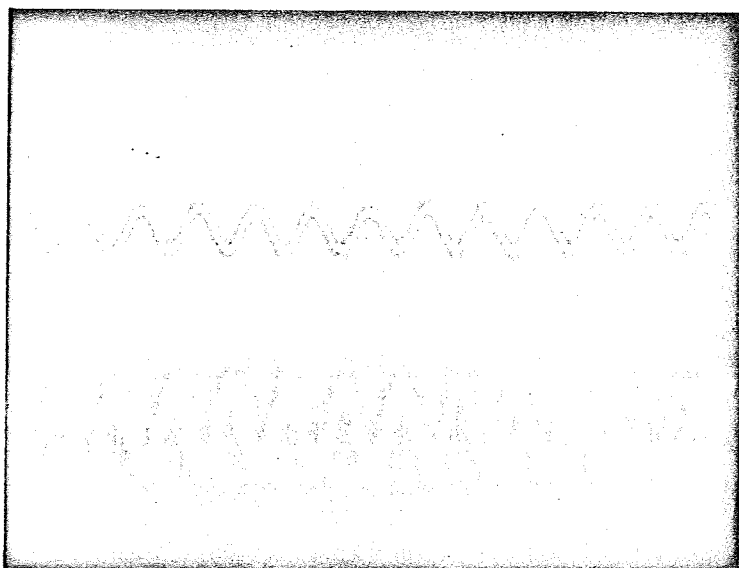
Amplitude: 0.2 m V/cm

500°F - 58 cps - wobble plate

Figure 29. Input - Output Signals - Dynamic Response (70 and 500°F)

TOP: Output

Sweep: 20 m sec/cm

Amplitude: 0.2 m V/cm

BOTTOM: Input

Sweep: 20 m sec/cm
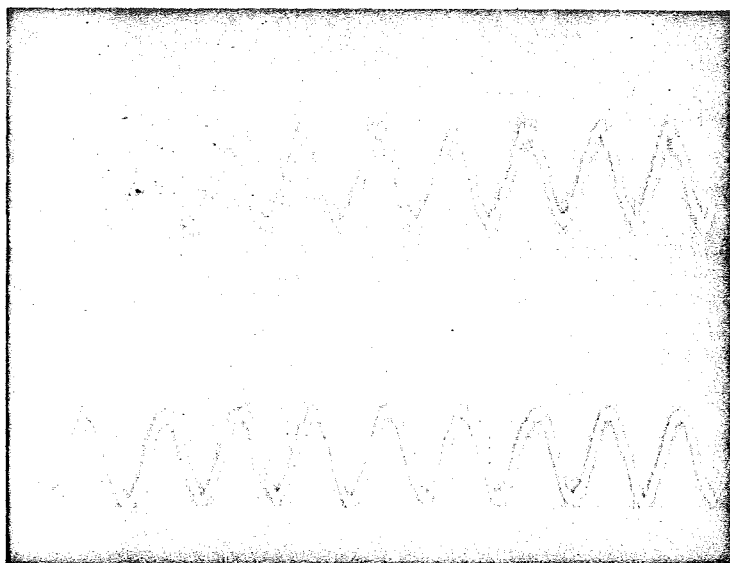
Amplitude: 0.2 m V/cm

1000°F - 45.5 cps - notched plate

TOP: Output

Sweep: 10 m sec/cm

Amplitude: 0.2 m V/cm

BOTTOM: Input

Sweep: 10 m sec/cm
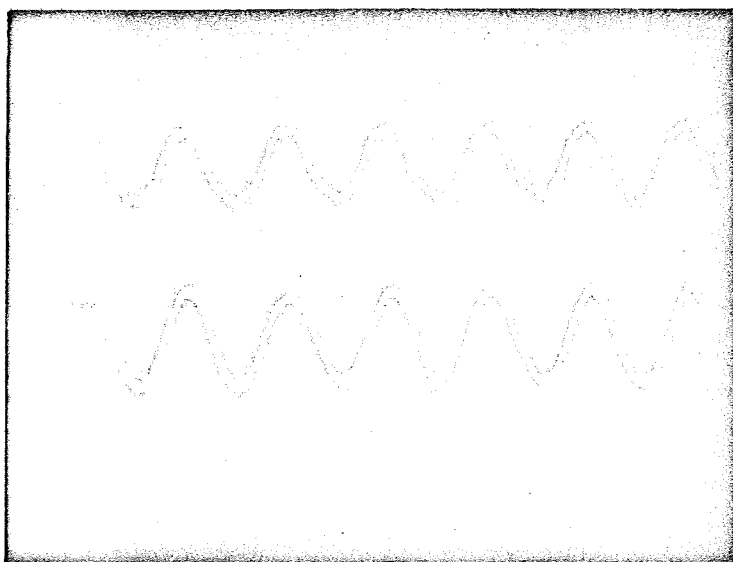
Amplitude: 0.2 m V/cm

1500°F - 66.6 cps - notched plate

Figure 30.   Input - Output Signals - Dynamic Response (1000 and 1500°F)

TOP: Output

Sweep: 50 m sec/cm

Amplitude: 0.5 m V/cm

BOTTOM: Input

Sweep: 50 m sec/cm
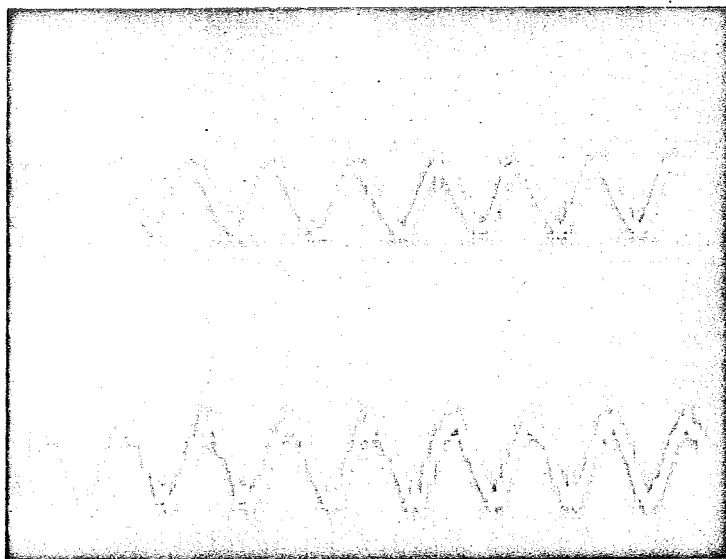
Amplitude: 0.2 m V/cm

·1800°F - 16.6 cps - wobble plate

TOP: Output

Sweep: 2 m sec/cm

Amplitude: 0.2 m V/cm

BOTTOM: Input

Sweep: 2 m sec/cm
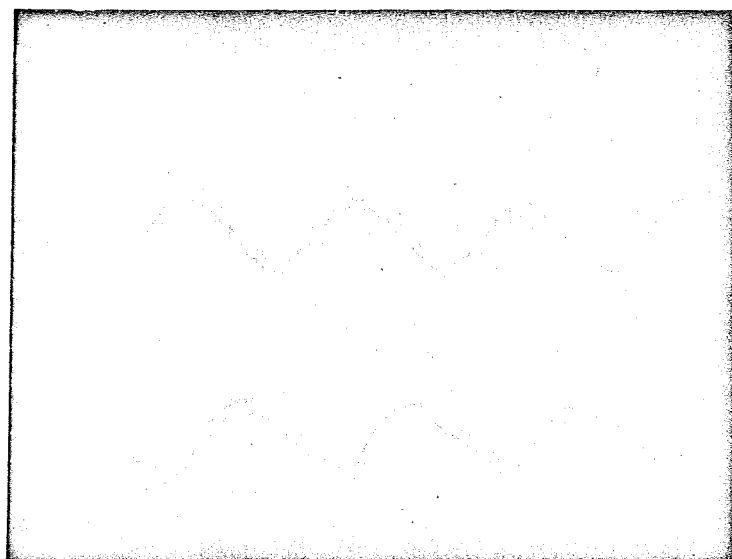
Amplitude: 0.2 m V/cm

2000°F - 208 cps - notched plate

Figure 31. Input - Output Signals - Dynamic Response (1800 and 2000°F)
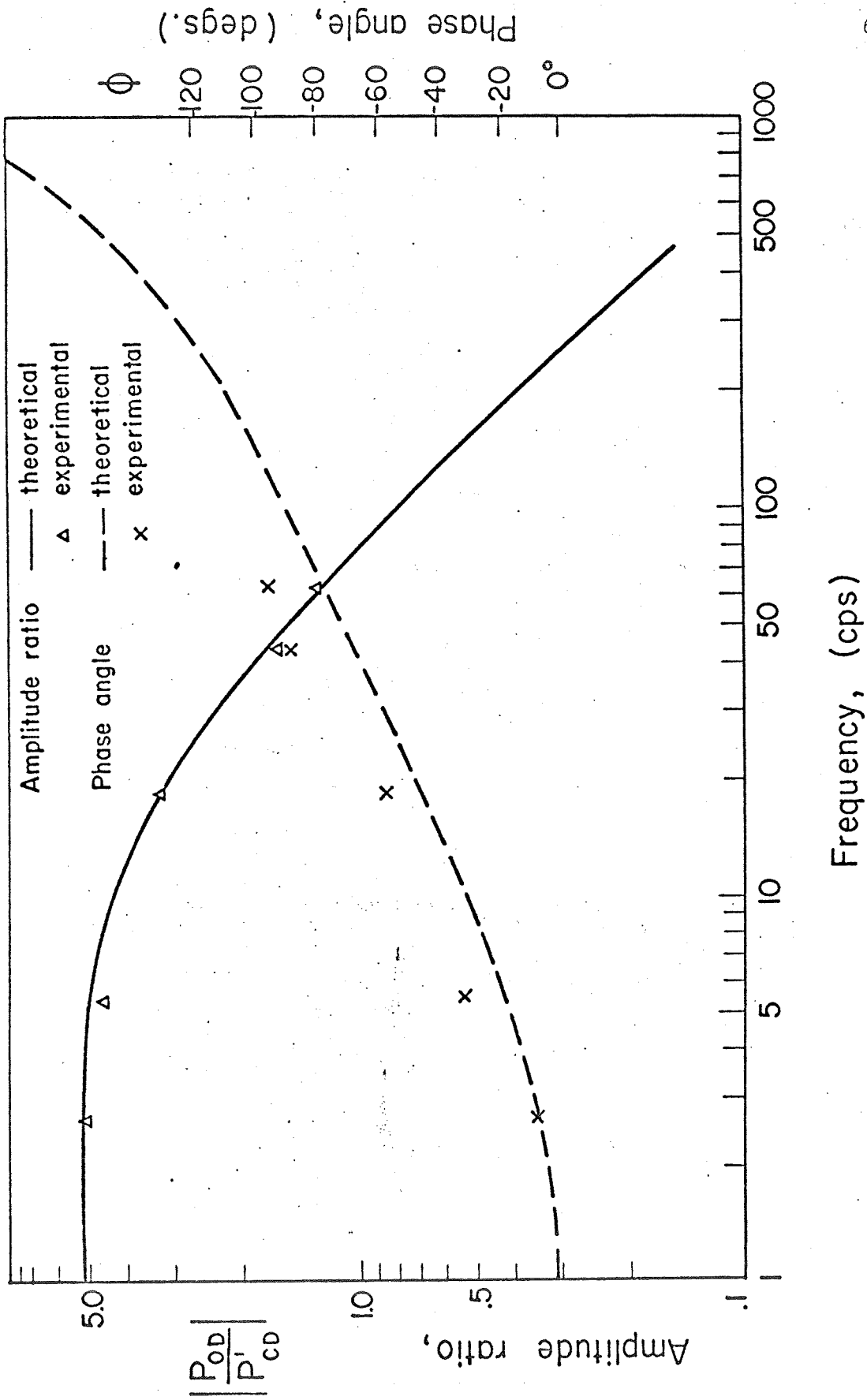
Figure 32   Frequency Response (70°F)

63
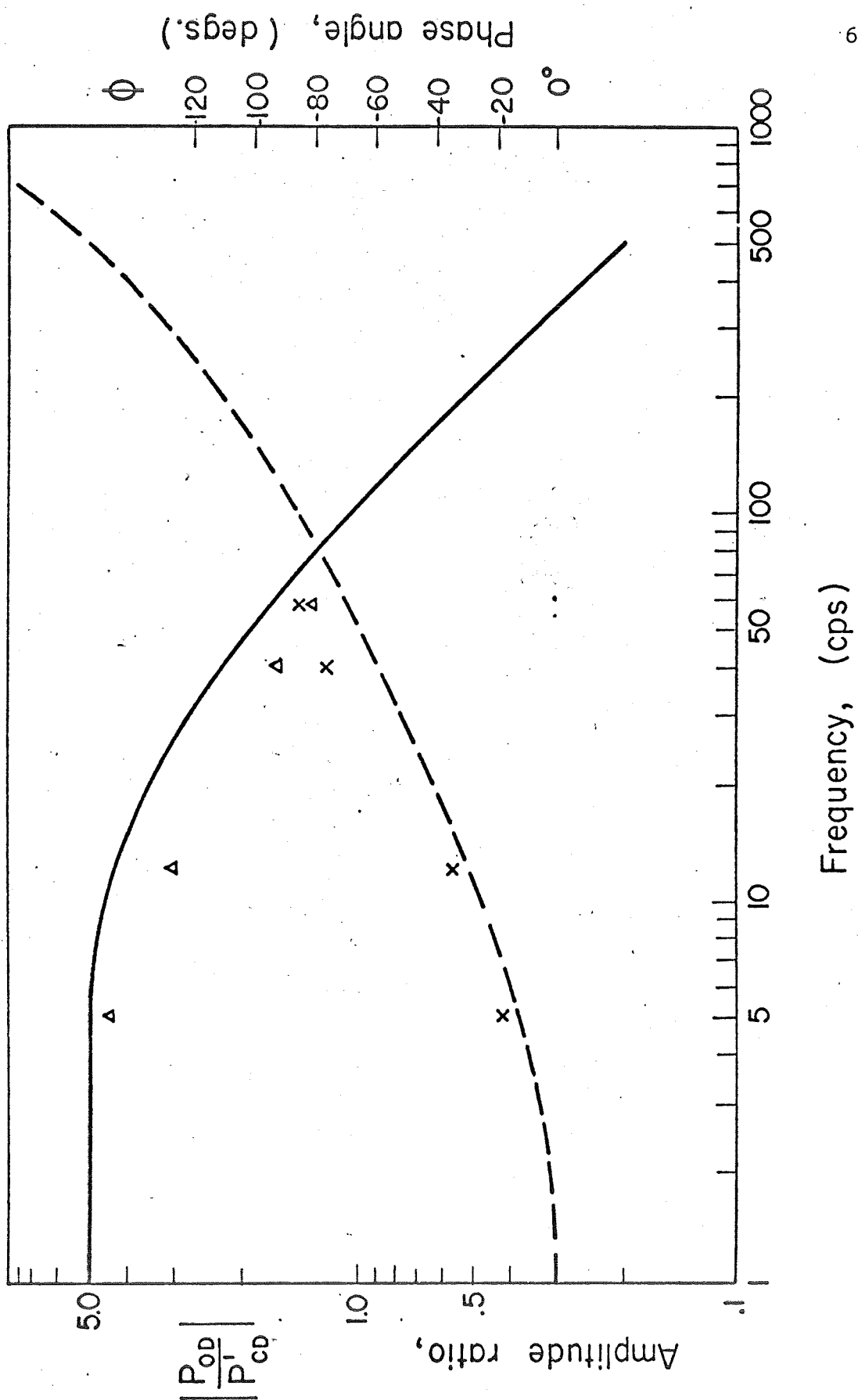
Figure 33   Frequency Response (500°F)
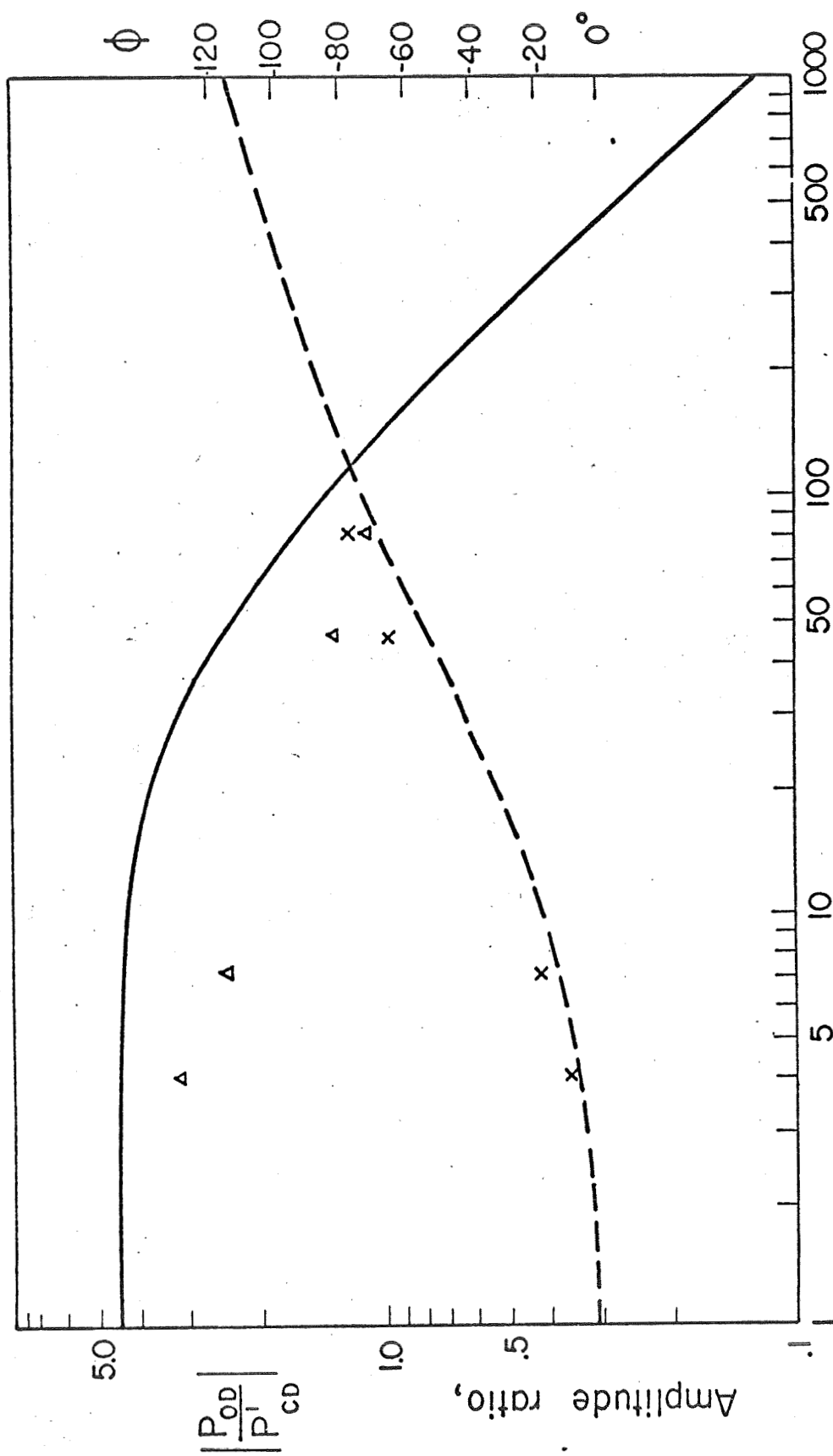
Figure 34   Frequency Response (1000°F)

64

65
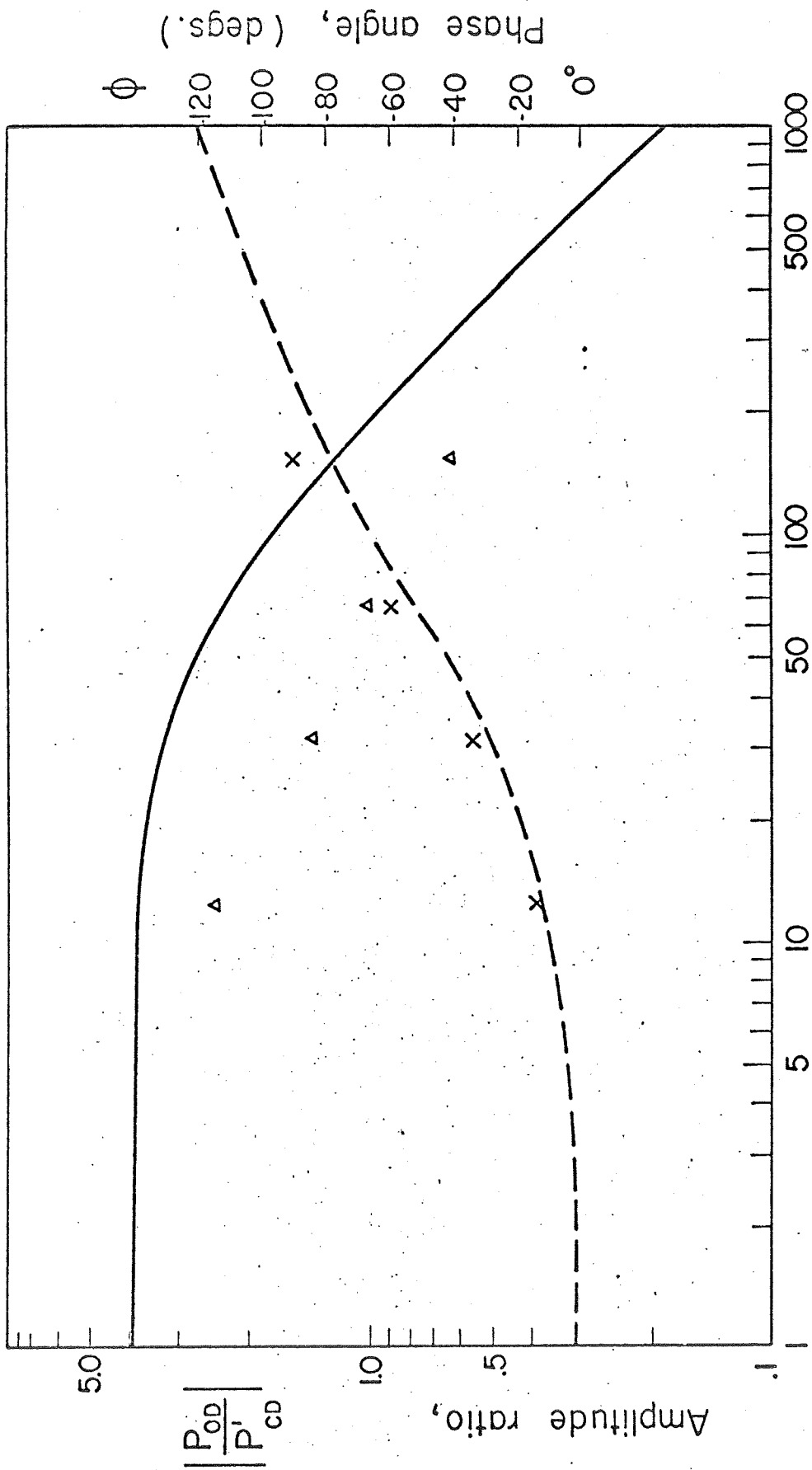
Figure 35   Frequency Response (1500°F)
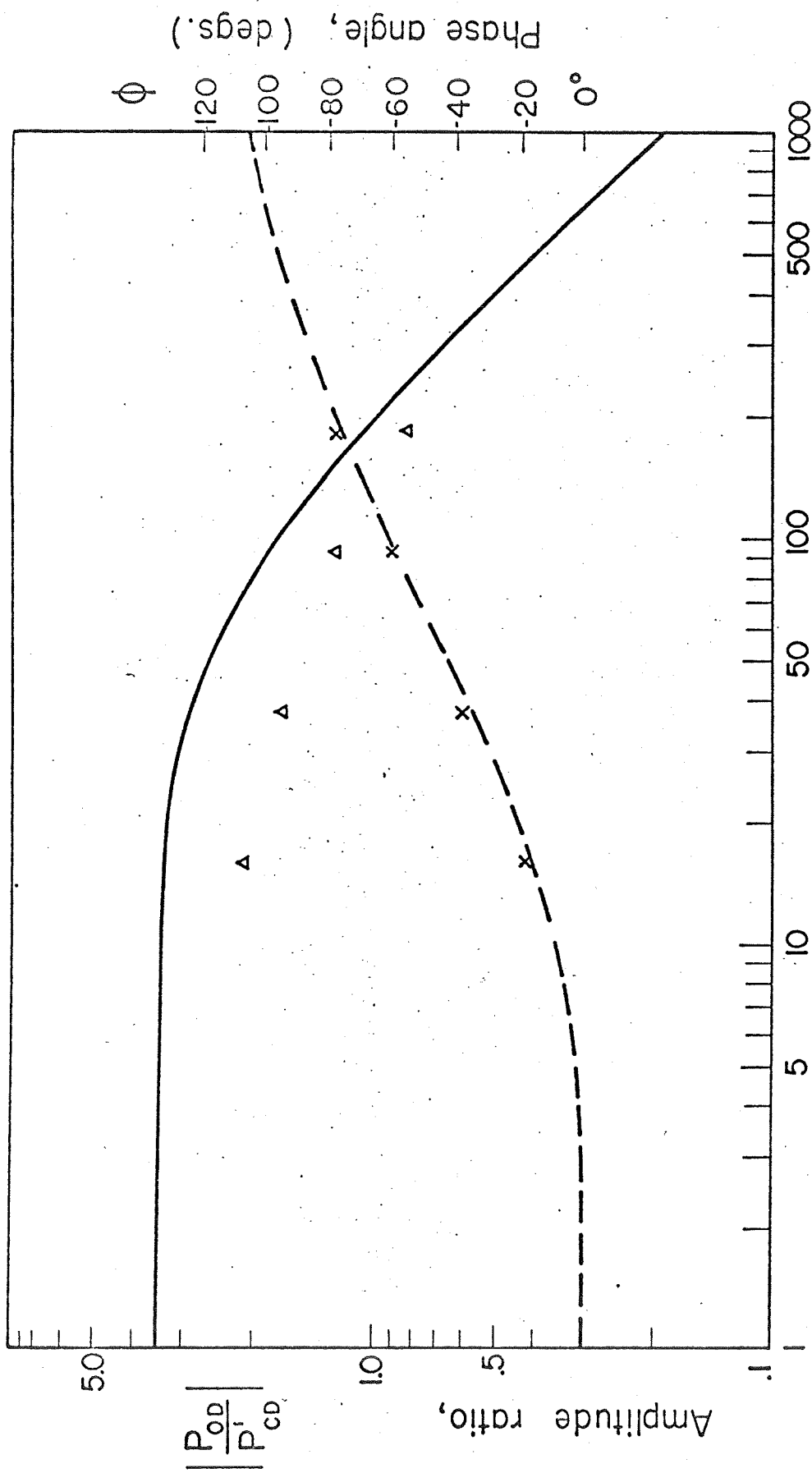
Figure 36   Frequency Response (1800°F)
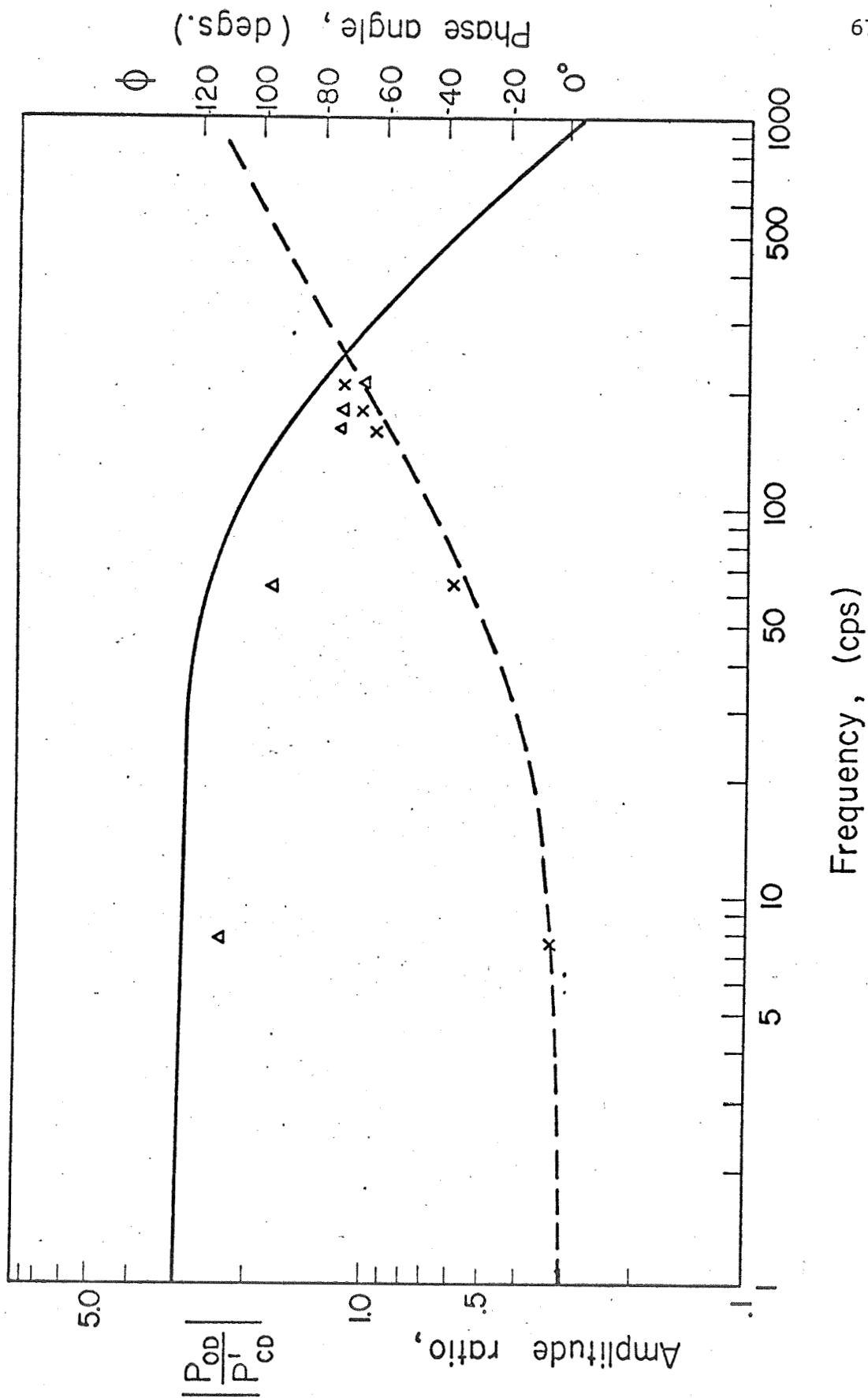
Figure 37   Frequency Response (2000°F)

Also from the pictures taken at different temperatures and
frequencies it was possible to observe the presence of noise in both
input and output signals.   In the input signal the noise was due to
some vibration affecting the rotating plate.   In the output signal
the noise was due particularly because the load line was close to the
unstable region particularly at room temperature.   This fact was
already mentioned in Chapter IV.   Noise limited the highest value at
which the frequency response could be checked.   As temperature increased
the noise in the output signal was reduced and therefore the amplifier
could be tested for a longer frequency range.   Sharp edges and rough
surfaces were possibly another source of noise in the frequency response.

CHAPTER VII

CONCLUSIONS AND RECOMMENDATIONS

The different researchers already mentioned in previous chapters, found a large variety in amplifier parameters, characteristic curves and frequency response depending upon the amplifier design. This says that this thesis related with only one fluidic amplifier cannot give general conclusions, but it provides a good starting point for further investigations.

Static response with normalized data showed that it is possible to predict values of the input characteristics for different temperatures, but this cannot be done for output characteristics where dissimilar values for the temperature range considered were found. Therefore it is necessary to perform the static amplifier test over its complete range of operation.

Amplifier parameters were in general affected by temperature. Amplifier linear range was probably the most constant parameter for the temperature range considered.

Even though it was possible to increase the pressure gain at room temperature taking P_s = 8 psig, the same incremental increase was not found at 2000°F. This says that increasing the supply pressure and therefore the mass flow at high temperatures, the amplifier gain was not appreciably increased.

The frequency response test can be considered successful. Values for other temperatures not considered in the experiment can be predicted.

An excellent correlation between experimental and theoretical values was found at room temperature. For other temperatures the values can be considered very well approximated to those predicted by theory. Larger discrepancies were observed for the amplitude ratio at 1000 and 1500°F. This success in the dynamic test also verified the static response and consequently the amplifier parameters evaluated.

The signal generator showed excellent results. The behavior of the wobble plate was already known but not that of the notched plate. Even though the last one was more difficult to level inside the oven and to machine because the depth of the notches had to be same with good accuracy, the notched plate's advantages of lower speed required, as compared to the wobble plate, can be taken in consideration for further research.

The material used (RA 330) was also very appropriate for this investigation and it is recommended in the future. The values of the mean coefficient thermal expansion for this material, from 70 to 1800°F, is equal to 10.2×10^{-6} in/in°F [17]. Therefore variations with temperature of the amplifier parameters, due to changes in amplifier dimensions, could be neglected. These variations could be considered mostly due to changes in air temperature, density and pressure.

It is important to mention that a better construction of the amplifier profile could have given better results. An etched profile is recommended. Rough surfaces and sharp edges were probably the the cause of noise in the amplifier. This, logically, affected the dynamic response.

The excellent results obtained from the brazing process and the
metal filler used in this project are important to be mentioned.

Finally the development of a complete theory to predict amplifier
parameter and performance, is required.   Also the test of the amplifier
as a part of a complete fluid system is left for further investigations.
These are therefore new challenges to control and fluidic researchers.

LIST OF REFERENCES

1. Lu, C. S., "A Pneumatic Control System for High Temperature Skin-friction Sensor", Sc.D. thesis. The University of Virginia, Charlottesville, Virginia, June, 1970.

2. Warren, R. W., and S. J. Peperone, Fluid Amplification. I. "Basic Principles", Diamond Ordnance Fuze Lab., TR-1039, Part II, August 15, 1962.

3. Dexter, E. M., "An Analog Pure Fluid Amplifier", presented at the ASME Fluid Jet Control Devices Symposium, New York, New York, November 28, 1962.

4. Katz, S., and R. J. Dockery, Fluid Amplification. "Staging of Proportional and Bistable Fluid Amplifiers", Harry Diamond Laboratories. TR-1165, Part I, August 30, 1963.

5. Van Tilburg, R. W., and W. S. Cochan, "Development of a Proportional Fluid Amplifier for Multistage Operation", Proceedings Second Harry Diamond Laboratories Fluid Amplification Symposium, Vol. II, May, 1964.

6. Kirsner, J. M., Fluid Amplifiers, New York, McGraw-Hill Company, 1966. Chapters 13, 16 and 17.

7. Belsterling, C. A., Fluidic System Design Manual, USAAVLABS Technical Report 67-32, Fort Eutis, Virginia, July, 1967.

8. Madonna, M. A., R. C. Anderson, and W. J. Harris, "Investigation of Environmental Effects on Pure Fluid Amplifiers", presented at the ASME Winter Annual Meeting and Energy Systems Expositon, New York, New York, December 1-5, 1968.

9. Moynihan, F. A., and R. J. Reilly, "Deflection and Relative Flow of Three Interaction Jets", Proceedings Second Harry Diamond Laboratories Fluid Amplification Symposium, Vol. I, May, 1964.

10. Chiu, P. C., and C. P. Man, "An Approximate Analysis of Three Two-Dimensional Interaction Jets", presented at tho ASME Winter Annual Meeting and Energy Systems Exposition, Pittsburgh, Pennsylvania, November 12-17, 1967.

11. Peperone, S. J., S. Katz, and J. M. Goto, Fluid Amplification. 4. "Gain Analysis of the Proportional Fluid Amplifier", Diamond Ordnance Fuze Laboratories. TR-1073, October, 1962.

12. Reid, K. N., "Static Characteristics of Fluid Amplifiers", presented at the Fluid Power Research Conference, Oklahoma State University, July 25-26, 1967.

13. Wall Colmonoy Corporation, <u>Nicrobraz</u>, Technical Data Book, Wall Colmonoy Corporation, Detroit, Michigan.

14. Dmitriev, V. N., "Computation of the Static Characteristics of a Pneumatic Relay", <u>Automation and Remote Control</u>, pp. 747 to 761, 1956.

15. Booth, W. A., "A Lumped Parameter Technique for Predicting Analog Fluid Amplifier Dynamics", presented at the Joint of Automatic Control Conference, Stanford University, June 24-25-26, 1964.

16. Belsterling, C. A., and Ka-Cheung Tsui, "Analysing Proportional Fluid Amplifier Circuits", <u>Fluid Amplifiers in Control Systems</u>, reprinted from Control Engineering, 1968.

17. Rolley Alloys, Inc. <u>Technical Data Book</u>, Rolley Alloys Inc., Detroit, Michigan.

18. Monostat Corporation, <u>Predictability Flowmeters</u>, Monostat Corporation, New York, New York.

19. Leeds and Northrup Company, <u>Directions for No. 8657-C Double Range Potentiometer Indicator</u>, Leeds and Northrup Company, Philadelphia, Pennsylvania.

APPENDIX A

EXPERIMENTAL APPARATUS

Oven

Tests were performed using an AMACO HF 65 kiln with the following chamber dimensions: 11 x 11 x 11 in. Temperatures in the chamber were kept within certain tolerances around the setting temperature by using a bang-bang controlled system.

For the calibration of the oven two chromel-alumel thermocouples were used. One of them was set at the center of the chamber; the other was touching one of the side walls. Due to the large volume of the chamber, the lowest temperature occurred just after the power was on and the highest after the power was off. Almost no difference was found in the thermocouples' readings.

After certain time (15 minutes) the temperature in the chamber became more stable and the variations were within ±20°F. For higher temperatures (1500°F up) this variation was smaller. Figure 38 shows the calibrated oven temperature.

Flowmeters

Volumetric flow measurements were taken with five Monostat flowmeters (36-541-23) and values were obtained using predictability charts [18]. For smaller flows, Monostat flowmeters (36-541-14) were used. A calibration curve for each model and for the conditions of the flow (T = 70°F; P = 1 atm) are given in Figures 39 and 40.
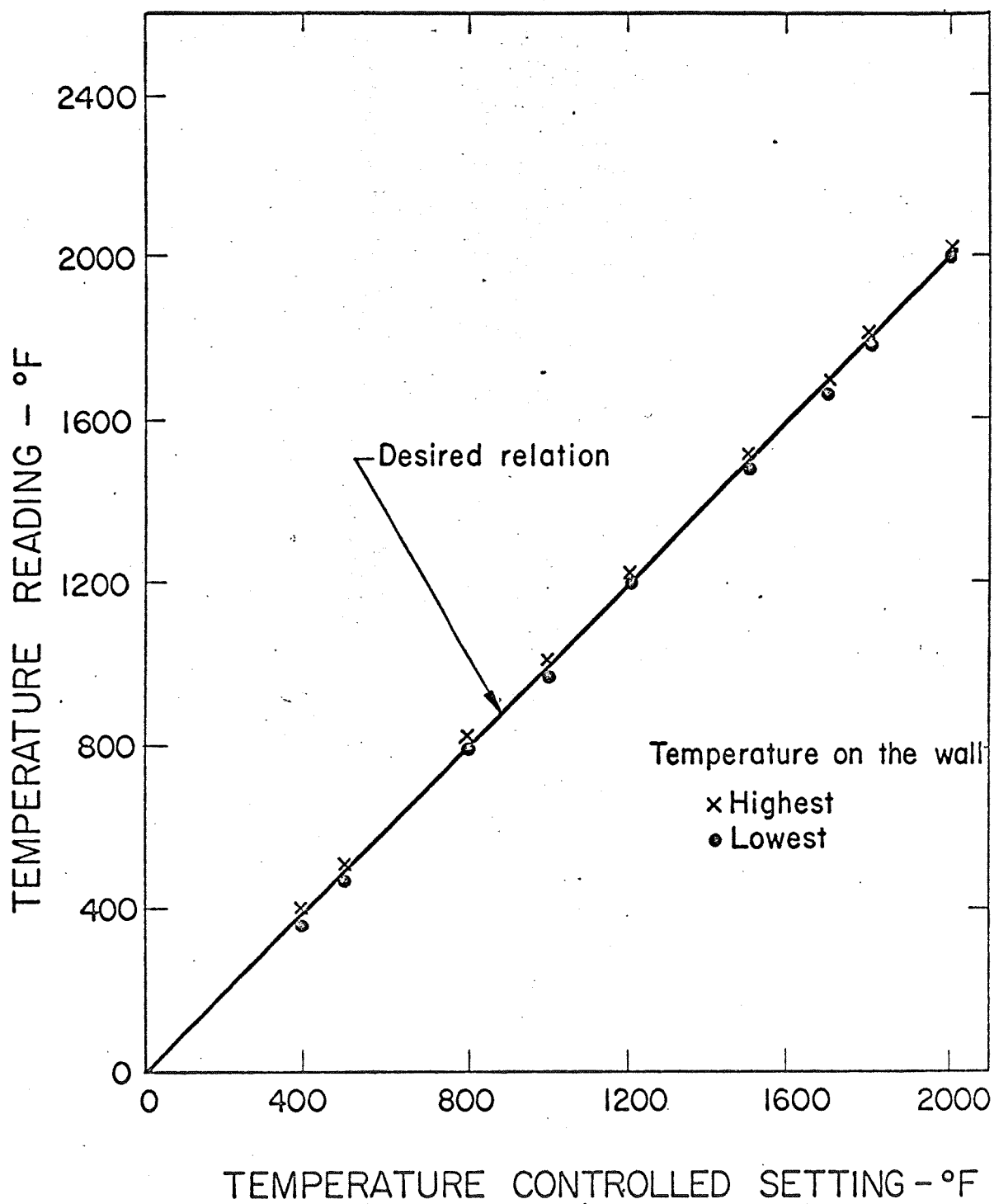
Figure 38   Calibration Data of the Oven
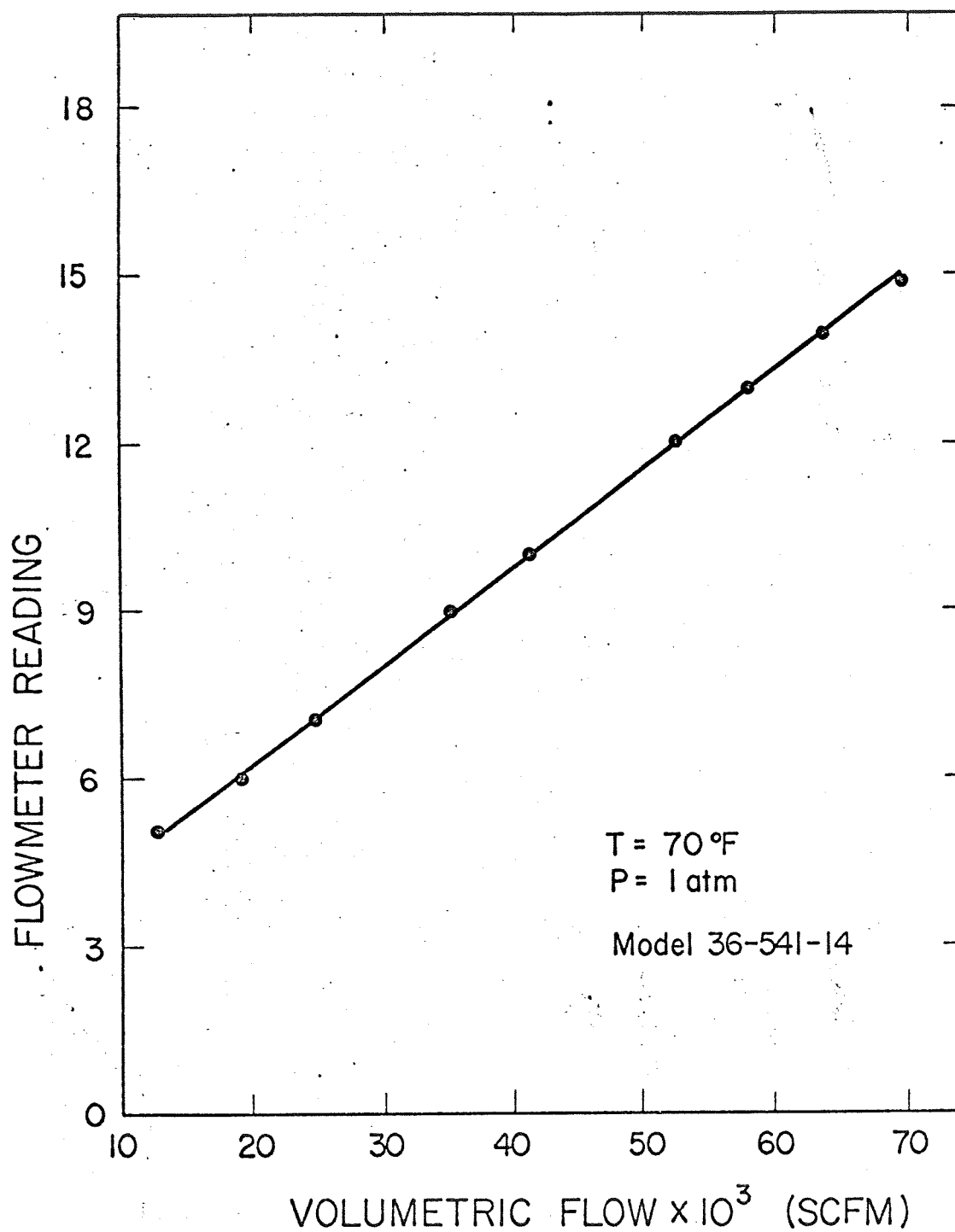
Figure 39   Predictability Flowmeter Calibration Curve
             (No. 36-541-14)
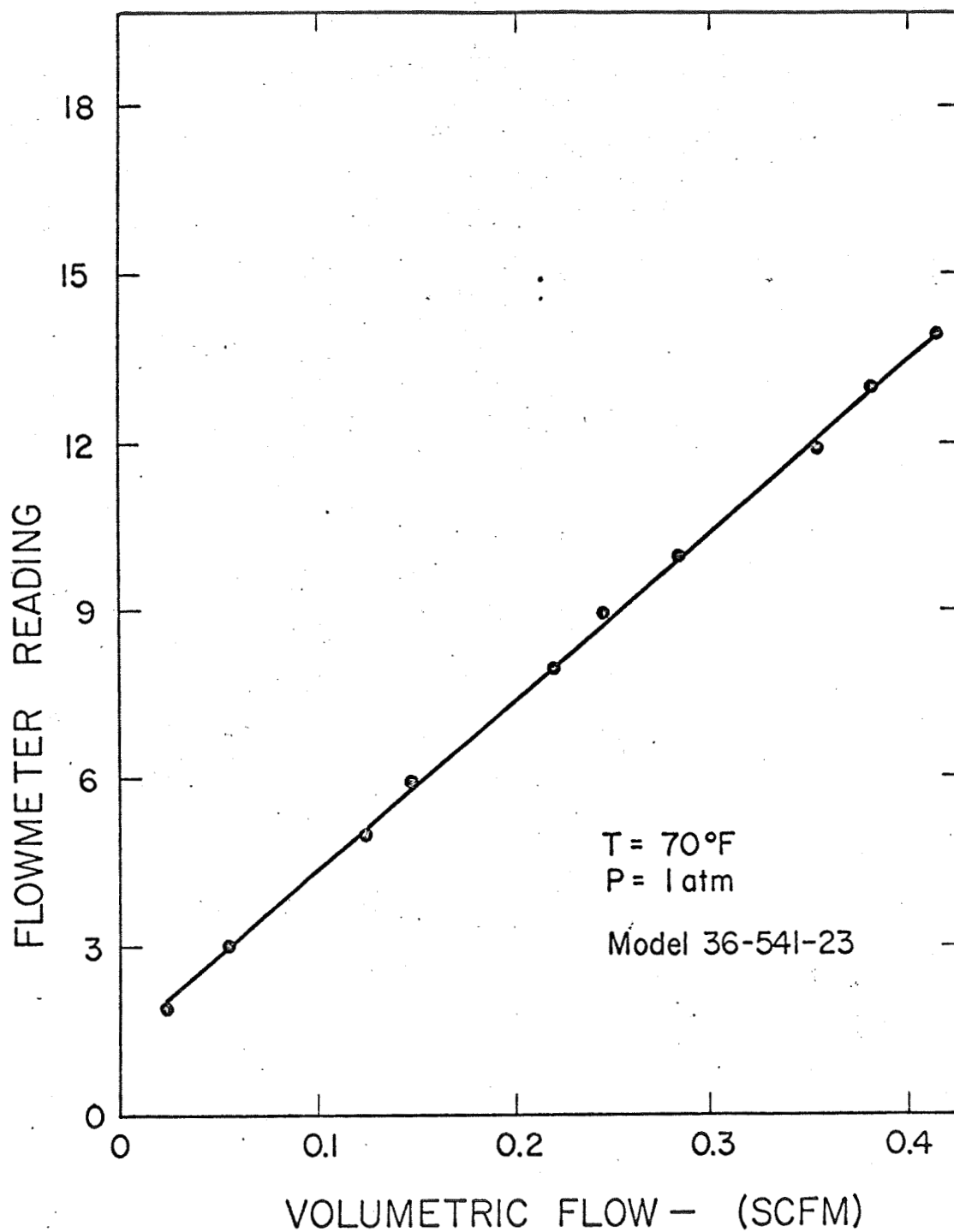
Figure 40   Predictability Flowmeter Calibration Curve
              (No. 36-541-23)

The volume of air when flowing at other than standard conditions, was calibrated from the colume at standard conditions by means of the equation:

$$Q' = Q \sqrt{\frac{P}{14.7} \times \frac{530}{T}}$$

where:

Q = volume of air measured and flowing at standard conditions

(as given in the calibration curve)

P = absolute pressure of air flowing in psia

T = absolute temperature of air flowing in °R.

The accuracy of these meters is within 2% full scale.

Pressure Gages

Two pressure gages were used in this research. Because each one was used to measure one predetermined value of the pressure, it was not necessary to perform the overall range calibration. Only the two values of pressure were checked using a water or mercury manometer.

Potentiometers

Double range potentiometer indicators (No. 8657-C) where used for air flow temperature measurements. These instruments are manufactured by Leeds and Northrup Company. Measurements were performed according to the manufacturer's instruction manual [19].

Oscilloscope and Camera

A 502A, dual beam model oscilloscope and a C-12 camera, both manufactured by Tektronix Inc., were used during the dynamic test of the amplifier. Calibration of both beams was done using the calibrator switch. The 0.3 cm delay in the upper beam was already mentioned in Chapter VI.

Pressure Transducers

The dynamic amplifier test circuit included also two pressure transducers. On the control line a Statham TM 131 was connected and on the output line a CEC 4-312-0002, manufactured by Consolidate Electrodynamic Corp., was set. Even though both were useful for a range 0-25 psig differential pressure, they were linear also for the low pressure range considered. Calibrated values for the relation pressure-voltage are presented in Figure 41.
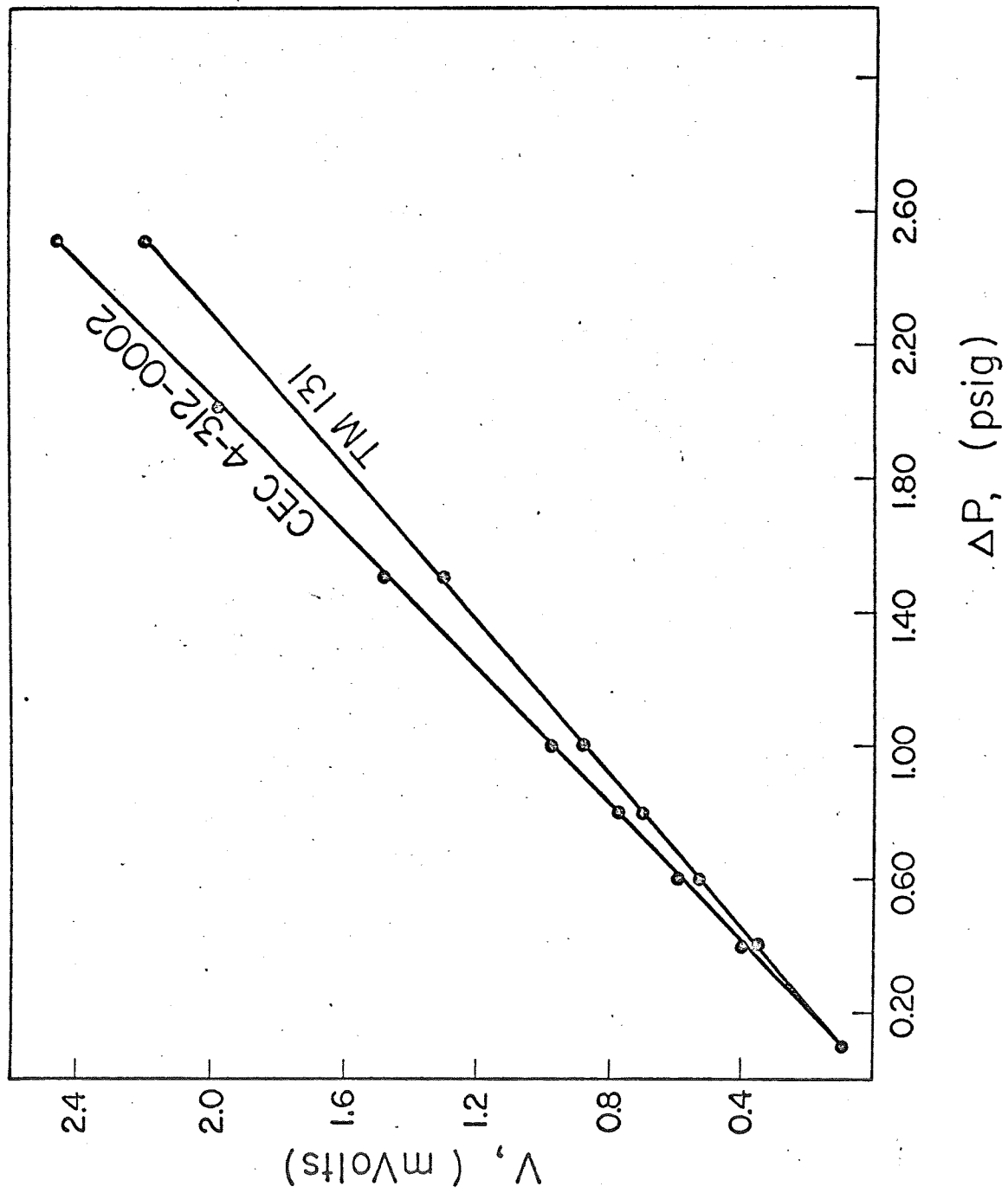
Figure 41   Calibration Data for Pressure Transducers

THE DESIGN OF A HIGH TEMPERATURE

SKIN FRICTION METER SYSTEM

———————

A Thesis

Presented to

the Faculty of the School of Engineering

and Applied Sciences

The University of Virginia

———————

In Partial Fulfillment

of the Requirements for the Degree

Master of Science (Electrical Engineering)

———————

by

David A. Kettler

December 1969

APPROVAL SHEET

This thesis is submitted in partial fulfillment

of the requirements for the degree of

Master of Science (Electrical Engineering)

_____

Author

Approved:

_____

Faculty Adviser

_____

Dean, School of Engineering and
Applied Science

December 1969

ACKNOWLEDGMENTS

ABSTRACT

A high temperature skin friction meter system has been developed

for direct measurement of skin friction force on a hypersonic ramjet

in actual flight or for wind tunnel experimentation. A closed loop

system is required to meet the specifications.

An integral unit consisting of a high temperature torque motor

and displacement transducer is designed for minimum power dissipation

and to meet definite size and torque specifications. The unit is

capable of operating in a 2000°F sustained temperature environment.

Applications of high temperature materials and their assembly for an

experimental unit are presented.

Experimental and analytical results on the final high temperature

motor-transducer assembly and closed loop system design show that the

system meets the size, torque, displacement error, and temperature

specifications. Results on the closed loop system employing a

molybdenum-wire motor are presented for temperatures up to 1900°F.

TABLE OF CONTENTS

TABLE OF CONTENTS – Continued

LIST OF FIGURES

LIST OF FIGURES - Continued

LIST OF SYMBOLS

a	distance from Bendix flexure center to point of force application on force balance apparatus
a'	one side of rectangular current loop
A	area of the rectangular current loop
A_c	cross sectional area
A_m	maximum cross sectional area perpendicular to the flux lines
b	distance from Bendix flexure center to point sting contact
b'	one side of rectangular current loop
b_c	length of the solenoid
B	damping factor
B_{11}	magnetic flux density parallel to the coil plane
$\vec{B}$	uniform magnetic field flux density
$|\vec{B}|$	absolute value of magnetic flux density
B_{mn}	magnetic flux density with respect to plane mn
$\overline{B}_{11_{mo}}$	molybdenum-wire model average magnetic flux density of a general point
B_{max}	maximum magnetic flux density
c(t)	control system output time domain response to a step input
c	distance from armature flexure center to point of sting contact
C	width of armature coil
C(s)	Laplace transform of control system closed loop response

xii

LIST OF SYMBOLS - Continued

d	mean diameter of solenoid
d_w	wire diameter
D	perpendicular distance from point P_0 to the wire of the field coils
e	EMF produced in volts
E_c	carrier frequency amplitude
$E_i(s)$	Laplace transform of input signal
E_I	inverting input signal
E_{NI}	non-inverting input signal
$E_o(s)$	Laplace transform of output signal
f_c	crossover frequency
f_p	frequency at which pole occurs
f_z	frequency at which zero occurs
F	force
G	gap between field coils
G_1, G_2, G_3	functional block gain functions
$G(s)$	Laplace transform of open loop function for unity ratio system
h	one-half the length of the side of the armature front view
i	current
i_a	armature current
i_f	field current
I	effective current
I_a	actual current

LIST OF SYMBOLS — Continued

I_A	armature current readout
J	current density
J_A	current density of aluminum-wire model
J_m	motor mass moment of inertia
J_{mo}	current density of molybdenum-wire model
k	coefficient of magnetic coupling
K_B	Bendix flexure torsional spring constant
K_f	armature flexure torsional spring constant
K_p	loop gain constant of the type 0 control system
K_t	motor torque constant
ΔL	inductance correction for a coil with appreciable radial thickness
L	overall coil length
L_A	armature inductance
L_F	field inductance
L_c	coil inductance
L_s	coil self inductance
$m,\ m'$	axis about which rectangular current loop is rotated
M	mutual inductance
$M_{FA},\ M_{AF}$	mutual inductance between field and armature coils
M_m	$\left\|C(j\omega/R(j\omega)\right\|_{max}$; amplitude of closed loop frequency response peak
M_p	ratio of the peak overshoot to the step input
$\vec{n}$	unit normal vector of magnetic field
N	number of equal turns on a coil

LIST OF SYMBOLS –Continued

P	power dissipation
P_0	general point
r	distance from center of flexure to point of probe displacement
r_w	winding thickness
R	inside radius of coil
R_A	armature resistance
R_F	field resistance
R_G	generator resistance
R_i	number of rows of insulated conductor
S	distance target displaced
(s)	Laplace transform operator
t	time
t_d	time delay
t_i	insulation thickness
t_r	rise time
t_s	settling time
t_w	wire thickness
V	effective voltage
V_A	effective armature voltage
W	variable point on field coil axis
x, y	orthogonal coordinates on current loop
Z	distance from P_0 to center of coil winding
Z_A	armature impedance

LIST OF SYMBOLS – Continued

Z_F	field impedance
Z_{FD}	feedback impedance
Z_I	parallel combination of inverting input impedances
Z_m	mutual impedance
Z_T	transfer impedance
Γ	distance from coil center to infinitesimal area
θ	angle target displaced
θ_B	angle the normal vector makes with the direction of flux density
θ_e	position error
$\theta_{e_{ss}}$	steady-state position error
θ_R	reference position
θ_C	output position
μ_o	permeability of free space
λ	variable of integration
l	finite length of wire
τ	torque
τ_d	disturbance torque applied to system; skin friction torque
τ_e	torque error
$\tau_{e_{ss}}$	steady-state torque error
τ_m	motor restoring torque
ϕ	flux in webers
ϕ_{FA}	flux induced in field coil by current in armature coil

LIST OF SYMBOLS —Continued

ω frequency in radians per second

ω_n natural resonant frequency

Ω dimension ohms

α angle between flux density and the flux density perpendicular to a plane of interest

β phase shift

ζ damping ratio

CHAPTER I

INTRODUCTION

This thesis presents data on an electrical skin friction meter
designed to meet the hostile environmental specifications of high
speed aircraft flight conditions, e.g., 2000°F. Experimental,
analytical, and design data are presented on a closed loop system.
A high temperature motor-transducer air-core unit is employed which
satisfies the temperature specifications to 1400°F.

The need for such a meter has arisen from efforts to measure the
in-flight thrust of a rocket or jet engine. In an attempt to correlate
theoretical parameters with the actual flight conditions, direct
measurement of aerodynamic skin friction drag is necessary. It is
desired that the sensor operate at the local temperature so that
thermal gradients will not affect the skin friction.

The skin friction meter is to be used to make thrust measurements
of a ramjet engine mounted below a high speed experimental aircraft
at altitudes up to 123,000 feet and at speeds up to Mach 8. Applica-
tion also exists for wind tunnel experimentation on high speed models.

Although no exact specifications have been written, the following
specifications [1] have been established to guide the development of
the skin friction meter:

   1.) Force measurement range: The meter is to be capable of

        measuring a force in the range of 0.7 to 7 millipounds.

2.) The meter must withstand sustained ambient temperatures of 2000°F. Flight duration will be approximately 700 sec.

3.) Vibration: The meter is to be capable of operating in environmental levels of 0.06 inch double amplitude at 10-55 Hz and 10 g vibration from 55 Hz to 2000 Hz.

4.) Acceleration: The maximum translation acceleration attained in the direction of flight is 3.5 g.

5.) Space requirements: The limiting dimension is the height (distance from skin to jet nozzle) which is 2 inches. The other two dimensions may be somewhat larger.

6.) Available power: The power supplies available in the X-15A-2 airplane are as follows:

a.c.: 3 phase, 115 V (± 11V), 400 Hz (± 4 Hz)

d.c.: 28 volts nominal, varies from 24 to 31 volts, ripple is ± 0.5 V at 2400 Hz, maximum of 10 amps available from each source.

7.) The maximum deflection of the "target" must not exceed 0.0005 inch. The target is a small area of the aircraft skin which is free to move when acted upon by a friction drag force.

A basic diagram of the system is shown in Figure 1 [1]. The motor-sensor assembly is an air core device, i.e., no ferromagnetic material in the surrounding medium. Air is used as the medium because there exists no ferromagnetic material with a Curie temperature above 2050°F. In addition, with no ferromagnetic material present, the flux
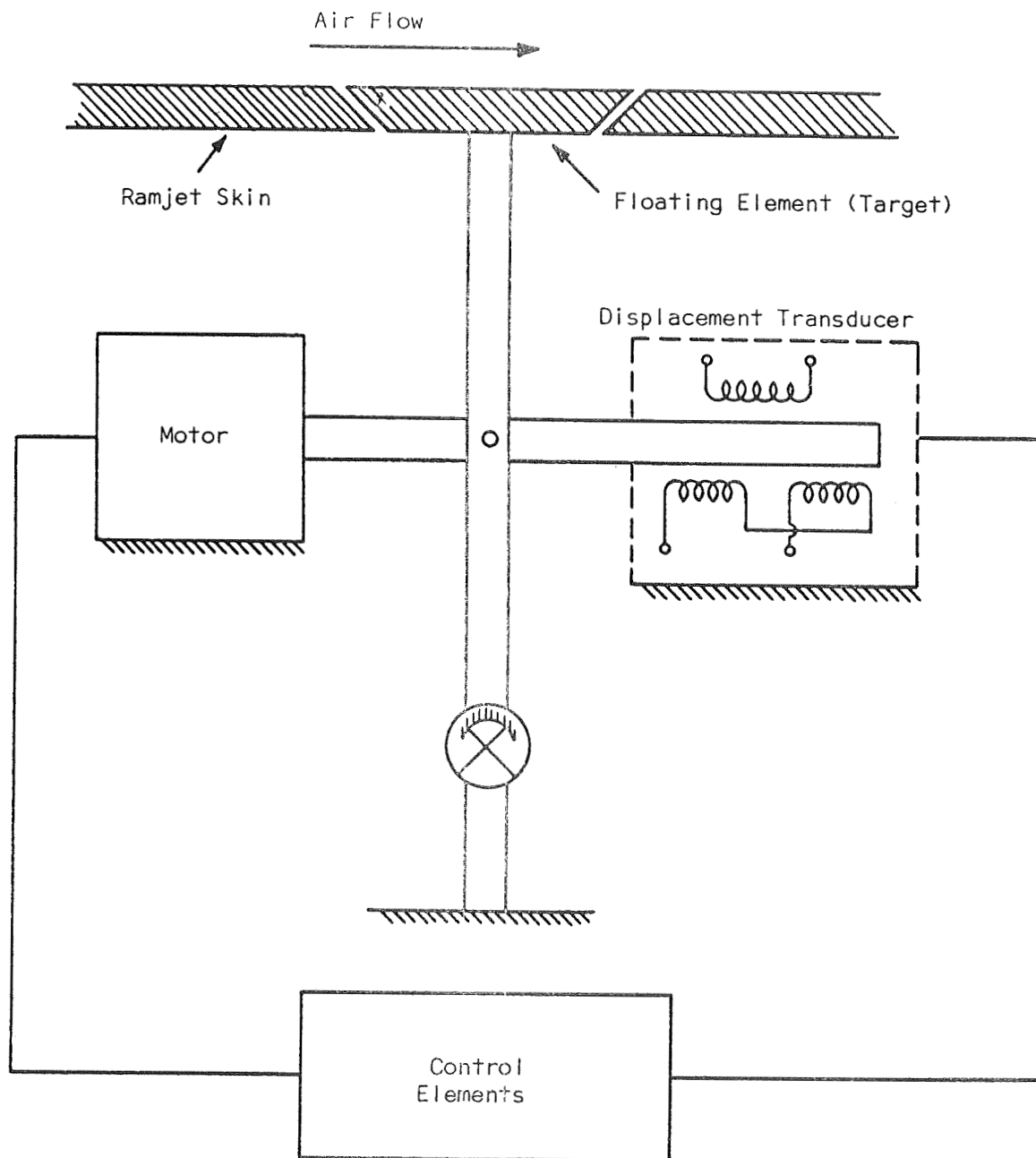
FIGURE 1. Schematic Diagram of Closed Loop System for Measuring Skin Friction

is directly proportional to the current. Hydrous aluminum silicate (lava) is the basic constituent used for the coil forms, while ceramics are used not only for the flexure structure but also for encapsulation. Molybdenum wire is used with a quartz fiber insulation.

The system employs the floating element technique in which a small portion of the aircraft skin is suspended so that it will move when acted upon by a drag force. The floating element (or target) is supported by a flexure. The flexure provides a frictionless support and a linear constraining force. Since parameters will vary with changes in temperature, the system has been designed for closed loop operation to minimize effects of the changes. A friction drag force will initiate a displacement of the flexure and transducer. The transducer produces an electrical signal proportional to the displacement. The electrical signal is amplified to drive the motor and return the arm to the null position. The motor and transducer are integrated as a single unit. Force measurements are obtained by observing motor armature current, because motor force is proportional to motor current in a linear system. Accuracy depends on motor calibration and loop gain.

Preliminary investigation of the air-core model by Seemuller [2] indicated that there was little change in the motor torque constant up to 1300°F. Lead contact pools, which were used to conduct the armature current, acquired a heavy layer of oxide at high temperatures and prevented free movement of the armature above this temperature.

However, the data were reliable enough to justify a continuation of the work as reported here.

Research has been conducted [3] on the development of a gas bearing which could replace the flexure presently used. The gas bearing will provide a nearly frictionless support without adding a constraining force to the system.

Although it does not appear at this time that the gas bearing can be incorporated into the motor-sensor developed, other flexures are being investigated. Among those in consideration is a high temperature stainless steel flexure developed for use in the pneumatic version of the skin friction meter [4]. The spring constant is approximately the same as that of the two-support flexure used in this system. It is also capable of supporting the mass in a vibrations and acceleration field as specified.

Utilization of any of these flexures requires the use of counterbalancing techniques, because the accelerations and vibrations of the aircraft will cause outputs due to the inertias of the floating element and support arm. These extraneous outputs may mask the readouts of the drag force to be measured. Counterbalancing techniques [5] will make the meter insensitive to both linear and angular accelerations of the vehicle.

Work is presently being done on the development of a three-support flexure which will eliminate theoretically the need for counterbalancing. In addition, the flexure spring constant will be approximately the same

as that currently used and will be designed such that minimal changes
in spring constant occur when the flexure is subjected to temperature
change, acceleration, and vibration.

Previous investigation [1] indicated that elongation of lead
wires produces a change in the null position. In this model the
leads are connected to the flexure supports which act also as
conductors for the current to the armature. In an attempt to
eliminate the need for supplying current to a movable element a cobalt
motor-sensor was studied. Cobalt is a ferromagnetic material. It has
the highest Curie temperature of the existing elements. With a high
enough incremental permeability and relatively large air gaps the motor
force constant can be made linear even though permeability changes
with temperature. The sensor is made of windings incorporated into
an electrical bridge circuit so that displacement of the armature
changes the air gap and effectively changes the inductance. Impedance
changes in the bridge produce an electrical output signal. However,
the Curie temperature of cobalt is 1121°C and the motor-sensor has
a 200°F temperature rise. This will limit application of this approach
to temperatures of not more than approximately 1600°F. Further
investigation of the permeability of cobalt is necessitated before
a final conclusion as to its applicability can be made. A control
system has been built [6] and the complete system operates satisfactorily
at room temperature.

The system is designed so that only the motor-sensor unit is

subjected to the hostile environment and space limitations. The

electronic control package is placed in a relatively benign environment

and connected to the integral unit control package by means of six (6)

80-20 nichrome leads.

The material which follows covers the development of the complete

electrical skin friction meter system. The design and analysis of

the motor-sensor unit, consideration of material properties, and the

synthesis and analysis of the closed loop system are presented and

evaluated. Although preliminary work was done [1, 2, 7] to establish

feasibility, all of the results presented are new unless otherwise

noted.

CHAPTER II

HIGH TEMPERATURE MOTOR DESIGN AND EVALUATION

The motor design selected for the skin friction meter employs
the basic operating principle of the electric motor and of most
electric meters used for measuring current or potential differences;
namely, a torque on a current loop. The principle of operation of
the configuration as shown in Figure 2 is as follows:

A d.c. current flowing through the two field coils produces a
magnetic field parallel to the armature coil plane. A d.c. armature
current produces a torque whose direction depends on field coil and
armature coil current direction.

General characteristics of the motor are as follows:

(1) The output torque is directly proportional to the armature
current. Therefore, the armature current may be monitored
to determine the null-restoring torque, which is equal to
skin friction drag torque. By employing materials with low
coefficients of thermal expansion, high temperature effects
have little influence on the motor torque constant. If
the current in either the armature or the field coils is
held constant, the only way for the torque constant to
change is for the armature to change its position relative
to the two fields coils. In this configuration, the motor
will expand so that the armature remains centered between
the field coils.
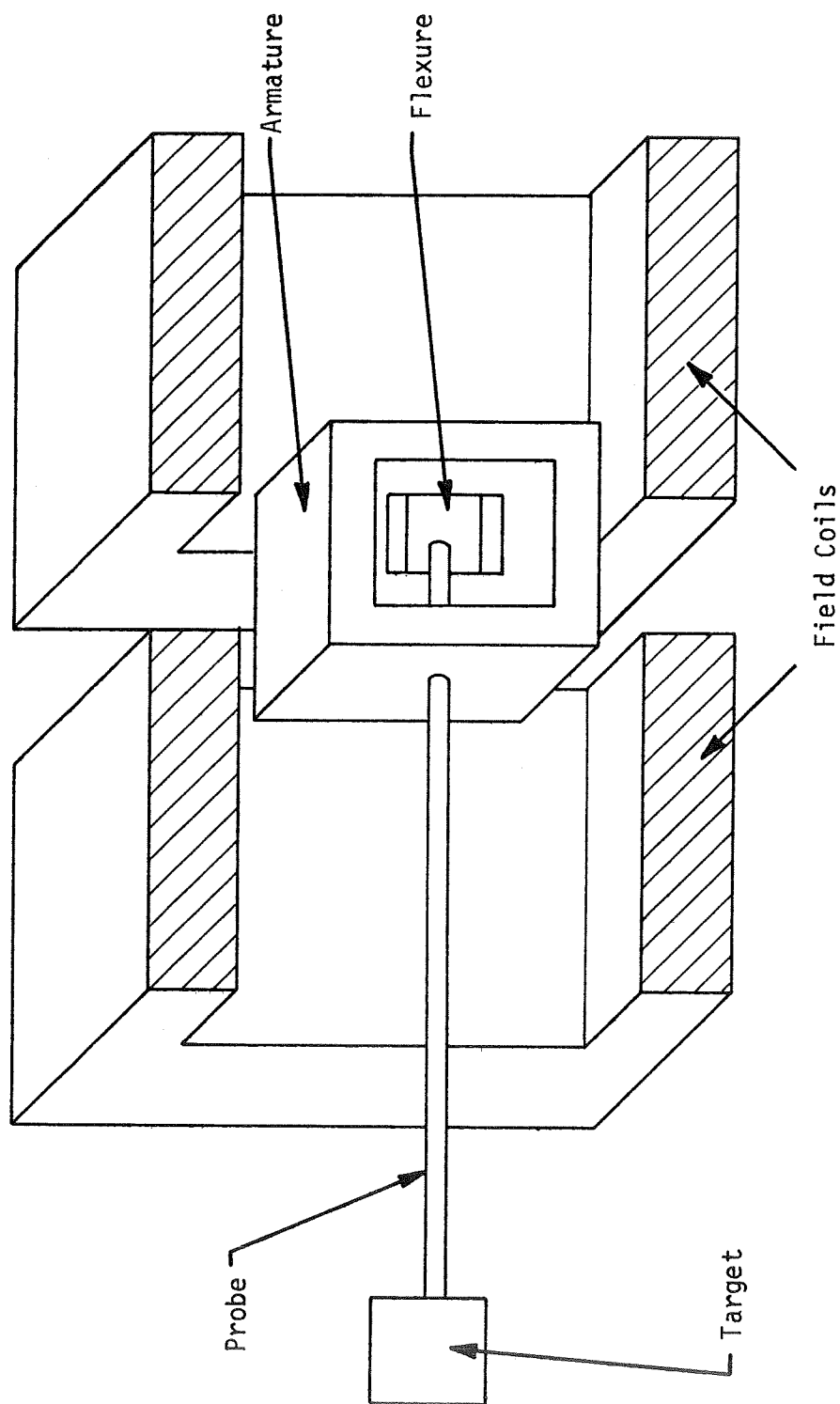
Figure 2. Sketch of High Temperature Motor

(2) It is an air core device. Molybdenum wire, Haynes Alloy
No. 25, quartz, hydrous aluminum silicate, and titanium
dioxide are the materials used in its construction. All
are capable of withstanding temperatures greater than
2000°F.

(3) The motor-sensor unit dimensions are:

Height: 2.0 inches

Width: 2.8 inches

Depth: 2.8 inches

(4) Position sensing is achieved by superimposing a 5 KHz carrier
signal on the d.c. current flowing in the armature coil.
Depending on the angular position of the armature coil, the
field coils have an emf induced into them due to generator
action. The null or zero induced voltage position occurs
when the armature coil plane parallels the field coil axis.

(5) The armature is supported by a rotational high temperature
two-support flexure which also conducts the supply current
to the armature.

A small gap is required in the field coil to mount the supporting
arms of the flexure. Since any gap reduces the effective length of
the coil, the gap introduced is kept at a minimum. A gap width of
0.40 inch was necessary in the motor to provide rigid support for
the flexure. It is a disadvantage that alignment must be accomplished
by positioning the motor-transducer unit in the three-dimensional space.
However, encapsulation of the unit will prevent any change in the rel-
ative coil and flexure orientations.

I. HIGH TEMPERATURE MATERIALS

Coil Forms

Square coils were used in the design because it has been shown [1] that when physical constraints are placed on the length, radius, and thickness of coil windings, the cross sectional shape is a factor in power minimization. Intuitively, it is apparent that minimum power dissipation exists when each field coil has the smallest cross sectional perimeter because it produces the greatest flux density for any armature coil shape.

Investigation of the optimum field geometry shows that for minimum power dissipation, the length of the coil should be as large as possible. Since it was also shown that the minimum space for the flexure is 1 inch, the minimum length for one side of the field coil is approximately 1.8 inches. This includes the air gap between the coil forms, the thickness of the forms, and the thickness of the armature windings.

The parameters of the coil dimensions used for the motor are therefore physically constrained by the height dimension and the flexure design. Also, taken into consideration was the fact that the other dimensions could be only somewhat larger. The field coils were therefore restricted to a winding thickness of 0.28 inch, although a second motor was wound with a winding thickness of 0.35 inch for comparison purposes.

Drawings of the coil forms are presented in Figure 3 and Figure 4.

The coil forms are machined from hydrous aluminum silicate. The material is purchased from the American Lava Compnay of Chattanooga, Tennessee in 6-inch or 9-inch prisms of Grade A lava. The material is capable of withstanding continuous heat at 2012°F. The thermal expansion linear coefficient is 3.6 x 10^{-6} per °C for a temperature range from 25-900°C. Although the unfired lava exhibits a density of approximately 0.1 lb/cu in [8], the fired lava has a measured density of 0.0879 lb/cu in. Literature sources indicate it can be 0.083 lb/cu in. See Appendix A for information on other properties.

Grade A lava expands on heating. The expansion reaches approximately 2 per cent at 1900°F. Since negligible change in dimension is noticed at 2000°F, this is established as the curing temperature. The speed of heating is approximately 150°F per hour until the curing temperature is reached. The heating is terminated and the pieces are taken from the furnace after cooling below 200°F.

Aluminum silicate has been chosen not only because of its capability to withstand extreme temperatures but also because a good insulator is needed to prevent eddy current loss. The loss factor at 1 MHz is 0.053.

The thermal resistance of each of the field coil forms was found to be 1.48°C/watt while the thermal resistance for the armature coil form was found to be 2.08°C/watt. The thermal resistance of molybdenum wire to the coil form was found to be 1.11°C/watt for both

Material: Hydrous Aluminum Silicate
           (American Lava Corporation)

Actual Size

Top View

Front View
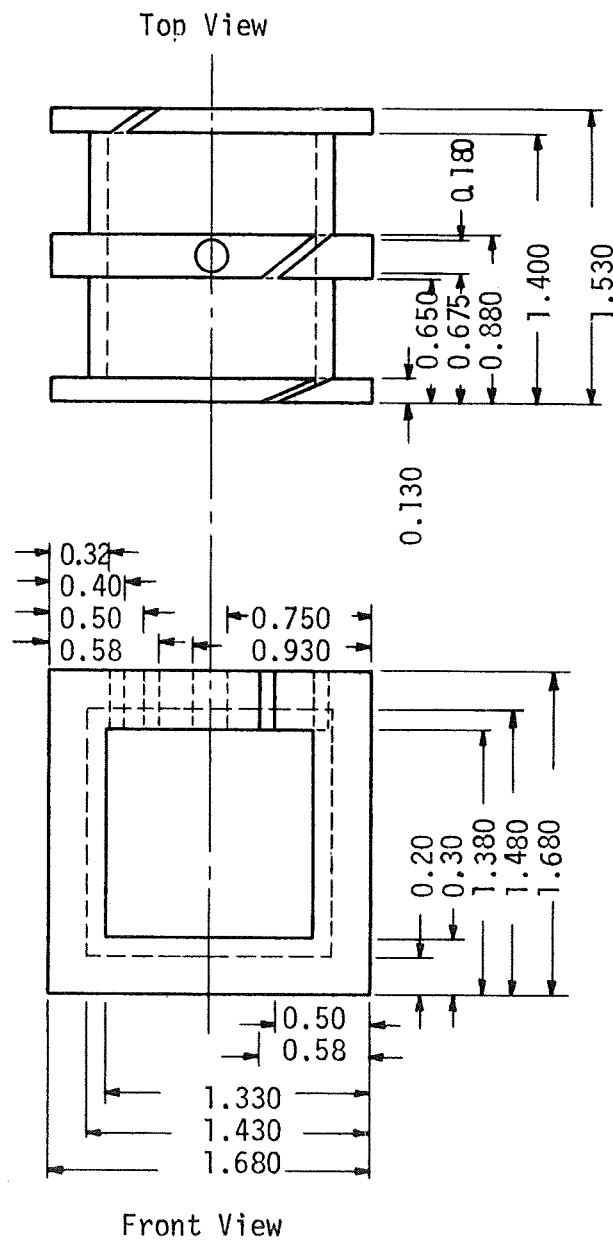
Figure 3. Armature Coil Dimensions

Material: Hydrous Aluminum Silicate (American Lava Corporation)

Top View

Actual Size
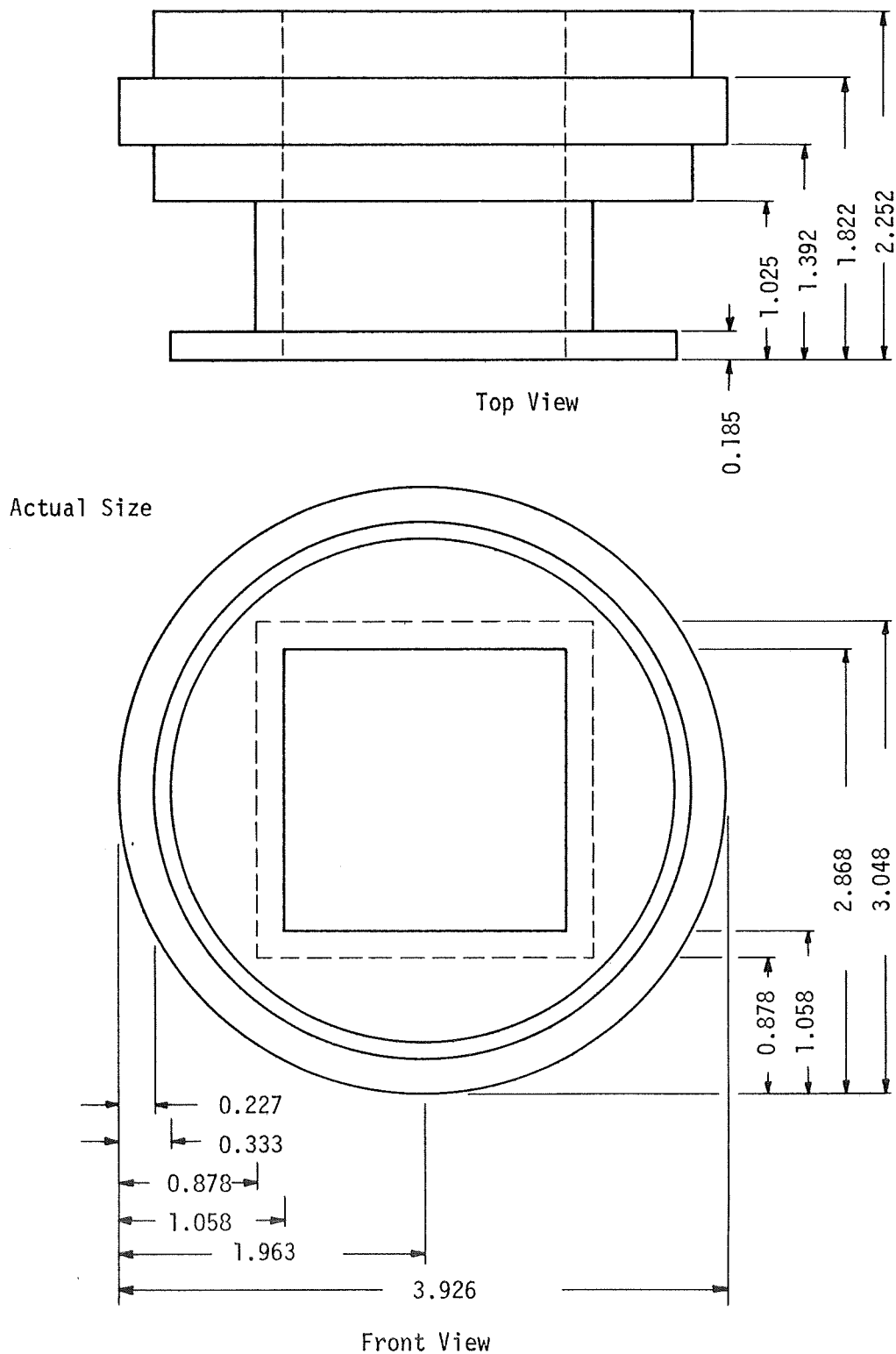
Front View
Figure 4. Field Coil Dimensions

the armature and field coils. It should be noted that the thermal conductivity generally decreases at the higher temperatures. Alumina, for example, has a thermal conductivity at 1800°F that is only 30% of its room temperature value [9]. The thermal conductivity of molybdenum at 2100°F is only 67% of its value at room temperature [10]. The motor field current has been set experimentally so that the temperature rise of the field coils and the armature coil are approximately equal. The rise is 400°F for a time duration of 15 minutes.

Experimental data shows that the field coils have a temperature rise of 230°F at 1800°F, while the armature coil has a temperature rise of 200°F for 5 minutes at 1600°F substantiating the above.

Coil Windings

While awaiting delivery of the insulated wire for the final model, the coil forms were wound with a bifilar winding of B & S No. 20 aluminum oxide insulated aluminum wire. The bifilar winding was used to simulate the insulated winding of the final model. One of the wires provides the approximate spacing of the insulation. The thickness of the aluminum oxide insulation is less than 3×10^{-4} in.

The coil forms of the high temperature model are wound with B & S No. 20 molybdenum wire insulated with a woven quartz fiber. The quartz insulation is manufactured by the Hi-Temp Wire Company of Westbury, New York. Tests indicate that the insulation is capable of withstanding 2200°F but loses its ductility at 1900°F. However, this presents no problem because the windings will remain secure once they have been formed.

Molybdenum has been chosen as the conducting material in order to keep the resistance low and the power dissipation to a minimum. Of all the materials capable of withstanding 2000°F, molybdenum has the lowest resistivity at that temperature. The electrical resistivity of molybdenum changes approximately linearly from 5.78 microhm-centimeters at room temperature to 34.8 microhm-centimeters at 2000°F. It is noted that the resistivity at 2000°F is 6 times that at room temperature. This is a definite factor in the design of the control system.

The wire diameter of 0.032 in was selected for two reasons. First, previous investigation had shown that the wire diameter should be made as large as possible for the winding of the excitation coil. Since it was not known at the time whether the field coils or the armature coils would be excited in the final design, all coils were to be wound with wire of the same diameter. Secondly, the thickness of the insulation is a determining factor. For a given rectangular cross section of winding and a given number of ampere-turns, the power dissipation is minimized by a winding in which the thickness of the insulation equals the conductor diameter as shown in Appendix B.

The total thickness of the insulation is between 0.030-0.035 in so B & S No. 20 wire was specified.

Oxidation

A search of literature [11, 12] revealed that molybdenum will oxidize rapidly in the atmosphere at elevated temperatures. The

time laws observed for the oxidation of molybdenum indicate that a parabolic oxidation occurs at 300°C. As the temperature is elevated (or the time of exposure is extended) the initial parabolic oxidation becomes linear. The surface of molybdenum remains bright up to 200°C and then temper colors appear. Two suboxides which are thought to have intermediate compositions between MoO_2 and MoO_3 have been found beneath an outer layer of MoO_3 at 570°C. Above 550°C, MoO_3 evaporates noticeably. Above 795°C, the melting point of MoO_3 , oxidation is accompanied by a total loss in weight [11].

Experimental investigation of the oxidation of the molybdenum wire to be used showed rapid oxidation starting around 750°C-800°C. The wire was completely destroyed at 830°C as shown in Figure 5. It should be noted that the oven heating time was very closely dictated by the relationship

$$t = t^2 - T \qquad (2.1)$$

where   t = time to reach elevated temperature

        T = elevated temperature expressed in multiples of 100°C

Thus, it required approximately one hour of heating to destroy the wire at a temperature of 830°C. Tests were made with the molybdenum wire in an inert atmosphere. Argon was forced into the oven chamber. The wire, subjected to 1700°F, had a resistance of 0.2 ohms/foot at that temperature. The environment could not be elevated to a higher temperature after 2.5 hours of heating, apparently because of thermal gradients introduced by the gas flow. The possibility of submersing the motor into an inert atmosphere was discarded primarily due to the

Figure 5.
Oxidation Data for Platinum-Clad
Molybdenum Wire and Molybdenum Wire

⊙ – 14% Platinum-clad Molybdenum Wire
    0.032 in.Dia. (Englehard Industries)
    Temperature Increase

▽ – Temperature Decrease of Pt-Mo Wire

△ – Molybdenum Wire – # 20
    0.032 in. Dia. Temperature Increase
    to Destruct.

18
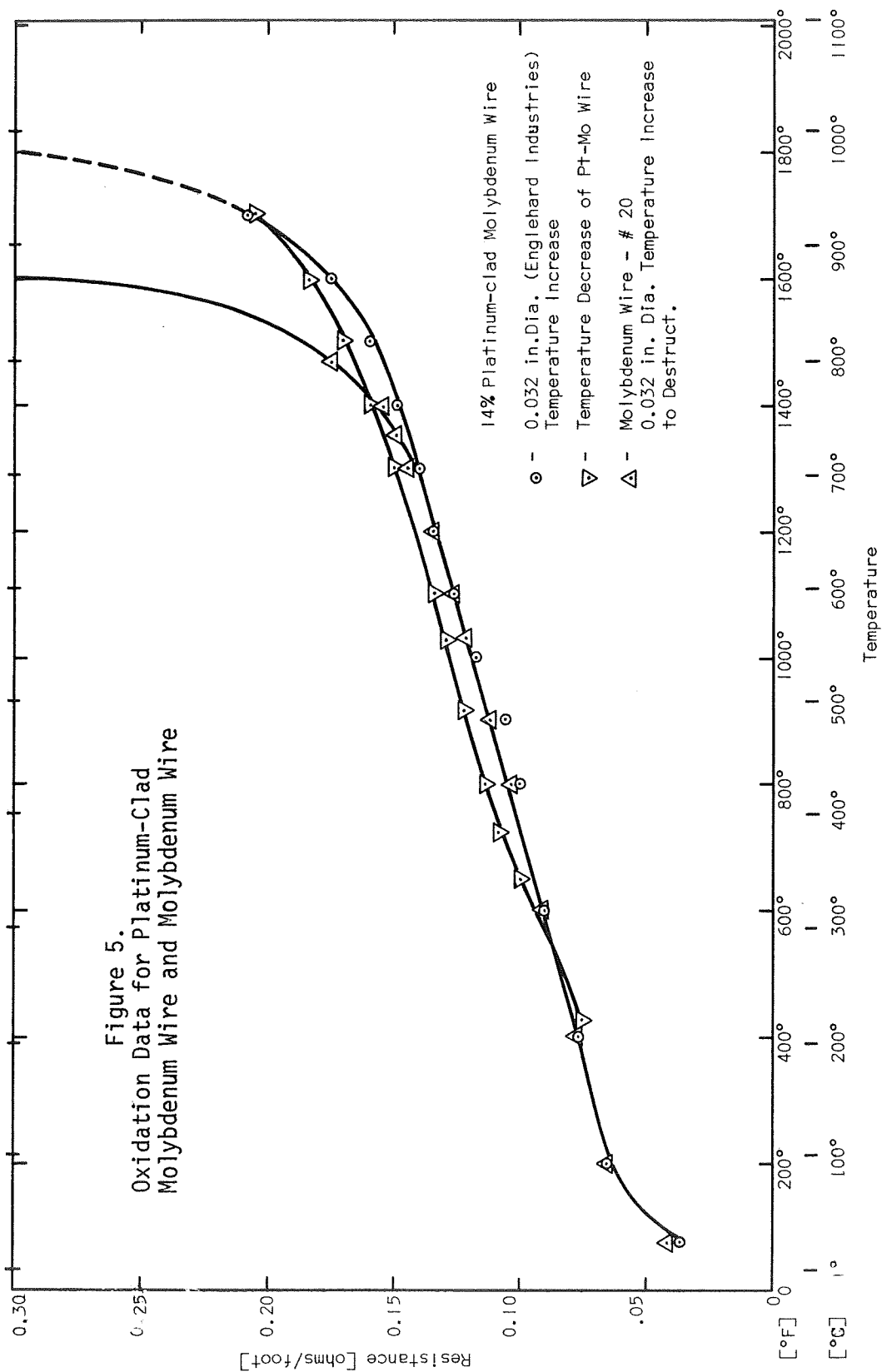
cost of argon and the fact that the motor unit could not be sealed.

In an attempt to solve the problem, oxidation resistant coatings of molybdenum were investigated. Disilicide coatings were ruled out because of their brittleness at room temperatures. Although the coatings have limited ductility at a red heat [13], the windings could not be wound at such a temperature. In recent developments [14] siliciding has been found to resist the oxidation of molybdenum test parts exposed to 3400°F in air flowing at Mach 4. Although it is reported that the silicide coatings are moderately flexible, no mention has been given of its application to wire. It is deemed, therefore, that because of the turning radius in the wiring in this application, the coating process is not applicable.

Platinum is outstanding in its resistance to oxidation. At temperatures above about 750°C (1400°F), an extremely small but measurable weight loss occurs due to the formation of a volatile oxide, PtO_2 and to volatilization of the metal. The weight loss of platinum is 5.2×10^{-3} mg/cm^2/hr at 2500°F [15] while the weight loss of molybdenum is 10^4 mg/cm^2/hr at the same temperature [12]. The melting point of platinum of 1769°C (3216°F) exceeds the expected system temperature but does not equal the melting point of molybdenum at 2622°C (4750°F).

The linear coefficient of thermal expansion of platinum is 9.1×10^{-6} per °C while that of molybdenum is 5.7×10^{-6} per °C. Although processes such as electrodeposition can produce a platinum coating, the cladding process appears to be the best for coating wire.

To investigate the possibilities of clad wire as a solution, molybdenum wire clad with 14% platinum by weight (approximately 0.002 in sheathing) and of 0.032 in diameter was purchased from Englehard Industries, Inc. Elevated temperature tests were run on the wire with the results shown in Figure 5. The wire resistance increased rapidly at 1700°F. Investigation of the results indicate that diffusion of the two metals is rapid enough to allow oxidation of the molybdenum base metal under these heating conditions. Failure occurs from the inward diffusion of oxygen and the outward diffusion of molybdenum [16].

The performance of platinum-clad molybdenum was thought to be enhanced by incorporating an efficient barrier such as rhenium [17]. However, although the wire has very high ductility, rhenium oxidizes severely in air, in a manner similar to molybdenum. The reaction as determined by simple weight change tests starts at 600°C and increases rapidly with temperature [15, 18]. Preliminary investigation of intermediate boundary layer combinations of a base layer and an oxidation resistant layer resulted in the selection of rhenium as an optimum combination with molybdenum and an oxidation resistant metal [19]. However, it was later concluded that the placement of a layer of rhenium, zirconia, alumina, tungsten, silicon carbide, or magnesia between platinum and molybdenum will not significantly reduce the degrading interdiffusion at 2550°F. An increase of the platinum thickness served as well as any barrier investigated [20]. Based on this conclusion, it is felt that an optimum thickness of platinum cladding could be selected based on the temperatures and time operations

at the respective temperatures.

In an effort to eliminate further perusal of the optimum wire constituents, encapsulation of the windings with an oxidation resistant ceramic was investigated. A suitable ceramic, Ceramabond 503 manufactured by Aremco Products, Inc., was used to hermetically seal the windings. Nichrome wires were welded to the molybdenum wires by electron beam and heli-arc methods. Thus, the only wires protruding from the motor into the atmosphere are the nichrome leads. Ceramabond 503 was chosen because of its low curing temperature (250°F) and its high operating limit (2600°F). It has good bonding characteristics to quartz, molybdenum, and lava. Although the coefficient of thermal expansion of 8.0×10^{-6} per °C is twice that of the lava, it is approximately equal to that of the quartz insulation. The major constituent of the ceramic is alumina [21]. The schedule followed for application of the potting compound is shown in Appendix C. It must be remembered that all materials used in the construction of the motor unit cannot possess any ferromagnetic properties since the unit is of free air design, i.e., the permeability must be unity.

Resistance data at elevated temperatures shown in Figure 6 at elevated temperatures was taken on an encapsulated coil wound with platinum-clad molybdenum wire. The results indicate that after 3 hours of heating to attain 2000°F, the resistivity was six times that at room temperature. This complies with the resistivity expected when no oxidation takes place. In fact, the temperature reached 2100°F without noticeable degradation of performance. Therefore, encapsulated platinum-
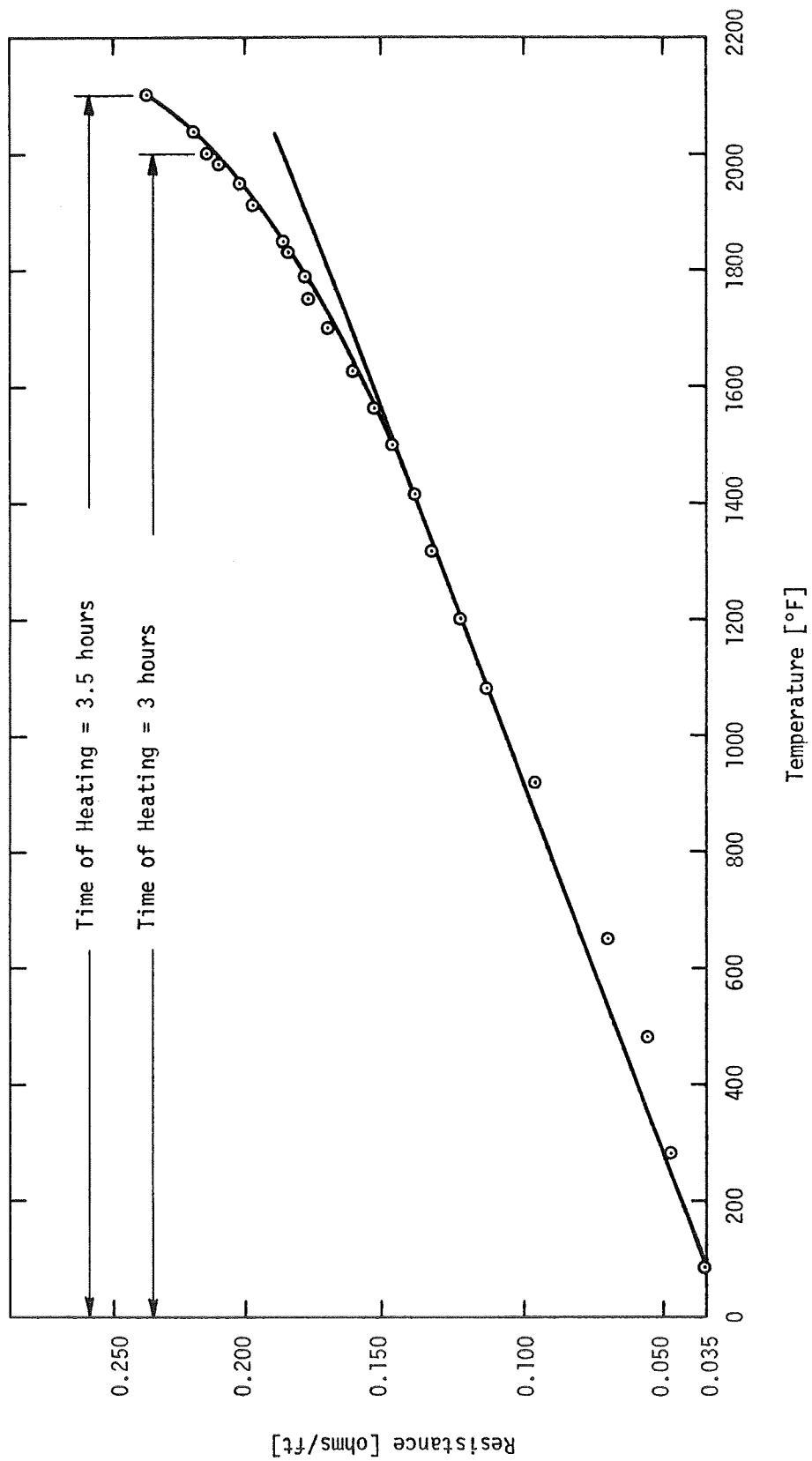
Figure 6. Resistance Data on Encapsulated Platinum-Clad Molybdenum Wound Coil At Elevated Temperatures

22

clad windings are capable of withstanding the hostile environment.

Flexure

The flexure used in the motor-transducer is pictured in Figure 7.
The flexure provides a near frictionless support for the armature.
The spring constant of the flexure has been determined experimentally
to be 0.51 lb-in/radian under the armature load of 0.262 lb (see
Chapter III). Molded ceramic supports the flexure. The support legs con-
necting the movable element to the fixed element are: 0.01 in x 0.030 in
Haynes Alloy No. 25 wire (see Appendix D). Since the wire supports
act also as conductors of the armature current, the ends are connected
in such a manner that the Joule heating of the supports is equally
balanced. Some drift occurs at room temperature when currents greater
than 2.5 amperes are passed through the flexure. The drift is less
noticeable at elevated temperatures.

The probe connects the armature to the movable element of the
flexure and is secured to the target. Both the probe and the two
securing units are manufactured from RA330 stainless steel rods.

Two nichrome leads (B & S No. 20) protrude from the bottom of
the flexure where they have been electron-beam welded to the connecting
wires of the flexure support wires. The leads are channeled into the
ceramic form and potted with Ceramabond 503. Two molybdenum wires
(or platinum-clad molybdenum wires) protrude from the floating side
of the flexure. They too are electron-beam welded to connecting ties.
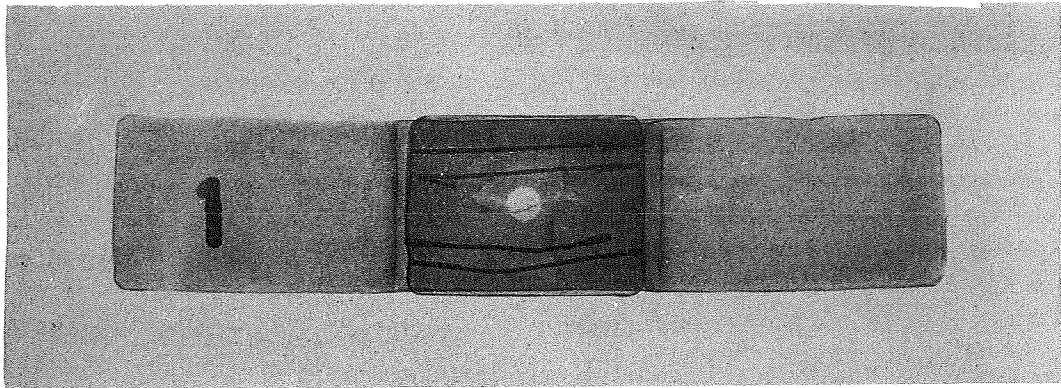
Top View
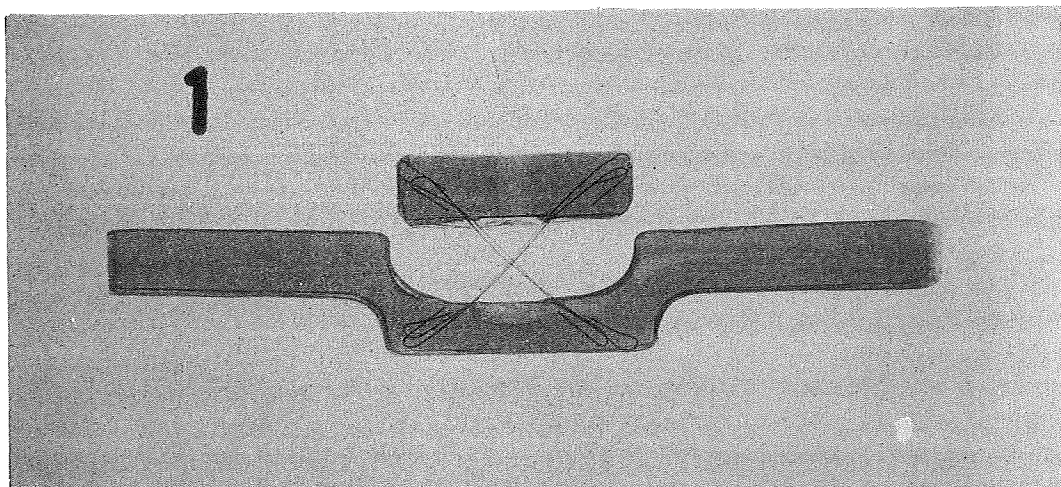
Side View

Figure 7.   X-Ray Photograph of Flexure

2. MOTOR ASSEMBLY

The armature is first assembled to the flexure. The floating element of the flexure is secured to the armature with the insertion of the probe and the tightening of the two nuts. The leads extending from the floating portion of the flexure are now heli-arc welded to the armature leads. The joins are embedded in the lava and the entire floating element is potted with Ceramabond 503. The flexure assembly is shown in Figure 8.

The motor coils shown in Figure 9 are now ready for final assembly. The flexure rests on the bottom field coil as shown in Figure 10. The two field coils are placed on adjustable mounts so that their respective orientations to each other can be changed. Adjustment within a base parallel plane is made by adjustment of collar screws while adjustment of the collar in a vertical direction is dictated by the adjustment of six screws on each collar. The flexure support is sandwiched between the field coils (see Figure 11).

3. DERIVATION OF MOTOR TORQUE

Figure 12 shows a rectangular current loop placed in a uniform magnetic field B. The normal vector n in Figure 12(b) makes an angle θ_B with the direction of the flux density. The torque about the axis mm' is [22]

$$\tau = iA|\vec{B}|\sin\theta_B$$

where A = a'b' = area of the rectangular loop   (2.2)
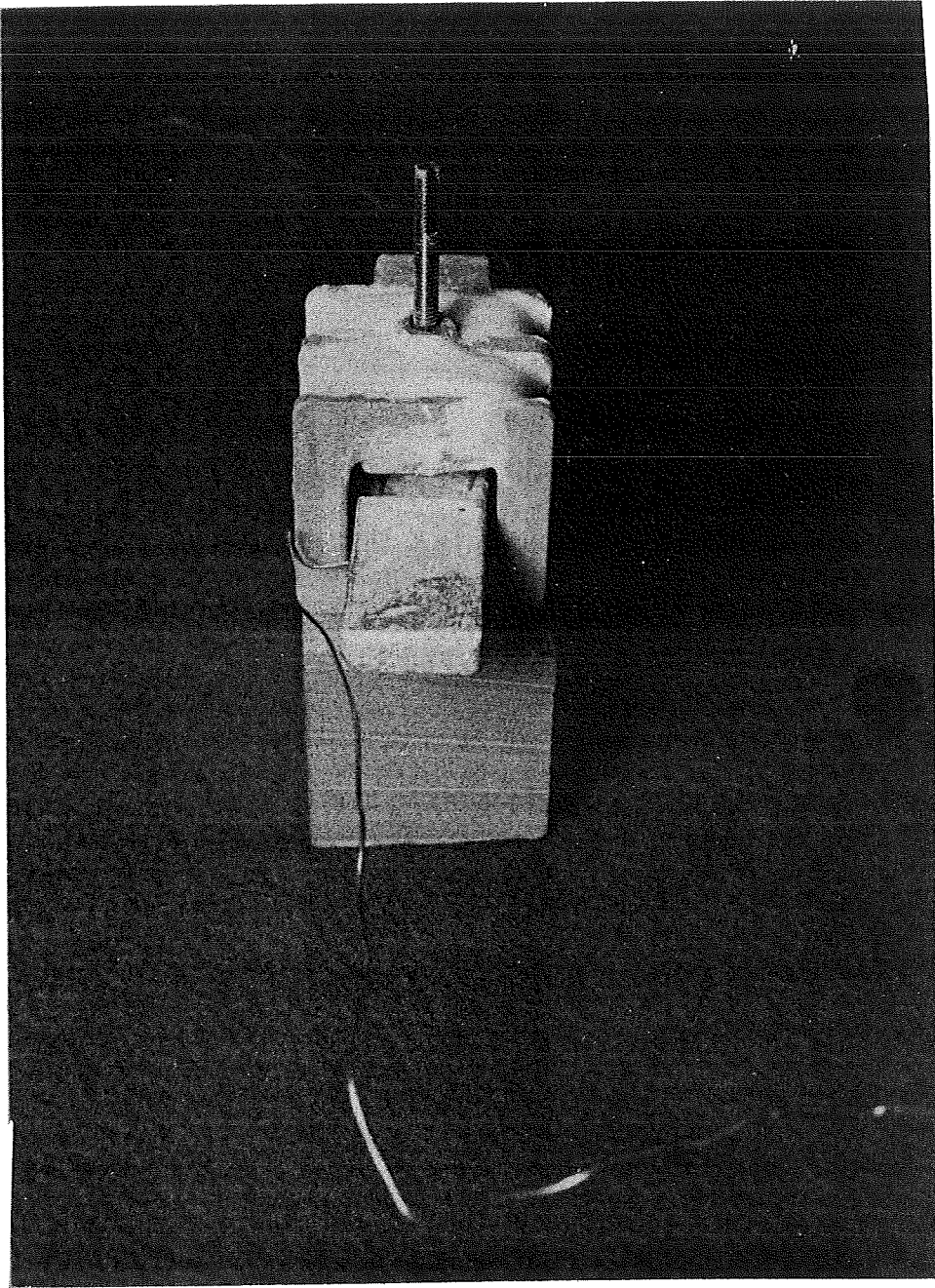
Figure 8. Flexure Assembly
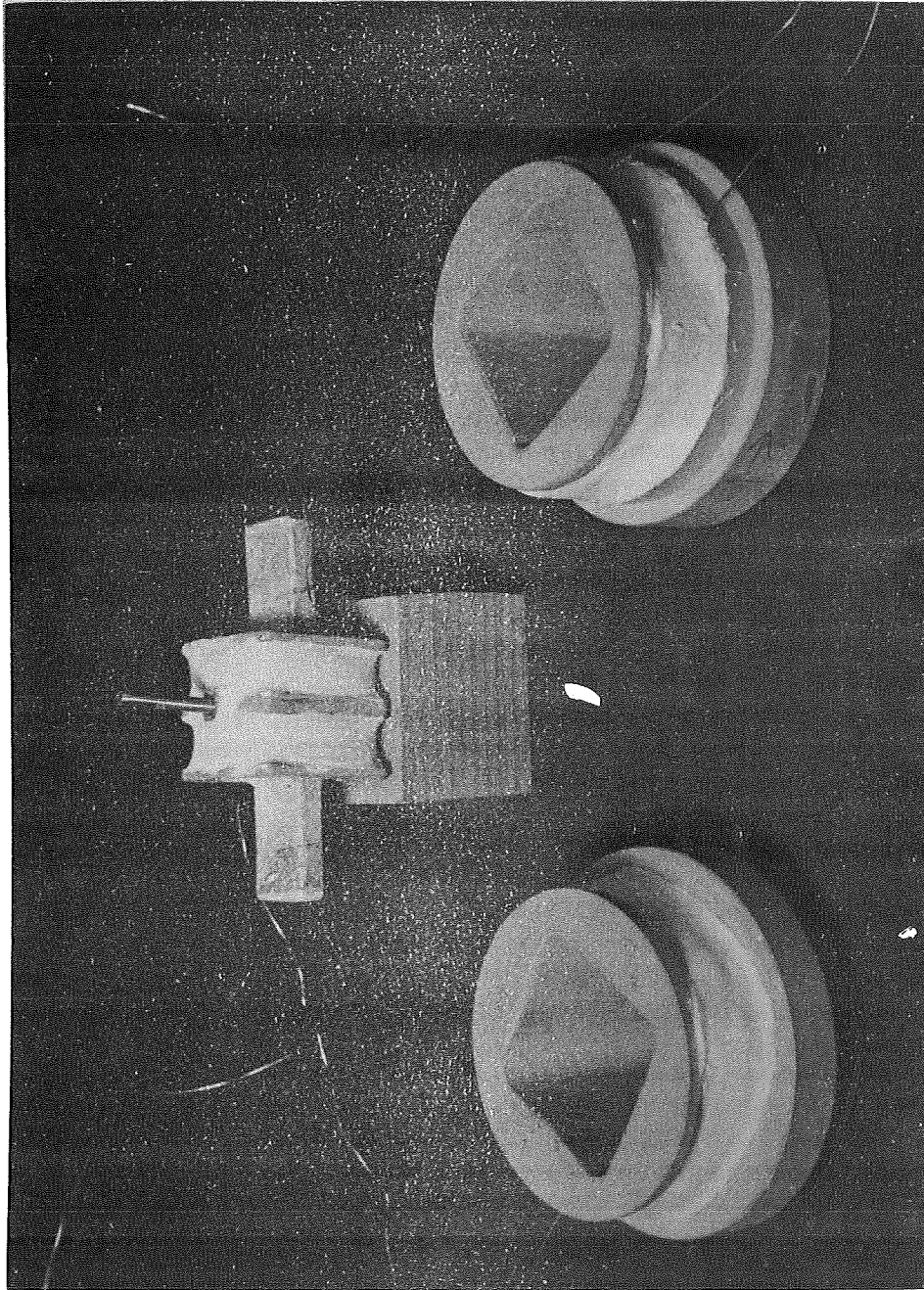
Figure 9. Coils Ready for Final Assembly
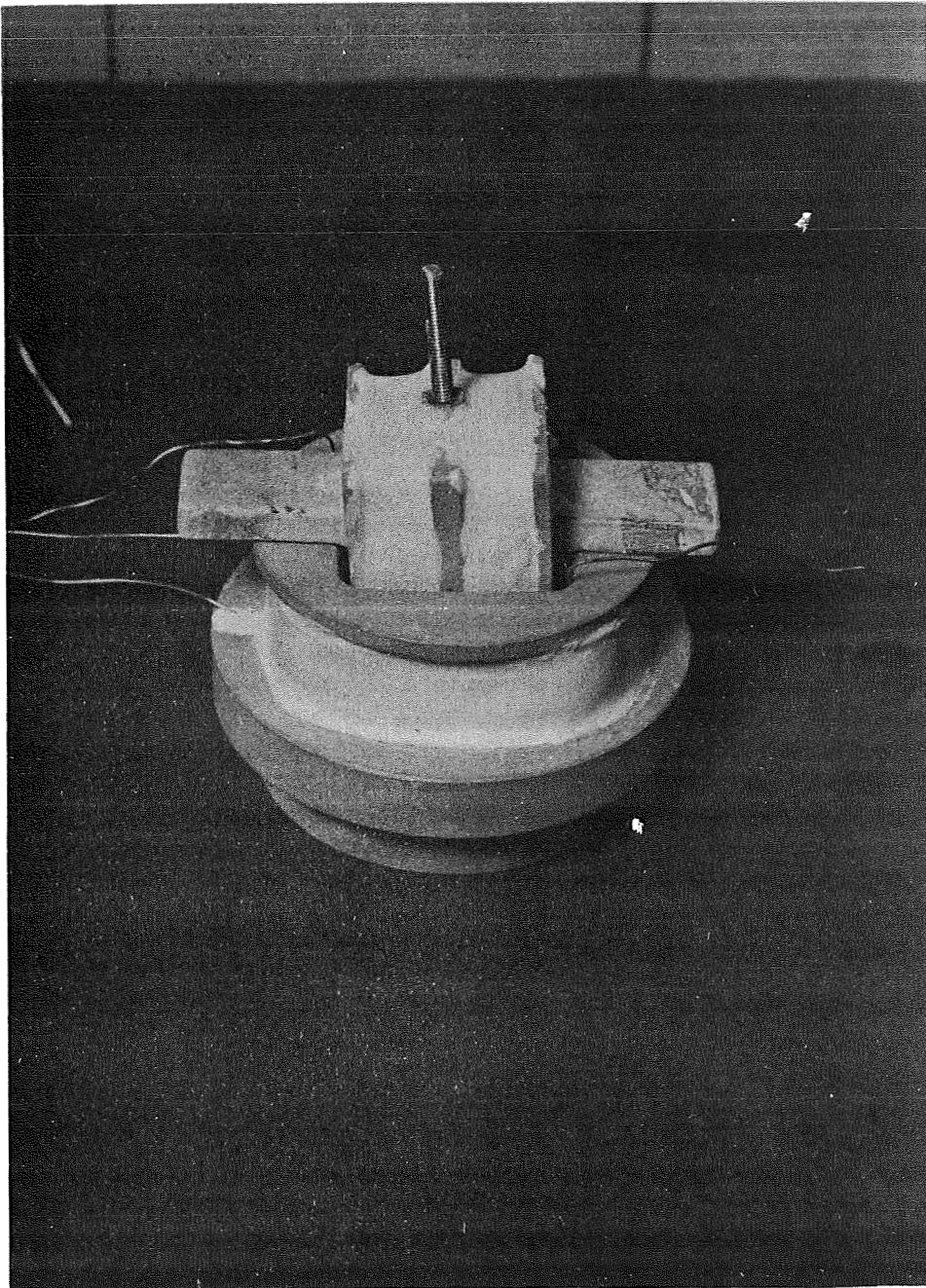
Figure 10. Flexure Assembly Mounted to Field Assembly
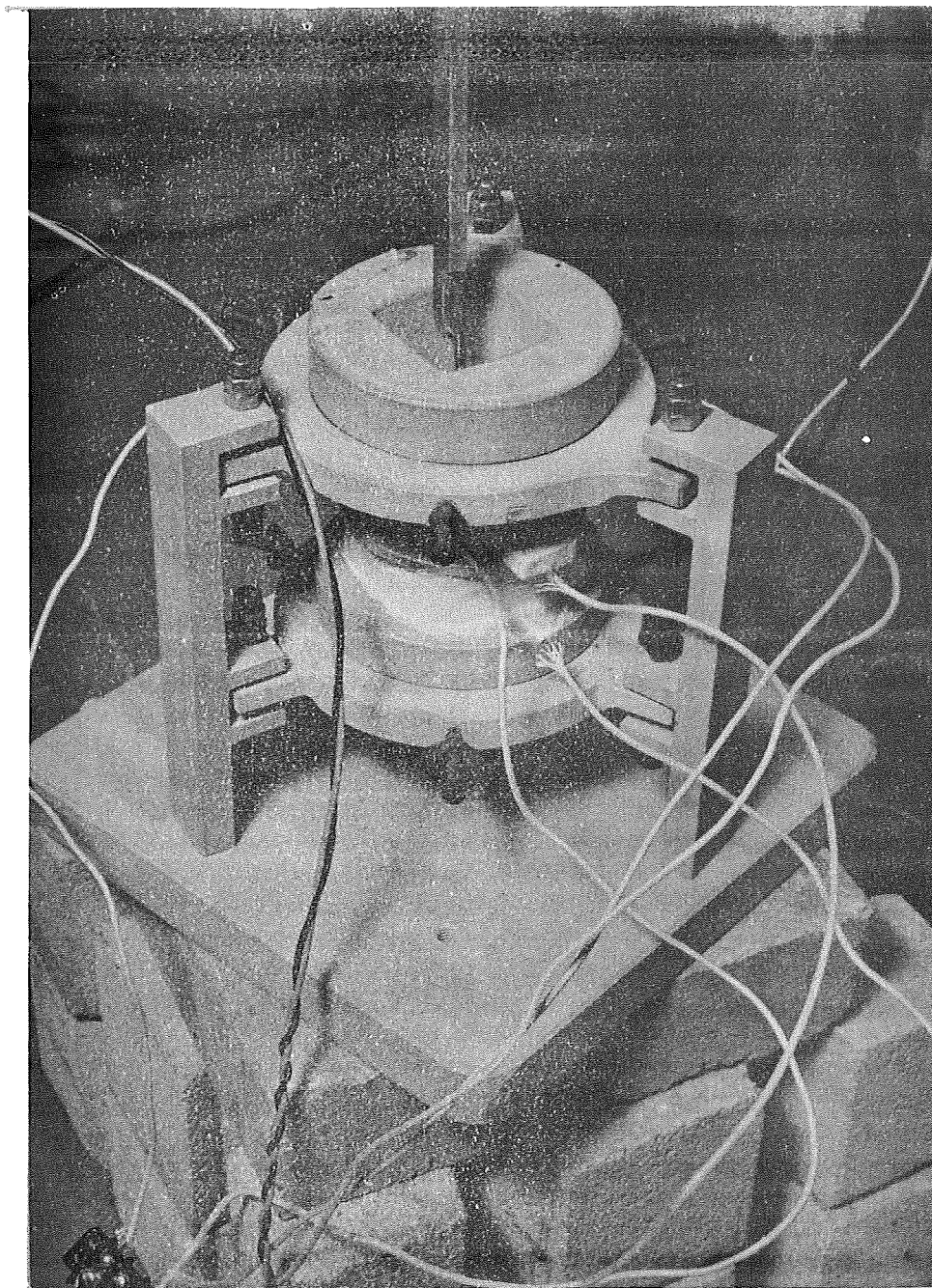
Figure 11. High Temperature Model Assembly
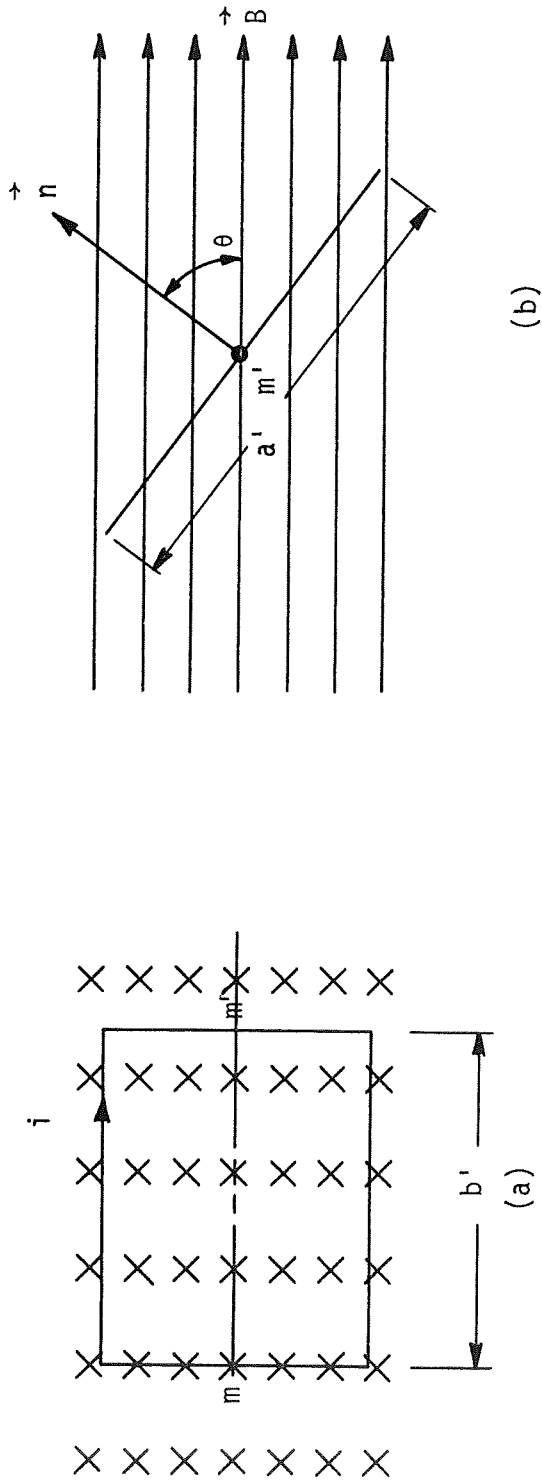
Figure 12.

A Rectangular Current Loop Placed in a Uniform Magnetic Field

This equation can be shown to hold for all plane loops of area A, regardless of their shape.

For the motor applied in this case $\theta_B \approx 90°$. Therefore, since there are N equal turns on the coil and the torque acts on every turn of the coil the following equation applies.

$$\tau = NiA|\vec{B}| \qquad\qquad (2.3)$$

In order to make the torque proportional to the loop current, the flux density must remain constant. Either field current or armature current can be held constant, since torque is proportional to the current product. For this design the field current has been chosen to be constant, although both were investigated as possibilities. Power dissipation and low voltage power supplies are the primary factors for this selection. Each of the two field coils has current supplied by a constant current source. Current sources are necessary because of the relatively large change in resistivity over the 2000°F temperature range. A maximum power dissipation of 84 watts on each coil is experienced at 2000°F.

The magnetic flux density at a general point due to a square current loop can be determined by extending application of the Biot-Savart Law to a wire of finite length. The magnitude of the field at a point due to a wire of finite length carrying a current i can be expressed as follows [22]:

$$\vec{|B|} = \frac{\mu_o i}{4\pi D} \left|_{-l/2}^{l/2} \frac{\lambda}{(D^2 + \lambda^2)^{1/2}}\right. \tag{2.4}$$

where

    D = perpendicular distance from Pt. P_0 to the wire

    λ = variable of integration

    l = finite length of wire

It has been shown [1] that the average field set up by a loop element is (see Figure 13).

$$d\bar{B}(\Gamma, Z) = \frac{\mu_o i}{4\pi h^2} \int_o^h \int_o^h B_{11}(x, y, \Gamma, z) dx dy dz d\Gamma \tag{2.5}$$

where

    h = one-half the length of the side of the armature front view

    Γ = varies from R to $R + r_w$

    Z = varies from $-l/2$ to $+l/2$

    μ_o = permeability of free space

       = $4\pi \times 10^{-7}$ weber/amp-M

  x,y = integrating factors

  $B_{11}(x, y, \Gamma, z)$ is defined in Appendix E.

    i = $J dz dy = \dfrac{i}{d_w^2} dz dy$

  d_w = wire diameter
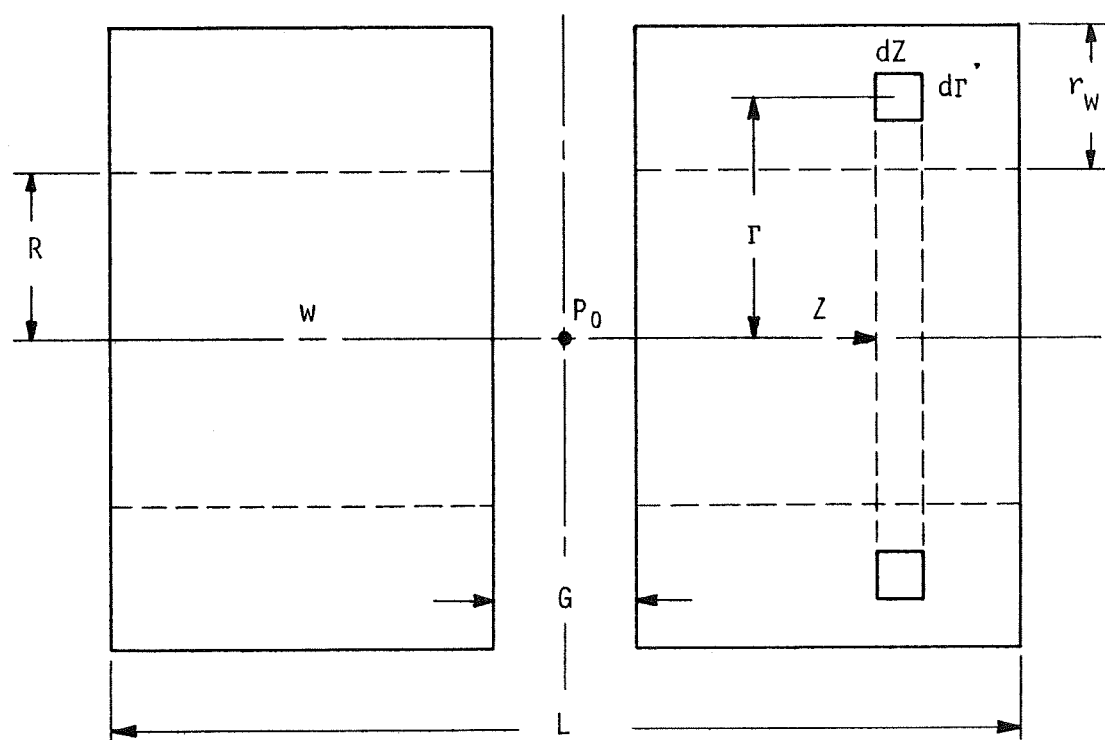
Figure 13. Field Coil Orientation

Thus,

$$\overline{B}_{11}(r, L, w, h) = \frac{10^{-7}}{d_w^2 h^2} \int_o^h \int_o^h \int_R^{R+r_w} \left[\int_{-\left(\frac{L}{2} - w\right)}^{w - \frac{D}{2}} B_{11}(x, y, \Gamma, z)dz + \right.$$

$$\left. \int_{w + \frac{D}{2}}^{w + \frac{L}{2}} B_{11}(x, y, \Gamma, z)dz \right]dxdyd\Gamma \qquad (2.6)$$

where w is a general point measured positive to the left of the center of point P_0. Only positive values of w need to be symmetrical since w is symmetrical with respect to P_0.

A computer program has been written to determine the average flux density by employing the above equation with slight modifications. Since the aluminum-wire motor had been wound with a single wire conducting bifilar winding, the current density,

$$J_A = J/2 = \text{current density of aluminum-wire motor} \qquad (2.7)$$

and

$$\overline{B}_{11_A} = \overline{B}_{11}/2 = \text{average flux density of a general point of the}$$
$$\text{aluminum-wire motor.} \qquad (2.8)$$

For the molybdenum-wire motor, the conducting molybdenum wire covered only one-fourth of the current sheet with the quartz insulation covering the remainder. Thus,

$$J_{mo} = J/4 = \text{current density of molybdenum-wire motor} \qquad (2.9)$$

and

$$\overline{B}_{11_{mo}} = \overline{B}_{11}/4 = \text{average flux density of a general point on the}$$
$$\text{molybdenum-wire model.} \qquad (2.10)$$

The computer program shown in Appendix F provides not only the average flux density for several values of field current, but also the armature current necessary to provide the maximum motor torque. Since the final device is a maximum of 2 inches, the target is mounted half the distance or 1 inch from the flexure center. Therefore, for a maximum force of 7 millipounds, the maximum torque required for the motor to produce is 7×10^{-3} in-lb.

4. MOTOR CALIBRATION

Experimental investigation of the motor torque constants was made on three motors: 1) the aluminum-wire low temperature motor; 2) the molybdenum-wire high temperature motor; 3) a platinum-clad molybdenum wire high temperature motor with more turns on the field coils. Figure 14 shows a typical test apparatus used to apply a known torque to the motor. The sting, that member which touches the motor probe, and the balance arm mounted perpendicular to the sting are supported by a Bendix 6016-800 free-flex pivot which has a spring
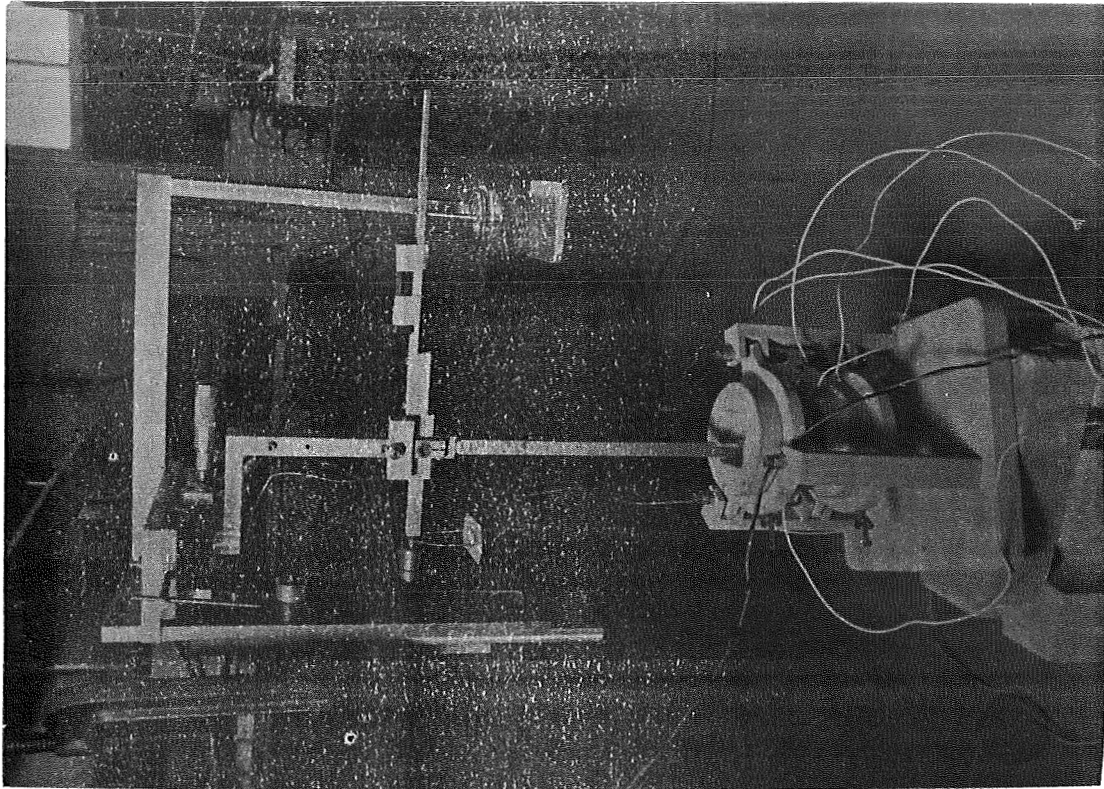
Figure 14. Force Balance Test Apparatus

constant of 0.813 lb-in per radian [23]. The entire balance system
can be adjusted so that the sting point is precisely aligned with the
armature probe. The micrometer adjustment is in the direction of
probe displacement. Weights are placed on the pan of the balance arm.
The necessary distances are known so moments and, consequently, the
applied torque are known. The counter weight balances the balance
arm to which is secured a rod placed in damping fluid.

The force balance was adjusted for balance. For a sensing device,
the control system to be used for the respective motors was energized
open loop and set for the null position. Output was measured in the
d.c. portion of the control loop with a Hewlett-Packard 410C Voltmeter.
The sting was adjusted until it touched the armature probe (noted by
a slight meter deflection). The field coils were energized with a d.c.
current by current source(s) and a known weight was applied to the
pan. Armature current was then introduced so that motor torque nullified
the applied torque. The armature current required to restore the
armature probe to the null position was recorded. The armature coil
of the aluminum-wire motor was energized by a current source and the
required field current was recorded.

The motor calibration curves for the motors are shown in Figures
15, 16, and 17. Note the linearity of ± 5% in all cases. Curves were
taken for field currents of 1-5 amperes on the aluminum-wire model
to show the motor currents product relationship. The two remaining
calibration curves were taken at the desired operating field current.
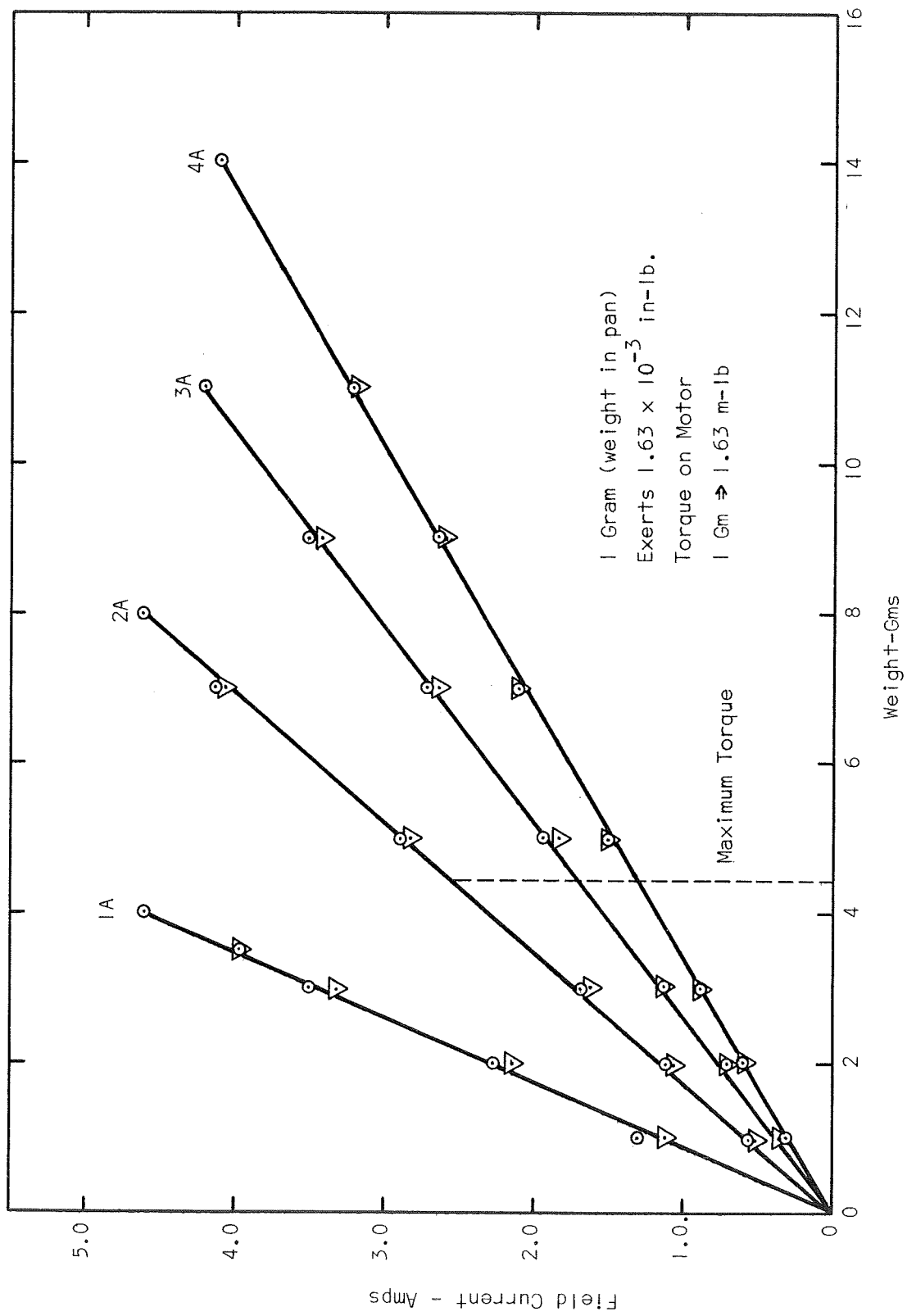
Figure 15. Motor Calibration for Different Armature Currents - Aluminum-Wire Model]
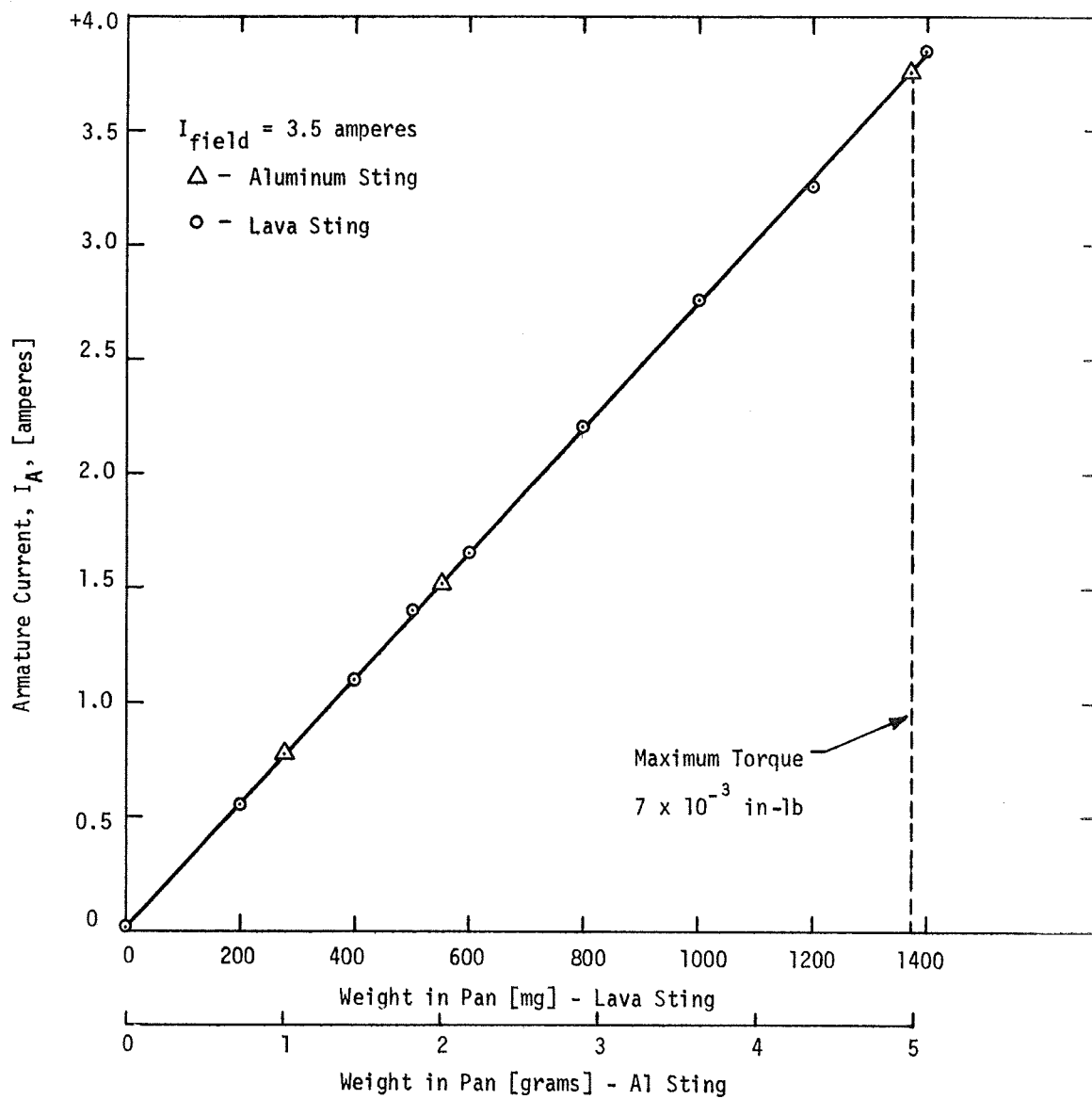
Figure 16.   Motor Calibration Curve
              Molybdenum-Wire Model
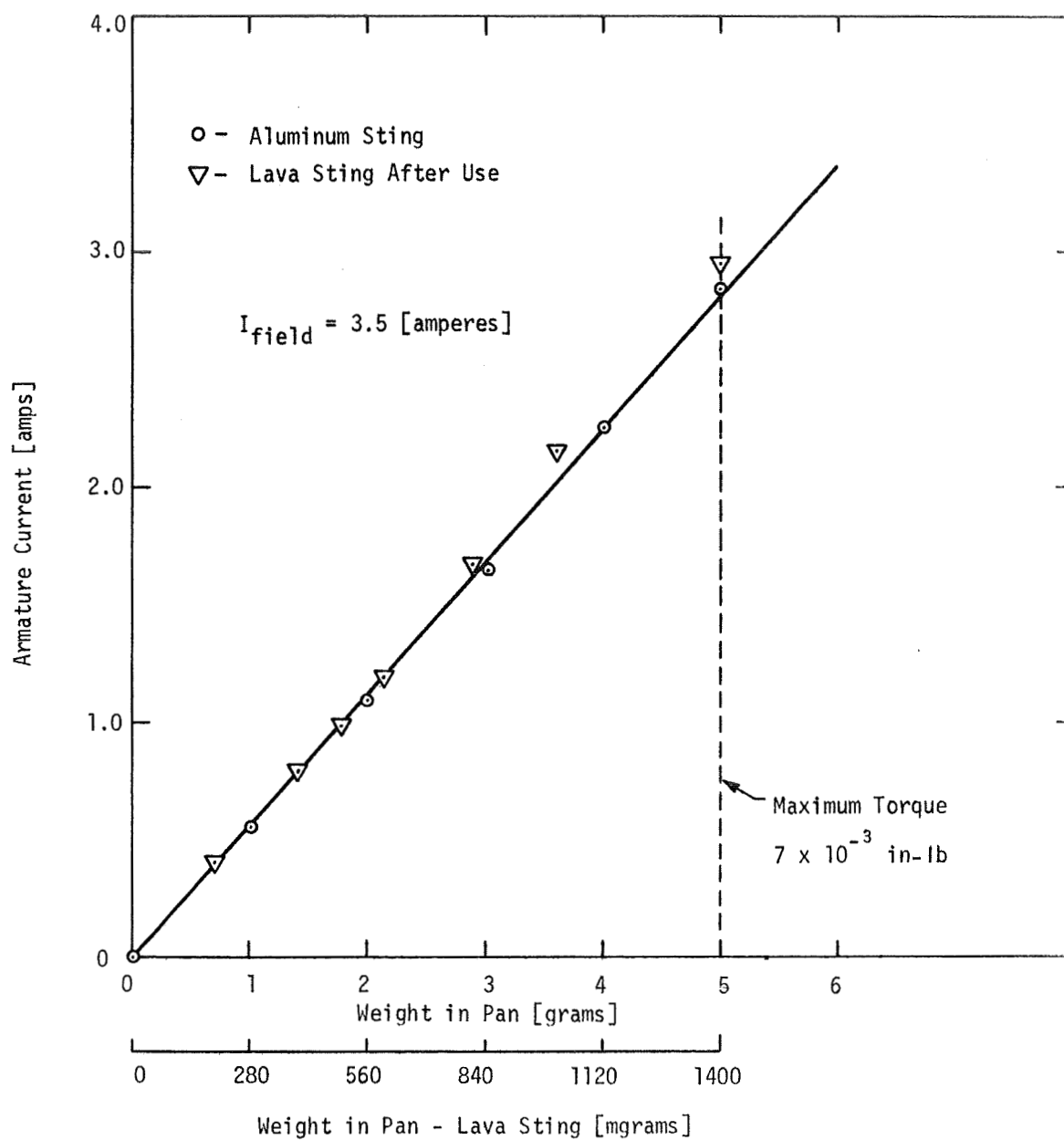
Figure 17. Motor Calibration Curve - Platinum-Clad Molybdenum-Wire Motor

The dimensions of the motors and other pertinent data are shown in Table I. It should be noted that the theoretical motor torque constants and those determined by measurement differ by only 5%. A ten per cent error can be expected due to the measurement of the distance from the motor center to the point of contact of the sting to the armature probe. Thus, the motors conform to the theory pertaining to their operation.

TABLE I

MOTOR PARAMETERS

A = Aluminum-wire motor

M = Molybdenum-wire motor

P = Platinum-clad molybdenum-wire motor

DIMENSION	SYMBOL	A	M	P
Field Coils				
Inside Radius	R	1.06	1.06	1.06
Overall length	L	2.06	2.06	2.06
Winding thickness	r_w	0.20	0.28	0.36
Gap Width	G	0.40	0.40	0.40
Wire size	d_w	0.032	0.032	0.032
No. turns per layer		12	11	11
Total no. turns/coil	N	72	44	55
Constant current (amps)	I	2	3.5	3.5
Max power dissipation/coil	P	–	70	84
Temperature rise (15 min)		–	400°F	480°F
Armature Coil Weight				
Inside Radius	R	0.64	0.59	0.59
Width	C	1.68	1.68	1.68
Winding thickness	r_w	0.20	0.21	0.21
Wire size	d_w	0.032	0.032	0.032
No. turns per layer		11	14	14
Total no. turns	N	64	42	42
Max power dissipation(watts)	P	–	70	41
Temperature rise (15 min)		–	400°F	230°F
Weight (lbs)		0.328	0.262	0.262
Max current received at specified field current				
a. theoretical		2.56	3.61	2.86
b. measured		2.60	3.75	2.85

CHAPTER III

DISPLACEMENT TRANSDUCER

According to Lenz's law, a coil of N turns placed in a time varying magnetic field will have induced into it a voltage

$$e = -N\frac{d\phi}{dt} \qquad\qquad (3.1)$$

where

e = the EMF produced in volts

N = the number of turns

ϕ = the flux in webers

t = time in seconds

The flux linkage between the field and armature coils is

$$\phi = |\vec{B}|A \qquad\qquad (3.2)$$

where A is the cross sectional area in square meters taken at right angles to the flux lines and $|\vec{B}|$ is the flux density in webers per square meter.

The flux in the core is

$$B(t) = B_{max}\sin\omega t \qquad\qquad (3.3)$$

Thus, combining Equations (3.1), (3.2) and (3.3) yields

$$E = NA\omega B_{max} \tag{3.4}$$

Note that for a given number of coil turns and a constant flux density maximum, varied at a fixed frequency, the maximum induced voltage is proportional to the cross sectional area perpendicular to the flux lines

$$A = A_m \sin\theta \tag{3.5}$$

where A_m is the maximum cross sectional area perpendicular to the flux lines. In this application, A_m is the area of a coil loop on the armature coil. The angle θ describes the displacement of the target from its initial position. Since the maximum deflection of the target is 0.5×10^{-3} in and the probe length from the flexure center to the target is one inch, the maximum angular change is 0.5×10^{-3} radians. Therefore, $\sin\theta$ can be replaced by θ. From Eq. (3.5)

$$A = A_m \theta \tag{3.6}$$

and

$$E = N\omega B_{max} A_m \theta \tag{3.7}$$

The flux can be varied by superimposing an a.c. carrier on the
d.c. torque current of either the field or the armature coil and
employing the induced voltage on the remaining coil as the transduced
signal to the system.

I.   TRANSFER CHARACTERISTICS

The frequency of the carrier has been chosen to be 5 KHz for the
following reasons: 1) the frequency should be low enough to avoid
capacitive coupling effects; 2) the gain-bandwidth product of the
operational amplifiers used in the electronic control package was
taken into consideration; 3) a ratio of 20:1 relating the frequency
of the carrier to the crossover frequency of the system is desirable.
Since a crossover frequency of 50 Hz was established for system design,
the carrier frequency was chosen as 5 KHz.

Measurement of the induced signal was made on all motors tested
with excitation of both the field coils and the armature. The linearity
of the air core device is evident from the data recorded in Figures
18, 19, and 20. Excitation for the energizing coil was provided by
a Hewlett-Packard 200 CD test oscillator and output measurements were
made with a Hewlett-Packard 400 FL a.c. voltmeter. The armature probe
was displaced by the sting of the test apparatus described in detail
in Chapter II. The sting was physically secured to a micrometer on
the test stand. Consequently, displacement of the probe at the point
of contact with the sting is known. The distance of the probe used
in testing from the center of the flexure to the point of sting contact

Freq = 5KHz

Slopes [volts/rad]

(1) 0.14
(2) 0.116
(3) 0.09
(4) 0.059

Excitation Voltage [mv]

250
200
150
100

1

2

3

4

Stator Voltage – mv rms

10^{-3} Radians
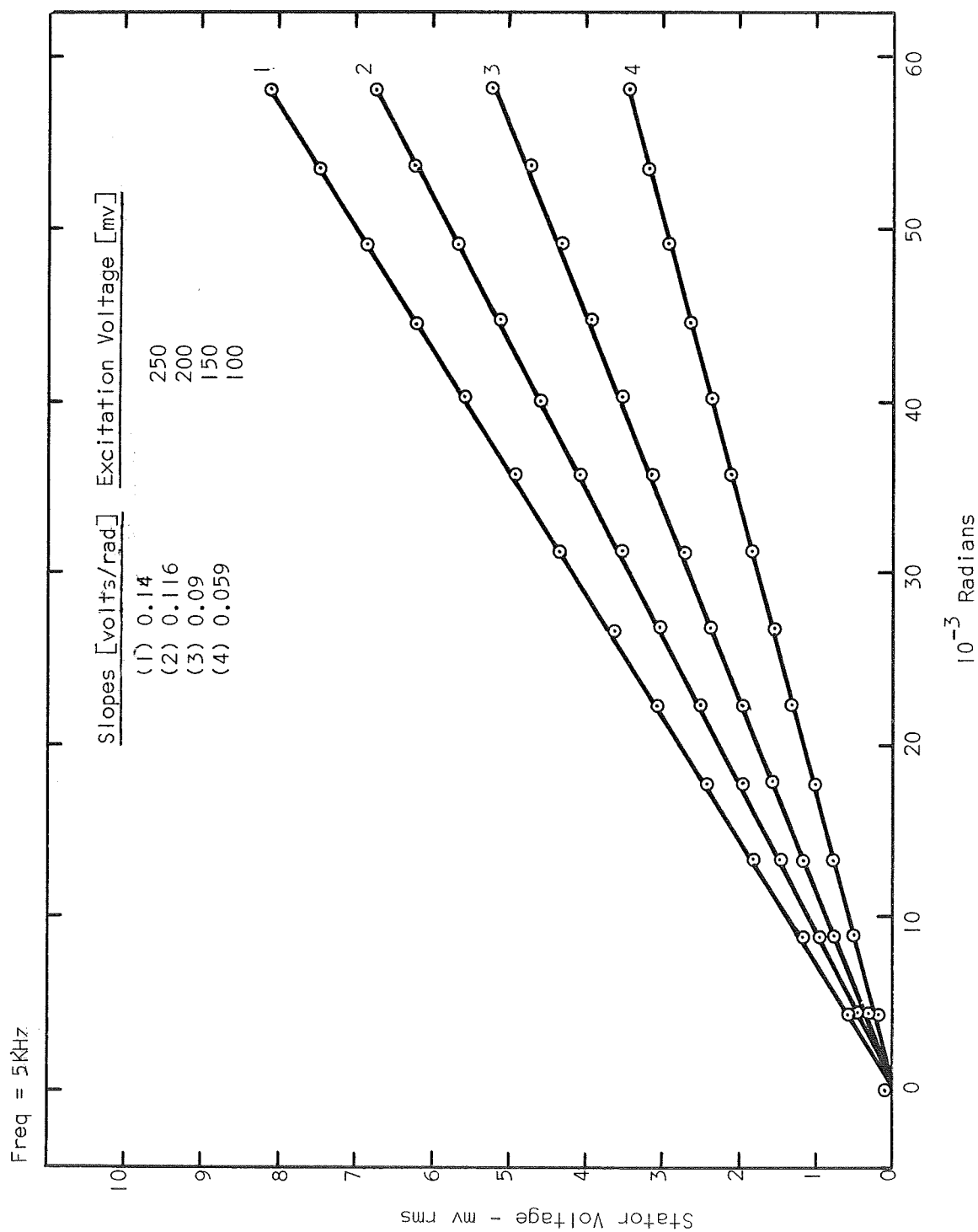
Figure 18. Sensor Sensitivity Curves for Different Armature Voltages
Aluminum-Wire Model

Freq = 5KHz
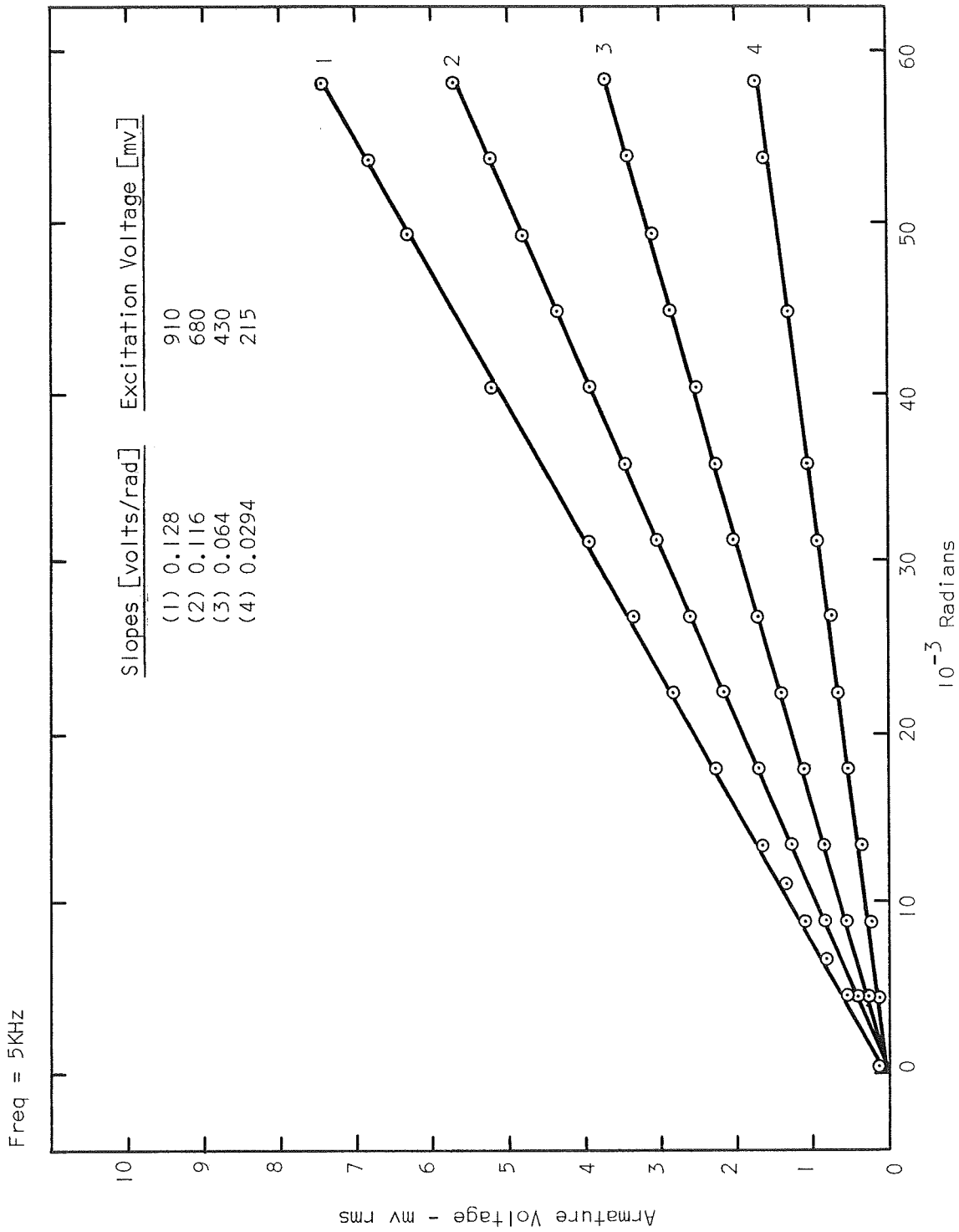
Figure 19. Sensor Sensitivity Curves for Different Stator Voltages
Aluminum-Wire Model
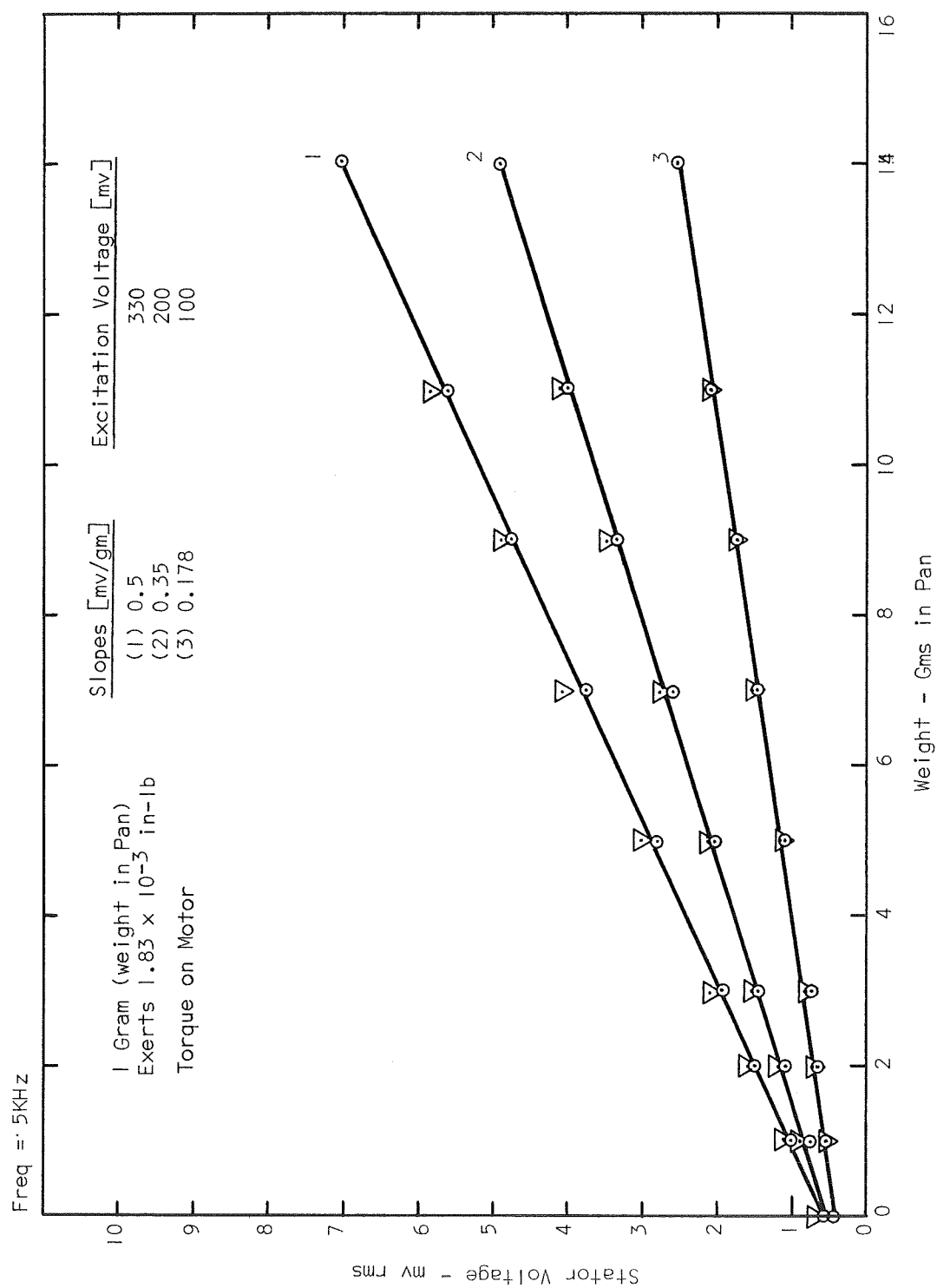
Figure 20. Torque Sensitivity Curves for Different Excitation Voltages
Aluminum-Wire Model

48

varied between 2.0 - 2.25 inches depending on the experimental set-up.

The first model under investigation was the aluminum-wire model. The equivalent model for the transformer is shown in Figure 21(a).

Therefore, since

$$s = r\theta \qquad (3.8)$$

and s can be approximated by a straight line for small angles

$$\theta = \frac{s}{r} \qquad (3.9)$$

where

s = distance sting-probe point is displaced

r = distance from center of flexure to point of probe displacement: 2.0 - 2.25 inches

The internal impedance of the test oscillator (R_g = 600Ω) is much larger than the equivalent impedance of the primary side of the transformer. Therefore, the excitation can be viewed as a current source which is constant at 35 ma rms. The open circuit voltage of the test oscillator is 22.5 volts rms.

The transfer impedance can be determined by measurement as shown in Figure 21. Once the transfer impedance has been found the coefficient of magnetic coupling, k, can be found. The conventional air-core

k = 0.38

R_G = 600Ω R_A = 4.2Ω R_F = 2.4Ω

HP 200CD
Test Oscillator

L_A = 120 μh L_F = 1 mh

HP 400FL
a.c. Voltmeter

(a) Aluminum-Wire Model

k = 0.42

R_G = 600Ω R_A = 3.0Ω R_F = 3.6Ω

HP 200CD
Test Oscillator

L_A = 50 μh L_F = 240 μh

HP 400FL
a.c. Voltmeter

(b) Molybdenum-Wire Model

k = 0.46

R_G = 600Ω R_A = 1.55Ω R_F = 4.3Ω

HP 200CD
Test Oscillator

L_A = 50 μh L_F = 460 μh

HP 400FL
a.c. Voltmeter

(c) Platinum-Clad Molybdenum-Wire Model
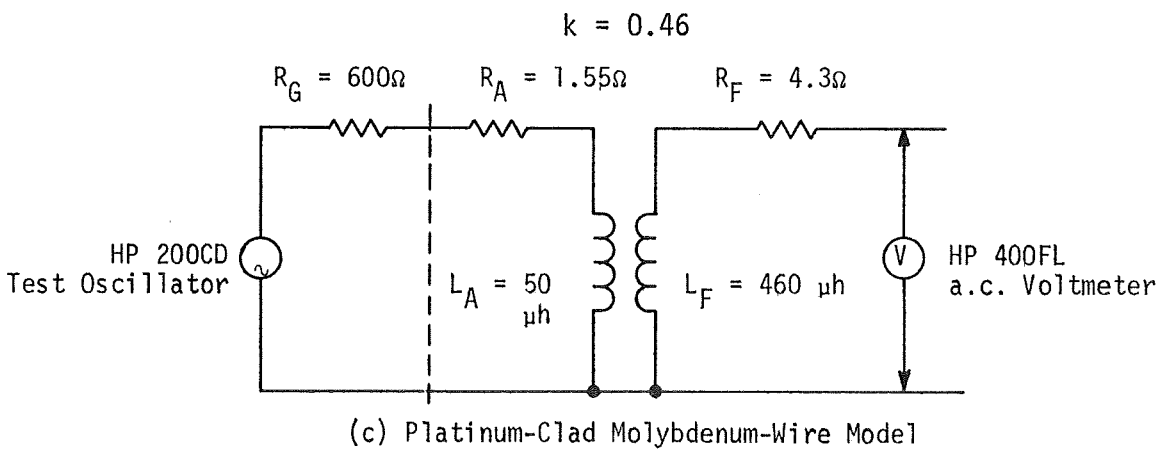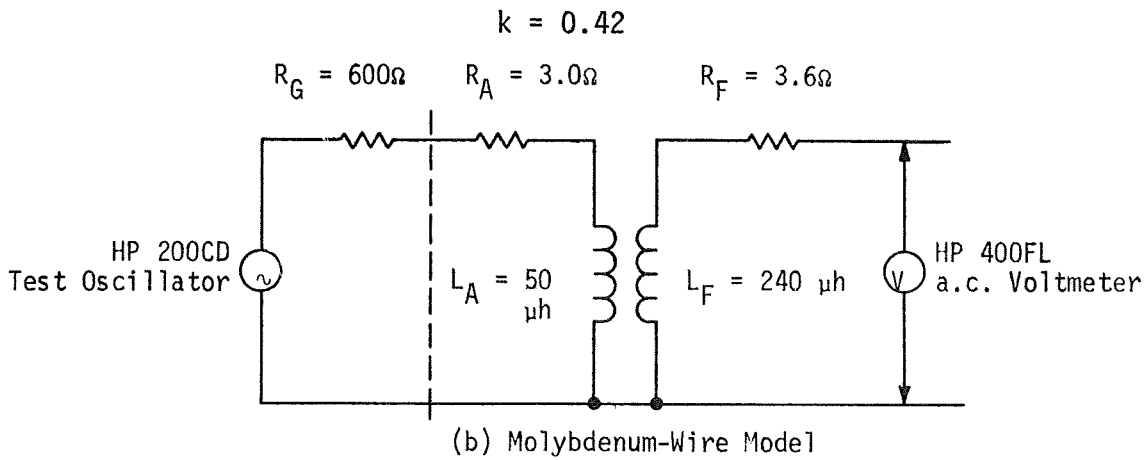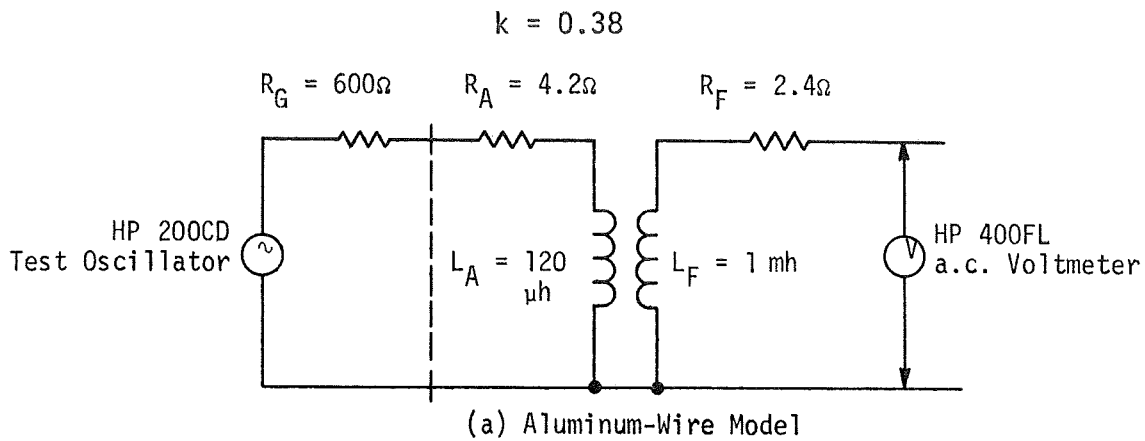
Figure 21.   Transducer Equivalent Models

transformer arrangement is shown in Figure 22. The circuit equations are

$$R_A L_A + L_A \frac{di_A}{dt} + M_{FA} \frac{di_F}{dt} = V_A \qquad (3.10)$$

and

$$(R_F + R) i_F + L_F \frac{di_F}{dt} + M_{AF} \frac{di_A}{dt} = 0 \qquad (3.11)$$

V_A is a sinusoidal waveform and all circuit parameters are constant. Thus, the above equations may be written in terms of effective values

$$(R_A + j\omega L_A) I_A + j\omega M I_F = V_A \qquad (3.12)$$

$$(R_F + R + j\omega L_F) I_F + j\omega M I_A = 0 \qquad (3.13)$$

For simplicity, let

$$Z_A = R_A + j\omega L_A \qquad (3.14)$$

$$Z_F = R_F + j\omega L_F \qquad (3.15)$$

$$Z = R \qquad (3.16)$$

and
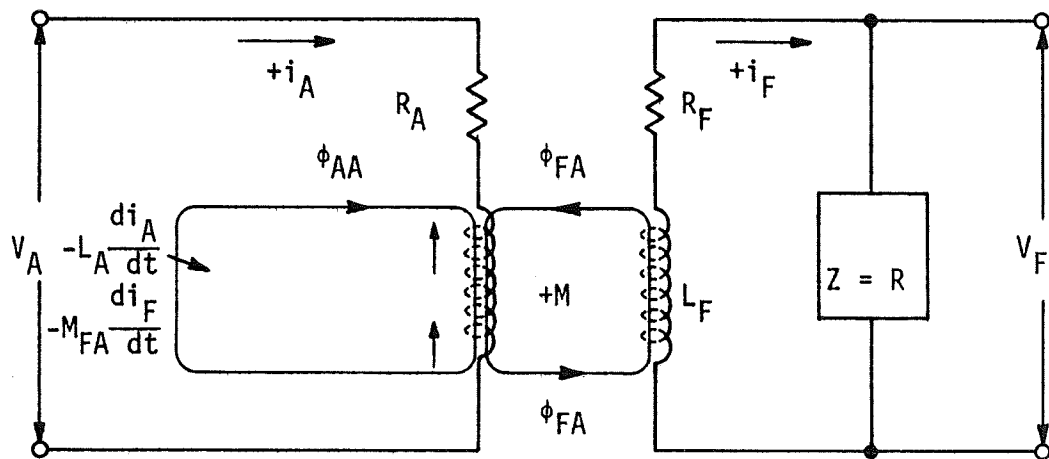
Figure 22. Conventional Air-Core Transformer Model

$$Z_m = 0 + j\omega M \qquad \text{(no core loss)} \qquad (3.17)$$

It follows that

$$Z_A I_A + Z_m I_F = V_A \qquad (3.18)$$

and

$$Z_m I_A + (Z_F + Z) I_F = 0 \qquad (3.19)$$

Therefore,

$$V_F = Z I_F = \frac{-Z Z_m V_A}{Z_A (Z_F + Z) - Z_m^2} \qquad (3.20)$$

and

$$Z_T = \frac{V_F}{I_A} = \text{Transfer impedance}$$

$$= \frac{-Z Z_m}{Z_F + Z} \qquad (3.21)$$

or

$$|Z_T| = \frac{|Z| \, |Z_m|}{|Z_F + Z|} \qquad (3.22)$$

For $Z \gg Z_F$

$$|Z_T| = |Zm| = \omega M = \omega k \sqrt{L_A L_F} \tag{3.23}$$

where k = coefficient of magnetic coupling. The voltage gain from Eq. 3.20 is (shown here for the armature excited)

$$A_v = \frac{V_F}{V_A} = \frac{-ZZm}{Z_A(Z_F + Z) - Zm^2} \tag{3.24}$$

$$|A_v| = \frac{|Z||Zm|}{|Z_A(Z_F + Z) - Zm^2|} \tag{3.25}$$

In these models $Z \gg Z_F$ and $Z \gg Zm^2$. Therefore,

$$|A_v| = \frac{|Zm|}{|Z_A|} = \frac{\omega M}{\sqrt{R_A^2 + \omega^2 L_A^2}} = \frac{\omega K \sqrt{L_A L_F}}{\sqrt{R_A^2 + \omega^2 L_A^2}}$$

$$= \frac{|Z_T|}{\sqrt{R_A^2 + \omega^2 L_A^2}} \tag{3.26}$$

Thus, from the above, the better approach to follow in determining the coefficient of coupling is by employing the transfer impedance since it is independent of coil resistance. The coefficient is

$$k = \frac{|Z_T|}{\omega \sqrt{L_A L_F}} \tag{3.27}$$

A listing of the transfer impedances and coefficients of coupling of the three motor-transducers is presented in Table II. The coefficient

Z_T = Transfer Impedance

k = Coefficient of Magnetic Coupling

Model	Z_T[ohms]	k
1. Aluminum-Wire Low Temperature	4.1	0.38
2. Molybdenum-Wire High Temperature		
a) Armature coupled to one field coil	0.72	0.30
b) Armature coupled to both field coils	1.43	0.42
3. Platinum-Clad Molybdenum Wire High Temperature	2.17	0.46

TABLE II

MOTOR-TRANSDUCER PROPERTIES

of coupling between the coils of all the motors is approximately

0.42, which indicates that the design utilized provides a good coupling

for an air-core device.

The molybdenum-wire motor, which was incorporated into the high

temperature system, has a transfer impedance of $|Z_T|$ = 1.43 [ohms].

This defines the transducer characteristic for use in the system block

diagram in Chapter V, because the armature is energized by a constant

current source to make its operation independent of coil and lead

resistance. Figures 23 and 24 show the sensor characteristics of the

high temperature model.

2. TORSIONAL SPRING CONSTANT

Figure 25 shows the output voltage versus weights placed in the

pan of the force applicator. Using this information in conjunction

with the signal coupling characteristics, the torsional spring constant

K_F of the motor-sensor unit can be determined. Figure 26 shows the

experimental arrangement. Since

$$+\downarrow \Sigma M_0 = 0$$

and $\tau = -K\Theta_0$ (3.28)

$$+\downarrow \Sigma M_A = 0$$

Using free-body diagrams, the moments about points 0 and A are

determined.
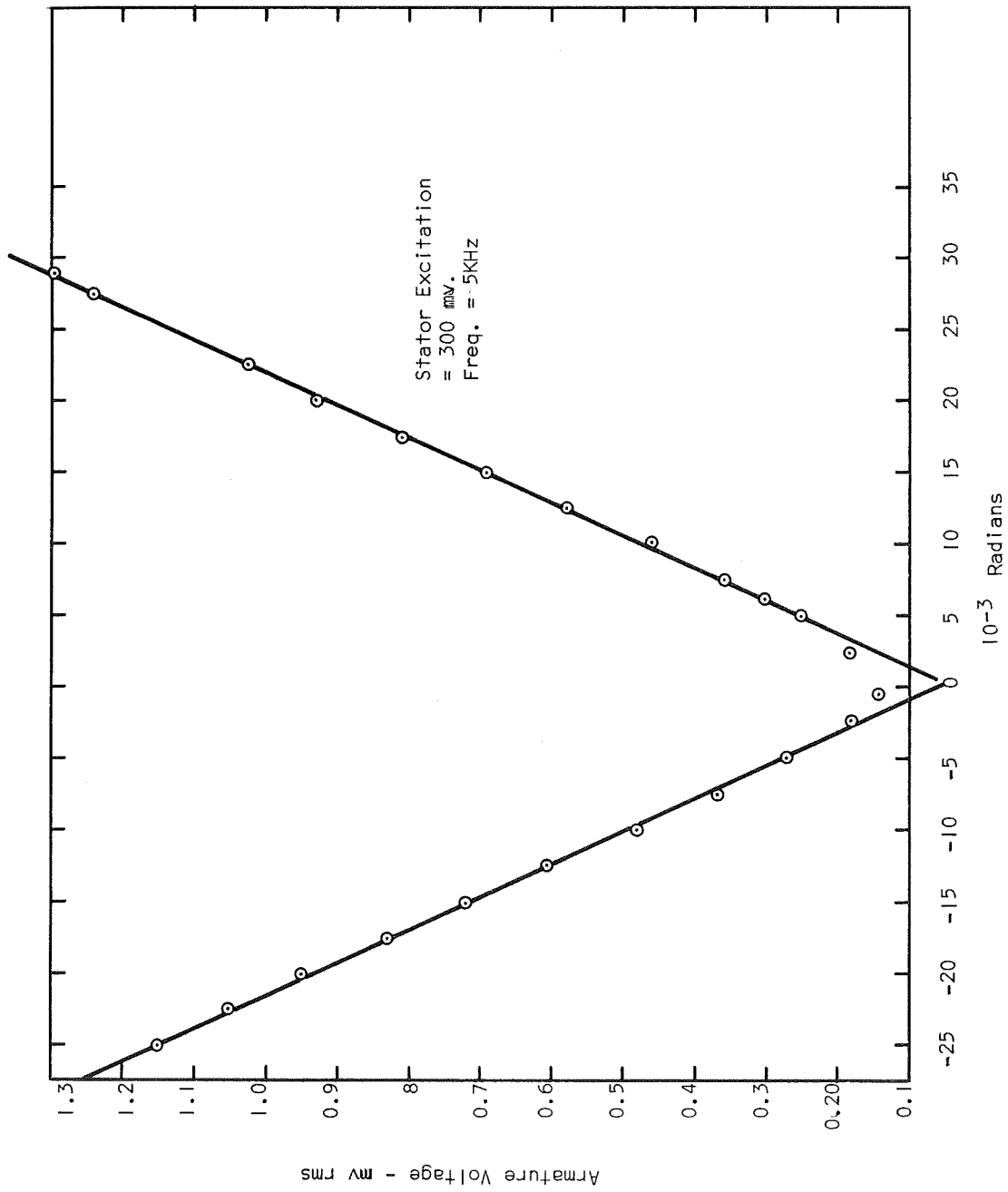
Figure 23. High Temperature Sensor Characteristics - Stator Excited
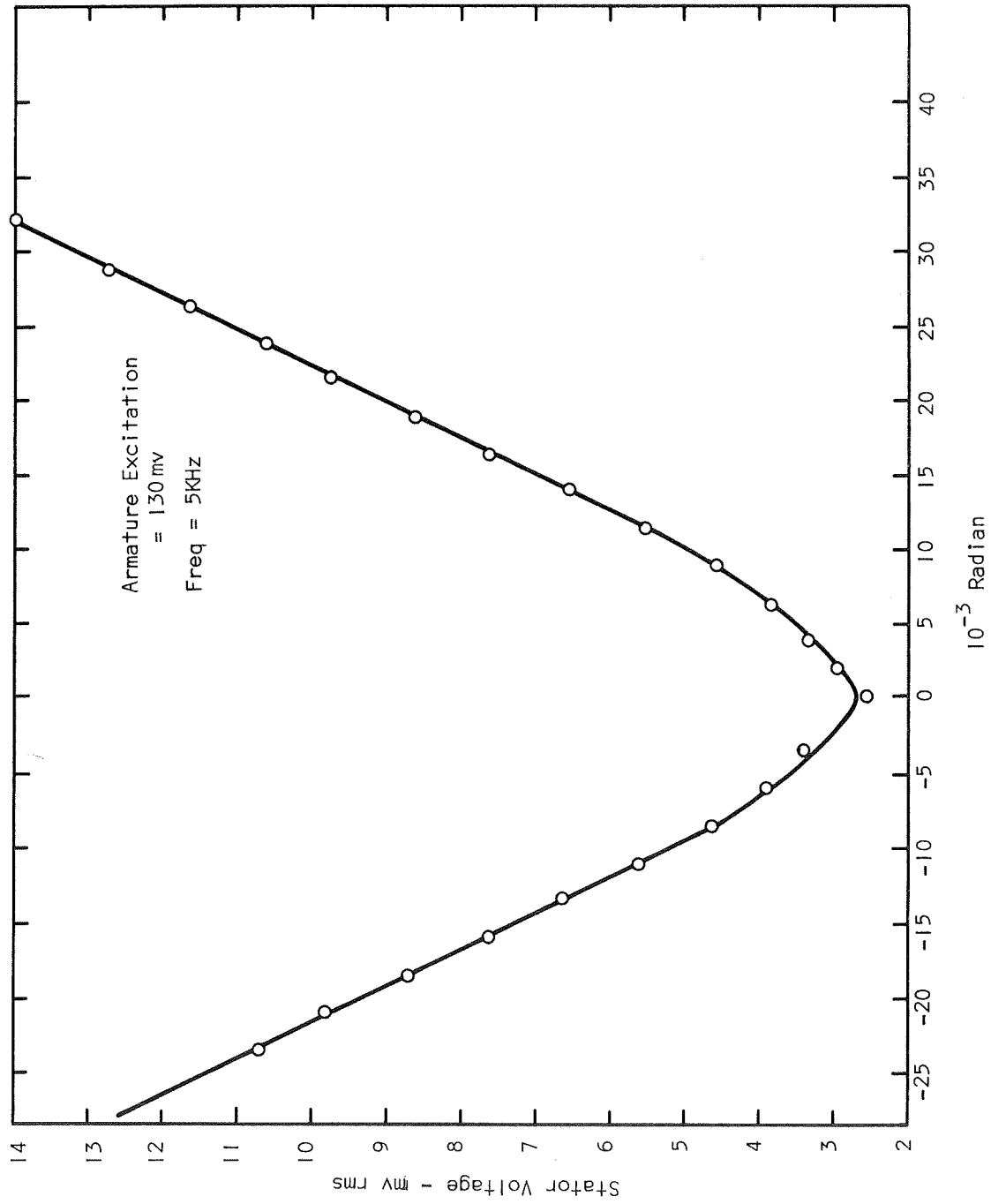
Figure 24. High Temperature Sensor Characteristics - Armature Excited
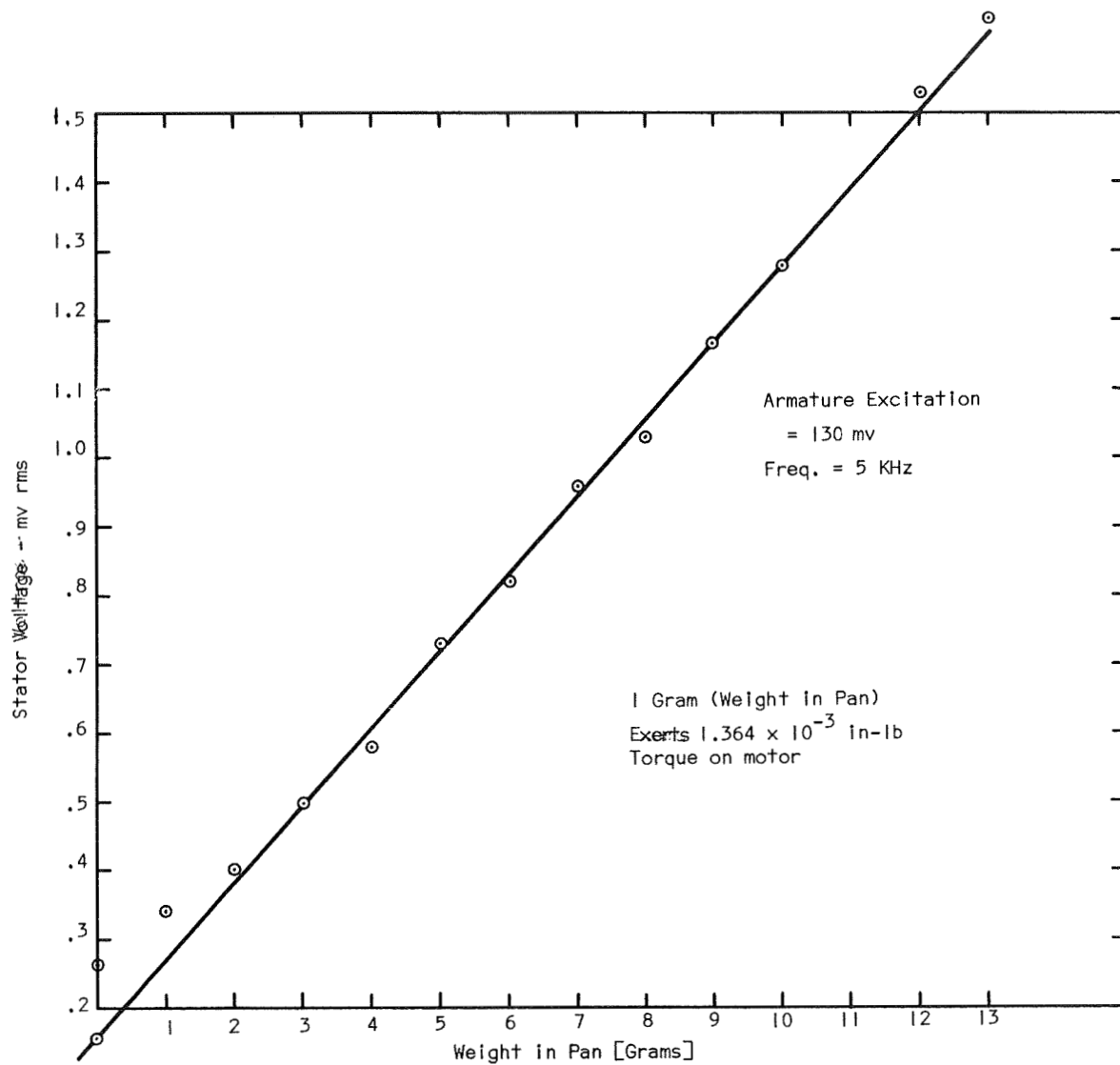
Figure 25. Torque Sensitivity Curves for High Temperature Sensor
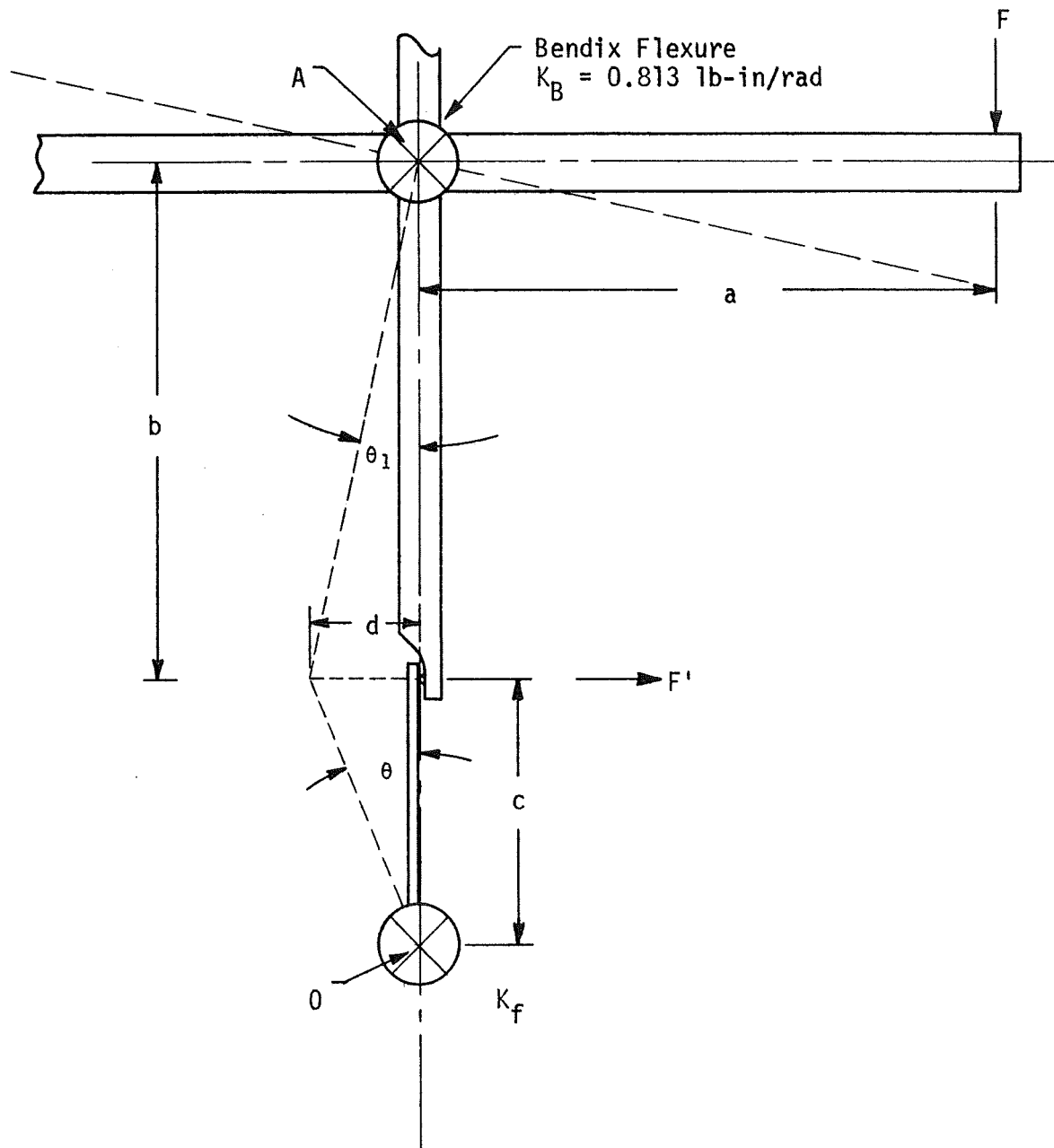
Figure 26. Force Balance Application

$$+\!\downarrow\Sigma M_A = Fa + \tau_B - F'b = 0 \qquad (3.29)$$

$$+\!\downarrow\Sigma M_0 = -F'C - \tau_f = 0 \qquad (3.30)$$

Therefore

$$F' = -\frac{\tau_f}{c} \qquad (3.31)$$

and

$$Fa + \tau_B + \tau_f\frac{b}{c} = 0 \qquad (3.32)$$

or

$$Fa = K_B\theta_1 - K_f\frac{b}{c}\theta = 0 \qquad (3.33)$$

where

K_B = Spring constant Bendix Flexure

= 0.813 lb-in/rad

K_f = Motor Flexure Spring Constant

But for small angles (<5°), $\tan\theta = \theta$ so that

$$\tan\theta_1 = \frac{d}{b} = \theta_1 \qquad (3.34)$$

$$\tan\theta = \frac{d}{c} = \theta \qquad (3.35)$$

Thus

$$\theta_1 = \frac{c\theta}{b} \qquad (3.36)$$

and from Eq. 3.33

$$Fa - K_B\frac{C\theta}{b} = K_f\frac{b}{c}\theta \qquad (3.37)$$

Multiplying Eq. 3.37 by $\frac{c}{b\theta}$ yields

$$K_f = \frac{Fac}{b\theta} - K_B\frac{C^2}{b^2} \qquad (3.38)$$

or

$$K_f = (\frac{F}{\theta})\frac{ac}{b} - K_B\frac{c^2}{b^2} \qquad (3.39)$$

From Figure 24 and Figure 25:

$$\frac{F}{\theta} = 0.9\ \frac{lb}{RAD}$$

The test apparatus has the following dimensions:

a = 3.0 in

b = 11.2 in

c = 2.25 in

Using these values in Eq. 3.39 yields

$$K_f = (0.9) \frac{(3)(2.25)}{11.2} - 0.813(\frac{2.25}{11.2})^2$$

or

$$K_f = 0.51 \frac{lb - in}{RAD}$$

The value can also be determined by using Figures 19 and 20 of the aluminum-wire model at an excitation voltage level of 200 millivolts. From this information

$$\frac{F}{\theta} = 0.731 \frac{lb}{RAD}$$

The test apparatus used on this model has the following dimensions:

a = 4.0 in

b = 10.75 in

c = 2.0 in

$$K_f = (0.731) \frac{(4.0)(2.0)}{10.75} - 0.813(\frac{2.0}{10.15})^2$$

$$K_f = 0.51 \frac{lb - in}{RAD}$$

3. COIL INDUCTANCE

The coil inductances are important parameters in determining the transducer characteristics. Since the coil form dimensions have been established and the coefficient of coupling is subject to little, if any, change due to an alteration in the number of wire turns, the gain of the transformer will vary directly with the number of turns. Inductance, of course, varies as the number of turns squared.

The graphs shown in Appendix G are used to determine the inductance of the field coils of the molybdenum-wire model. The coils exhibit the following parameters:

$b_c = 0.84$ in $\qquad\qquad$ N = 44 turns

$d = 2.45$ in

$b_c/d = 0.34$ $\qquad\qquad$ $r_w/d = 0.114$

Applying these data to graph I in Appendix G yields

$$L_S = \frac{d^2 N^2}{b_c} (8.8 \times 10^{-9}) = 123 \ \mu h \qquad\qquad (3.40)$$

$$L_C = (0.9)L_S = 110 \ \mu h$$

The inductance of the field coils was measured and found to be 110 uh each. A mutual inductance of 22 uh exists between the field

coils in their design configuration. The coefficient of coupling

for the field coils with a gap of 0.4 in is k = 0.2.

The field coils of the platinum-clad model exhibit the following

parameters:

r_w = 0.35 in   N = 55 turns

b_c = 0.84 in

d = 2.52 in

b_c/d = 0.334 r_w/d = 0.139

From graph I in Appendix G

$$L_S = \frac{d^2N^2}{b} (8.8 \times 10^{-9}) = \frac{(2.52)^2(55)^2}{0.84} (8.8 \times 10^{-9}) \qquad (3.41)$$

$$= 204 \ \mu h$$

and

$$L_C = 0.9(204) = 184 \ \mu h$$

The self-inductance of circular coils without iron is determined from

the following equation:

$$L_S = \frac{2\pi dN^2}{0.3937 \times 10^2} \left[(Log_{nb_c} \frac{4d}{nb_c})(1 + \frac{b_c^2}{8d^2} - \frac{b_c^4}{64d^4} + \frac{5}{1024} \frac{b_c^6}{d^6} - \right.$$

$$\frac{35}{16,384} \frac{b_c^8}{d^8} \ldots) - \frac{1}{2} + \frac{b_c^2}{32d^2} + \frac{b_c^4}{96d^4} - \frac{109}{24,516} \frac{b_c^6}{d^6} +$$

$$\frac{431}{196,608} \frac{b_c^8}{d^8} \ldots] \text{ Henries} \qquad [24] \qquad (3.42)$$

where

$d = 2a$ = mean diameter of solenoid

b_c = length of the solenoid

N = number of turns

and dimensions are in inches.

Although this equation is intended to be used for circular coils, the results obtained from its application to the square coils employed in the design indicate that it yields results with less than 10% error.

L_S is the inductance of a thin solenoid whose radial thickness is neglected. The inductance of a coil of appreciable radial thickness t is

$$L_C = L_S - \Delta L$$

ΔL for coils where r_w/d is approximately 5% - 10% of L_S is

$$L_C = 0.9L_S \qquad (3.43)$$

Experimentally, the inductance of the field coils was measured by connecting the coils in additive and subtractive coaxial magnetic

field configurations.   The results obtained were

$$L_1 + L_2 + 2m = 466 \quad uh \qquad\qquad (3.44)$$

$$L_1 + L_2 - 2m = 317 \quad uh \qquad\qquad (3.45)$$

Since

$$L_1 = L_2 = L_C$$

$$4L_C = 783 \quad uh$$

or

$$L_C = 196 \quad uh$$

The mutual inductance, M, is 37 uh and the coefficient of coupling of the two field coils is k = 0.2.

The inductance of the armature coil L_A is the same for both high temperature models. Some discrepancy exists between the theoretical value of 35 uh and a measured value of 50 uh. Since both coils measured 50 uh, this value was used for the control system design. It is not possible to obtain data for the mutual inductance of each side of the coil as was done above without severing the wire in an inaccessible location.

CHAPTER IV

LOW TEMPERATURE MODEL CONTROL SYSTEM DESIGN

Preliminary investigation of the control system required for the
skin friction sensor was begun with the aluminum-wire model. Aluminum-
wire was wound bifilarly (to simulate insulation spacing) on the ceramic
forms, while awaiting delivery of the molybdenum wire with quartz in-
sulation. The motor-sensor characteristics are shown in the block
diagram in Figure 29. These characteristics include those of the
force applicator. It was necessary to position the armature probe
with the sting to the null position, since no electrical null injector
had as yet been designed. The armature mechanical resonant frequency
is approximately equal to the 7 Kz predicted by the spring constant
of the motor flexure and the armature moment of inertia.

It was the intent at this point in the design stage to completely
design the control system, simulating the final motor with the aluminum-
wire motor until the materials were received. However, certain
observations were made at room temperature on the experimental system.
The null position shifted, following successive deflecting, as much
as 2.5 milliradians. This position change was due to the spring constant
of the armature leads. To counteract this action, the leads were bent
orthogonally to the direction of the applied force and placed in pools
of mercury, installed to provide a liquid contact and the subsequent
freedom of movement of the loads. However, difficulties were encountered
with poor contact developing at times with the aluminum wire because of

68

the rapid oxidation of the bare wire upon exposure to atmosphere.

In an attempt to eliminate this problem, the high temperature motor used the flexure support members as armature current conductors.

The basic control system was completed with the units shown in the schematic block diagram in Figure 27. The armature coil is energized with the constant a.c. carrier signal via the power amplifier, specifically designed so that the voltage induced into the field coils is independent of the armature series and lead resistance. A constant d.c. current generator energizes the field coils. Demodulation is performed by the ring demodulator followed by a low pass filter. The reference signal for the demodulator is provided by the filtered reference amplifier and a unity gain phase shifter, which establishes the necessary phase relationship. The compensating amplifier, which introduces a series lag and simple pole network into the loop, provides the necessary adjustment to loop gain for system stability. The d.c. signal from the compensating amplifier is applied to the power amplifier. This power amplifier provides the motor with the current required to produce the restoring torque.

Figure 28 presents a schematic of the control system. A functional block is included in the block diagram in Figure 29 to simulate a secondary loop coupling. The gain of this loop is constant as a function of armature position and varies linearly with a change in the carrier amplitude. It appears as though the coupling through the power supplies generated this signal although it could not be proven; and, since this
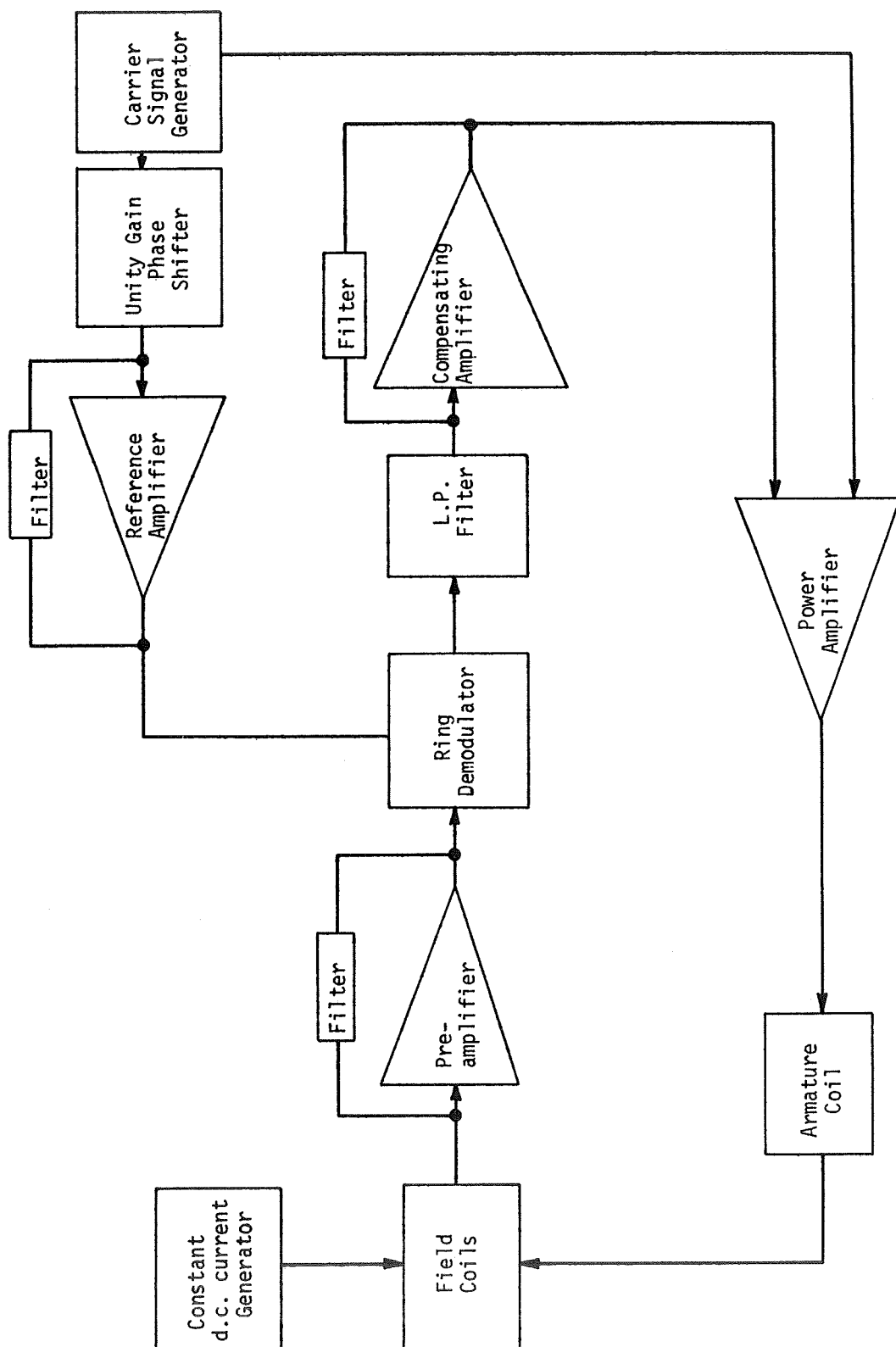
Figure 27. Schematic Diagram of Low Temperature Closed Loop System

Figure 28. Electrical Schematic of Low Temperature System
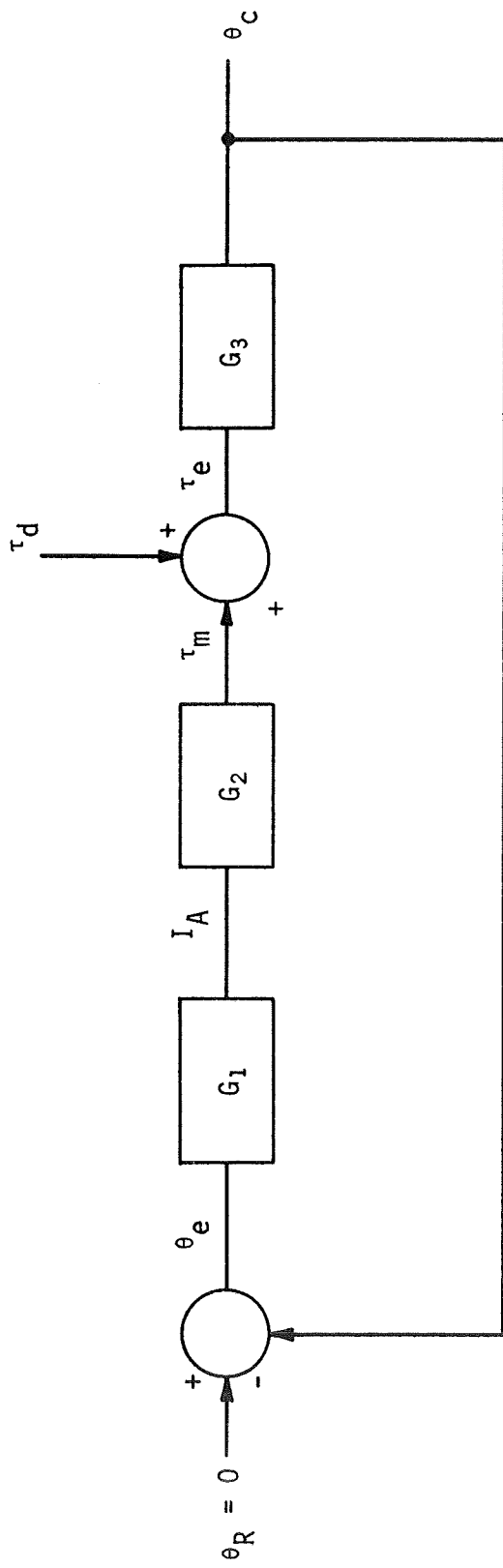
Figure 29. Low Temperature System Block Diagram

was not to be the final design, further investigation was not worth while.

A more detailed analysis of the functional units will not be described here, because coupling between the power supplies prevented the closed loop system from performing according to theory. This problem was eliminated in the final design for the high temperature motor and, therefore, a more detailed description is given in the next chapter.

There are, however, certain parameters of the system which are of interest. Figure 29 represents its functional behavior as a feedback control system. To represent its characteristics as a torque measurement sensor, this can be redrawn as shown in Figure 30. The loop gain of the carrier loop of the system can be determined from the block diagram in Figure 30 to be

$$\text{Loop Gain} = \frac{-K_p(1+2.04\times10^{-3}s)(1+1.45\times10^{-4}s)(1+0.016s)^2(1+1.4\times10^{-3}s)}{[(4.2\times10^{-4})s^2+0.41s+1](1+2.7\times10^{-4}s)(1+1.11\times10^{-4}s)^2(1+(8\times10^{-5})s)} \times$$

$$\frac{1}{(1+0.016s)(1+0.016s)(1+(1.6\times10^{-3})s)} \qquad (4.1)$$

For E_c, the carrier signal source amplitude, equal to 150 millivolts the loop gain constant, K_p, equals 110. The torque of the flexure must be a small fraction of motor torque. For a step input of skin friction torque
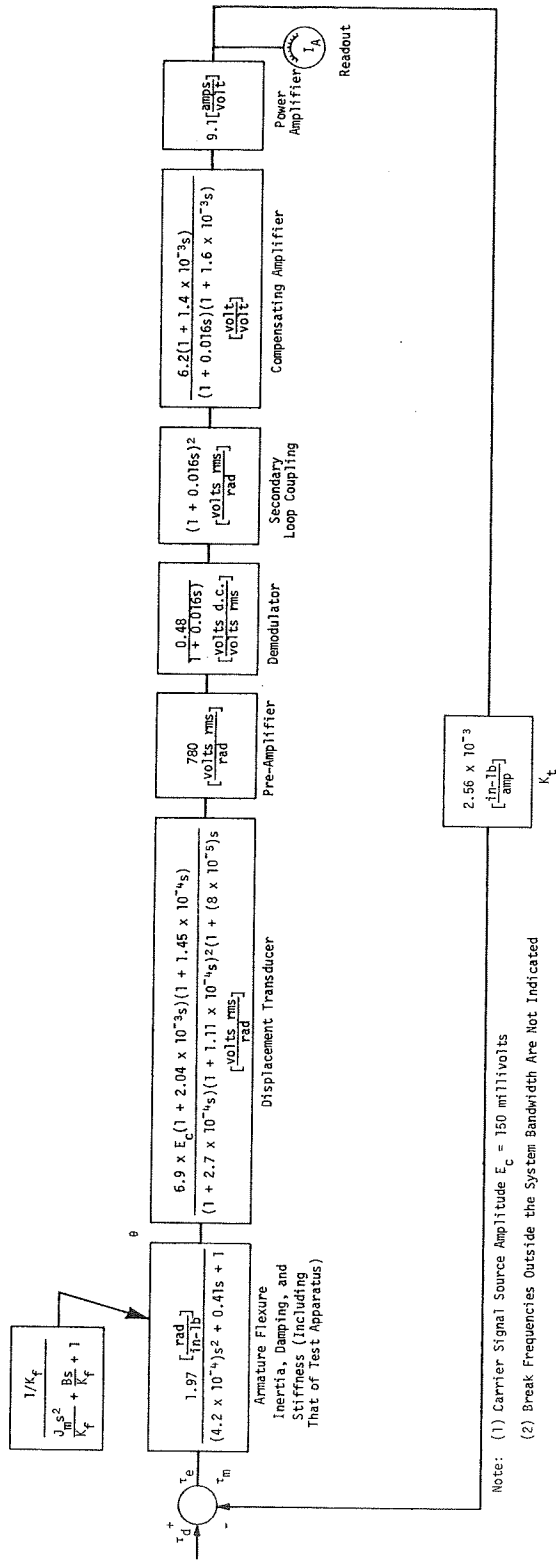
Figure 30. Block Diagram of Low Temperature System Carrier Loop

$$\frac{1/K_f}{\frac{J_m s^2}{K_f} + \frac{Bs}{K_f} + 1}$$

θ

$$\frac{1.97 \left[\frac{rad}{in\text{-}lb}\right]}{(4.2 \times 10^{-4})s^2 + 0.41s + 1}$$

Armature Flexure Inertia, Damping, and Stiffness (Including That of Test Apparatus)

$$\frac{6.9 \times E_c(1 + 2.04 \times 10^{-3}s)(1 + 1.45 \times 10^{-4}s)}{(1 + 2.7 \times 10^{-4}s)(1 + 1.11 \times 10^{-4}s)^2(1 + (8 \times 10^{-5})s)s} \left[\frac{volts\ rms}{rad}\right]$$

Displacement Transducer

$$780 \left[\frac{volts\ rms}{rad}\right]$$

Pre-Amplifier

$$\frac{0.48}{1 + 0.016s} \left[\frac{volts\ d.c.}{volts\ rms}\right]$$

Demodulator

$$(1 + 0.016s)^2 \left[\frac{volts\ rms}{rad}\right]$$

Secondary Loop Coupling

$$\frac{6.2(1 + 1.4 \times 10^{-3}s)}{(1 + 0.016s)(1 + 1.6 \times 10^{-3}s)} \left[\frac{volt}{volt}\right]$$

Compensating Amplifier

$$9.1\left[\frac{amps}{volt}\right]$$

Power Amplifier

I_A

Readout

τ_e

τ_m

τ_d

$$2.56 \times 10^{-3} \left[\frac{in\text{-}lb}{amp}\right]$$

K_t

Note: (1) Carrier Signal Source Amplitude E_c = 150 millivolts

(2) Break Frequencies Outside the System Bandwidth Are Not Indicated

$$\tau_d(s) = \frac{\tau_d}{s} \qquad (4.2)$$

to produce a steady state motor torque error, $\tau_{e_{ss}}$, of 1% where

$$\frac{\tau_{e_{ss}}}{\tau d} = \frac{1}{1 + K_p} = 0.01 \qquad (4.3)$$

the system gain constant must be 99. In order to meet the position error specification:

$$\theta_{e_{ss}} = \frac{\tau_{e_{ss}}}{K_f} = \frac{\tau_d}{(1 + K_p)K_f} \qquad (4.4)$$

or

$$K_p = \frac{\tau_d}{\theta_{e_{ss}} K_f} - 1 \qquad (4.5)$$

where

$$\tau_d = 7 \times 10^{-3} \text{in-lb maximum}$$

$$K_f = 0.51 \text{ lb-in/rad}$$

$$\theta_{e_{ss}} = 5 \times 10^{-4} \text{rad maximum}$$

and

$$K_p = 26.4$$

Therefore, with K_p equal to 110, both conditions can be satisfied.

This system was designed for the maximum bandwidth practical. Of course, much phase shift and many singularities due to the carrier frequency amplifier are encountered above the frequency 1 KHz. A ratio of 20:1 of carrier frequency to system crossover frequency is generally considered necessary for the demodulation [25]. The cross-over frequency f_c is 200 Hz as indicated on the open loop frequency response shown in Figure 31. The phase margin at crossover is approximately 90°.

The system response was determined by breaking the loop at the input to the power amplifier. A sinusoidal perturbation of the system was provided through a low impedance source. For frequencies greater than 30 Hz a Hewlett-Packard Model 302A wave analyzer with a BFO was used for input and monitoring of output of the compensating amplifier. For low frequencies (0.01 - 50 Hz), the input was provided by a Wavetek Model 110 function generator. The output of the compensating amplifier and the input to the system were monitored both with a Clevite Brush Recorder Mark 280 and a Tektronix 561B oscilloscope.

The response of the system to a step input indicates the damping, the rise time, and the settling time where

t_r = rise time = the interval between the intersection of a line tangent to $c(t)$ at $t = t_d$ and the intersection of $c(t) = 0$ and $c(t) = 1$ ($t_r = \pi/\omega_c = \frac{1}{2f_c}$)
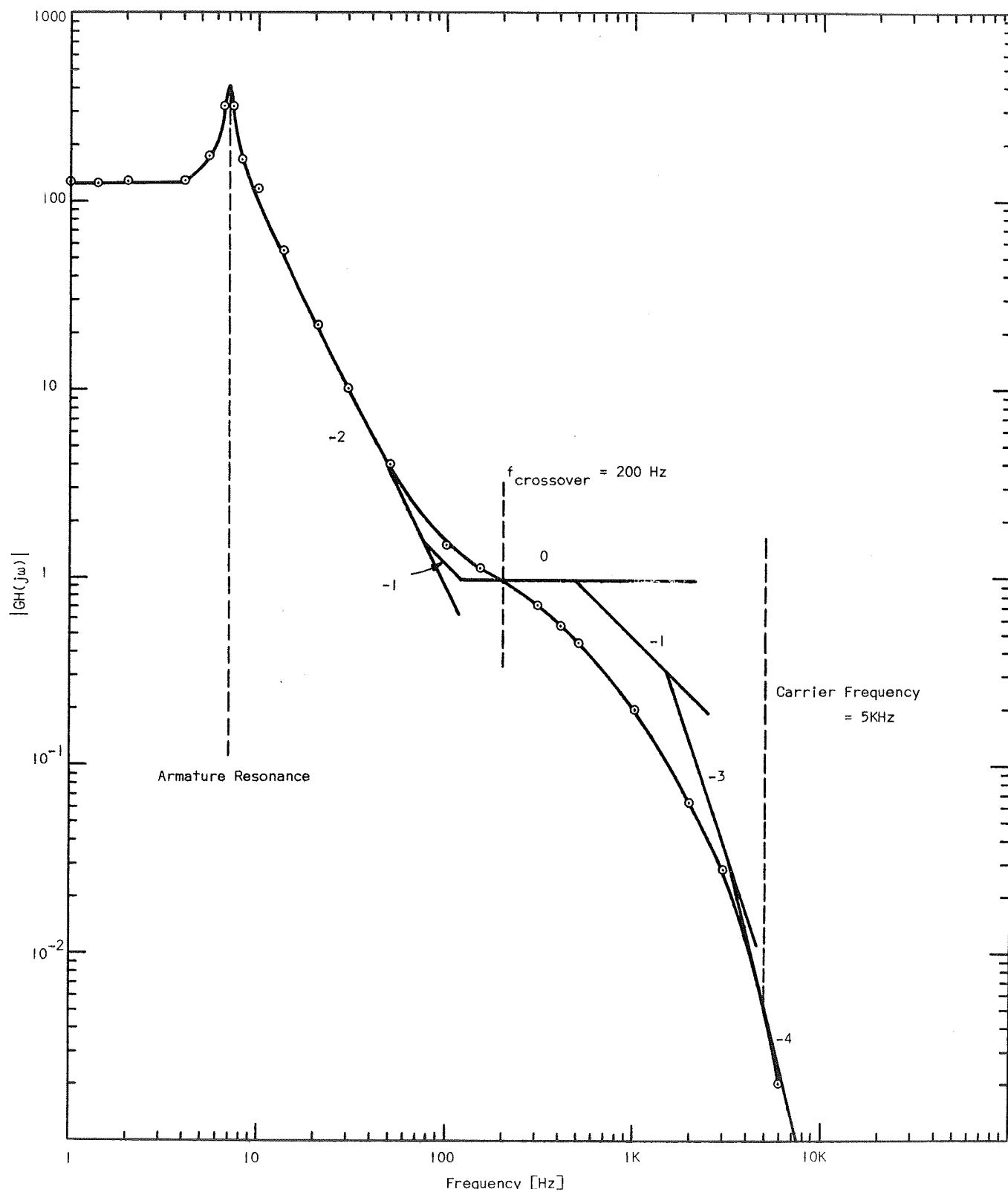
Figure 31. Low Temperature System Open Loop Frequency Response

t_d = time delay = interval between the application of input step

and instant when response reaches 1/2 final

value [26]

and

t_s = settling time = time required for the output response first

to reach and thereafter remain within a pre-

scribed percentage of the final value. Common

values are 2 and 5 per cent [27]

Experimentally the step response was obtained by driving the system

with a low frequency square wave injected at the summing point of the

operational amplifier of the power amplifier. It is desirable, of

course, to drive the system with a torque step input but this was not

available.

The transient response of the system to a step input is shown

in Figure 32. The input is to the power amplifier and the response

is taken at the output of the compensating amplifier. From Figure

32

t_r = 2.5 msec

t_d = 1.2 msec

t_s = 7   msec

The system is critically damped. These results agree with the

crossover frequency of 200 Hz and the phase margin of almost 90°.
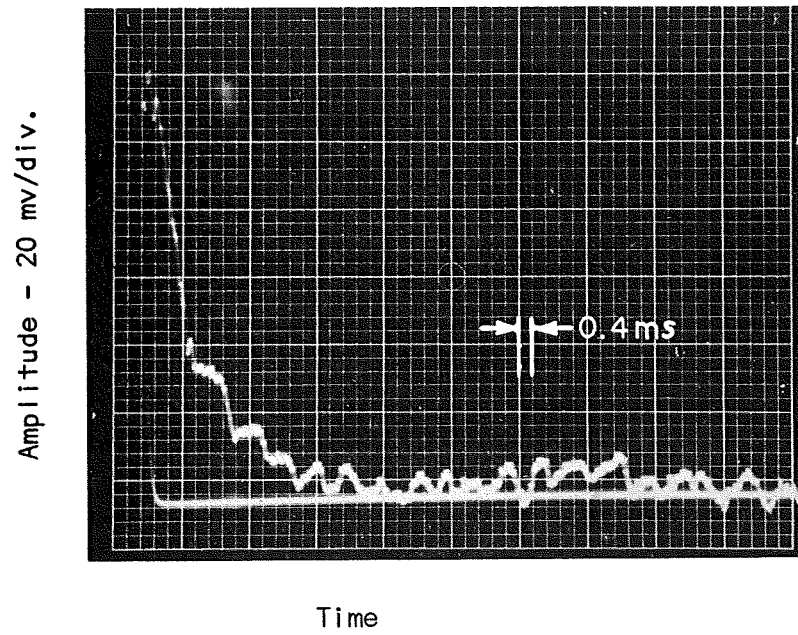
Figure 32.   Transient Response of Low Temperature System

CHAPTER V

HIGH TEMPERATURE MODEL CONTROL SYSTEM DESIGN

I. GENERAL

The molybdenum-wire motors are incorporated into the basic control

system shown in the schematic block diagram in Figure 33. For the

final high temperature application the armature coil is energized with

the constant amplitude a.c. carrier signal via the power amplifier,

specifically designed so that the voltage induced into the field coils

is independent of the armature series and lead resistance. Two constant

current field supplies energize the field coils. The field coils are

energized separately in order that the supply voltage can be kept to

a minimum. Based on the design and the maximum resistance of each

field coil (7.5 ohms at elevated temperatures), the supply voltage was

set at 30 volts. Although this does not meet the voltage requirement

specification (6), the design of an appropriate power supply is not

difficult. The voltages induced into the field coils are summed at

the input to the preamplifier with a null signal.

The null signal voltage is developed in a sensing resistor in

series with the armature coil in the power amplifier. After the signal

is filtered and amplified in the null signal amplifier, the unity gain

phase shifter is adjusted such that the null signal is 180° out of

phase with respect to the summed output of the field coils. The

amplitude is set in the null signal amplifier for exact cancellation

and signal null at the summation point in the preamplifier. It
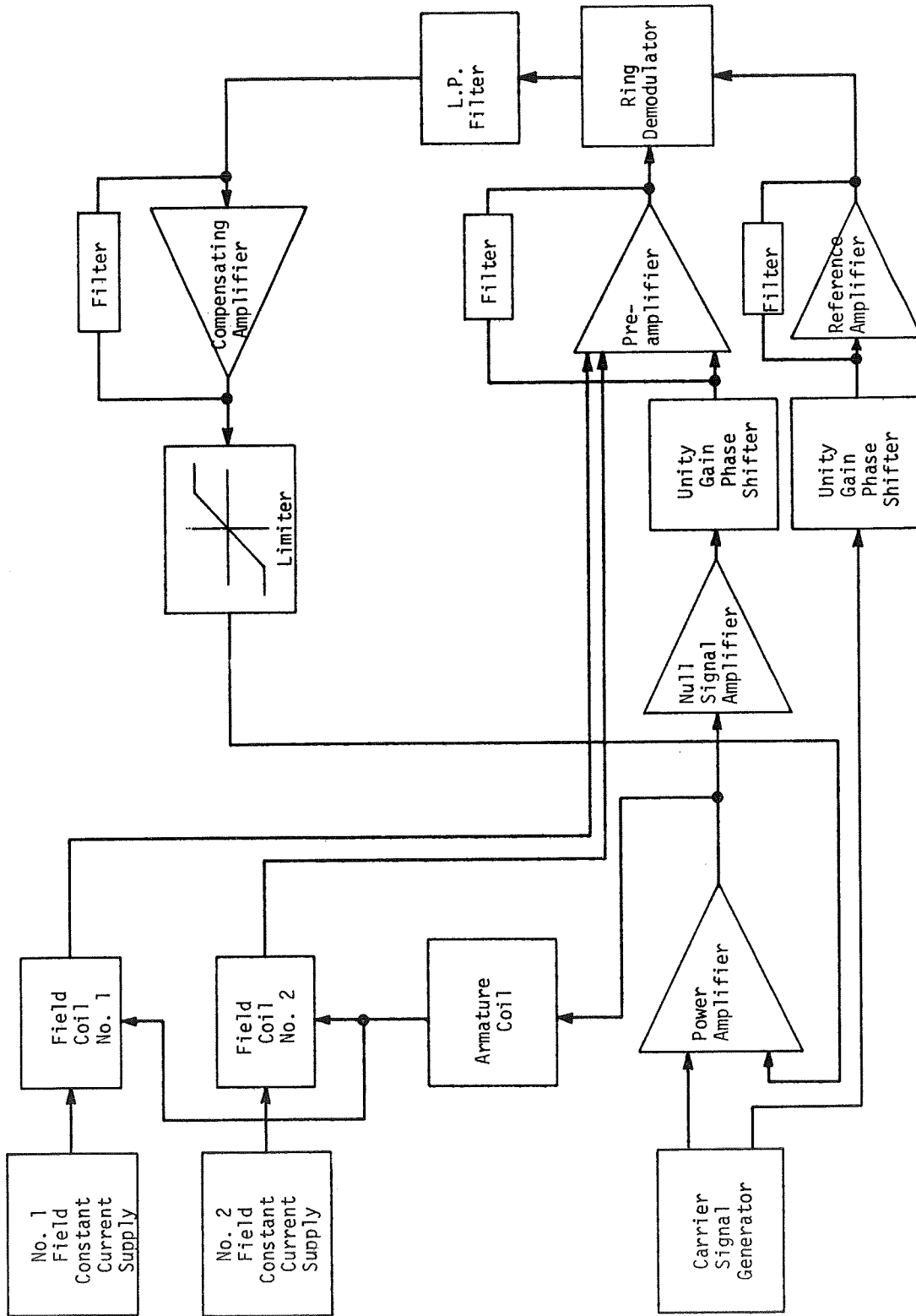
Figure 33. Schematic Block Diagram of High Temperature Closed Loop System

should be noted that the null signal path introduces a secondary loop
into the system. The effect of this loop is discussed later in the
chapter.

The preamplifier is a high gain operational amplifier with associated
filtering and a summing amplifier as stated above. Demodulation is
performed by the ring demodulator which is followed by a low pass filter.
The reference signal for the demodulator is provided by the filtered
reference amplifier and a unity gain phase shifter. The unity gain
phase shifter establishes the necessary phase relationship. The com-
pensating amplifier, which introduces an active composite series
equalizer into the carrier loop, provides the necessary adjustment
to loop gain for system stability.

A limiter is inserted between the compensating amplifier and the
power amplifier to allow the system to operate in the active region
during energizing and to prevent latch-up. Thus, the primary function
of the limiter is utilized only during turn-on.

The d.c. signal from the limiter flows to the power amplifier
which provides the motor with the current required to produce the
restoring torque. The control loop is now complete. Readout of the
disturbance torque is proportional to the armature current required
to produce the restoring torque. Remember that the torque has the
same magnitude as the applied force since a 1-inch moment arm is
employed.

2. SYSTEM GAIN

The high temperature model control system is a Type zero system.

Since a constant actuating aignal results in a constant value for the controlled variable, the zero integration system will not bring the output into exact correspondence with the input. The desired degree of accuracy is obtained by making the system gain sufficiently large, since the final error varies linearly with the magnitude of the input step and inversely with the d.c. loop gain.

According to the specifications stipulated, the position error is not to exceed 5×10^{-4} radians. In order to meet the position error requirement, it has previously been established that $K_p \geq 26.4$. For a step input of skin friction torque and a motor torque error of 1% the gain of the system K_p must be equal to or greater than 99. Since no specification had been established on the motor torque error (also readout error), the gain of system was set at $K_p = 90$ based on the above information. Subsequently, the theoretical steady-state position error and motor torque error are

$$\theta_{e_{ss}} = \frac{\tau_{d_{max}}}{(1 + K_p)K_f} = 0.15 \times 10^{-3} \text{ radians} \tag{5.1}$$

and

$$\frac{\tau_{e_{ss}}}{\tau_d} = \frac{1}{1 + K_p} = 0.011 \tag{5.2}$$

where

$$\tau_{d_{max}} = 7 \times 10^{-3} \text{ in-lb}$$

and

$$K_f = 0.51 \text{ lb-in/rad}$$

3. ELECTRONIC CONTROL CIRCUIT

The system electronics is shown in the schematic in Figure 34.
The functional units already described are enclosed by dotted lines
and labeled.

The carrier signal of 5 KHz is generated by a Hewlett-Packard
Test Oscillator 651A at a constant amplitude of 200 millivolts. The
output of the signal source is connected to C41 of the unity gain phase
shifter in the reference circuit of the ring demodulator and is paralleled
by potentiometer R1, which serves as the system gain adjustment. The
attenuated output at R1 is coupled through an emitter follower to the
input of the power amplifier at C1.

The carrier frequency was selected as 5 KHz for two reasons. First,
the filtering of the displacement transducer, capacitive coupling and
the gain-bandwidth product of the operational units employed were
determining factors. Secondly, a ratio of 20:1 of carrier frequency
to system crossover frequency [25] is generally considered necessary
for the demodulation. Based on a system crossover frequency of
approximately 25 Hz, the carrier frequency is ten times that stipulated
as necessary. The system gain is nominally set by R1 for 100 millivolts.
The system gain can be changed as long as changes in the specifications

All resistors 1/2 watt unless otherwise
    indicated
All resistances in ohms
All capacitances in microfarads unless
    otherwise indicated
±15-volt supplies are type Hewlett-Packard
    Model 721A
±30-volt supplies are type Harrison Lab
    Model 6433B
Signal generator is Hewlett-Packard Test
    Oscillator 651A
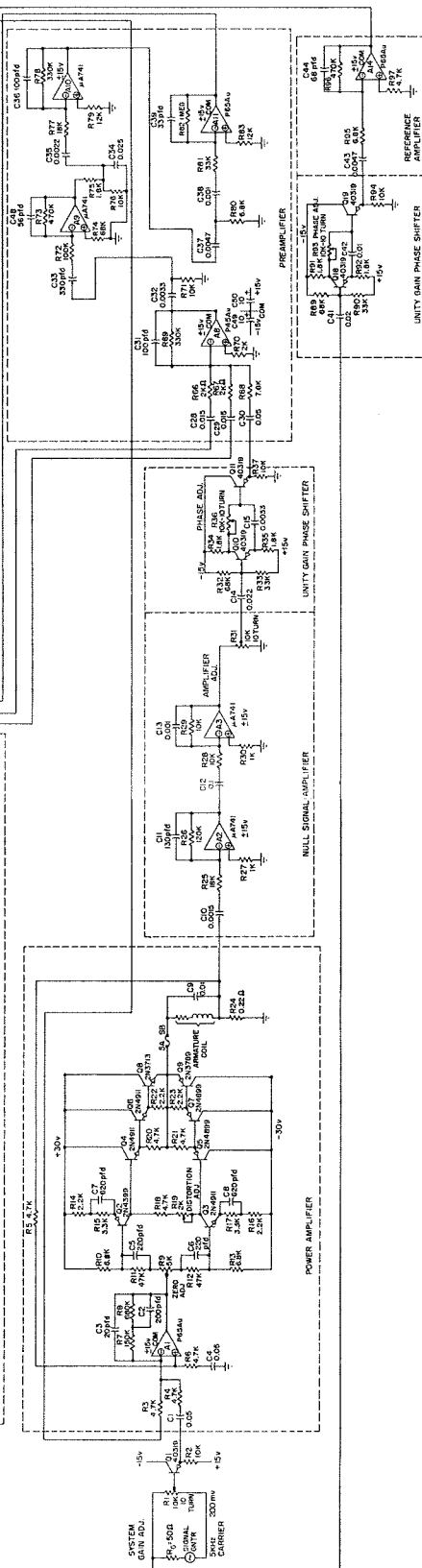
Figure 34. Electrical Schematic of High Temperature System

can be tolerated and the system stability can be maintained.

Demodulator Reference Circuit

A unity gain phase shifter composed of transistors Q18 and Q19
and associated circuitry and the reference amplifier A14, an active
RC filtering network, provide the necessary signal to the reference
side of the transformer T3 of the ring demodulator. For proper
operation of the ring demodulator, the reference signal must be greater
than twice that of the input signal. Since the maximum closed loop
signal is less than 1 volt rms, the amplitude of the reference signal
must be greater than 2 volts rms.

The unity gain phase shifter provides a means for adjusting the
reference signal so that it is in phase 180° out of phase with the
amplified transducer signal. Potentiometer R93 is adjusted for the
desired phase relationship. The phase shifter inverts the signal
received at C41 and increases the shift, β , by the relationship
(see Appendix H)

$$\beta = -2 \tan^{-1} \omega R93 \; C42 \tag{5.3}$$

$$= -2 \tan^{-1}(3.14 \times 10^{-4})R93$$

The emitter follower Q19 is used to prevent loading of R93 and
to provide a low output impedance to the reference amplifier. Some
filtering takes place in the phase shifter by the R-C network C41 and

the input impedance at the base of Q18 which is approximately 18 kilohms. Therefore, the transfer function of the unity gain phase shifter is

$$\frac{E_o}{E_i}(s) = \frac{s(3.6 \times 10^{-4})}{1 + s(3.6 \times 10^{-4})} \qquad (5.4)$$

The reference amplifier provides additional filtering of the signal and yields a gain of 40 at 5 KHz. This is the maximum gain allowed to remain in the active region of A14 with an oscillator signal source amplitude of 200 millivolts rms. The reference voltage of the ring demodulator is, therefore, 8 volts rms. This greatly exceeds the voltage necessary for proper operation. The load on A14 is the same as that rated on the operational unit, 5 kilohms.

The transfer function of the reference amplifier

$$\frac{E_o}{E_i}(s) = \frac{s(2.25 \times 10^{-3})}{(1 + s(3.18 \times 10^{-5}))^2} \qquad (5.5)$$

has two poles at the break frequency of 5 KHz. Combining the two transfer functions, the transfer function of the reference circuit is determined to be

$$\frac{E_o}{E_i}(s) = \frac{s^2(8.1 \times 10^{-7})}{(1 + s(3.18 \times 10^{-5}))^2(1 + s(3.6 \times 10^{-4}))} \qquad (5.6)$$

Power Amplifier

The power amplifier employed in this system must not only provide direct current to the motor to produce the restoring torque but must also provide a means of superimposing the 5 KHz carrier signal on the armature at a constant current amplitude. Of course, the frequency response of the power amplifier would be ideally flat from d.c. to 50 KHz. However, a smaller passband can be tolerated as long as the loop gain is high enough at the carrier frequency. The power amplifier is a unity feedback module and a Type 0 control system.

As previously stated, the motor required 3.75 amps to produce 7×10^{-3} in.-lb of torque as required by the system. Since the force is applied to the system bidirectionally, the power amplifier must be capable of providing at least 3.75 amps in both directions through the armature coil of the motor. A sensing resistor R24 had to be used since the armature series resistance increases to 5.2 ohms at the elevated temperature of 2000°F. The unit stability is maintained by the necessary compensation for this wide parameter variation.

Many basic designs were considered for the power amplifier. Since a d.c. amplifier cannot employ transformer or capacitor coupling to the output, drift in the operating point on bias network presents a serious design problem. A single supply transistor bridge amplifier was considered. However, the supply voltage required and the problems encountered with superimposing the carrier signal eliminated this possibility.

With the advent of complementary power transistors, the problem

of drift and coupling is alleviated. The power amplifier consists

basically of a high gain operational amplifier, Al, which serves both

as a summer and a comparator in conjunction with its associated

circuitry, hereafter referred to as section one and a symmetrical

positive and negative power section.

The power amplifier, as stated above, is a unity feedback Type 0

control system. Therefore, the error is inversely proportional to the

loop gain. The unit has been designed so that at the maximum load

resistance of 7.2 ohms, assuming lead resistance of 2 ohms, the minimum

loop gain at d.c. is 100. The minimum gain at the carrier frequency

of 5 KHz is 6 at the maximum temperature to which the armature coil

is subjected and 12 at room temperature.

One break frequency occurs due to the R-C network comprised of

the load resistance and the capacitance of the power transistors. The

pole occurs between 1 KHz and 2 KHz varying inversely in frequency with

respect to an increase of armature series resistance. Another pole

occurs in the loop frequency response due to the interaction of the

armature coil inductance L_A =50 microhenries and the series resistance.

The power amplifier has been stabilized with the premise that the

armature coil has at all times at least 2 ohms of lead resistance.

This pole occurs at the frequency of 10 KHz when the motor is at room

temperature and at 24 KHz when the motor is subjected to 2000°F. Since

the operational amplifier Al requires some capacitance feedback for

stability, it is obvious that the system as it exists without compensation

is unstable, even disregarding higher frequency effects.

Section one of the power amplifier has the transfer function for
an input to R3

$$\frac{E_o}{E_c}(s) = \frac{175(1 + s(2.4 \times 10^{-5}))}{(1 + s(1.33 \times 10^{-4}))(1 + s(2.86 \times 10^{-6}))} \tag{5.7}$$

Capacitor C1 blocks the d.c. and allows only the carrier signal to
pass. A signal inserted at C1 has the same transfer characteristic
as the above at the carrier frequency.

Since the open loop signal at the output of the power amplifier
must be 180° out of phase with respect to the input signal for a
negative feedback system, the operational amplifier serves as a
difference amplifier. Because filtering is required on the carrier
signal input to the summing junction of A1, some pole-zero cancellation
is necessary on the non-inverting input. The output of the difference
amplifier is defined by

$$E_o(s) = \frac{Z_{FD}}{R_3}(-E_I(s)) + \frac{Z_{FD} + Z_I}{Z_I}(E_{NI}(s)) \tag{5.8}$$

where

Z_{FD} = feedback impedance of A1

Z_I = parallel combination of inverting input impedances

E_I = inverting input signal

E_{NI} = non-inverting input signal

E_o = output signal

Since the desired output of the difference amplifier is

$$E_o(s) = \frac{Z_{FD}}{R_3}(E_{NI}(s) - E_I(s)) \qquad (5.9)$$

the output signal of the power amplifier must be modified with a lag
network for comparison purposes. The circuit has been designed such
that $|Z_{FD}| >> |R3(I + sCIR4)sCI|$. Therefore, the lag network comprised
of R5, R6, and C4 produces the desired result. Although the output
impedance of the limiter of 1.93 kilohms has some effect on the desired
transfer function, the output impedance of emitter follower QI of
approximately 500 ohms has virtually none. The total effect of this
loading is no more than 10% amplitude variation at the carrier frequency
in the closed loop output of the power amplifier.

Potentiometer R9 provides a means whereby the bias can be adjusted
so that the output is zeroed when the input is grounded. The bias
network adjoined to the potentiometer includes a lead network composed
of R12, R13, C6 and a portion of R9. As previously stated, the power
section has symmetric positive and negative output drivers. The
negative output counterpart consists of R16, R17, C8 and the remaining
portion of R9. The transfer function of this series equalizer is

$$\frac{E_o}{E_i}(s) = \frac{0.12(I + s(1.1 \times 10^{-5}))}{(I + s(1.6 \times 10^{-3}))} \qquad (5.10)$$

A lead network consisting of R14, R15, R16, and C7 completes the
necessary compensation for the power amplifier. The negative counterpart

contains R16, R17 and C8. Since the output impedance of emitter followers Q2 and Q3 is less than 100 ohms, this has no effect on the transfer function. Therefore, the zero occurs at a frequency of 80 KHz and the pole occurs at 200 KHz.

Capacitor C9, which is used to attenuate at high frequencies, effects a pole at 250 KHz. The open loop transfer function for the power amplifier at room temperature with armature lead resistance of 2 ohms is

$$G(s) = \frac{145(1 + s(2.4 \times 10^{-5}))(1 + s(1.1 \times 10^{-5}))(1 + s(2 \times 10^{-6}))}{(1 + s(1.33 \times 10^{-4}))(1 + s(10^{-4}))(1 + s(1.6 \times 10^{-5}))} \times$$

$$\frac{1}{(1 + s(2.86 \times 10^{-6}))(1 + s(1.6 \times 10^{-6}))(1 + s(8.4 \times 10^{-7}))} \times$$

$$\frac{1}{(1 + s(6.25 \times 10^{-7}))} \qquad (5.11)$$

The gain margin is 4.7 and the phase margin is 40°.

Based on the above assumption of lead resistance, the open loop transfer function for the power amplifier when the armature coil is at 2000°F is

$$G(s) = \frac{100(1 + s(2.4 \times 10^{-5}))(1 + s(1.1 \times 10^{-5}))(1 + s(2 \times 10^{-6}))}{(1 + s(1.6 \times 10^{-4}))(1 + s(1.33 \times 10^{-4}))(1 + s(7.15 \times 10^{-6}))} \times$$

$$\frac{1}{(1 + s(2.86 \times 10^{-6}))(1 + s(1.6 \times 10^{-6}))(1 + s(8.4 \times 10^{-7}))} \times$$

$$\frac{1}{(1 + s(6.25 \times 10^{-7}))} \qquad (5.12)$$

The power amplifier has increasing relative stability for increasing temperatures applied to the armature coil. The phase margin is 64° and the gain margin is 7.1.

According to the design criterion used, the amplitude at the carrier frequency of the closed loop system should not change more than 3% over the temperature range of interest nor should the phase at this frequency shift more than 5°.

The experimental closed loop frequency response of the power amplifier is shown in Figure 35. The input to the unit was supplied by a Wavetek Model 110 function generator for low frequencies and a Hewlett-Packard Model 302A wave analyzer for high frequencies. The output was taken across R24. The BFO of the wave analyzer was used for the input and output monitoring at high frequencies. The low frequencies were monitored with a Clevite Brush Recorder Mark 280.

A 5 ohm resistor was inserted in series with the armature coil to simulate the coil resistance at 2000°F. At the carrier frequency, the amplitude variation over the temperature range is 1%. The phase shift was measured on an oscilloscope and found to be approximately 2°. The pass band is approximately 20 KHz.

All of the transistors employed are complementary pairs. The final power transistors Q8 and Q9 dissipate a maximum of 75 watts at room temperature and require adequate thermal cooling. The thermal resistance for these transistors is θ_{sc} = 1.2 °C/watt. With a maximum junction temperature of 200°C (plus a safety factor), the maximum thermal resistance case-to-air should be less than 0.7 °C/watt.
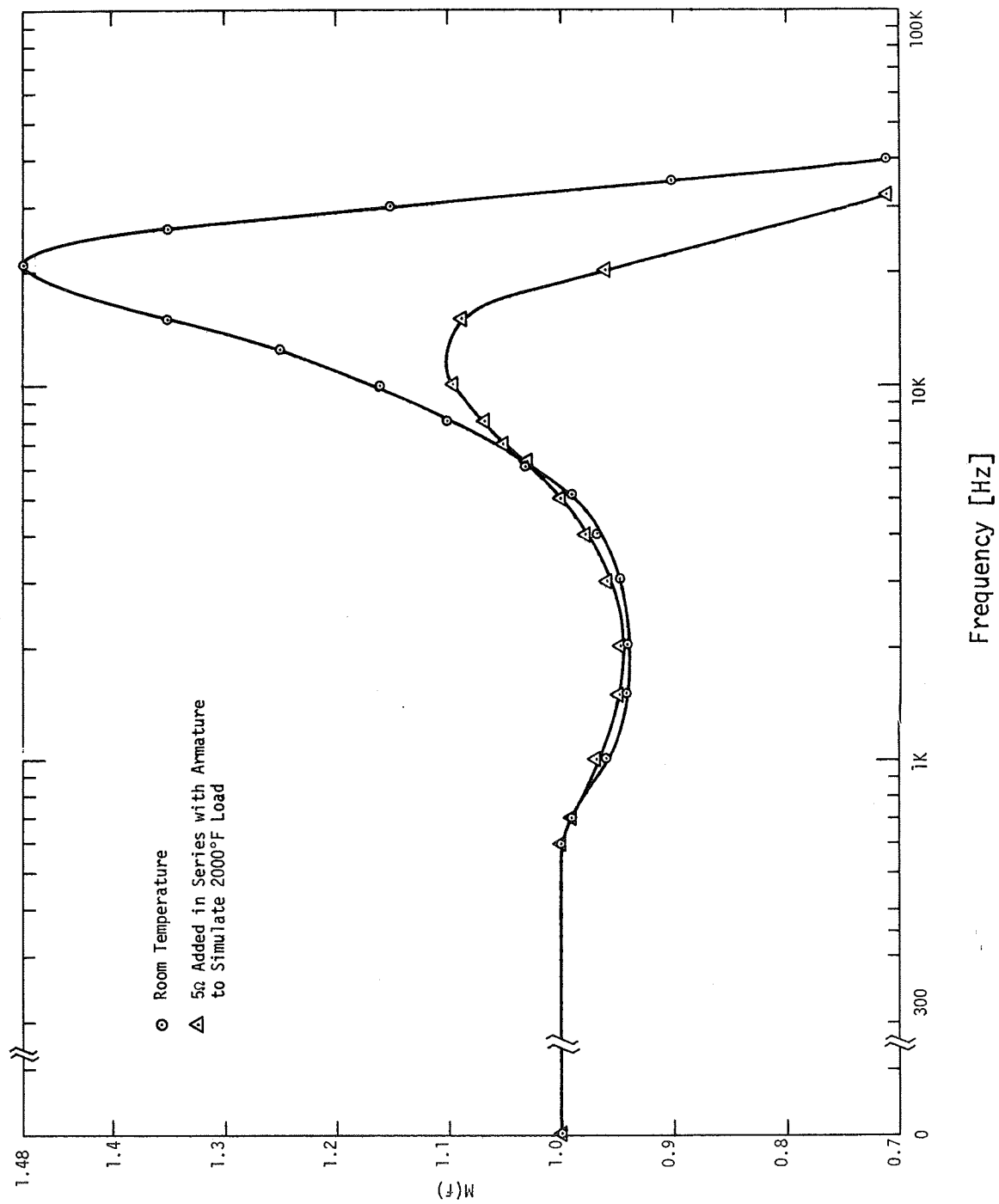
Figure 35. Closed Loop Frequency Response of Power Amplifier

The transistors have a V_{CEO} = 60 volts. If the power supply voltages should be increased to accommodate an increased load, high voltage transistors will be required.

An adjustment for altering the bias is available. The distortion adjustment R19 eliminates crossover distortion. The quiescent current in the driver stages is 150 milliamperes. If the unit is to be subjected to large temperature variations, diodes paralleled by the distortion potentiometer can be used in place of existing circuitry. The diode junctions are used to stabilize the changes in the BE junctions of the transistors.

The standby power consumption is only 10 watts. This is relatively small.

The power amplifier is a current source which drives the armature to restore torque and energizes the coil with the carrier signal. Since the output of the power amplifier is taken across R24, the power amplifier is represented by a 4.54 amps/volt transfer characteristic for the carrier loop. The resistance of R24 is 0.22 ohms. For high frequency considerations, the power amplifier can be represented by a double pole at 20 KHz.

Preamplifier

The preamplifier amplifies the nulled 5KHz carrier signal. The outputs of the two field coils are summed with the null signal at the input of the preamplifier. The signal received at the input is filtered

extensively. Both power supply harmonics and carrier harmonics cause problems in the closed loop system. Therefore, in order to have a large signal-to-noise ratio, the passband is limited.

Operational amplifiers A8, A9, A10, and A11 combined with their associated circuitry comprise the preamplifier. The summer amplifier A8 is a Philbrick P45AU operational amplifier. This device is more expensive than others employed in the system because of its high gain-bandwidth product of 30 megahertz. It has the highest closed loop gain of the units used in the preamplifier. Because of its high gain and relatively high input capacitance, it is recommended that the input be preceded by an emitter follower and that large electrolytic capacitors be placed across the power supplies at their inputs to the amplifier. In the schematic, capacitors C49 and C50 are used for this purpose. Although their schematic is unconventional, it is done in this manner for clarification. Since a low impedance signal source exists, emitter followers are not used. The transfer function of stage #1 of the preamplifier for field coil input signals is

$$\frac{E_o}{E_i}(s) = \frac{s(4.95 \times 10^{-3})}{(1 + s(3.3 \times 10^{-5}))(1 + s(3 \times 10^{-5}))} \qquad (5.13)$$

The gain at the carrier frequency is 78.

For the null signal input, the transfer function is

$$\frac{E_o}{E_i}(s) = \frac{s(1.65 \times 10^{-2})}{(1 + s(4.5 \times 10^{-4}))(1 + s(3.3 \times 10^{-5}))} \qquad (5.14)$$

Stage #2 is an active filter and inverter for the carrier frequency. Insertion of filtering at this particular location was found to be necessary to keep the signal-to-noise ratio large. And, without the filtering at this point, the system saturates. Operational amplifier A9 is a type μA741. It can be used because the d.c. drift is not of any great concern. The total transfer function for this stage, assuming the input signal at C32 and the output signal taken at R76 is

$$\frac{E_o}{E_i}(s) = \frac{(4.3 \times 10^{-9})s^2(1 + s(3.96 \times 10^{-5}))}{(1 + s(2.44 \times 10^{-5}))(1 + s(4.56 \times 10^{-5}))(1 + s(2.63 \times 10^{-5}))} \times$$

$$\frac{1}{(1 + s(5.3 \times 10^{-5}))(1 + s(2.84 \times 10^{-5}))} \qquad (5.15)$$

The third stage consists of another μA741, operational amplifier A10, and the associated circuitry which completes the active filter network. The transfer function of this stage, assuming an input at C35 and the output measured at the output of A10 is

$$\frac{E_o}{E_i}(s) = \frac{s(7.25 \times 10^{-4})}{(1 + s(3.96 \times 10^{-5}))(1 + s(3.3 \times 10^{-5}))} \qquad (5.16)$$

This stage has a gain of 10 at the carrier frequency.

A Philbrick operational amplifier P65AU is used for A11 in the final stage of the preamplifier. The P65AU was chosen because d.c. drift can be of importance here and also because the load is inductive.

The 5 K ohm reflected impedance of the ring demodulator is the rated load on the P65AU. The transfer function on this stage, assuming the signal input to C37 and the signal output at the output of A11, is:

$$\frac{E_o}{E_i}(s) = \frac{s^2(3.2 \times 10^{-8})}{(1 + s(3.3 \times 10^{-5}))(1 + s(1.98 \times 10^{-5}))(1 + s(5.5 \times 10^{-5}))}$$

$$(5.17)$$

The gain of this stage at the carrier frequency is 10.

Combining the above individual transfer functions of the four stages of the preamplifier, the total transfer function is

$$\frac{E_o}{E_i}(s) = \frac{(4.95 \times 10^{-22})s^6}{(1 + s(3.3 \times 10^{-5}))^3(1 + s(3 \times 10^{-5}))(1 + s(2.44 \times 10^{-5}))} \times$$

$$\frac{1}{(1 + s(4.56 \times 10^{-5}))(1 + s(2.63 \times 10^{-5}))(1 + s(5.3 \times 10^{-5}))} \times$$

$$\frac{1}{(1 + s(2.84 \times 10^{-5}))(1 + s(1.98 \times 10^{-5}))(1 + s(5.5 \times 10^{-5}))}$$

$$(5.18)$$

The gain for the total preamplifier at the carrier frequency of 5 KHz is 7000. Therefore, the unit is represented in the carrier loop by this gain only, since other frequencies are not of interest in the a.c. portion of the loop.

Null Signal Amplifier and Phase Shifter

The combination of the null signal amplifier and unity-gain phase

shifter takes the output of the power amplifier, modifies the gain and phase relationship and feeds the signal to the input of the preamplifier. At this point, the null signal is summed with the signals induced into the field coils until the signal is nulled. The signal now corresponds to the zero position of the armature probe.

The first stage of the null signal amplifier is an active filter amplifier consisting of operational amplifier A2 and associated circuitry. The second stage is an inverter with filtering. Both A2 and A3 are operational amplifiers type μA741 since d.c. drift is not of significance. The transfer function of the first stage is

$$\frac{E_o}{E_i}(s) = \frac{(1.8 \times 10^{-4})s}{(1 + s(2.71 \times 10^{-5}))(1 + s(1.6 \times 10^{-5}))} \tag{5.19}$$

The gain of this stage at the carrier frequency is 4.2. The transfer function of the second stage is

$$\frac{E_o}{E_i}(s) = \frac{10^{-3}s}{(1 + s(10^{-3}))(1 + s(10^{-5}))} \tag{5.20}$$

Some filtering takes place in the unity-gain phase shifter. Depending on the amplitude determined by potentiometer R31, a pole in the frequency response will occur between 320-440 Hz. For a maximum amplitude setting the transfer function of the combination of the null signal amplifier and the phase shifter is

$$\frac{E_o}{E_i}(s) = \frac{s^3(7.1 \times 10^{-11})}{(1 + s(2.71 \times 10^{-5}))(1 + s(1.6 \times 10^{-5}))(1 + s(10^{-3}))(1 + s(10^{-5}))} \times$$

$$\frac{1}{(1 + s(5.06 \times 10^{-4}))} \qquad (5.21)$$

Of course, the phase shift in the unity-gain phase shifter completes the final phase relationship. Potentiometer R36 is adjusted until the phase shift is increased to the desired value by the following relationship (see Appendix H)

$$\beta = \text{phase shift} = 2 \tan^{-1} \omega R36C15$$

$$= 2 \tan^{-1}(1.03 \times 10^{-4})R36 \qquad (5.22)$$

As previously mentioned, the emitter follower Q11 is used to prevent loading of R36 and to provide a low output impedance to the preamplifier. When establishing the desired null signal, the phase is first adjusted with R36 and then the amplitude is set with adjustment of R31.

Because of the feed forward path introduced with the injection of the null signal, a minor loop is introduced into the system. In order to keep this loop from interacting with the main carrier loop, the gain of this loop is kept below unity at the maximum amplitude setting of R31.

It should be noted that the experimental motor used had the armature probe displaced 15° from the perpendicular to the horizontal

plane. The null position was established at this point with the idea
in mind that the final motor transducer could be adjusted as a
complete unit.

Field Constant Current Supplies

The amount of torque developed in the motor for restoring the
armature probe to the null position is proportional to the armature
current for a constant flux generated in the field windings. Or,
for a constant flux in the armature coil, the torque is proportional
to the field current. Armature control is used in this system so
a constant d.c. current source is required for each coil. As mentioned
before, two supplies are used since the power supply voltages are to
be held to a minimum. The two supplies, hereafter referred to as No. 1
and No. 2 field supplies, are identical except for those characteristics
noted below.

The control loop of these units is Type 0 with a gain constant
K_p = 100. In order to have no loading effect on the induced signal
in the field coils, the impedance at the collector of the driver
transistors (Q14, Q17) must be infinite. To achieve the minimum
loading effect, the loop gain must be as high as possible at the
carrier frequency. The loop gain was designed to be 50 at 5 KHz. It
is obvious that without a high loop gain, the 10 ohm resistors R50
and R63 used to minimize transistor power dissipation, would load the
induced field signals. In addition, the field coil signals would be
subjected to large variations with coil resistive parameter change.

The coil resistance at 2000°F is six times the room temperature value.

Differential amplifiers A4 and A6 compare the output voltage across the 0.47 ohm resistors in their respective circuits to the reference voltage established by the current adjustment R38 or R51. The adjustment for the experimental model was set for a field coil current of 3.5 amperes. The differential gain of the amplifiers with a 2.7 kilohm load resistor is 25. The frequency response of this amplifier exceeds 150 KHz. Electrolytic capacitors C16 and C22 are used in the bias network to filter high frequency signals because only d.c. signals are desired at the reference. Resistor R112 and reference diode Z3 provide the necessary negative bias (-9 volt) for the WC115T in the No. 1 field current supply. Electrolytic capacitor C21 provides some necessary filtering of power supplies at this point. The negative bias (-39 volt) for the WC115T and the negative power supply for A7 (-45 volt) in the No. 2 field current supply is provided by an R-C filtered full-wave rectifier with reference diodes Z1 and Z2 establishing the desired voltages.

Two poles occur in the uncompensated loop frequency response at 35 KHz and 40 KHz due to the transistor capacitances and related resistance. Since higher frequency poles exist such as in the WC115T and due to the attenuation of the μA741, compensation is required for relative stability.

Operational amplifiers A5 and A7 are used as differential amplifiers and filters. The transfer function of this combination is

$$\frac{E_o}{E_i}(s) = \frac{8.9(1 + s(2.5 \times 10^{-6}))}{(1 + s(3.3 \times 10^{-5}))(1 + s(4.5 \times 10^{-8}))} \qquad (5.23)$$

The power supply voltages for A5 are ± 15 volts. It should be mentioned at this point that the µA741's do not require a common power supply lead while the P45AU and P65AU do. The power supply voltages for A7 are -15 volts and -45 volts.

The required compensation is completed with the series composite equalizer consisting of R44, R45, R46, C19, and C20 in the No. 1 field current supply and R57, R58, R59, C25, and C26 in the No. 2 field current supply. The input impedance of the cascaded emitter followers is approximately 18 kilohms. The transfer function of the loaded equalizer network is

$$\frac{E_o}{E_i}(s) = \frac{0.75(1 + s(6.72 \times 10^{-6}))(1 + s(3.8 \times 10^{-6}))}{(1 + s(4 \times 10^{-5}))(1 + s(8.5 \times 10^{-7}))} \qquad (5.24)$$

Since the resistance in the emitter of the power transistor is only 0.47 ohm to minimize power consumption, there is some attenuation of the signal for the cascaded emitter followers. For an input signal at the base of Q12 or Q15 with the output taken across the 0.47 ohm resistor the gain is 0.7.

The complete transfer function for this circuit is

$$\frac{E_o}{E_i}(s) = \frac{100(1 + s(2.5 \times 10^{-6}))(1 + s(6.72 \times 10^{-6}))(1 + s(3.8 \times 10^{-6}))}{(1 + s(3.3 \times 10^{-5}))(1 + s(4.5 \times 10^{-8}))(1 + s(4 \times 10^{-5}))} \times$$

$$\frac{1}{(1 + s(8.5 \times 10^{-7}))(1 + s(4.55 \times 10^{-6}))(1 + s(4 \times 10^{-6}))}$$

$$(5.25)$$

As previously stated, the gain at the carrier frequency is 50. Based on this value, the input impedance at the collector of the power transistors is approximately 1 kilohm. Therefore, for the maximum change in field coil series resistance, a 3% change will occur in the transducer signal. This was checked experimentally with the system in an open loop configuration. The elevated temperature was simulated by inserting resistance in series with the field coils. In the closed loop system, the maximum change under simulated elevated temperature conditions was found to be 0.1 ampere of armature current. This corresponds to a force applied to the system of 1.87×10^{-4} lb or approximately one-fourth of the minimum force to be measured.

Diode D1 is inserted in the No. 2 field current supply to prevent breakdown of A6 during turn-on. If the -30 volt supply is not energized at the same time as the -15 volt supply, the WC115T experiences a reverse voltage of 15 volts which destroys it. Diode D1 blocks the current flow in this direction.

The power dissipation of Q14 and Q17 is a major concern in this design. It was mentioned before that the 10 ohm resistors R50 and R63 are used to minimize the dissipation in these components. For no lead resistance to the field coil, the power dissipation of the components is 84 watts. Even with lead resistance of 2 ohms, the power dissipated is 65 watts, which equals the rated dissipation of the power transistors at room temperature considering a thermal resistance of case-to-air of 1.2 °C/watt. The power dissipation of the transistors had to be reduced to allow for ambient temperature variation. With

the existing design, the maximum power dissipated in the transistors never exceeds 31 watts. Heat sinks type NC-421 mounted in the vertical position were used in the breadboard. Dale type RH-50 20 ohm resistors were used in parallel. The maximum dissipation of these resistors is 56 watts for the combinations of two 20-ohm resistors. Thus, they operate at 50% of their commercial rating and at 90% of their military specification.

Ring Demodulator

The ring demodulator is a full-wave discriminator which produces a polarized d.c. voltage corresponding to the phase relationship of the signal from the preamplifier with respect to the reference signal on T3 and the amplitude of the input signal. The reference signal is approximately six times larger than the maximum closed loop signal of 1 volt rms. This is necessary for proper operation because the circuit will not work if the input signal exceeds one-half the reference signal.

Potentiometers R84 and R85 are adjusted to achieve both zero d.c. output for no input and a balanced full-wave output. The output impedance of the demodulator due to the arm impedance is approximately 4.7 kilohms.

A low pass filter (C40 and R88) is required to attenuate undesired harmonics. Since the secondary impedance of T1 and T2 is twice that of the primary impedance, and the output impedance is the same order of magnitude as the load, the transfer function of the complete ring demodulator is

$$\frac{E_o}{E_i}(s) = \frac{0.48}{1 + s(2.74 \times 10^{-3})} \qquad (5.26)$$

Experimental results indicate a transfer characteristic of 0.49 volts d.c./volt rms. The circuit is linear for input signals as large as 7.5 volts rms.

Compensating Amplifier

For system relative stability, the compensating amplifier provides the necessary lag and lead networks. A bandwidth of approximately 20 Hz is desired for the system and a gain constant of 90 is necessary. Since the armature has a mechanical resonance at 5.7 Hz, a simple lag network cannot be used. However, all criterion is met if a lag network is used before the resonance occurs in the frequency response and a lead network is used following the resonance at a point in frequency where the characteristics of the uncompensated response approach a second order system. Operational amplifier A12 and the related circuitry achieve this compensation. A Philbrick P65AU amplifier is used for A12 since d.c. drift is of utmost importance at this section of the system.

The transfer function of the compensating amplifier is

$$\frac{E_o}{E_i}(s) = \frac{2.3(1 + 0.176s)(1 + 0.0156s)}{(1 + 2.33s)(1 + s(2.71 \times 10^{-3}))} \qquad (5.27)$$

Limiter

The limiter, inserted between the compensating amplifier and the

power amplifier, is required for the system to be energized and achieve

proper operation. The function of the limiter is to limit the signal

input to the power amplifier so that the power amplifier does not

saturate. Since the carrier signal is injected at the input to the

power amplifier, it is imperative that the signal energizes the

armature coil for the signal to attain a return path. The limiter

serves this purpose in an economical and reliable manner.

Operational amplifier A13 is an Analog Devices Type AD118 chosen

because of its d.c. drift characteristics. Potentiometers R107 and

R108 are set for the negative and positive output limits respectively.

The approximate resistance of the potentiometers for these limits is

2.36 kilohms measured between output and wiper. The output voltage

magnitude is set at 0.93 volt. The gain of the amplifier for voltages

less than 0.81 volts is 1.115, while the gain for input signals exceeding

this is 0.01. The unit can be categorized as a soft limiter as opposed

to a hard limiter.

Experimental results yielded a gain of 1.110 for input signals

less than 0.81 volts. System turn-on is reliable with this innovation.

4. SYSTEM RESPONSE

The system is shown in Figure 36, which represents its functional

behavior as a feedback control system. The control circuit transfer

function is combined with the motor-transducer transfer equation for

the molybdenum-wire model shown in the redrawn block diagram of Figure 37.

The armature has a mechanical resonance at 5.7 Hz. The predicted resonant
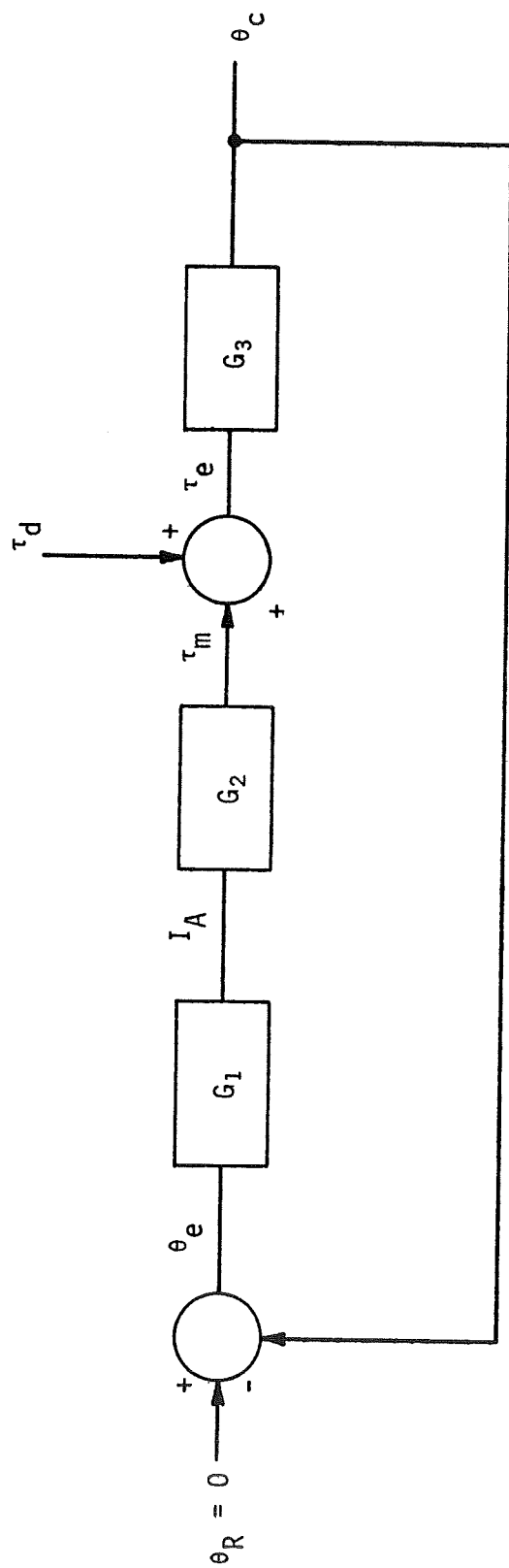
Figure 36. High Temperature System Block Diagram
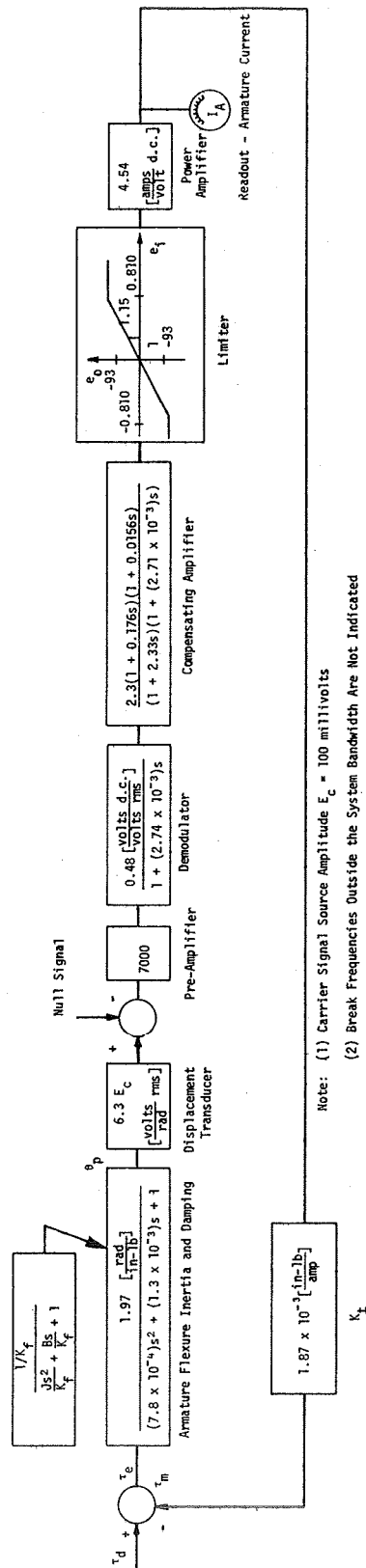
Figure 37. Block Diagram of High Temperature System Carrier Loop

frequency based on the design of the coil form was 6 Hz. A more accurate prediction cannot be made because both the mass change due to application of the ceramic encapsulation and the spring constant of the flexure cannot be better determined. The flexure spring constant was previously determined to be 0.51 lb-in/rad. The damping ratio was experimentally determined to be 0.023. The carrier source amplitude was set by R1 to be E_c = 100 millivolts. For this potentiometer setting, the system gain K_p = 90.

The frequency response for the molybdenum-wire model is shown in Figure 38. The crossover frequency is 30 Hz. The predicted crossover frequency of 25 Hz produces a phase margin of 25° and a M_m = 2.56. The theoretical closed loop frequency response of the molybdenum-wire model is shown in Figure 40. The passband is approximately 25 Hz. The experimentally determined crossover frequency indicates that the system will deviate only slightly from the nominal system design. The frequency response of the platinum-clad molybdenum-wire model is shown in Figure 39 for comparison purposes. The crossover frequency in this case f_c = 20 Hz because of the lower resonant frequency. Also of interest is the fact that the carrier amplitude E_c = 50 millivolts to achieve this frequency crossover. For the same system gain constant K_p = 90, the carrier amplitude E_c = 32 millivolts due to the flexure spring constant K_f = 0.4 lb-in/rad, the increased displacement transducer amplitude, and the increased motor torque constant which were noted earlier. However, the frequency response asymptotes are verified by both models.
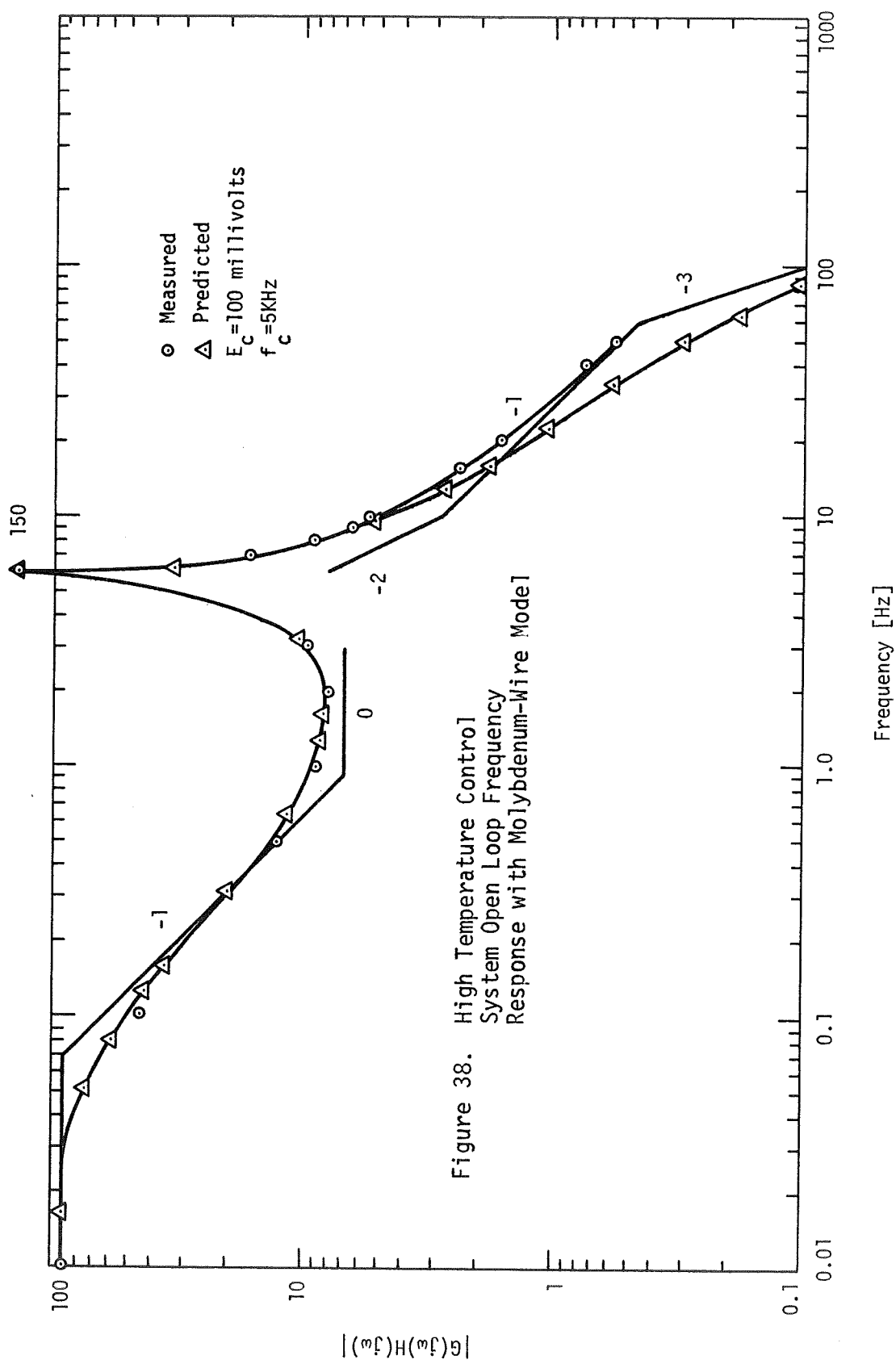
Figure 38. High Temperature Control System Open Loop Frequency Response with Molybdenum-Wire Model
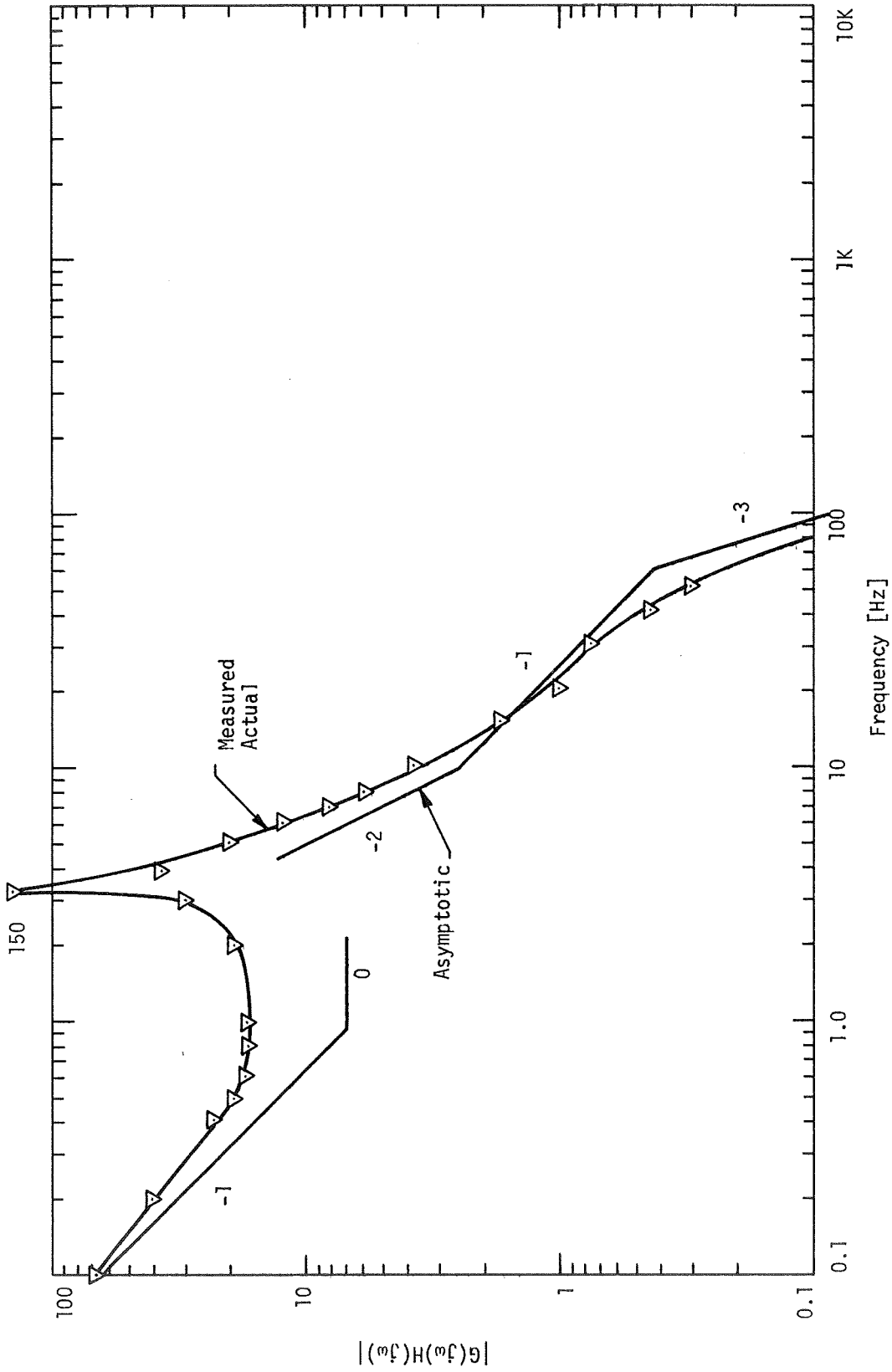
Figure 39. High Temperature Control System Open Loop Frequency Response
With Platinum-Clad Molybdenum-Wire Model

The system response was determined by opening the loop at the input to the power amplifier. The input was provided by a Wavetek Model 110 function generator. The output of the limiter and the input to the system were monitored both with a Clevite Brush Recorder Mark 280 and a Tektronix 561B oscilloscope.

The carrier loop gain is as follows:

$$\text{Loop Gain} = \frac{-K_p(1 + 0.176s)(1 + 0.0156s)}{(1 + 2.33s)(1 + (2.74 \times 10^{-3})s)^2[(7.8 \times 10^{-4})s^2 + (1.3 \times 10^{-3})s + 1]}$$

where

$$K_p = (1.97)(6.3E_c)(7000)(0.48)(2.3)(1.15)(6.56)(1.87 \times 10^{-3})$$

$$= 94 \text{ for } E_c = 100 \text{ millivolts} \tag{5.28}$$

It should be noted that if the motor calibration does not change over the temperature range 0-2000°F, the error in the armature current readout is determined by the system loop gain. Of course, the error varies inversely with the loop gain. For the experimental value of loop gain at 90 the readout error is 1.1%. The theoretical closed loop system frequency response is shown in Figure 40. The system $M_m = 2.56 = \left|\frac{C(jw)}{R(jw)}\right|_{max}$ occurs at the resonant frequency, ω_n, of 145 rad/sec.

The response of the system to a step unput yields the damping, the rise time, and the settling time where
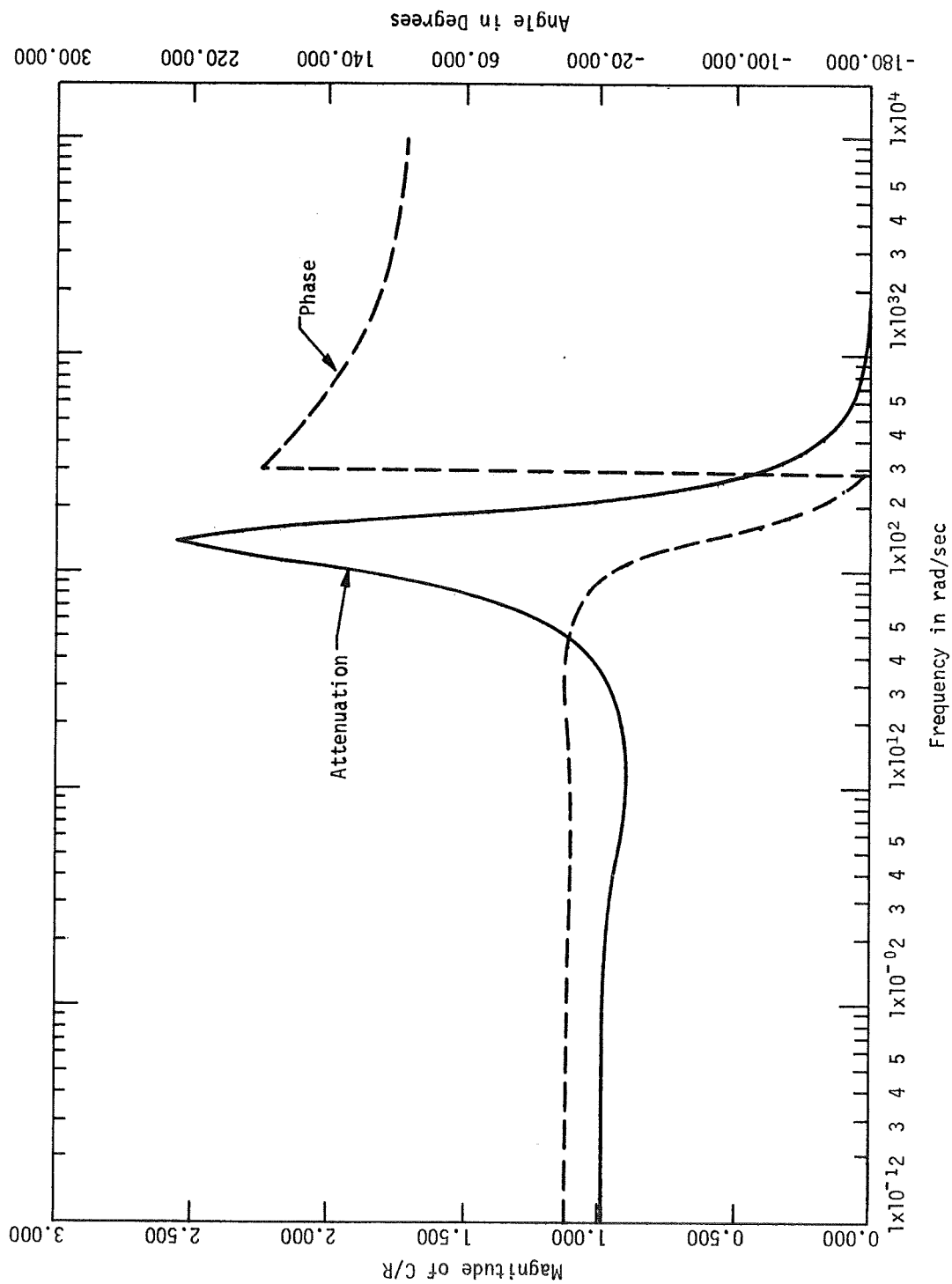
Figure 40. High Temperature Closed Loop Frequency Response With Molybdenum-Wire Model

t_r = rise time = the interval between the intersection of a line

tangent to c(t) at t = t_d and the intersection

of c(t) = 0 and c(t) = 1 (t_r = π/w_c = $1/2f_c$)

t_d = time delay = interval between the application of input step

and instant when response reaches 1/2 final

value [26].

t_s = settling time = time required for the output response first

to reach and thereafter remain within a

prescribed percentage of the final value.

Common values are 2 and 5 per cent [27].

The step response was obtained by perturbing the system with a square
wave low frequency signal injected at the summing point of A1 through
a 470 kilohm resistor. A Wavetek function generator Model 110 provided
the perturbing signal. As before, it is desirable to perturb the system
with a torque step input but a test apparatus was not available so
this method was used.

The transient response of the system to a step input is shown
in Figure 41. The input is to the power amplifier and the response
is taken at the output of the limiter. From Figure 41 the parameters
are

t_r = 11 msec

t_d = 5 msec

t_s = could not be determined with the prescribed accuracy -estimated

at 80 msec
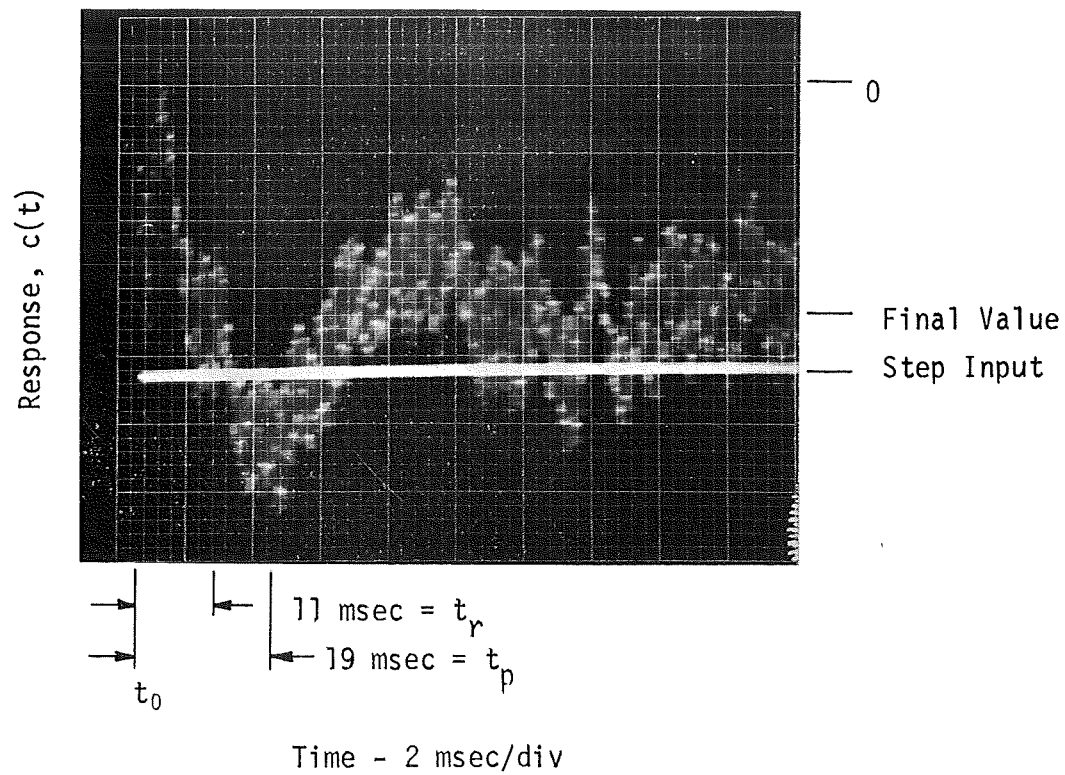
Figure 41. Transient Response of Molybdenum-Wire
Model Closed Loop System

M_p = 1.77 = the ratio of the peak overshoot to the step input.

t_p = 19 msec = time required to reach overshoot peak

The system is underdamped as is evidenced by the several overshoots shown in the transient response. Although the gain margin is 3.2, the phase margin is 25°. In this system, the gain margin specification can be misleading. The flexure torsional spring constant not only affects the gain of the system but is also the determining factor of the armature resonant frequency. If desired, either a lead network can be added for additional phase margin or the attenuation produced by the low pass filter of the ring demodulator could be modified. On the other hand, it should be noted that the system was stable throughout the laboratory testing.

The rise time of the system t_r = 11 msec corresponds to a crossover frequency of 29 Hz. The theoretical crossover frequency of 25 Hz and the experimental value of 30 Hz are verified by this measurement.

Investigation of the root-loci of the system indicates that the effective damping is 0.257. The natural resonant frequency, ω_n, is 145 rad/sec as indicated above. For K_p = 90, the closed loop system transfer function is

$$\frac{C}{R}(s) = \frac{1.86 \times 10^7 (s + 64.5)(s + 5.7)}{(s + 4.97)(s + 118)(s + 554)(s + 37.6 + j141)(s + 37.6 - j141)}$$

$$(5.29)$$

The system performance is determined by the pair of complex poles, and one real pole and zero because (1) the other pole is far to the left of the dominant poles, and (2) any pole which is not far to the left of the dominant poles is near a zero so the magnitude of the transient term due to that pole is small. Thus, the closed loop transfer function can be approximated by

$$\frac{C}{R}(s) \simeq \frac{3.71 \times 10^4 (s + 64.5)}{(s + 118)(s + 37.6 + j141)(s + 37.6 - j141)} \tag{5.30}$$

The theoretical response c(t) with a step input is defined by

$$c(t) \simeq 1 + 0.665\varepsilon^{-118t} + 1.68\varepsilon^{-37.6t} \sin(141t - 1.5)$$

and is shown by computer plot in Figure 42. From the solution of c(t) the following parameters are derived:

$$M_p = 1.82$$

$$t_s = 100 \text{ msec}$$

$$t_r = 10 \text{ msec}$$

$$t_p = 20.5 \text{ msec}$$

$$t_d = 6.5 \text{ msec}$$

Although no significant difference between the theoretical and measured parameters is observed, there exists a distinct difference between M_m and M_p. For a simple second order system in which $0.40 < \zeta < 0.707$
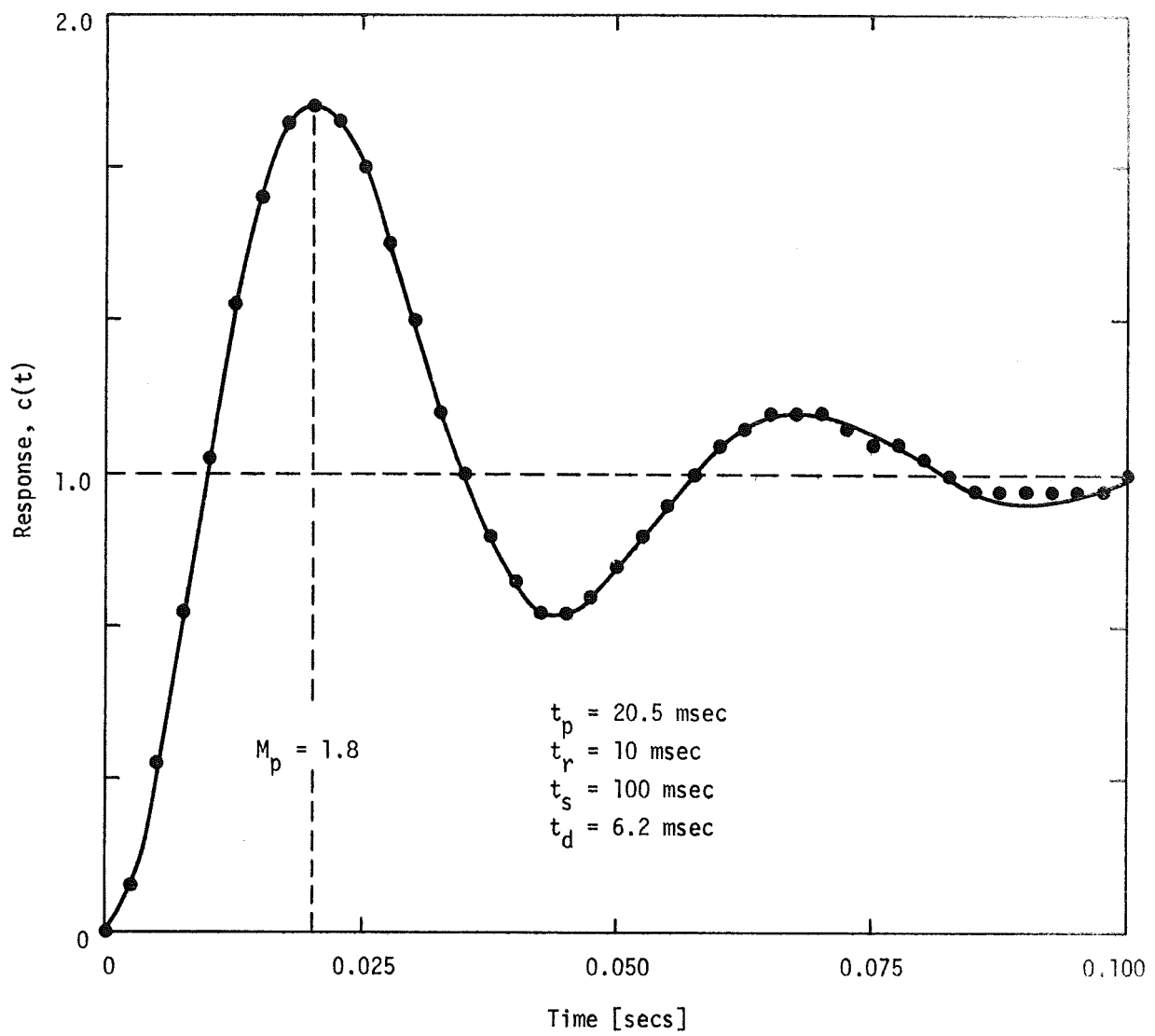
Figure 42. Predicted System Response to a Step Input

M_m and M_p differ by a maximum of 5%. However, even though this system behaves approximately as a second order system while it is, in fact, fifth order; it does not behave as a simple second order system. A comparison of this system to a simple second order system reveals that a simple second order system has only approximately 45% overshoot in the step response while this system has approximately 80% for the same effective damping. The time-to-peak overshoot is the same for the systems. It is $\omega_n t \simeq 3.0$.

It is apparent that the closed loop zero yields not only an exponential but also its derivative and increases the overshoot of the system.

The position error was determined experimentally by two methods. First, a 0.001 in diameter gold wire was attached to the end of the force balance. The balance was adjusted to make contact with the armature probe. The system was operating closed loop. A sighting was made on the wire with a Unitron MMU microscope with a KE 10 X mag micrometer. The wire was focused to a definite image and the maximum force was applied to the armature probe via the force balance. The system position change was optically determined to be 1.65×10^{-4} in. The flexure spring constant was also verified in this manner to insure reliability in the measurement. Another measurement was made with the Wayne Kerr capacitive displacement transducer and the position change was found to be 1.65×10^{-4} in. As shown in Eq. 5-1, the steady-state position error should be 0.15×10^{-3} radians for a displacement of the

probe of 0.15×10^{-3} in. The experimental values agree within 10%
of those predicted for steady-state position error at maximum force.

CHAPTER VI

HIGH TEMPERATURE DATA

The molybdenum-wire motor was subjected to an extreme temperature
environment of 1900°F while operating as an integral unit of the control
system described in the previous chapter. Data was recorded indicating

(1) The temperature rise of the motor coils (see Chapter II).

(2) The closed loop null as a function of temperature.

(3) Armature current as a function of applied torque, indicating
not only absolute values but also linearity as functions of
elevated temperatures.

I. PROCEDURE

The model was placed in an oven as described in Chapter II. A
hole was cut in the removable oven top to allow the sting of the torque
applicator to enter. The sting used for the high temperature measurements
was machined from alumunum silicate and the contact point was machined
from RA 330 stainless steel. The damping fluid of the high temperature
force balance is placed within an ice bath to maintain a constant
temperature throughout the temperature run. Displacement of the
armature probe is measured with a Wayne Kerr C probe. Since it appeared
in the beginning that the force balance was shifting or that elongation
of the contact point of the sting was taking place, the sting was only
applied to the armature probe when force was to be applied. In this

manner, null shift in the motor control system was measured as a change in armature current. The Wayne Kerr displacement measurement was used to determine the position error of the system at elevated temperatures with applied torque. Although the flexure of the force balance is not placed in the oven, it is, however, subjected to elevated temperatures produced both by thermal conduction and convection.

Therefore, the spring constant used in the force balance for high temperatures measurement, K_B, is 13.3 lb-in/radian. This ensures temperature independent operation of the force balance and allows sturdier construction. Based on the lever arm magnitudes of the force balance and the spring constant of the control system, $(K_p + 1)K_f \simeq 45$, error introduced by the large flexure spring constant is less than 2%.

2. RESULTS

Measurement of the data was done in the following manner at 200°F intervals:

(1) The armature current was recorded.

(2) The micrometer was adjusted until the sting point touched the probe. Weights were applied to the balance in increments of 200 milligrams and the corresponding armature current was recorded.

(3) The change in displacement measured with the displacement probe was noted with the maximum torque of 7×10^{-3} in-lb.

(4) The d.c. voltage across the coils was monitored. From this information, the maximum coil resistance at elevated temperatures and the maximum power dissipation were determined (Chapter II).

It should be noted that a high temperature simulation was performed on the electronics package of the control system at room temperature by placing resistance in series with the coils. This was performed before the unit was subjected to high temperatures. A resistance of 5 ohms was inserted in series with each of the coils. The closed loop system responded the same as shown in Figure 44 for the 0-600°F data. The null shift was less than 0.1 ampere of armature current. Therefore, any deviation from the calibration curve at elevated temperatures must be due to changes in the motor characteristics or wire oxidation.

In an attempt to prohibit stiction between the sting contact point and the armature probe, the force balance was perturbed with a speaker placed parallel to a circular plate attached to the balance arm. A frequency of 2 KHz was used.

The system null at elevated temperatures is shown in Figure 43. The armature current was monitored not only with a d.c. ammeter but also with a Hewlett-Packard 410C d.c. voltmeter across R24, 0.22 ohm sensing resistor in the power amplifier. A shift in the null position is not discernible from room temperature data to 600°F. The shift in null produces a maximum indication of force of 4.7×10^{-4} lb between 600° - 1180°F. The null shift due to the extreme temperature environment produces a readout equivalent to the minimum error to be measured, 7×10^{-4} lb, at 1250°F. The null shifts enough at 1560°F to indicate that the maximum measurable force of 7×10^{-3} lb is being applied to the system when, in fact, zero force is applied. The data
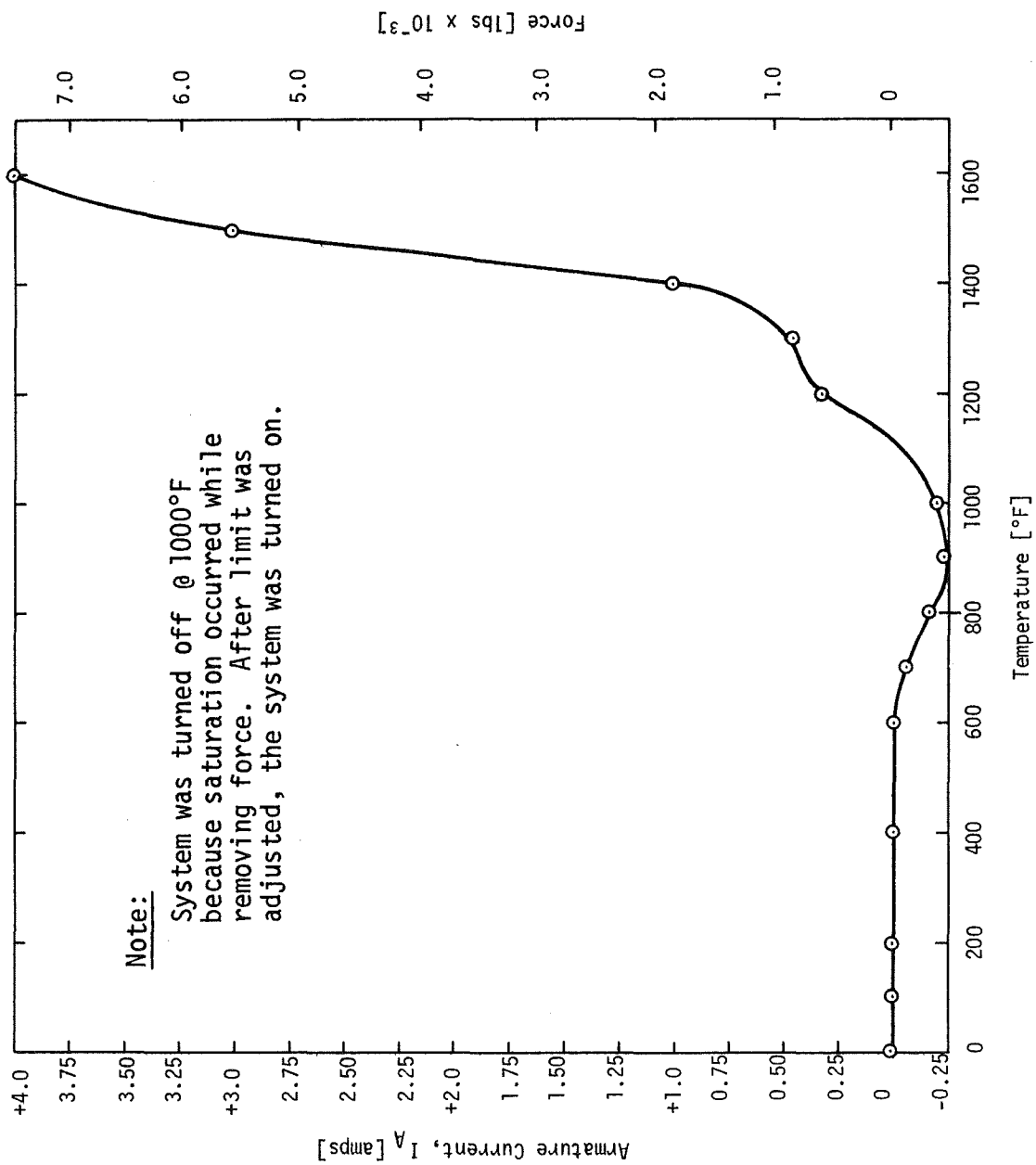
Figure 43. High Temperature System Closed Loop Null

for higher temperatures indicates that a deformation of the model is taking place. Although the flexure spring constant may have changed, it could not have changed more than approximately 30% or the system would have become unstable. Failure analysis of the model at the termination of the high temperature run revealed that the molybdenum wire had opened due to oxidation at points on the coils where air bubbles had been formed during the encapsulation process. The potting blistered at the bonding of the nichrome wire leads and the ceramic potting on the two field coils. Oxidation also occurred at three hairline cracks which had been observed on the armature coil at room temperature. It is apparent that field coil #2 started oxidizing before the other coils since the coil opened at 1870°F, whereas, 7.4 ohms was the measured resistance of field Coil #2 and 6.65 ohms was the armature resistance at the same temperature (these resistance values include lead resistance). Therefore, it seems feasible to conclude that the shift in the null was effected by the rapid oxidation of the molybdenum wire of field #2 with respect to the other motor coils. Of course, with platinum-clad molybdenum-wire and a complete potting of the exposed perimeters of the coils, the model can be used for higher temperature application. In performing the high temperature run, the system was deenergized at 1000°F when a saturation occurred while removing a weight from the balance. After adjustment of the limiter, the system was energized and the system returned to its state before this occurrence.

The linearity and stability of the motor with temperature are important. The readout, expressed as armature current, with respect to the applied force is shown in Figure 44. All data coincide for the temperature range 0-600°F. The points on the ordinate axis correspond to the null point shift with zero force applied to the system. The linearity of the calibration curve remains the same over the complete temperature range but is shifted due to the null range. No force was applied above 1400°F since the disturbance produced by placing and removing weights on the force balance would saturate the system. At 1870°F, there was no torquing action provided by the system due to oxidation of field #2.

The displacement of the armature probe was measured by a capacitance probe placed near the weight pan of the balance arm. The linearity of the displacement of the probe with respect to the metallic plate on the balance arm (used as a ground) is 98%.

The position of the armature probe never exceeded the position error specification of 5×10^{-4} in. The armature probe was displaced 2×10^{-4} in at 700°F and was found to reach 1.34×10^{-4} in for 800 mg weight which corresponds to 4.12×10^{-3} lb force at 1200°F. Extrapolating this data, it appears that a maximum displacement of the armature probe of 2.28×10^{-4} in occurs at this temperature. This is approximately a 20% increase in displacement and could be caused in part by a change in the flexure spring constant. However, it should be noted that some drift in displacement reading at the elevated temperatures was observed.
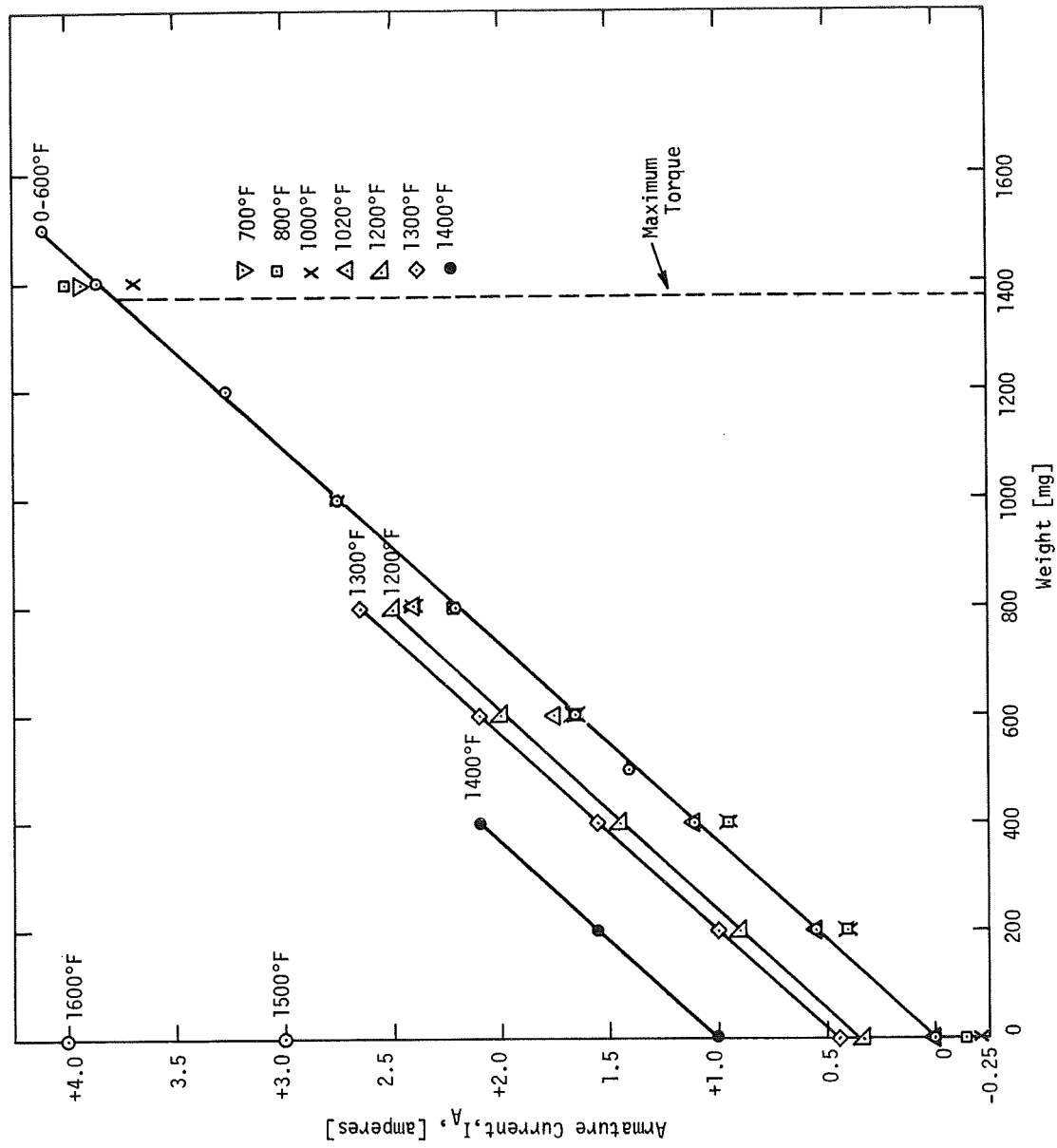
Figure 44. High Temperature System Calibration

Whether an elongation of the sting point when placed in contact with the armature probe occurred or a parameter change in the force balance due to weight loading produced the drift could not be determined. The drift is also noticeable in the system readout. Above 2.2 amperes of armature current, there is some drift from an initial reading when greater force is applied to the system. It is believed that one source contributing to the drift is the heating unbalance in the flexure supports. For instance, an initial reading of 2.2 amperes will become 2.34 amperes after 30 seconds and stabilize at this value. A reading of 3.75 amperes will drift to 4.0 amperes after approximately 30 seconds and stabilize. A solution to this problem, of course, is to increase the size of the flexure supports. They are presently not large enough for the required load and current.

The data indicates that the system performs well in the 0-600°F range with little system degradation up to 1250°F. It is concluded, therefore, that with the platinum-clad molybdenum wire model and the final control system configuration, the desired skin friction meter can be realized.

CHAPTER VII

CONCLUSIONS

Experimental results demonstrate the feasibility of designing a closed loop system to measure skin friction which is capable of operating in temperatures up to 2000°F. Although the meter cannot be subjected to severe vibrations because it has not been counter-balanced, it is capable of operating in more benign environments such as wind tunnel applications.

High temperature data on the skin friction meter indicates satisfactory operation to 1000°F with relatively good operation to 1400°F. Although the oxidation of the molybdenum wire introduced considerable error above that temperature, experimental data of the platinum-clad molybdenum-wire model subjected to 2000°F indicates no oxidation problem. It is concluded, therefore, that the skin friction meter is capable of 2000°F operation.

The final configuration meets all of the desired specifications. The bandwidth of the system is approximately 25 Hz. Therefore, the system has a relatively fast response to input forces. System rise time is 10 milliseconds and settling time is 100 milliseconds.

It is recommended that the flexure supports be designed with more strength in the members and that the members be as symmetrical as possible to eliminate Joule heating unbalance. Encapsulation of the exterior periphery of the completed model is suggested once the final adjustments have been made on the coil orientation.

BIBLIOGRAPHY

1. Seemuller, William W., "The Design of a Skin Friction Meter for Use in Extreme Environmental Conditions", Master's Thesis, The University of Virginia, Charlottesville, August 1966, pp. 1-7, 100, 49, 51.

2. Seemuller, McVey, Moore, Ramey, "Skin Friction Meter", Second IFAC Symposium Proceedings, Vienna, Austria, September 1967 (with J. W. Moore, W. Seemuller, R. Ramey).

3. Schilbe, Andrew Ludwig, "Design and Evaluation of a Gas Bearing Support for a Skin Friction Meter", Master's Thesis, University of Virginia, Charlottesville, June, 1969, pp. 1-3.

4. Lu, Chang-Shi, "A Pneumatic Control System For a High Temperature Skin Friction Sensor", Dissertation for Doctor of Science, University of Virginia, Charlottesville, November, 1970, pp. 1-4.

5. Ashby, Richard G., "The Counterbalancing of Accelerations in a Skin Friction Meter", Master's Thesis, The University of Virginia, Charlottesville, August, 1968, p. 4.

6. "A Force Balance System for the Measurement of Skin Friction Drag Force in the Presence of Large Vibrations and Temperatures," Interim Technical Report, NASA Grant NGR 47-005-026, The University of Virginia, Charlottesville, September, 1969, p. 6.

7. E. S. McVey and J. W. Moore, "A Skin Friction Balance," Proceedings of the Second Electrical and Electronics Measurement and Test Instrumentation Conference, Ottawa, Canada, January, 1967.

8. American Lava Corporation, Bulletin No. 656, Chattanooga, Tennessee.

9. American Lava Corporation, Bulletin No. 675, Chattanooga, Tennessee.

10. Mikol, Thermal Conductivity of Molybdenum Over Temperature Range 1000-2100°F, p. 1.

11. Kubaschewski, O. and Hopkins, B. E., "Oxidation Mechanisms of Niobium," "Tantalum, Molybdenum, and Tungsten," Journal of Less-Common Metals, 1960, p. 173-174.

12. "Platinum, the Metal, its Properties and Applications", International Nickel Company, Inc., 1968, pp. 4-5.

13. Beidler, E. A. , Powell, C. F., Campbell, I. E., Tema, L. F., "The Formation of Molybdenum Disilicide Coatings on Molybdenum", Journal of Electro-Chemical Society, 1951, p. 21.

14. "Coated-Molybdenum Parts Good For 3400 F" Machine Design, 12 June 1969 (General Electric Company).

15. Hill, J. S. and Albert, H. J., "Loss of Weight of PLatinum, Phodium and Palladium at High Temperatures", Englehard Ind. Tech. Bulletin, 1963, 4, 2, pp. 59-60.

16. Rhys, D. W., "The Use of Platinum For Protecting Molybdenum Against Oxidation at High Temperatures," paper given at the symposium on glass meeting held by the Union Scientifique Continentale du Verre, Brussels, October, 1958.

17. Deak, M., "A New Method of Suppressing Thermonic Emission From the Grids of Transmitting Tubes", Brown Boveri Review, 1961, 48, (7) p. 339.

18. Batelle Memorial Institute, WADC Technical Report 54-371, June, 1954.

19. Passmore, E. M., Boyd, J. E., and Lemero, B. S., "Investigation of Diffusion Barriers for Refractory Metals, ASDTOR 62-432, July, 1962.

20. E. H. Girard, et. al., "Study of Ductile Coatings For the Oxidation Protection of Columbium and Molybdenum Alloys", May, 1966, p. 20.

21. Aremco Data Instructions, "Ceramabond 503 . . . High Temperature Ceramic Adhesive", Aremco Corporation.

22. D. Halliday and R. Resnick, Physics for Students of Science and Engineering, January, 1961, pp. 696-697, 733.

23. Bendix Corporation Publ. No. 19U-6-661A, "Technical Information For Bendix Free Flex Pivots", Utica Division, p. 5.

24. Dwight, H., Electrical Coils and Conductors, 1945, p. 266.

25. J. Gibson and F. Tuteur, Control System Components, pp. 261-265.

26. J. Bower and P. Shulteiss, Introduction to the Design of Servo-mechanisms, February, 1964, pp. 231-232.

27. J. D'Azzo and C. Houpis, Feedback Control System Analysis and Synthesis, 1966, p. 84.

APPENDIX A

Properties of Fired and Unfired Lava[1]

I. Properties of Unfired Lava	
Type	Grade A – Hydrous Aluminum Silicate
Density	0.098 lbs/cu in
Color	Gray
Hardness	1 – 2 MOH's Scale
Shrinkage Factor	0.980
	Material Grows, 0.980 inch unfired will be 1.000 inch fired
II. Properties of Fired Lava	
Density	0.083 lbs/cu in
Water Absorption	2 – 3%
Color	Pink
Softening Temperature	1600°C 2912°F
Resistance to Heat (Safe Limit of Constant Temperature)	1100°C
Hardness	6 MOH's Scale
Linear Coefficient 25 – 100°C	2.9×10^{-6} per °C
of Thermal 25 – 600°C	3.4×10^{-6}
Expansion 25 – 900°C	3.6×10^{-6}
Flexural Strength	9000 lbs/sq in
Dielectric Strength	80 volts/mil
Volume 25°C 77°F	$> 10^{-4}$ ohms/cm^3

II. Properties of Fired Lava continued

Resistivity	100°C	212°F	6×10^{11} ohms/cm^3
at Various	300°C	572°F	2×10^9
Temperatures	500°C	932°F	5×10^6
	700°C	1292°F	3.5×10^5
	900°C	1652°F	5×10^4
Dielectric Constant	1 MHz	25°C	5.3
Dissipation Factor	1 MHz	25°C	0.010
Loss Factor	1 MHz	25°C	0.053

Bibliography

1. American Lava Corporation, Bulletin No. 656, Chattanooga, Tennessee.

APPENDIX B

INSULATION: CONDUCTOR THICKNESS RATIO

For a given area, the thickness of insulation and conductor relative

to each other for minimum power dissipation are to be determined.

Given: A coil of rectangular cross section of winding

Conductor

$t_w + t_i$
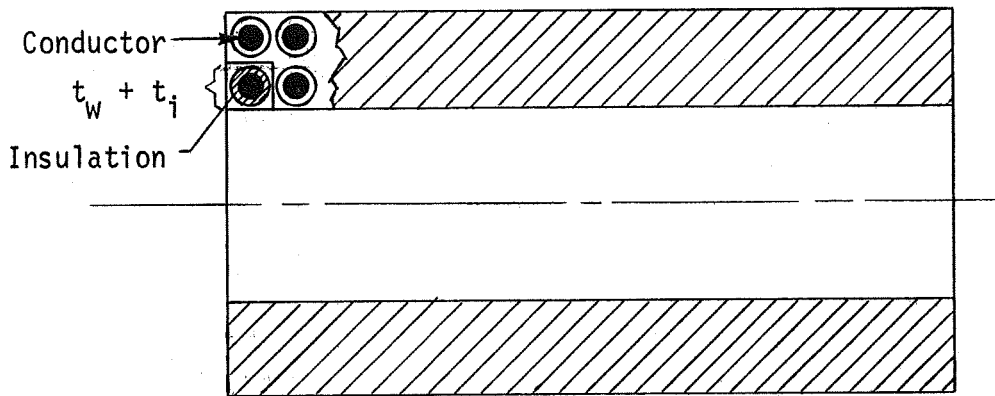
Insulation

where

t_i = thickness of insulation

t_w = thickness of wire

I = current required flowing through a bare conductor of square
cross section

I_a = actual current required to flow through insulated conductor

A_c = cross sectional area

N = total number of turns in area

R_i = no. rows of insulated conductor

135

$$A_c = [(t_w + t_i)\frac{N}{R_i}][R_i(t_w + t_i)] = (t_w + t_i)^2 N$$

$$N = \frac{A_c}{(t_w + t_i)^2}$$

$$I = \frac{(NI)}{N} = \frac{(NI)}{A_c}(t_w + t_i)^2$$

However, the actual current now required is

$$I_a = \frac{I(t_w + t_i)^2}{\frac{\pi}{4}(t_w)^2} = \frac{4}{\pi} I \frac{(t_w + t_i)^2}{t_w^2}$$

Note that as $t_w \to \infty$, $I_a = \frac{4}{\pi} I$

Therefore,

$$I_a = \frac{4}{\pi} I (\frac{t_w + t_i}{t_w^2})^2 = \frac{4}{\pi} \frac{(NI)}{A_c} \frac{(t_w + t_i)^4}{t_w^2}$$

To find the minimum current required:

$$\frac{dI_a}{dt_w} = \frac{t_w^2[4(t_w + t_i)^3] - (t_w + t_i)^4 2t_w}{t_w^4} = 0$$

$$\therefore \quad 2t_w = t_w + t_i$$

or $t_w = t_i$

Thus

$$\frac{t_w}{t_i} = 1 \text{ for minimum power dissipation}$$

Note that the resistance of the total length of the conductor does not change for a bare conductor of with a conductor insulated per the above ratio.

APPENDIX C

COIL POTTING - CERAMABOND 503

CURE SCHEDULE

TEMPERATURE	TIME
AMBIENT (75 ± 5°F)	3 hours
110°F	2 hours
150°F	16 hours
200°F	2 hours
225°F	2 hours
250°F	1 hour

Leave in oven; let oven cool to room temperature.

NOTE: Because of the thickness of the Ceramabond 503 applied to the coils, it is applied as three (3) coats, with the ambient temperature and 110°F portions of the cure cycle being applied between coats and after the final coat.

APPENDIX D

PROPERTIES OF HAYNES ALLOY NO. 25[1]

Haynes Alloy No. 25 is a cobalt-base alloy which has high strength and good oxidation resistance at temperatures up to 1800°F. This alloy can be formed, machined and welded by conventional methods.

Approximate Chemical Compositions, Per Cent		
Nickel	–	10
Cobalt	–	Balance
Chromium	–	20
Tungsten	–	15
Iron .	–	3
Carbon	–	0.10
Others	–	3

PHYSICAL PROPERTIES		
Density	25°C	0.330 lb/ cu in
Melting Range		2423-2570°F
Electrical Resistivity	25°C	34.9 microhm/in

Mean Coefficient Of Thermal Expansion	70-200°F	6.8 microinches/in-°F
	70-400	7.2
	70-600	7.6
	70-800	7.8
	70-1000	8.0
	70-1200	8.2
	70-1400	8.6
	70-1500	-
	70-1600	9.1
	70-1800	9.4
Thermal Conductivity	200°F	74 BTU-in/ft^2-hr-°F
	400	89
	600	104
	800	119
	1000	134
	1200	159
	1400	164
	1500	172
	1600	179
	1700	191
Specific Heat		0.092 BTU/lb-°F

Bibliography

1. "Haynes and Hastelloy Alloys", Union Carbide Corporation, 1962, pp. 2-7.

FLUX DENSITY FOR A GENERAL POINT DUE TO A SQUARE CURRENT LOOP[1]

Referring to Figure I and employing equation 2.4, the magnetic flux density at P_0 due to wire MN is:

$$B_{MN} = \frac{\mu_o i}{4\pi \sqrt{(R+x)^2 + z^2}} \left| \left[\frac{R-y}{\sqrt{((R+x)^2 + z^2) + \lambda^2}} \right] \frac{\lambda}{- (R+y)} \right.$$

$$= \frac{\mu_o i}{4\pi \sqrt{(R+x)^2 + z^2}} \left[\frac{R-y}{\sqrt{(R+x)^2 + (R-y)^2 + z^2}} + \right.$$

$$\left. \frac{R+y}{\sqrt{(R+x)^2 + (R+y)^2 + z^2}} \right]$$

B_{MN} is perpendicular to the plane formed by MP_0N and to the line P_0M'. Plane P_0xym' is perpendicular to plane MP_0N. Thus, B_{MN} lies in plane P_0xym'. If we resolve B_{MN} into two components, one, $B_{MN_{11}}$, along the line perpendicular to MUAL plane and another, $B_{MN\perp}$ at parallel to the MNAC plane. Only $B_{MN_{11}}$ will contribute to total induction at point P_0 since the components of B_{11} for all current elements lie on the x, yP_0 axis and add directly; whereas those of $B_\perp$ will cancel.

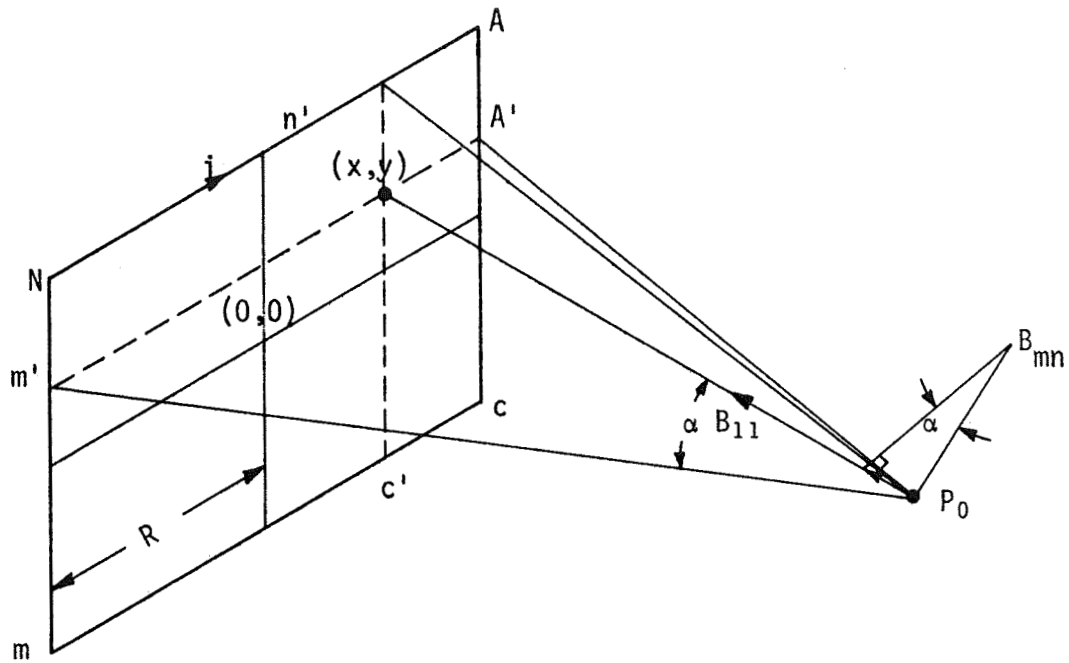If α is the angle between $\vec{x, yP_0}$ and $\vec{P_0M'}$, then $B_{MN_{11}}$ can be expressed as

Figure 1. Square Current Loop

$$B_{MN_{11}} = B_{MN}\sin\alpha = B_{MN}\left[\frac{R + x}{\sqrt{(R + x)^2 + z^2}}\right]$$

$$= \left[\frac{R + x}{\sqrt{(R + x)^2 + z^2}}\right]\left[\frac{\mu_o i}{4\pi \sqrt{(R + x)^2 + z^2}}\right] \times$$

$$\left[\frac{R - y}{\sqrt{(R + x)^2 + (R - y)^2 + z^2}} + \frac{R + y}{\sqrt{(R + x)^2 + (R + y)^2 + z^2}}\right]$$

In a similar manner, the flux density for the other elements is determined and

$$B_{11}(x, y, z, r) =$$

$$\frac{\mu_o i}{4\pi}\left\{\left[\frac{R - y}{z^2 + (R - y)^2}\right]\left[\frac{R - x}{\sqrt{(R - x)^2 + (R - y)^2 + z^2}} + \frac{R + x}{\sqrt{z^2 + (R + x)^2 + (R - y)^2}}\right] + \right.$$

$$\left[\frac{R - x}{z^2 + (R - x)^2}\right]\left[\frac{R - y}{\sqrt{z^2 + (R - x)^2 + (R - y)^2}} + \frac{R + y}{\sqrt{z^2 + (R - x)^2 + (R + y)^2}}\right] +$$

$$\left[\frac{R + x}{z^2 + (R + x)^2}\right]\left[\frac{R - y}{\sqrt{z^2 + (R + x)^2 + (R - y)^2}} + \frac{R + y}{\sqrt{z^2 + (R + x)^2 + (R + y)^2}}\right] +$$

$$\left[\frac{R + y}{z^2 + (R + y)^2}\right]\left[\frac{R - x}{\sqrt{z^2 + (R + y)^2 + (R - x)^2}} + \frac{R + x}{\sqrt{z^2 + (R + y)^2 + (R + y)^2}}\right]\right\}$$

$$B_{11}'(x, y, z, R) = \frac{4\pi}{\mu_o i} B_{11}(x, y, z, R)$$

Bibliography

1. Seemuller, William W., "The Design of a Skin Friction Meter for Use in Extreme Environmental Conditions," Master's Thesis, The University of Virginia, Charlottesville, August, 1966, p. 109.

APPENDIX F

MOTOR TORQUE COMPUTER PROGRAMS

The computer programs used to determine the motor torque constants
for all three models examined are shown below. The programs are written
in Algol and the computer used is the Burroughs B5500.

First, the flux density is computed using Eq. 2.6 and employing
a procedural determination by Simpson's Rule. Then, the required armature
current to produce the necessary restoring torque for a given field
current is computed. All three of these parameters, in addition to
the dimensions of each model, are displayed on the printout. This
process is done for a limited number of torque values since the equation
relationship is linear.

The program immediately following is used for the aluminum-wire
model which was wound bifilarly. The second program is for the finalized
high temperature molybdenum models. Both the molybdenum and platinum-
clad molybdenum-wire model torque constants were determined by this
program. The only difference between the two programs is the spacing
factor used in the flux density computation.

Some condensed output is shown with each program. For the aluminum-
wire model, 2.56 amps is required to produce the maximum torque with a
field current of 2 amps. The molybdenum-wire model requires 3.61 amps
while the platinum-clad molybdenum-wire model requires 2.86 amps for
a field current of 3.5 amps to provide the maximum torque.

144

145

02:46 AM   AUG, 08, 1969   *****************   DAVID A. KETTLER RLES

```
BEGIN
    FORMAT IN FIN(8(F6.3,X2));
    FORMAT OUT FOUT1(X2,E10.2,X6,E10.2,X6,I1));
    REAL  X,Y,Z,W,R,RR,INT1,INT2,BYD,D,L,L1,L2,TORQUE,NA,B11,A,R1,
      IA,DIA;
    INTEGER  I,J;
    REAL ARRAY DATA[0:6,0:11],DATUM[0:6];
    REAL PROCEDURE SIMPS(X,X1,X2,DELTA,F);VALUE X1,X2,DELTA;REAL X,X1,X2,DEL
    TA,F;BEGIN BOOLEAN TURNING;LABEL BOX,BOX2;REAL Z1,Z2,Z3,H,K;TURNING+FALS
    E;IF X1=X2 THEN BEGIN Z1+0;GO TO BOX2 END;IF X1>X2 THEN BEGIN H+X1;X1+X2
    ;X2+H;TURNING+TRUE;END;X+X1;Z1+F;X+X2;Z3+Z1+F;K+X2-X1;POX;Z2+0;H+K/2;
    FOR X+X1+H STEP K UNTIL X2 DO Z2+Z2+F;Z1+Z1+4*Z2;IF  H*ABS((Z1-2*Z3)/(IF
    Z1=0THEN 1.0ELSE Z1))<DELTA THEN GO TO BOX2 ELSE Z3+Z1;Z1+Z1-2*Z2;K+H;GO
    TO BOX;BOX2:IF TURNING THEN H+=H;SIMPS+H*Z1/3END;
    READ(CR,FIN,L,R1,D,W,RR,DIA,A,NA);
    DIA+DIA/39.37;
    A+A/(39.37*2);
          L1+=(L/2=W);
          L2+W=D/2;
          INT1+1/(0.65*2)*SIMPS(X,0,0.65,0=4,SIMPS(Y,0,0.65,0=4,
          SIMPS(R,R1 ,RR,0=4,SIMPS(Z,   L1,   L2,0=4,((R=X)/SQRT(
          Z*2+(R=Y)*2+(R=X)*2)+(R+X)/SQRT(Z*2+(R=Y)*2+(R+X)*2))*(
          R=Y)/(Z*2+(R=Y)*2)
          +((R=Y)/SQRT(Z*2+(R=X)*2+(R=Y)*2)+(R+Y)/SQRT(Z*2+(R=X)*2+
          (R+Y)*2))*(R=X)/(Z*2+(R=X)*2)+
          ((R=Y)/SQRT(Z*2+(R+X)*2+(R=Y)*2)+(R+Y)/SQRT(Z*2+(R+X)*2+
          (R+Y)*2))*(R+X)/(Z*2+(R+X)*2)+
          ((R=X)/SQRT(Z*2+(R+Y)*2+(R=X)*2)+(R+X)/SQRT(Z*2+(R+Y)*2+
          (R+X)*2))*(R+Y)/(Z*2+(R+Y)*2)))));
          L1+W+D/2;
          L2+W+L/2;
          INT2+1/(0.65*2)*SIMPS(X,0,0.65,0=4,SIMPS(Y,0,0.65,0=4,
          SIMPS(R,R1 ,RR,0=4,SIMPS(Z,   L1,   L2,0=4,((R=X)/SQRT(
          Z*2+(R=Y)*2+(R=X)*2)+(R+X)/SQRT(Z*2+(R=Y)*2+(R+X)*2))*(
          R=Y)/(Z*2+(R=Y)*2)
          +((R=Y)/SQRT(Z*2+(R=X)*2+(R=Y)*2)+(R+Y)/SQRT(Z*2+(R=X)*2+
          (R+Y)*2))*(R=X)/(Z*2+(R=X)*2)+
          ((R=Y)/SQRT(Z*2+(R+X)*2+(R=Y)*2)+(R+Y)/SQRT(Z*2+(R+X)*2+
          (R+Y)*2))*(R+X)/(Z*2+(R+X)*2)+
          ((R=X)/SQRT(Z*2+(R+Y)*2+(R=X)*2)+(R+X)/SQRT(Z*2+(R+Y)*2+
          (R+X)*2))*(R+Y)/(Z*2+(R+Y)*2)))));
          BYD+(INT1+INT2)/39.37;
    I+1;    J+1;
    FOR I+1 STEP 1 UNTIL 5 DO
    BEGIN
        B11+1E-7*I*BYD/(2*(DIA*2));
        DATUM[I]+B11;
        FOR J+1 STEP 1 UNTIL 10 DO
        BEGIN
            TORQUE+80=5*J;
            IA+TORQUE/(NA*A*B11));
            DATA[I,J]+IA;
        END;
    END;
    WRITE(LP,<"THE TOTAL MOTOR LENGTH IS",F6.3,X1,"INCHES">,L);

    WRITE(LP,<"THE RADIUS OF THE FIELD COILS IS",F6.3,"INCHES">,R1);
    WRITE(LP,<"THE FLEXURE GAP BETWEEN FIELD COIL WINDINGS IS",
      F6.3,"INCHES">,D);
    WRITE(LP,<"DISTANCE FROM CENTER OF FIELD COIL TO POINT OF",X1,
      "AVERAGE FLUX DENSITY IS",F6.3,"INCHES">,W);
    WRITE(LP,<"FIELD COIL RADIUS+WINDING THICKNESS IS",F6.3,"INCHES">,
      RR);
    WRITE(LP,<"WIRE DIAMETER IS",F6.3,"INCHES">,DIA*39.37);
    WRITE(LP,<"ARMATURE FACE AREA IS",F6.3,"INCHES">,A*39.37*2);
    WRITE(LP,<"# OF WIRE TURNS ON ARMATURE IS",F6.3>,NA);
    WRITE(LP[DBL]);
    WRITE(LP,<"FLUX DENSITY",X3,"ARMATURE CURRENT",X2,"FIELD CURRENT">)
    ;
    FOR I+1 STEP 1 UNTIL 5 DO BEGIN
    WRITE(LP[DBL]);
    FOR J+1 STEP 1 UNTIL 10 DO BEGIN
    WRITE(LP,FOUT1,DATUM[I],DATA[I,J],I);
    IF J=10 THEN WRITE(LP,<"AN ARMATURE CURRENT OF",F5.2,"AMPERES",X1,
      "WILL PRODUCE THE MAXIMUM TORQUE WITH A FIELD CURRENT OF",
      I2,"AMPERES">,DATA[I,10],I);
    END; END;
    WRITE(LP[DBL]);    WRITE(LP[DBL]);
    WRITE(LP,<"THE PROCESSOR TIME IS",F10.4,"SECONDS">,TIME(2)/60);
END.
```

THE TOTAL MOTOR LENGTH IS 2.060 INCHES
THE RADIUS OF THE FIELD COILS IS 1.060INCHES
THE FLEXURE GAP BETWEEN FIELD COIL WINDINGS IS 0.400INCHES
DISTANCE FROM CENTER OF FIELD COIL TO POINT OF AVERAGE FLUX DENSITY IS 0.730INCHES
FIELD COIL RADIUS+WINDING THICKNESS IS 1.260INCHES
WIRE DIAMETER IS 0.032INCHES
ARMATURE FACE AREA IS 1.780INCHES
OF WIRE TURNS ON ARMATURE IS64.000

FLUX DENSITY   ARMATURE CURRENT   FIELD CURRENT
   4.25@-03   2.56@+00   2
AN ARMATURE CURRENT OF 2.56AMPERES WILL PRODUCE THE MAXIMUM TORQUE WITH A FIELD CURRENT OF 2AMPERES

   6.37@-03   1.71@+00   3
AN ARMATURE CURRENT OF 1.71AMPERES WILL PRODUCE THE MAXIMUM TORQUE WITH A FIELD CURRENT OF 3AMPERES

   8.50@-03   1.28@+00   4
AN ARMATURE CURRENT OF 1.28AMPFRES WILL PRODUCE THE MAXIMUM TORQUE WITH A FIELD CURRENT OF 4AMPERES

```
   10:07  PM      AUG, 07, 1969    ****************    DAVID A. KETTLER RLES
BEGIN
      FORMAT IN FIN(8(F6.3,X2)));
      FORMAT OUT FOUT1(X2,E10.2,X6,E10.2,X6,I));
      REAL   X,Y,Z,W,R,RR,INT1,INT2,BYD,D,L,L1,L2,TORQUE,NA,B11,A,R1,
             IA,DIA;
      INTEGER  I,J;
      REAL ARRAY DATA[0:6,0:11],DATUM[0:6];
REAL PROCEDURE SIMPS(X,X1,X2,DELTA,F));VALUE X1,X2,DELTA;REAL X,X1,X2,DEL
TA,F;BEGIN BOOLEAN TURNING;LABEL BOX,BOX2;REAL Z1,Z2,Z3,H,K;TURNING+FALS
E;IF X1=X2 THEN BEGIN Z1+0;GO TO BOX2 END;IF X1>X2 THEN BEGIN H+X;X1+X2
;X2+H;TURNING+TRUE;END;X+X1;Z1+F;X+X2;Z3+Z1+F;K+X2=X1;BOX;Z2+0;H+K/2;
FUR X+X1+H STEP K UNTIL X2 DO  Z2+Z2+F;Z1+Z1+4xZ2;IF HxABS((Z1=2xZ3)/(IF
Z1=0THEN 1.0ELSE Z1))<DELTA THEN GO TO BOX2 ELSE Z3+Z1;Z1+Z1=2xZ2;K+H;GO
TO BOX;BOX2;IF TURNING THEN H+=H;SIMPS+HxZ1/3END;
      READ(CR,FIN,L,R1,D,W,RR,DIA,A,NA);
      DIA+DIA/39.37;
      A+A/(39.37*2);
              L1+=(L/2=W);
              L2+W=D/2;
              INT1+1/(0.65*2)xSIMPS(X,0,0.65,0=4,SIMPS(Y,0,0.65,0=4,
              SIMPS(R,R1 ,RR,0=4,SIMPS(Z,   L1,   L2,0=4,((R=X)/SQRT(
              Z*2+(R=Y)*2+(R=X)*2)+(R+X)/SQRT(Z*2+(R=Y)*2+(R+X)*2))x(
              R=Y)/(Z*2+(R=Y)*2)
              +((R=Y)/SQRT(Z*2+(R=X)*2+(R=Y)*2)+(R+Y)/SQRT(Z*2+(R=X)*2+
              (R+Y)*2))x(R=X)/(Z*2+(R=X)*2)+
              ((R=Y)/SQRT(Z*2+(R+X)*2+(R=Y)*2)+(R+Y)/SQRT(Z*2+(R+X)*2+
              (R+Y)*2))x(R+X)/(Z*2+(R+X)*2)+
              ((R=X)/SQRT(Z*2+(R+Y)*2+(R=X)*2)+(R+X)/SQRT(Z*2+(R+Y)*2+
              (R+X)*2))x(R+Y)/(Z*2+(R+Y)*2)))));
              L1+W+D/2;
              L2+W+L/2;
              INT2+1/(0.65*2)xSIMPS(X,0,0.65,0=4,SIMPS(Y,0,0.65,0=4,
              SIMPS(R,R1 ,RR,0=4,SIMPS(Z,   L1,   L2,0=4,((R=X)/SQRT(
              Z*2+(R=Y)*2+(R=X)*2)+(R+X)/SQRT(Z*2+(R=Y)*2+(R+X)*2))x(
              R=Y)/(Z*2+(R=Y)*2)
              +((R=Y)/SQRT(Z*2+(R=X)*2+(R=Y)*2)+(R+Y)/SQRT(Z*2+(R=X)*2+
              (R+Y)*2))x(R=X)/(Z*2+(R=X)*2)+
              ((R=Y)/SQRT(Z*2+(R+X)*2+(R=Y)*2)+(R+Y)/SQRT(Z*2+(R+X)*2+
              (R+Y)*2))x(R+X)/(Z*2+(R+X)*2)+
              ((R=X)/SQRT(Z*2+(R+Y)*2+(R=X)*2)+(R+X)/SQRT(Z*2+(R+Y)*2+
              (R+X)*2))x(R+Y)/(Z*2+(R+Y)*2)))));
              BYD+(INT1+INT2)/39.37;
      I+1;     J+1;
      FOR I+1 STEP 1 UNTIL 5 DO
      BEGIN
              B11+10=7xIxBYD/(4x(DIA*2));
              DATUM[I]+B11;
              FOR J+1 STEP 1 UNTIL 10 DO
              BEGIN
                  TORQUE+80=5xJ;
                  IA+TORQUE/(NAxAxB11));
                  DATA[I,J]+IA;
              END;
      END;
      WRITE(LP,<"THE TOTAL MOTOR LENGTH IS",F6.3,X1,"INCHES">,L));




      WRITE(LP,<"THE RADIUS OF THE FIELD COILS IS",F6.3,"INCHES">,R1));
      WRITE(LP,<"THE FLEXURE GAP BETWEEN FIELD COIL WINDINGS IS",
          F6.3,"INCHES">,D));
      WRITE(LP,<"DISTANCE FROM CENTER OF FIELD COIL TO POINT OF",X1,
          "AVERAGE FLUX DENSITY IS",F6.3,"INCHES">,W));
      WRITE(LP,<"FIELD COIL RADIUS+WINDING THICKNESS IS",F6.3,"INCHES">,
          RR));
      WRITE(LP,<"WIRE DIAMETER IS",F6.3,"INCHES">,DIAX39.37));
      WRITE(LP,<"ARMATURE FACE AREA IS",F6.3,"INCHES">,AX39.37*2));
      WRITE(LP,<"# OF WIRE TURNS ON ARMATURE IS",F6.3>,NA));
      WRITE(LP[DBL]);
      WRITE(LP,<"FLUX DENSITY",X3,"ARMATURE CURRENT",X2,"FIELD CURRENT">)
      ;
      FOR I+1 STEP 1 UNTIL 5 DO BEGIN
      WRITE(LP[DBL]);
      FOR J+1 STEP 1 UNTIL 10 DO BEGIN
      WRITE(LP,FOUT1,DATUM[I],DATA[I,J],I);
      IF J=10 THEN WRITE(LP,<"AN ARMATURE CURRENT OF",F5.2,"AMPERES",X1,
          "WILL PRODUCE THE MAXIMUM TORQUE WITH A FIELD CURRENT OF",
          I2,"AMPERES">,DATA[I,10],I);
      END;  END;
      WRITE(LP[DBL]);   WRITE(LP[DBL]);
      WRITE(LP,<"THE PROCESSOR TIME IS",F10.4,"SECONDS">,TIME(2)/60));
END.
```

THE TOTAL MOTOR LENGTH IS 2.060 INCHES
THE RADIUS OF THE FIELD COILS IS 1.060INCHES
THE FLEXURE GAP BETWEEN FIELD COIL WINDINGS IS 0.400INCHES
DISTANCE FROM CENTER OF FIELD COIL TO POINT OF AVERAGE FLUX DENSITY IS 0.730INCHES
FIELD COIL RADIUS+WINDING THICKNESS IS 1.340INCHES
WIRE DIAMETER IS 0.032INCHES
ARMATURE FACE AREA IS 1.640INCHES
OF WIRE TURNS ON ARMATURE IS42.000

FLUX DENSITY   ARMATURE CURRENT   FIELD CURRENT

4.37@-03   4.12@+00   3
AN ARMATURE CURRENT OF 4.12AMPERES WILL PRODUCE THE MAXIMUM TORQUE WITH A FIELD CURRENT OF 3AMPERES

5.82@-03   3.09@+00   4
AN ARMATURE CURRENT OF 3.09AMPERES WILL PRODUCE THE MAXIMUM TORQUE WITH A FIELD CURRENT OF 4AMPERES

THE TOTAL MOTOR LENGTH IS 2.050 INCHES
THE RADIUS OF THE FIELD COILS IS 1.060INCHES
THE FLEXURE GAP BETWEEN FIELD COIL WINDINGS IS 0.400INCHES
DISTANCE FROM CENTER OF FIELD COIL TO POINT OF AVERAGE FLUX DENSITY IS 0.730INCHES
FIELD COIL RADIUS+WINDING THICKNESS IS 1.420INCHES
WIRE DIAMETER IS 0.032INCHES
ARMATURE FACE AREA IS 1.640INCHES
OF WIRE TURNS ON ARMATURE IS42.000

FLUX DENSITY   ARMATURE CURRENT   FIELD CURRENT

5.50@-03   3.27@+00   3
AN ARMATURE CURRENT OF 3.27AMPERES WILL PRODUCE THE MAXIMUM TORQUE WITH A FIELD CURRENT OF 3AMPERES

7.34@-03   2.45@+00   4
AN ARMATURE CURRENT OF 2.45AMPERES WILL PRODUCE THE MAXIMUM TORQUE WITH A FIELD CURRENT OF 4AMPERES
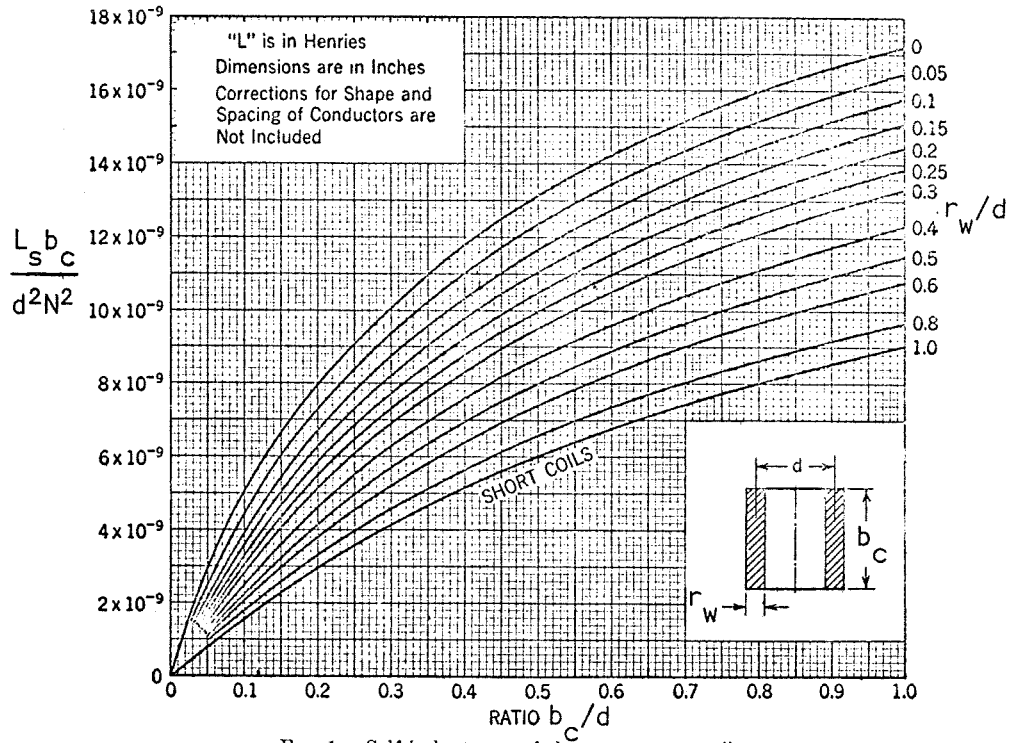
APPENDIX G

INDUCTANCE OF CIRCULAR COILS[1]

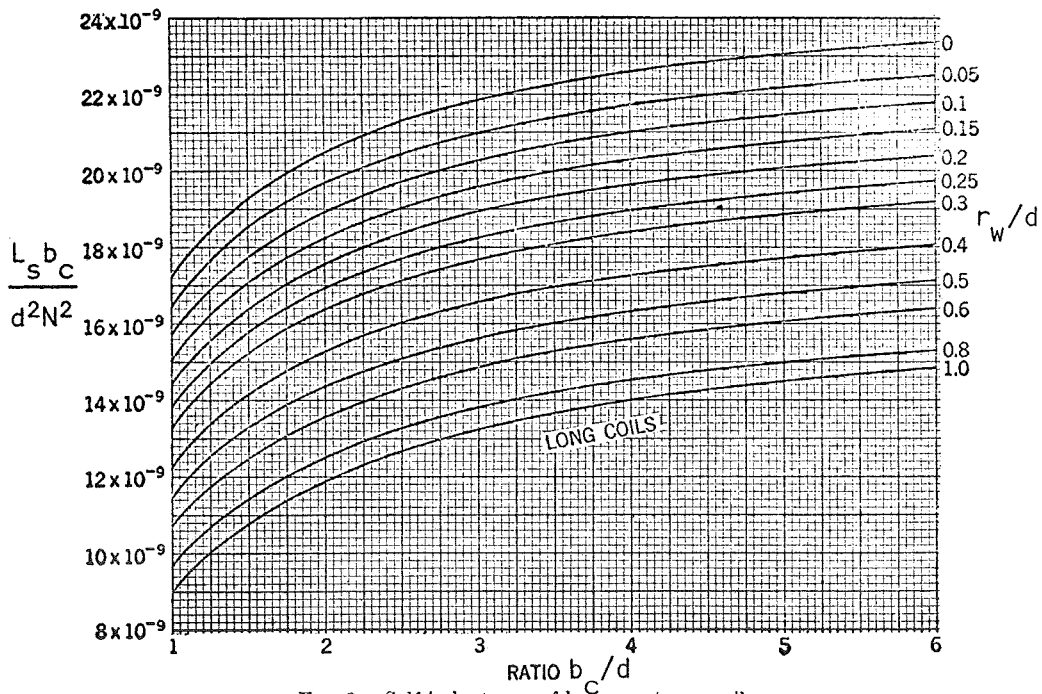Fig. 1.—Self-inductance of short reactance coils.

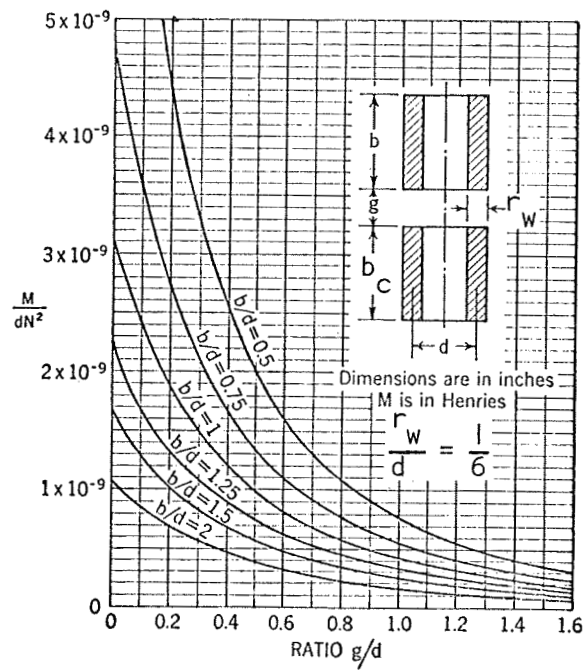Fig. 2.—Self-inductance of long reactance coils.

FIG. 3.—Mutual inductance of reactance coils with the same axis.

Bibliography

1. Dwight, H., _Electrical Coils and Conductors_, 1945, p. 266.

APPENDIX H

ANALYSIS OF THE UNITY GAIN PHASE SHIFTER

The unity gain phase shifter was originally developed by James
J. Collins[1]. Since no analysis of the circuit was presented, examination
of the circuit operation was undertaken. The following schematic presents
the unity gain phase shifter in a general form.
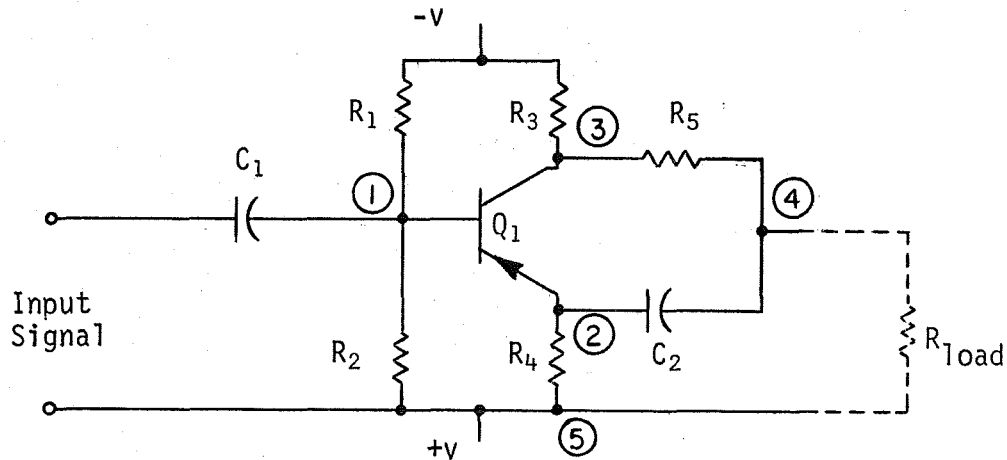
For purposes of analysis, C_1 is considered a virtual short at
the frequencies of interest. In addition, the following parameters
are considered equal to zero:

hoe = 0

hre = 0

G_{Load} = 0

The following floating admittance can be formed from the above schematic:

	①	②	③	④	⑤
①	$g_1 + g_2 + \dfrac{1}{hie}$	$\dfrac{-1}{hie}$	0	0	$-g_1 - g_2$
②	$\dfrac{-1}{hie} - \dfrac{hie}{hie}$	$g_4 + sC_2 + \dfrac{+1}{hie} + \dfrac{hfe}{hie}$	0	$-sC_2$	$-g_4$
③	$\dfrac{hfe}{hie}$	$\dfrac{-hfe}{hie}$	$g_3 + g_5$	$-g_5$	$-g_3$
④	0	$-sC_2$	$-g_5$	$g_5 + sC_2$	0
⑤	$-g_1 - g_2$	$-g_4$	$-g_3$	0	$g_4 + g_3 + g_1 + g_2$

Node 5 is grounded

$$\frac{E_4}{E_1} = \frac{E_4}{I_1} \cdot \frac{I_1}{E_1} = \frac{\Delta_{55,\,14}}{\Delta_{55,\,11}} = A_v$$

$$\Delta_{55,\ 14} = (\frac{1}{hie} + \frac{hfe}{hie})(\frac{hfc}{hie}\ g_5 + sC_2g_3 + sC_2g_5) +$$

$$(g_4 + sC_2 + \frac{1}{hie} + \frac{hfe}{hie}(\frac{-hfeg_5}{hie})$$

$$\Delta_{55,11} = (g_4 + sC_2 + \frac{1}{hie} + \frac{hfe}{hie})(g_3g_5 + sC_2g_3 + g_5sC_2)$$

$$-sC_2(\frac{hfe}{hie}g_5 + sC_2g_3 + sC_2g_5)$$

$$A_v = \left[\frac{\frac{1}{hie}(sC_2g_3 + sC_2g_5 + sC_2g_3hfe - hfeg_5g_4)}{g_3g_4g_5 + sC_2g_3g_4 + g_4g_5sC_2 + g_3g_5sC_2 + \frac{g_3g_5}{hie}} + \right.$$

$$\left.\frac{sC_2g_3}{hie} + \frac{g_5sC_2}{hie} + \frac{hfe}{hie}g_3g_5 + sC_2g_3\frac{hfe}{hie}\right]$$

$$= \frac{[[\frac{sC_2(g_5 + g_3(1 + hfe))}{hfeg_5g_4}] - 1]}{[\frac{sC_2[(g_3g_4 + g_4g_5 + g_3g_5)hie + g_5 + g_3(hfe + 1)]}{hfeg_5g_4} +}$$

$$\frac{g_3[g_4hie + (hfe + 1)]}{hfeg_4}]$$

$$= \frac{\frac{hfeg_4}{g_3[g_4hie + (hfe + 1)]} \cdot [[\frac{sC_2(g_5 + g_3(1 + hfe))}{hfeg_5g_4}] - 1]}{\left[\frac{sC_2[(g_3g_4 + g_4g_5 + g_3g_5)hie + g_5 + g_3(hfe + 1)]}{hfeg_5g_4} + 1\right]}$$

Now, let

(1) $g_3 = g_4, (hfe + 1) \gg g_4 hie, hfe \approx (hfe + 1)$

$$A_v = \frac{1\left[\dfrac{sC_2(g_5 + g_3(1 + hfe)}{hfe g_5 g_3} - 1\right]}{\left[sC_2\left[\dfrac{(g_3{}^2 + 2g_3 g_5)hie + g_5 + g_3(hfe + 1)}{hfe g_5 g_4}\right] + 1\right]}$$

Also

(2) $g_3(hfe + 1) \gg g_5$

$g_3((hfe + 1) \gg (g_3{}^2 + 2g_3 g_5)hie$

The voltage gain is now in time-constant form.

$$A_v = \frac{-1(-s\tau_1 + 1)}{(s\tau_2 + 1)}$$

where

$$\tau_1 = \frac{C_2 g_3(1 + hfe)}{hfe g_5 g_3} \approx \frac{C_2}{g_5}$$

$$\tau_2 = \frac{C_2 g_3(hfe + 1)}{hfe g_5 g_4} \approx \frac{C_2}{g_5}$$

Using assumptions

(1) & (2)

$$\tau_1 = \tau_2 = \tau = C_2R_5 \qquad\qquad (3)$$

$$A_v = \frac{-1(-sC_2R_5 + 1)}{(sC_2R_5 + 1)} = \frac{-1(1 - sC_2R_5)}{(1 + sC_2R_5)}$$

Let $s = j\omega$

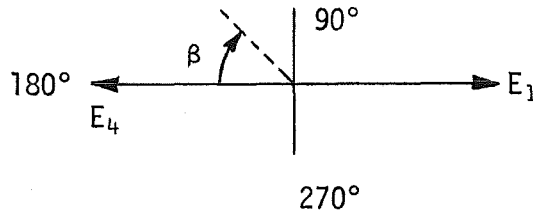$$A_v = \frac{-1(1 - j\omega C_2R_5)}{(1 + j\omega C_2R_5)}$$

$$\beta \stackrel{\Delta}{=} \text{Phase Shift} = \alpha_1 - \alpha_2 = \tan^{-1}(\omega(-\tau_1)) - \tan^{-1}(\omega\tau_2)$$

From (3)

$$\beta = -\tan^{-1}\omega\tau - \tan^{-1}\omega\tau = -2\tan^{-1}\omega\tau$$

$$= -2\tan^{-1}\omega R_5C_2$$

Conclusion

At $s = 0$, the phase of the voltage gain is $180°$. As $s \to \infty$ the phase $\to 0$ in a CW direction as the following phasor so indicates.

156

The effect of hoe on the analysis was investigated on a Burroughs

B5500 Algol machine. Hoe was varied between $0 - 5 \times 10^{-5}$ mhos. The

maximum phase shift was found to be $0.1°$ for R_5 varied between 10-100

kilohms.

Bibliography

1. Collins, James J., "Single Transistor Produces Low Cost Phase Shifter,"
   Electronics Handbook of Circuit Design, New York, 1967, McGraw-Hill
   Book Co., Inc.